



Universitat Autònoma de Barcelona

ADVERTIMENT. L'accés als continguts d'aquesta tesi queda condicionat a l'acceptació de les condicions d'ús establertes per la següent llicència Creative Commons:  http://cat.creativecommons.org/?page_id=184

ADVERTENCIA. El acceso a los contenidos de esta tesis queda condicionado a la aceptación de las condiciones de uso establecidas por la siguiente licencia Creative Commons:  <http://es.creativecommons.org/blog/licencias/>

WARNING. The access to the contents of this doctoral thesis it is limited to the acceptance of the use conditions set by the following Creative Commons license:  <https://creativecommons.org/licenses/?lang=en>

Post-Synthetic Modification of Metal-Organic Frameworks by Solid-Gas Ozonolysis

Heng Xu

Doctoral Thesis
PhD in Chemistry

Supervisors

Prof. Dr Daniel Maspoch and Dr. Inhar Imaz

Tutor

Dr. Félix Busqué

Catalan Institute of Nanoscience and Nanotechnology
Department of Chemistry-Faculty of Science

2019

TABLE OF CONTENTS

<i>Table of content</i>	i
<i>Acknowledgements</i>	v
<i>Abstract</i>	vii
<i>Resumen</i>	ix
CHAPTER 1: INTRODUCTION TO METAL-ORGANIC FRAMEWORKS AND POST-SYNTHETIC MODIFICATION	1
1.1 INTRODUCTION OF MOFs.....	3
1.2 DESIGN AND SYNTHESIS OF MOFs	6
1.2.1 Isorecticular synthesis	6
1.2.2 Modulated synthesis	12
1.3 POST-SYNTHETIC MODIFICATION OF MOFs.....	15
1.3.1 Solid–liquid phase post-synthetic modification	16
1.3.1.1 Covalent post-synthetic modification (CPSM)	16
1.3.1.2 Pos- <i>tsynthetic</i> metal exchange (PSME).	19
1.3.1.3 Post-synthetic linker exchange (PSLE).....	22
1.3.1.4 Post-synthetic insertion (PSI).....	25
1.3.1.5 Post-synthetic elimination	29
1.3.2 Solvent-less post-synthetic modification.....	32
1.3.2.1 Solid-solid phase post-synthetic modification	32
1.3.2.2 Solid-gas phase post-synthetic modification.....	36
1.3.3 Post-synthetic modification by solid-gas ozonolysis.....	40
1.4 APPLICATIONS OF METAL-ORGANIC FRAMEWORKS	44
1.4.1 Gas storage.....	44
1.4.2 Molecular separation	48
1.4.3 Catalysis.....	50
1.5 REFERENCE	54
CHAPTER 2: OBJECTIVES	63
CHAPTER 3: SINGLE-CRYSTAL-TO-SINGLE-CRYSTAL POST- SYNTHETIC MODIFICATION OF A METAL–ORGANIC FRAMEWORK VIA OZONOLYSIS	67

3.1 INTRODUCTION.....	69
3.2 RESULTS AND DISCUSSION	70
3.2.1 Synthesis of zirconium-based MOF (ZrEBDC)	70
3.2.2 Establishment of set up for solid-gas ozonolysis.....	72
3.2.3 Solid-gas ozonolysis of ZrEBDC	74
3.2.4 Identification of SC-SC transformation.....	75
3.2.5 Selectively transformation to carboxylic or aldehyde.	90
3.2.6 Extended application exploration: anti-virus investigation based on ozo-ZrBDC particles.....	93
3.3 CONCLUSIONS	94
3.4 EXPERIMENTAL SECTION	95
3.4.1 Materials and Characterization	95
3.4.2. Synthesis.....	97
3.4.3 Solid-gas phase procedure.	98
3.4.4 Soft-ligand exchange experiment.	98
3.4.5 Reduction and oxidation work up of Ozo-ZrBDC.	98
3.5 REFERENCE	99
CHAPTER 4: POST-SYNTHETIC SELECTIVE LIGAND CLEAVAGE BY SOLID-GAS PHASE OZONOLYSIS FUSES MICROPORES INTO MESOPORES IN METAL-ORGANIC FRAMEWORKS	103
4.1 INTRODUCTION.....	105
4.2 RESULTS AND DISCUSSION	107
4.2.1 Zr-fcu-azo/sti System.....	107
4.2.1.1 System Validation	107
4.2.1.2 Synthesis and Porosity of Zr-fcu-azo/sti-X%.....	110
4.2.1.3 Ozonolysis of Zr-fcu-azo/sti-X%	112
4.2.1.4 Washing of Zr-fcu-azo/sti-X%_OZ.....	114
4.2.1.5. Porosity Properties of Washed, Ozonated Zr-fcu-azo/sti-X%	116
4.2.2 Zr-fcu-bpdc/pdac System.....	120
4.2.2.1 Synthesis of Zr-fcu-bpdc/pdac-X%.....	122
4.2.2.2 Ozonolysis of Zr-fcu-bpdc/pdac-X%	124
4.2.2.3 Porosity of Zr-fcu-bpdc/pdac-X%_OZ	126
4.3 CONCLUSIONS	129

4.4 EXPERIMENTAL SECTION	130
4.4.1 Materials and Instruments.....	130
4.4.2 Synthesis and Activation of MOFs.....	130
4.4.3 Solid-gas Ozonolysis Treatment.....	131
4.5 REFERENCE	133
CONCLUSIONS	139
ANNEX 1	143
ANNEX 2	149

Memoria presentada per aspirar al Grau de Doctor per Heng Xu

Heng Xu

Vist i plau

Prof. Dr. Daniel Maspoch

ICREA Research Professor & Group Leader

Supramolecular Nanochemistry & Materials Group

Catalan Institute of Nanoscience and Nanotechnology

Dr. Inhar Imaz

Senior Research & Division Coordinator

Supramolecular Nanochemistry & Materials Group

Catalan Institute of Nanoscience and Nanotechnology

Dr. Félix Busqué Sánchez

Professor Agregat

Departament de Química

Universitat Autònoma de Barcelona

Bellaterra, 25 de Febrero de 2019

Abstract

This present PhD Thesis has been dedicated to the exploration and study the solid-gas phase ozonolysis as a quick, simple and versatile method for post-synthetic modification of metal-organic frameworks (MOFs).

In the first Chapter, a brief introduction to the origin of MOFs is given, followed by typical concepts for design and synthesis of the porous materials. We then pay special attention to the current methodologies that used for post-synthetic modifications of MOFs with state-of-the-art advancements and selected examples, aiming to place the reader in the context of the thesis. Additionally, the main applications of post-synthetically functionalized MOFs are provided.

In Chapter 2, the general and specific objectives of the Thesis are introduced.

In Chapter 3, we develop a new post-synthetic methodology for functionalization of MOFs based on the solid-gas ozonolysis. The generated ozonide rings are identified by nuclear magnetic resonance (NMR) technique. Moreover, the generality of this method has been proven by a single-crystal-to-single-crystal transformation, as confirmed by single-crystal X-Ray diffraction together with density functional theory (DFT) calculation. Finally, the amenability of ozonide functionality is demonstrated by selectively workup treatment.

Chapter 4 extends the use of the solid-gas ozonolysis to post-synthetic modification of MOF porosity. We show that, by carefully selecting mixed-ligand Zr-fcu-MOFs based on organic ligand pairs in which one ligand has ozone-cleavable olefin bonds and the other ligand is ozone-resistant, we were able to selectively break the cleavable ligand via ozonolysis to trigger fusion of micropores into mesopores within MOF framework. Thus, the mesoporous MOFs are subsequently created through removal of ligand fragments by washing or sublimation, as evidenced by their distinct gas sorption properties.

Resumen

Aquesta Tesi doctoral està dedicada a la investigació i l'estudi de l'ozonòlisi en fase solid-gas com un mètode ràpid, simple i versàtil per a la modificació post-sintètica de xarxes metalorgàniques (MOFs).

El primer Capítol inclou una breu introducció a l'origen dels MOFs i els conceptes per al disseny i síntesi de materials porosos. Després, fem èmfasi a les actuals metodologies utilitzades en les modificacions post-sintètiques de MOFs il·lustrant els principals avenços i exemples, amb l'objectiu de centrar al lector en el context d'aquesta Tesi. També s'hi expliquen les principals aplicacions de MOFs funcionalitzats post-sintèticament.

En el Capítol 2 s'hi exposen els objectius generals i específics d'aquesta Tesi.

En el Capítol 3 es desenvolupa la nova metodologia per a realitzar funcionalitzacions post-sintètiques de MOFs basades en l'ozonòlisi sòlid-gas. Els anells ozònids generats s'identifiquen per ressonància magnètica nuclear (RMN). Cal remarcar que aquest nou mètode s'ha demostrat mitjançant transformacions dins d'un mateix cristall, com s'ha confirmat per difracció de raigs X de monocristall conjuntament amb càlculs de teoria del funcional de la densitat (DFT). Finalment, la disposició de la funcionalitat ozònid és demostrada mitjançant un tractament selectiu posterior.

En el Capítol 4 s'estén l'ús de l'ozonòlisi sòlid-gas per a la modificació post-sintètica de la porositat de MOFs. Demostrem que, a través de la selecció de MOFs Zr-fcu amb mescla de lligands que consisteixen en parelles on un dels lligands conté enllaços olefina capaços de ser trencats per ozonòlisi i l'altre lligand és resistent a l'ozó, podem realitzar el trencament selectiu dels lligands mitjançant l'ozonòlisi per aconseguir la fusió de microporus en mesoporus en la mateixa estructura del MOF. Així, els MOFs mesoporosos es generen eliminant els fragments de lligand a través de rentats o sublimació, com ho evidencien les seves noves propietats d'adsorció.

Chapter 1

Introduction to Metal-Organic Frameworks and Post-Synthetic Modification

1.1 Introduction of MOFs

The interest of porous coordination polymers surfaced in the early 1990s by Robson and Hoskins^{1,2}. In their seminal work, they have shown the synthesis and construction of series of scaffold-like materials with extensive 3D frameworks by covalently bonding the rod-like connecting units.¹ Significantly, general principles concerning the design and construction of infinite frameworks were presented and they proposed the accessibility of constructing a large range of crystalline with porous and stable frameworks. Applications such as ion-exchange, sorption or catalytic properties were suggested. They even predicted that the introduction of catalytic species throughout the framework could be achieved by chemical functionalization. These visionary concepts set the basis for development of porous coordination polymers that would later be known as metal-organic frameworks (MOFs).

The term metal-organic framework (MOF) was popularized by Yaghi et al. in 1995 with report of a 3D crystalline material $[\text{Cu}(4,4'\text{-bpy})_{1.5}\cdot\text{NO}_3(\text{H}_2\text{O})_{1.25}]$ containing large opening channels by hydrothermal synthesis³, in addition of another microporous layered cobalt-trimesic framework that exhibited reversible sorption of aromatic guest molecules.⁴ Around the same time, Kitagawa et al. started exploring the methane adsorption properties of porous MOF materials at room temperature.⁵ In 1999, two archetypical MOF structures MOF-5⁶ and HKUST-1⁷ were reported with permanent porosity and maintained robust after removal of guest molecules. Several years later, Férey et al. reported a remarkable 3D framework combining judicious computational design and targeted chemistry. The highly stable MOF (named as MIL-101) exhibited large pore size ($\sim 30 - 34 \text{ \AA}$) and high surface area,⁸ which subsequently led to the creation of “breathing” MOFs with flexible frameworks.^{9,10} Up to date, more than 20,000 MOF structures have been successfully synthesized ranging from the frameworks with very low densities (0.126 g/cm^3)¹¹ to ultrahigh surface areas (more than $6000 \text{ m}^2/\text{g}$).^{12,13} Afterwards of that, a large number of exciting new MOF structures have been synthesized and widely investigated with their impressive stability including UiO-66¹⁴, MIL-101⁸, CAU-1¹⁵ and ZIF-8¹⁶, et al.

MOF structures are usually constructed by covalently linking inorganic metal nodes (metal ions or clusters) and organic linkers to make porous crystals of extended structures.^{6,17} The general principal formation of metal-organic frameworks is illustrated in Figure 1.1.

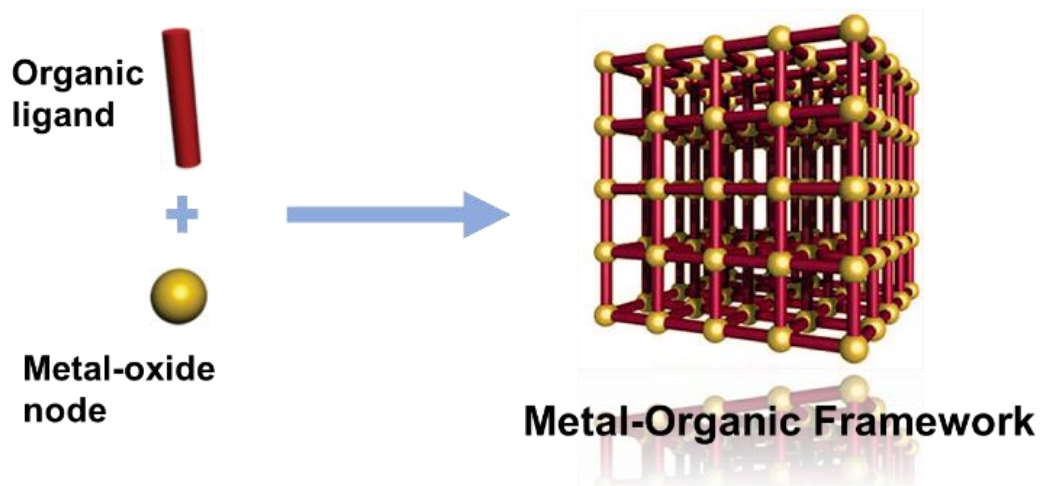
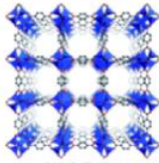

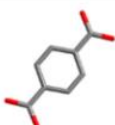
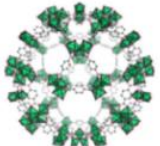
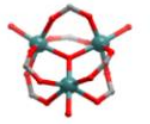
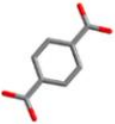
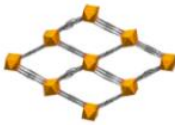
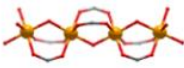
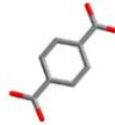
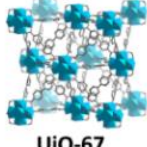
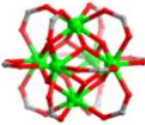
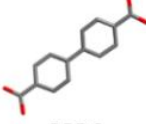
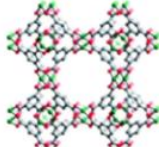
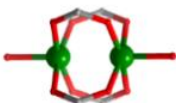
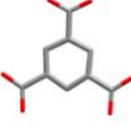

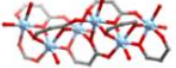
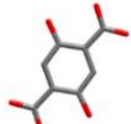

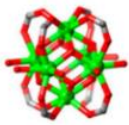
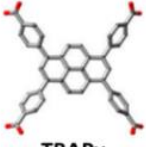
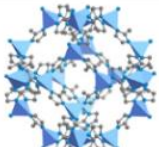
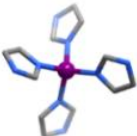



Figure 1.1. Schematic formation of metal-organic framework by combining organic linkers and metal ions.

Beyond the simpler single atoms used in early coordination networks,² diverse geometrical and multiple-connected metal clusters with rigid shapes were constructed according to their different coordination nature (e.g. paddle-wheel $\text{Cu}_2(\text{CO}_2)_4$ or octahedra $\text{Zn}_4\text{O}(\text{CO}_2)_6$). Even different connected metal clusters can be formed with the same metal (e.g. zirconium clusters). The geometrical combination of the adjacent metal clusters through covalent bonds with organic linkers has led to one-, two-, three-dimensional, even multi-dimensional frameworks (Table 1.1). The framework can infinitely expand in any direction to finally generate a porous polymer type structure with channels, voids or cavities depending on the connection design of the initial metal clusters. In addition, the design of organic linkers plays a significant role in the construction of MOFs. By judiciously selecting metal clusters and organic linkers, the resulting MOF materials can be designed and synthesized with predictable topology, pore size/shape, and functionalities for specific applications.

Table 1.1 Representations of MOF structures and corresponding metal clusters and organic linkers constituents.

MOF	Metal cluster	Organic linker
 MOF-5	 $Zn_4O(CO_2)_6$	 BDC
 MIL-101-Cr	 $Cr_3O(OH)_3(CO_2)_6$	 BDC
 MIL-53-Fe	 $[Fe(OH)(CO_2)]_n$	 BDC
 UiO-67	 $Zr_6O_4(OH)_4$	 BPDC
 HKUST-1	 $Cu_2(CO_2)_4$	 TMA
 MOF-74-Mg	 $[Mg_3O_3(CO_2)_3]_n$	 DBDC
 NU-1000	 $Zr_6O_4(OH)_8$	 TBAPy
 ZIF-8	 Zn	 MIM

1.2 Design and synthesis of MOFs

Metal-organic frameworks (MOFs) are typically obtained by direct synthesis such as “one-pot” mixing of metal ions and organic precursors, modulated synthesis or slow diffusion¹⁸, in which the organic linkers remain intact and maintain their functionality to the final crystalline MOF materials. Besides, some additive reagents are often employed as modulators during the MOF synthesis process in order to slow down the crystal growth and nucleation process,¹⁹ which lead to controlled manipulation in crystallinity, crystal size and morphology for obtaining MOF materials. It is feasible to use more than one type linkers in the synthesis of mixed-linker MOFs (also known as multivariate-MOF), by which multiple functionalities are incorporated into one unique MOF material.²⁰

1.2.1 Isoreticular synthesis

The concept of isoreticular synthesis or isoreticular expansion was proposed by Yaghi et al.²¹ in 2002 which is now used as a popular strategy in synthesis of MOFs. By increasing the length of similar organic linkers, isoreticular synthesis expands the metrics of MOF frameworks without changing the underlying topologies. Many highly porous MOFs have been successfully created with enlarged pore openings,¹¹ ultra-high surface areas and tunable functionalities.²² This strategy is accomplished through utilizing the same metal clusters and increasing size of organic linkers while maintaining the same coordination geometry as the parent MOF.

One of the first examples of the isoreticular MOF series was based on the MOF-5 topology. In this prototype MOF structure, each octahedral $[Zn_4O(CO_2)_6]$ cluster was built from four zinc ions, one oxygen atom and six carboxylate groups generated from the ditopic BDC (terephthalate) linkers. Octahedral zinc clusters were covalently linked by adjacent BDC linkers to form an extending 3-dimensional *pcu* topology network with elegant crystallinity and highly porosity. Depending on the different orientations of zinc SBUs, two types of spheres with diameter 15.1 Å and 11.0 Å fitting the large and small cavity are present, respectively (Figure 1.2). The architectural robustness of MOF-5 allows for gas sorption performance-up to 2320 m²/g, which is substantially higher than those found for the zeolites and activated carbon.²³

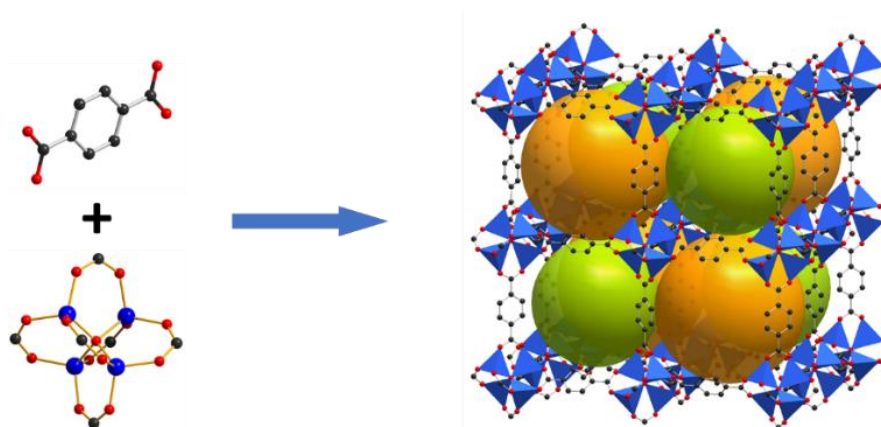


Figure 1.2. The archetypal MOF-5 structure constructed from organic BDC linker and $[\text{Zn}_4\text{O}(\text{CO}_2)_6]$ cluster.

The framework rigidity of MOF-5 also make it possible to be expanded by replacing the BDC linker with other linear ditopic carboxylic linkers. Following the strategy of isorecticular synthesis, a series of robust MOF structures (termed IRMOFs) with identical cubic topology but distinctive functionalities were synthesized by changing the sizes of organic linkers.²¹ These IRMOF structures with elongated linkers usually exhibited expanded interior cavities and exceptional porosities. For example, utilizing BPDC (biphenyldicarboxylate) and TPDC (terphenyldicarboxylate) as organic linkers created IRMOF-10 and IRMOF-16 structures with larger diameter of pores up to 18.5 Å and 28.8 Å, respectively (Figure 1.3). Moreover, the smallest isorecticular structure $[\text{Zn}_4\text{O}(\text{fumarate})_3]$ was generated by replacing BDC linkers with fumarate.²⁴ The successful practicals of isorecticular expansion of MOF-5 demonstrated that it is feasible to reticulate suitable metal clusters and organic linkers into extensive networks with predicted topology and multiple functionalities.

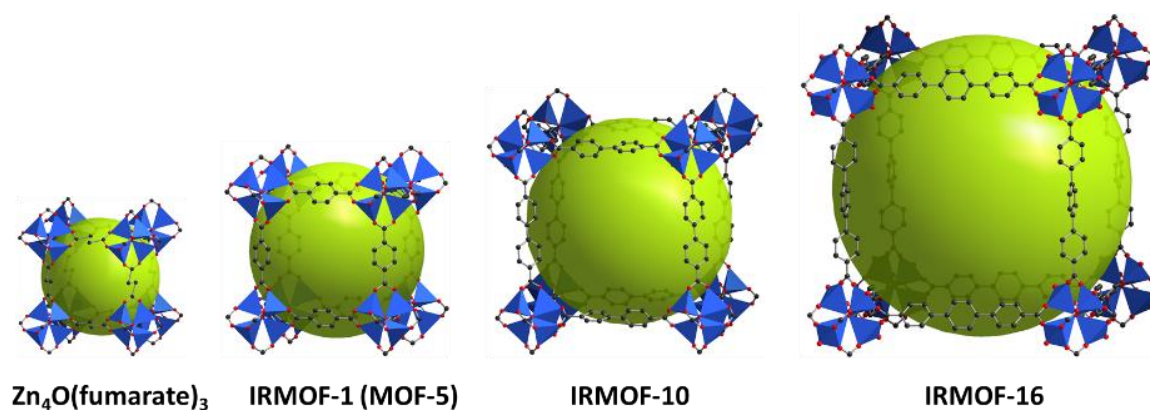


Figure 1.3. Representative extended MOF structures based on MOF-5 with rigid ditopic linkers from Zn-fumarate to IRMOF-16 by isorecticular synthesis strategy.

Another key point in preparing an isorecticular series is that one must ensure specific reaction condition generates the same inorganic cluster in each reaction.¹¹ Any change of a metal cluster including size, geometry or coordination environment probably causes the change in the final framework topology. Indeed, controlling the metal clusters consistency should be an essential prerequisite to successful isorecticular synthesis in which the coordination geometry and topology is maintained as the same as parent MOF. In spite of the typical feature of isorecticular expansion is to maintain the characteristics of parent MOF, there have been some isorecticular MOF series reported using different metal clusters. One of the most representative examples was demonstrated in the flexible MIL-53(Cr)²⁵ structure in which the isorecticular synthesis were accomplished with other trivalent metals, including Al³⁺, Fe³⁺, Sc³⁺, and V³⁺.²⁶⁻²⁹

Normally, longer organic linkers provide larger interior space and more adsorption sites within a given MOF structure. However, the large cavity within the crystal framework makes it prone to form interpenetration structures, such as the doubling penetrating structures IRMOF-9, -11, -13 and -15.²¹ The existence of interpenetration always leads to a reduction of porosity, surface area and accessibility of opening sites in the MOFs. Although interpenetrating frameworks often enhance guest-framework interactions and increase adsorption sites for small gases such as H₂, O₂ and N₂,³⁰ those are unfavorable for applications involving large molecules such as catalysis and drug delivery.³¹⁻³³ Due to the framework topology tends to influence the structural interpenetration significantly, one of most effective way to prevent interpenetration is by constructing MOFs whose topology does not allow to accommodate an additional net, thus prohibit the framework interpenetrations during isorecticular synthesis of MOF materials.^{34,35}

A rather famous example demonstrating the topology benefit of network was the isorecticular expansion of MOF-74 structures.²² Early investigation of Mg-MOF-74 structures showed that the infinite inorganic rod-like clusters were bridged by the organic linker DOT (dioxidododecaphthalic acid) to produce *bnn* (hexagonal boron nitride) parallel rod packing with one-dimensional 10.3 × 5.5 Å channels.³⁶ The structural feature of the infinite Mg-O-C connection and the short distance between the carboxylate linkers provide steric hindrance for the formation of a secondary network. Stepwise expansion of the original DOT phenylene unit to 2, 3, 4, 5, 6, 7, 9, 11 phenylene units leads to a series of non-interpenetrating Mg-MOF-74 isorecticular structures (termed IRMOF-74-I to IRMOF-74-XI) with increasing pore diameters ranging from 14 to 98 Å. Remarkably, IRMOF-74-XI possess the largest pore diameter of 98 Å in the reported MOFs to date (Figure 1.4). All the IRMOF-74 members show the non-interpenetrating topologies and the rigid frameworks as confirmed by their permanent porosity

and high thermal stability. The expanded channels can even encapsulate the large biomolecules such as green fluorescence protein without folding. Significantly, isoregular expansion also provide open coordination metal sites within the IRMOFs, which are of benefit to preform post-synthetic modifications on the surface of frameworks.

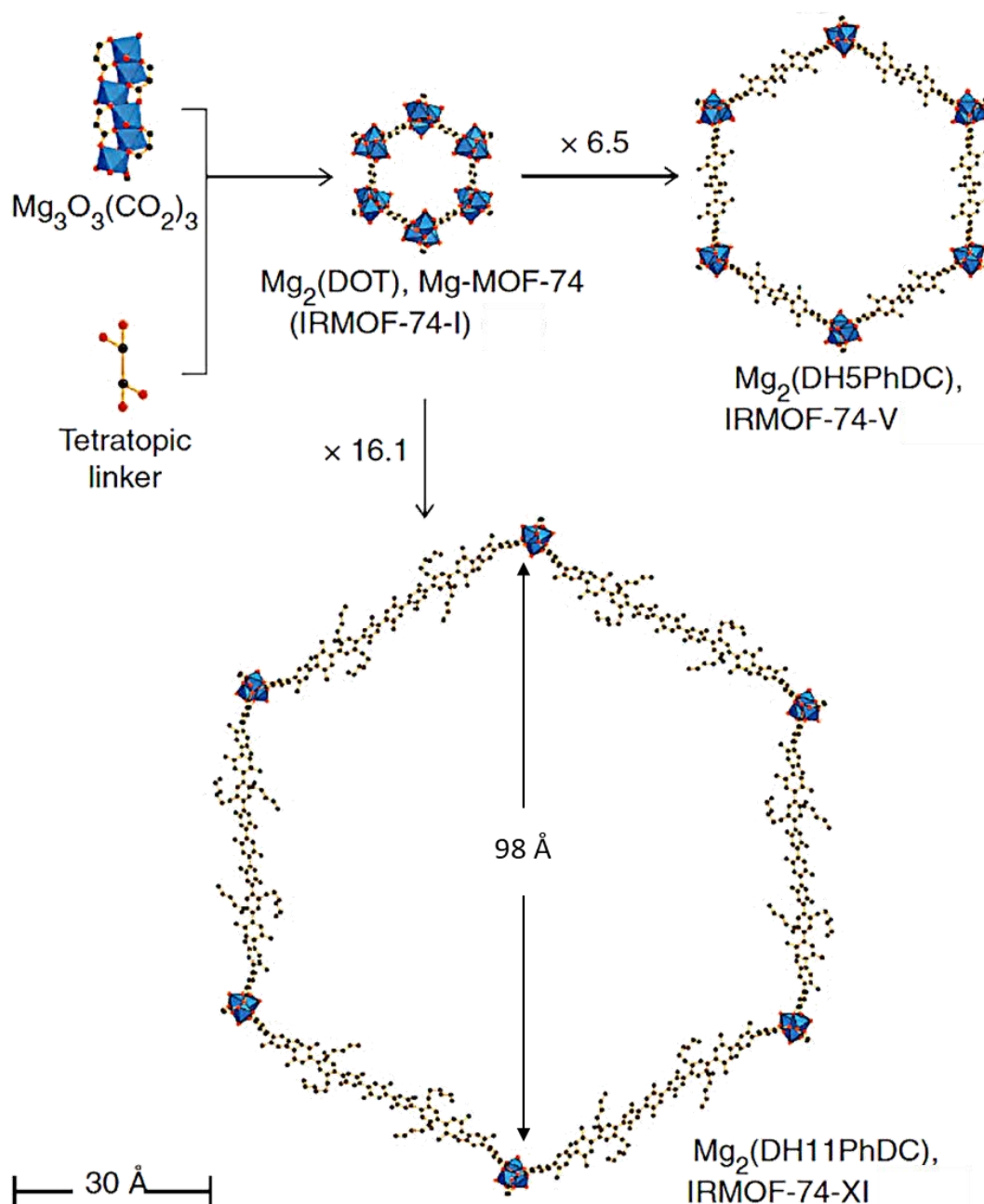


Figure 1.4. Illustration of isoregular synthesis of IRMOF-74 series with organic linkers from DOT to extended ones with 11 phenylene units, expanding the pore aperture up to 98 Å.

After functionalization with hydrophilic oligoethylene glycol, IRMOF-74-VII-oeg exhibits substantial uptake of myoglobin molecules because of myoglobin's hydrophilic surface. However, IRMOF-74-VII functionalized by hydrophobic hexyl chains only shows a negligible

amount of myoglobin inclusion. It is remarkable that the crystallinity of the IRMOF-74 materials is fully maintained throughout the inclusion process, which is proved by the coincident PXRD patterns as the starting materials.

Associated with isorecticular expansion, computational modelling has been employed to design and screen MOFs in recent years,¹² except for its widely application in calculation of adsorption isotherms, binding energies and transport behavior of MOFs.³⁷⁻³⁹ Among them, NU-100 series is the representative example of combining the computational modelling and topology-guided design in isorecticular synthesis. The initial structure was designed based on a copper (3,24)-paddlewheel connected network which had the non-interpenetrated *rht*-topology. Through computational modelling method, by elongating the dendritic hexatopic linker, a target MOF structure was established *in silico* and predictively characterized its structure, surface area and storage capacity. Experimental synthesis and characterization of the obtained NU-100 crystals revealed the highly consistency between the simulated structure and experimental results. The final framework featured hierarchical porosity and three types of cavities of 13.4, 15.4 and 27.4 Å in diameter, as evidenced by the computational simulation and sorption-based pore size analysis (Figure 1.5). Upon the removal of guest solvent by elegant SCD (supercritical CO₂) processing, NU-100 was activated without significantly diminishing the porosity. Subsequent experimental BET measurement reveals its large pore volume (2.82 cm³/g) and high surface area (6143 m²/g), which stands out as one of the highest reported for porous materials. The extremely high accessible porosity also endowed NU-100 excellent performance in high-pressure H₂ and CO₂ storage.³⁸ Moreover, capitalizing on the same topology as NU-100, two more isorecticular frameworks termed NU-109 and NU-110 were successfully synthesized with expanded hexacarboxylate linkers, both of which exhibited record ultrahigh surface areas up to 7010 and 7140 m²/g, respectively.³⁹

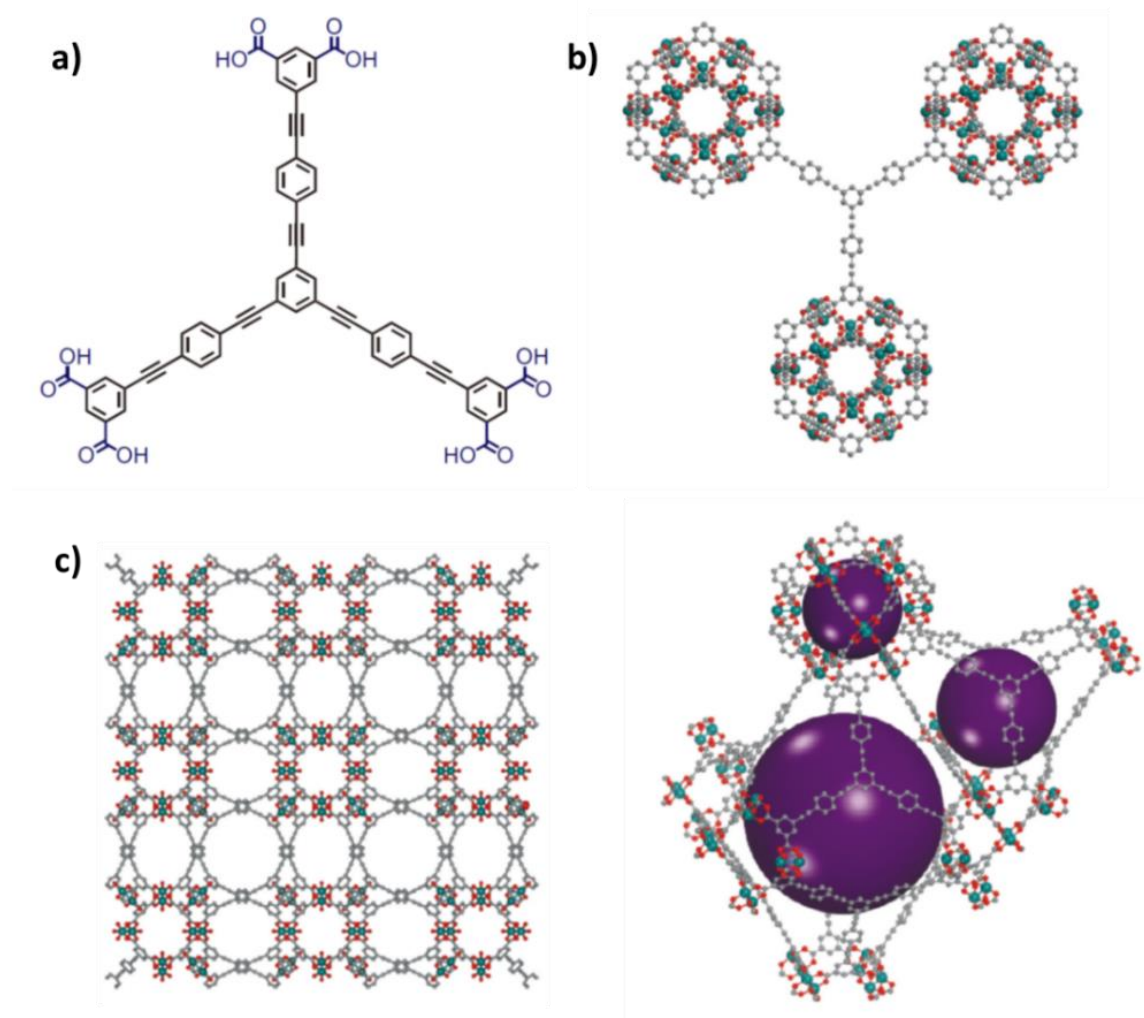


Figure 1.5. Illustrations of NU-100 by the structural composition of a) hexa-carboxylate organic linker, b) cubaooctahedral building units connected by the linker and c) hierarchical pores and three different cages within the framework.

The flexibility of isorecticular synthesis is further demonstrated in the preparation of multivariate metal-organic frameworks (MTV-MOFs), which contain a vast array of components within their structures.^{20,40} These MOFs are often achieved by incorporating mixed-linkers or mixed-metals into unique topological framework during one-pot synthesis or through post-synthetic modification. An early example of mixed-linker MOFs was the series of MTV-MOF-5 reported by Yaghi and coworkers.⁴³ In their study, eight distinctive functionalities including $-\text{NH}_2$, $-\text{NO}_2$, $-\text{Br}$, $-\text{Cl}_2$, $-(\text{CH}_3)_2$, $-(\text{OC}_3\text{H}_5)_2$, $-\text{C}_4\text{H}_4$, and $-(\text{OC}_7\text{H}_7)_2$ were incorporated into a singular framework (Figure 1.6). The backbone (zinc oxide and phenylene units) of these structures is ordered, although the distribution of functional groups is disordered. The resulted multifunctional material exhibits up to 400% selectivity increment for carbon dioxide over carbon monoxide compared with its best same-link counterparts.

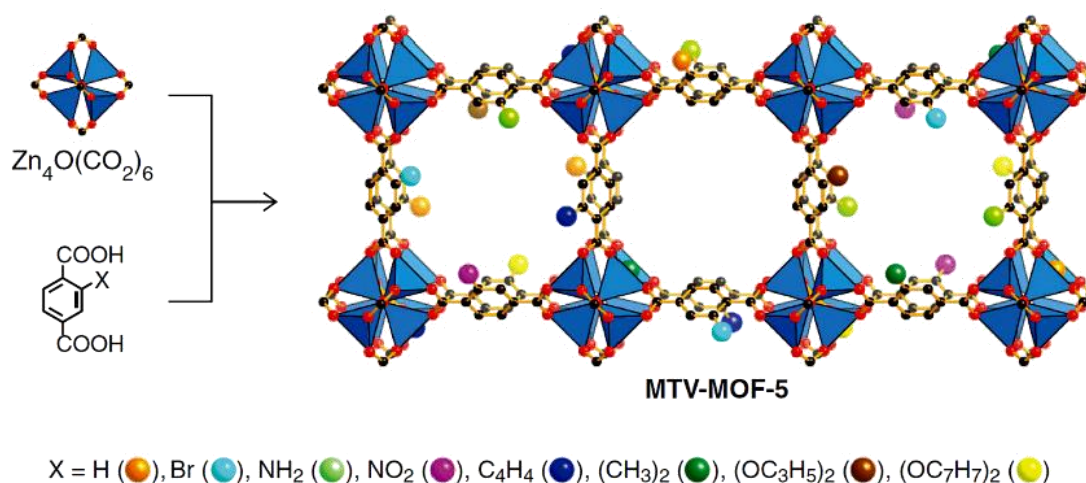


Figure 1.6. The MTV-MOF-5 structure with heterogeneous interior bearing multiple functionalities.

The mix-linker method largely extended the utility of the concept of isoreticular synthesis that desired functionalities can be achieved by selectively tuning the length or geometry of organic linkers. In addition, an interesting feature for some mix-linker MOFs with robust backbones is that they have quite high tolerance for partial building units' absence. This feature makes them suitable for developing other functional isoreticular structures through post-synthetic linker installation/elimination, which has been a major focus of study in recent years.⁴¹⁻⁴³

1.2.2 Modulated synthesis

During synthesis of crystalline MOF materials, mixture of metal ions and organic linkers in some cases only lead to amorphous products rather than crystalline MOF materials as expected.⁴⁴ By means of adding competitive modulating agents into the reaction mixture, the nucleation process was inhibited thus the crystal growth was slowed down. This reversibly binding between the modulator and metal clusters allows for the equilibrium to correct and regulate the defects, resulting in increased crystallinity for MOF products. Modulating agents normally have the similar binding fashion with metal clusters but have a lower binding affinity than the desired linkers. One of the most commonly used modulators in MOF synthesis, including but not limited to acetic acid, benzoic acid, hydrochloric acid and trifluoroacetic acid.^{45,46}

Early examples of modulated synthesis were reported by Kitagawa and coworkers in controlling the morphology of crystalline MOFs.^{47,48} In their study, acetic acid was employed as the modulated reagent to perturb the framework extension. The nucleation process is induced to

construct the framework, leading to anisotropic crystal growth in the nanorod morphology.⁴⁷ Another notable work from the same group by modulation method was controlling the morphological transition of HKUST-1 crystals. By tuning the proportion of lauric acid as modulator during synthesis process, crystal growth orientation was selectively and precisely controlled in determining the $\langle 100 \rangle$ or $\langle 111 \rangle$ -growth under microwave irradiation, which finally produced homogeneous crystals in octahedron, cuboctahedron and cube morphology, respectively (Figure 1.7). Furthermore, this method successfully led to designed crystal morphologies with oriented growth on gold-coated substrates, which allowed potentials application in MOF crystal engineering as well as selectively catalytic activity.⁴⁸

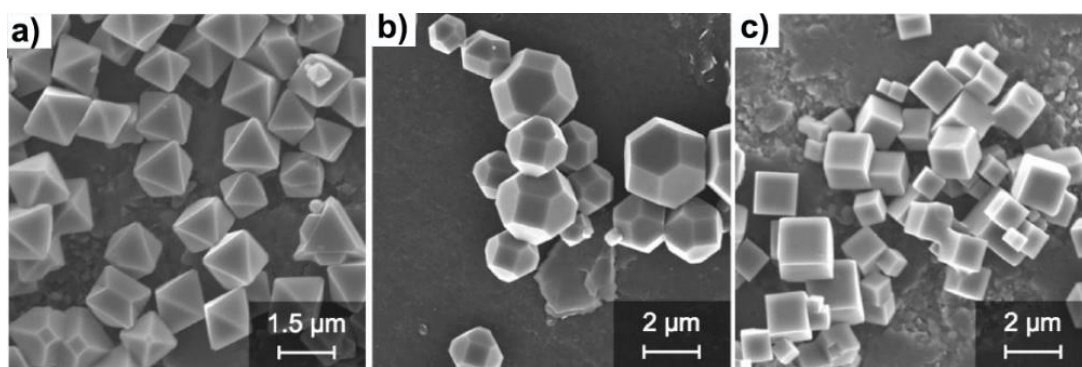


Figure 1.7. Morphology transition of HKUST-1 crystals modulated by lauric acid in a) 50, b) 75 and c) 125 equivalence.

As a useful crystallization method, modulated synthesis has been developed in the past few years in order to increase the crystallinity, stability and porosity of MOFs, especially for those with high hydrothermal and chemical stability such as UiO-66 (Zr) or MIL-101 (Cr) MOFs.⁴⁹⁻⁵¹ To investigate the influence of the modulators, Behrens and coworkers did the early research in the synthesis of UiO-66 (Zr-BDC-NH₂), UiO-67 (Zr-BPDC) and UiO-68 (Zr-TPDC-NH₂) by adopting benzoic acid, acetic acid and water as three different modulators. It was found that the increasing addition of benzoic acid resulted in larger size of UiO-66 crystals. Both the acetic acid and benzoic acid had the ability to tune the size and morphology of the Zr-based MOFs. Moreover, the synthesis method also led to the first reported single crystal structure of UiO-68 with expanded linker.⁴⁹

Except that, other modulating agents have also been explored.⁵⁰ In a recent notable report, Forgan and coworkers studied the influence of a series of amino acids as modulators in the preparation of UiO-66 series MOF materials.⁵¹ In their study, seven different amino acids including *DL*-Threonine, *L*-arginine, *L*-tryptophan, *L*-leucine, β -alanine, 4-amino benzoic acid

and *L*-proline were systematically investigated in controlling the morphology and size of MOF crystals. It was demonstrated that the *L*-proline stood out as the most effective modulator as evidenced by the powder-XRD characterization (Figure 1.8). Addition of small amount of *L*-Proline significantly improved the crystallinity and size of the Zr/Hf-BPDC (UiO-67) MOFs, which exhibited much better efficiency than that using hydrochloride acid alone. In addition, this approach greatly reduced the modulators required for synthesizing defect free single crystals when compared with the big amount of acetic acid or hydrochloric acid in preparation of UiO-66 MOF material.⁴⁶

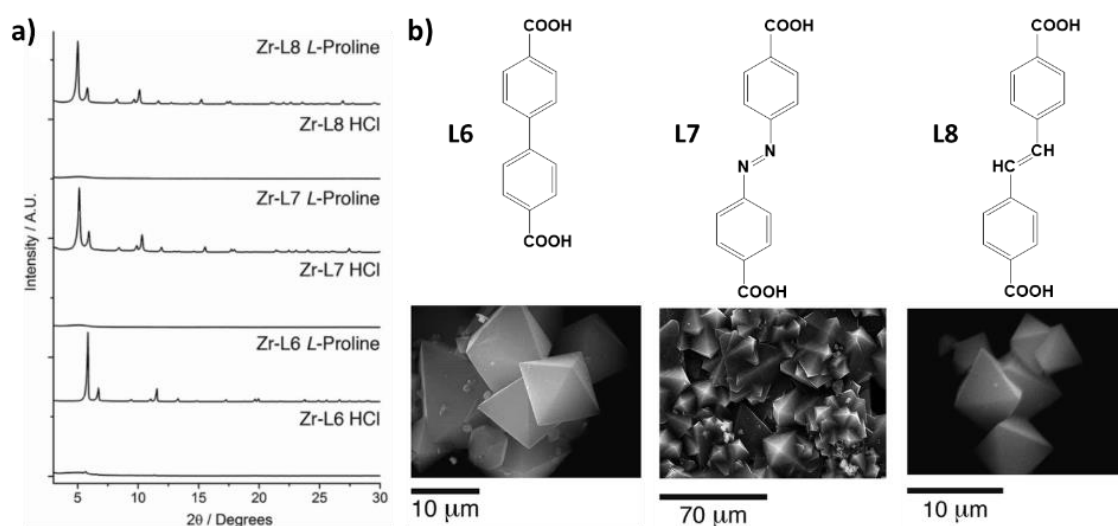


Figure 1.8. a) Enhanced crystallinity of Zr-MOFs by adding *L*-proline as modulator, comparing with those modulated by HCl. b) Organic linkers used during the synthesis and corresponding large single crystals by this modulation method.

Further optimization of the synthesis condition by introducing small amount of hydrochloric acid into the *L*-proline modulation system allowed access to large single crystals based on expanded flexible linkers such as ABDC (azobenzene-4,4'-dicarboxylic acid) and STDC (4,4'-stilbenedicarboxylic acid). Moreover, the discrete large single crystals facilitated the detailed investigation of their mechanical properties by single crystal X-ray diffraction. A Zr-EDB (4,4'-ethynylendibenzoic acid) MOF synthesized by *L*-proline modulation method enabled a fully structural characterization in single-crystal to single-crystal fashion (SCSC) after post-synthetic bromination on the integral alkyne units.⁵²

1.3 Post-synthetic modification of MOFs

Compared with the conventional solid-state materials consist of only inorganic components, hybrid nature of MOFs offers special opportunity for tuning or functionalizing their frameworks in order to expand their functional or structural diversity. Post-synthetic modification (PSM) of MOF frameworks plays significant role in achieving the diverse functionalities without compromising their crystallinity.⁵³⁻⁵⁷ This approach usually involves chemical functionalization of organic linkers or metal clusters of a MOF to create a variation of the parent framework but maintains the structural stability. To date, there have reported a variety of different post-synthetic modifications including but not limited to post-synthetic exchange, post-synthetic metalation, tandem post-synthetic modification, post-synthetic surface functionalization, post-synthetic deprotection and post-synthetic polymerization. Each of these forms of modification has the capacity to alter the physical and chemical properties of the framework.⁵³

A key point, which appears not be always recognized is that the solvent reagent used in the procedure could impede the efficiency of post-synthetic modification. Up to date, most of successful post-synthetic modification have to be performed in a solid–liquid fashion by rinsing a solid MOF in a liquid solution containing reactive agent.⁵⁸ However, the synthetic conditions of post-synthetic modifications typically require long reaction times and high temperatures that many MOFs cannot sustain; and for those MOFs that can resist such conditions, the yields are only low to moderate. This is partly because the methods are based on solid–liquid phase processes, whereby reaction progress is limited by the diffusion of reagents inside the porous frameworks to reach the target sites, especially for MOFs whose surfaces are already partially tagged, as the surface groups block access to the pores.⁵⁹

Solvent-less reactivity, particularly solid–gas phase reactivity, is a widely explored approach in metallurgy and polymer science. Indeed, reactive gases (e.g., fluorine gas in the steel industry) have been used to quantitatively passivate, cleave, or switch the hydrophobic character of diverse materials.⁶⁰⁻⁶² Such an approach provides an alternative way to overcome the aforementioned limitations in post-synthetic functionalization of MOF pores.

Distinct from the general categorization, in this section, the post-synthetic functionalization of MOFs will be categorized and discussed by two major types: **solid–liquid phase** and **solvent–less** post-synthetic modification. Taking into account of the advantages of the

solvent-less reaction, this overview will touch on several typical post-synthetic modification methods and present some recent advancements of **solid-gas** post-synthetic modification.

1.3.1 Solid–liquid phase post-synthetic modification

Clearly, solid-liquid system has dominant advantage in post-synthetic modification because organic solvent can not only dissolve the reactive species by dispersing them into discrete molecules, but also provide a gentle environment to prevent MOF materials from some harmful species such as humidity which possibly causes collapsing/damaging of vulnerable frameworks. Since that most post-synthetic modifications are achieved in solid-liquid phase, five typical post-synthetic modification: covalent modification, linker exchange, metal exchange, insertion and elimination will be provided with selected examples in this section.

1.3.1.1 Covalent post-synthetic modification (CPSM)

The highly porosity and chemically-rich components of MOFs provide excellent opportunities to perform covalent reactions on the surface to extent their chemical complexity and functionality for various applications. Covalent post-synthetic modification usually involves organic linkers containing a chemical functionality that does not interfere with MOF assembly, but can be used as the site for modification in subsequent post-synthetic modification. Abundant of reported post-synthetic modification methods are associated with covalent modification upon the pendant functional moieties of organic struts in MOFs.⁶³

Cohen and coworkers did the primitive research and demonstrated the possibility of covalently modification of porous MOFs in PSM manner.⁶⁴ Isoreticular framework IRMOF-3 with functional amino groups was selected as the model system for PSM study. By soaking the MOF crystals in CH_2Cl_2 solution of acetic anhydride for a period of hours to days, modified material was achieved with up to 80% conversion after 5 days. The crystallinity was well retained after covalent modification with the acetyl groups (Figure 1.9). The unique modification strategy at that time exhibited great potential in systematically modifying structures and facilitating the generation of functional MOF materials not accessible from conventional direct synthesis.

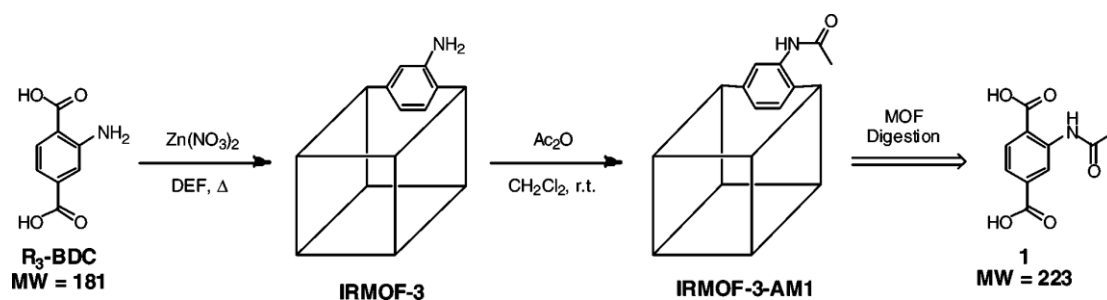


Figure 1.9. Schematic post-synthetic modification of IRMOF-3 with pending amino group by reacting with acetic anhydride.

In the consecutive research by the same group,⁶⁵ a tandem modification strategy was introduced for post-synthetic functionalization of MOFs, which meant more than one covalent reaction would happen within an individual MOF framework. In this work, IRMOF-3 was firstly reacted with crotonic anhydride to introduce alkenyl groups, then further treated with acetic anhydride/bromine to generate more complex groups. Significantly, this tandem strategy not only expand the scope of PSM method but also demonstrate the feasibility route to obtain diverse MOF structures.

In recent years, the zirconium based MOFs are often selected by researchers as ideal platform for introducing functionalities because of their advanced chemical and mechanical stabilities as well as being resistant to harsh conditions.⁶⁶ For example, a series of impressive covalent post-synthetic modification protocols were achieved based on zirconium MOFs with pendant amino groups.⁶⁷ The amino-tagged zirconium MOF, UiO-66-NH₂ with composition of $[Zr_6O_4(OH)_4(NH_2-BDC)_6]$ (NH_2 -BDC = 2-amino-1,4-benzenedicarboxylate) was first reported and used for post-synthetic modification by Cohen and coworkers.⁶⁸ The activated UiO-66-NH₂ materials were reacted with various alkyl anhydrides to produce amide functionalized framework (Figure 1.10). As a result, the smaller anhydrides get the higher conversion due to the pore size restriction during the post-synthetic modification procedure, in which the acetic anhydride achieved 88% conversion to amide based the bulk materials. The transformation was verified through combination of NMR, IR, and ESI-MS analysis, and PXRD patterns showed the functionalized structures retained as the parent MOF. In addition of that, UiO-66-NH₂ can be covalently functionalized with 2-methylaziridine to produce novel MOF catalyst with primary amino groups.⁶⁹

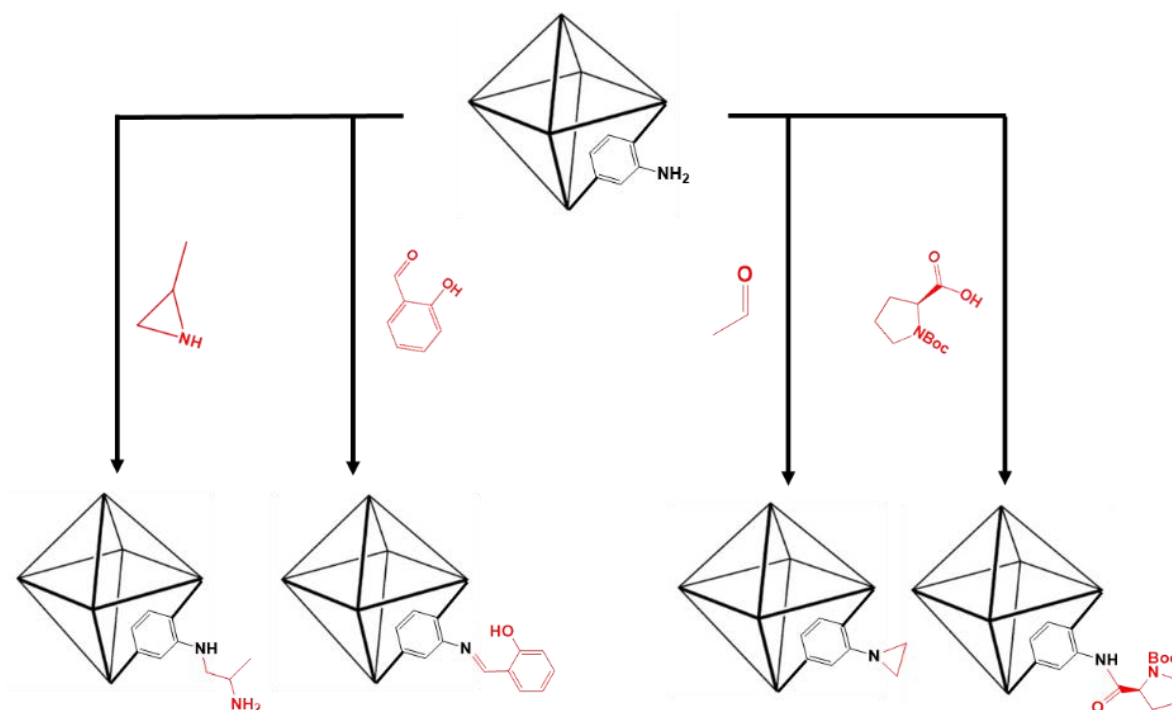


Figure 1.10. Representative examples of covalent post-synthetic modifications at the pendant amino groups of UiO-66-NH₂.

Except the amino group, many other pending groups have been employed for modification into various functionalities by PSM methods. For example, Rieger and coworkers used UiO-66-allyl as platform to successfully perform a series of tandem PSM reaction.⁷⁰ The integrated double bond was firstly converted to crystalline UiO-66-dibromide then treated under pressured ammonia (8 bar), and diamine-functionalized MOF material was obtained (Figure 1.11). Compared to the parent UiO-66 structures, the modified materials showed higher ability for CO₂ uptake with molecular gate functionalities at low temperature, which revealed structure-selectivity correlations.

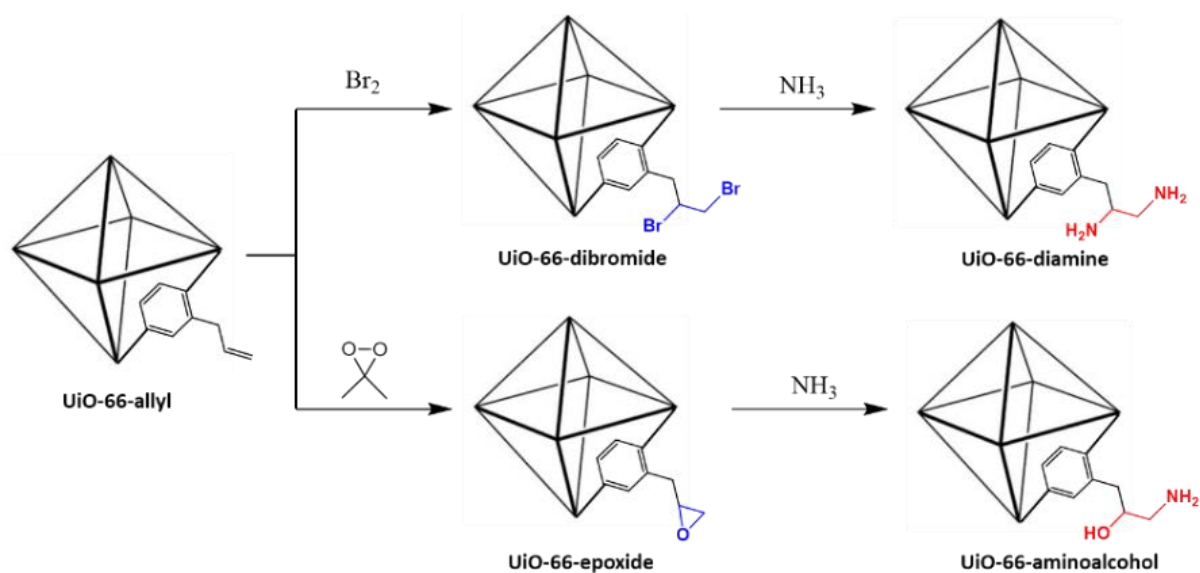


Figure 1.11. Sequential modification of UiO-66-allyl by bromination and nucleophilic substitution.

An extremely example of sequential PSM of MOF was reported from Yaghi group containing as many as seven tandem post-synthetic covalent reactions within the pores of a mixed-ligand IRMOF-74.⁷¹ The selected analogue multivariate MOF was constructed from magnesium oxide rods joined by two types of organic linkers: 60% 3,3''-dihydroxy-(1,1':4',1''-terphenyl)-4,4''-dicarboxate and 40% Boc-protected (Boc = tert-butyloxycarbonyl) amine derivative, possessing 25 Å 1D channels. Then, sequential deprotection and peptides loading reactions were performed within the large pores, resulting in a heterogeneous functionalized tripeptides MOF product. Importantly, the material retained identical crystallinity and high porosity ($BET = 1920 \text{ m}^2 \text{ g}^{-1}$) even after seven reactions (Figure 1.12). The final modified IRMOF-74-Ala-Gly-Pro-NH₂ with 20% loading exhibits significant enantioselectivity increase for α -chlorination of butyraldehyde compared to the homogeneous-phase proline catalysis (20% ee vs 2% ee). In addition, IRMOF-74-Asp-His-Cys-NH₂ with 10% loading showed selective cleavage of the peptide of serine in a pentapeptide compound, while the formation of cleaved products was not found by using other analogue MOFs.

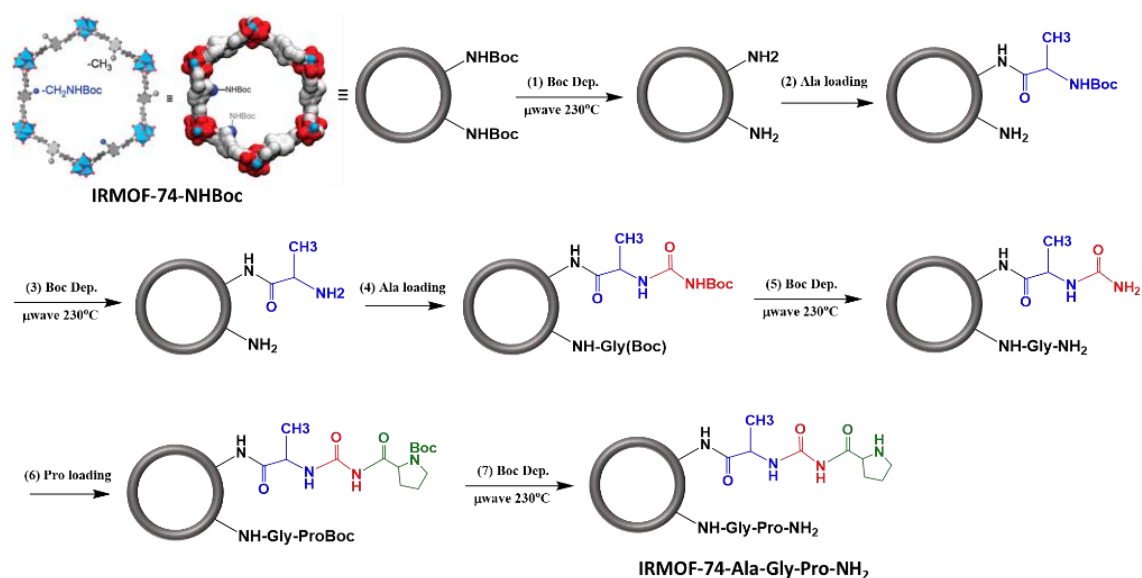


Figure 1.12. Illustration of seven post-synthetic reactions performed within the pore of IRMOF-74-NHBoc to final modified tripeptides IRMOF-74-Ala-Gly-Pro-NH₂ material. Evolution of one potential reaction byproduct is presented in black.

1.3.1.2 Post-synthetic metal exchange (PSME).

Ion exchange techniques have been widely utilized to tailor the composition of zeolites for changing the material properties, such as in catalysis or gas sorption.⁷² However, it is relatively novel approach to incorporate different metal ions by post-synthetic metal exchange

process involving metal nodes and metalated struts in metal-organic frameworks. Introducing new metal ions may lead to MOFs new catalytic property or improve the gas sorption. Therefore, it is of great interest for researchers to develop feasible metal ion exchange approaches to create isomorphous MOFs containing various metals that cannot be available by direct synthesis.^{73,74}

Early studies by Dinca and Long showed that cation exchange in MOF structure not only change the charge balance of framework but also alter the inorganic clusters/metal nodes of the structure.⁷⁵ By simply immersing a Mn-MOF ($\text{Mn}_3[(\text{Mn}_4\text{Cl})_3(\text{BTT})_8(\text{CH}_3\text{OH})_{10}]_2$, BTT = 1,3,5-benzenetristetrazolate) into series of selected cations solution of methanol for approximately one month, the partially cation-exchanged MOF crystals were obtained, in which the exchanged cations were verified by the elemental analysis. Gas adsorption confirmed similar BET surface area as the parent MOFs after exchange process. Interestingly, the cation-exchanged MOFs exhibited different isosteric heat of adsorption in H_2 storage measurement, revealing the difference binding strength between H_2 molecules and unsaturated metal centers within each framework. Especially, the Co^{2+} -exchanged material exhibited the highest initial enthalpy of adsorption of 10.5 kJ mol^{-1} among the series of heterometallic MOF materials, much more than that of the parent material.

In another example of PSME process, MOF-5 was employed as host material to synthesize heterogenous MOFs containing various transition metal ions (Figure 1.13). By soaking crystals of MOF-5 in concentrated DMF solutions of series of metal ions, divalent (V^{2+} , Cr^{2+} , Mn^{2+} , or Fe^{2+}) or trivalent (Ti^{3+} , V^{3+}) transition metal ions were slowly inserted and coordinated to the SBU clusters by exchanging the zinc ions of parent MOF-5, which could not be obtained by direct synthesis (Figure 14).

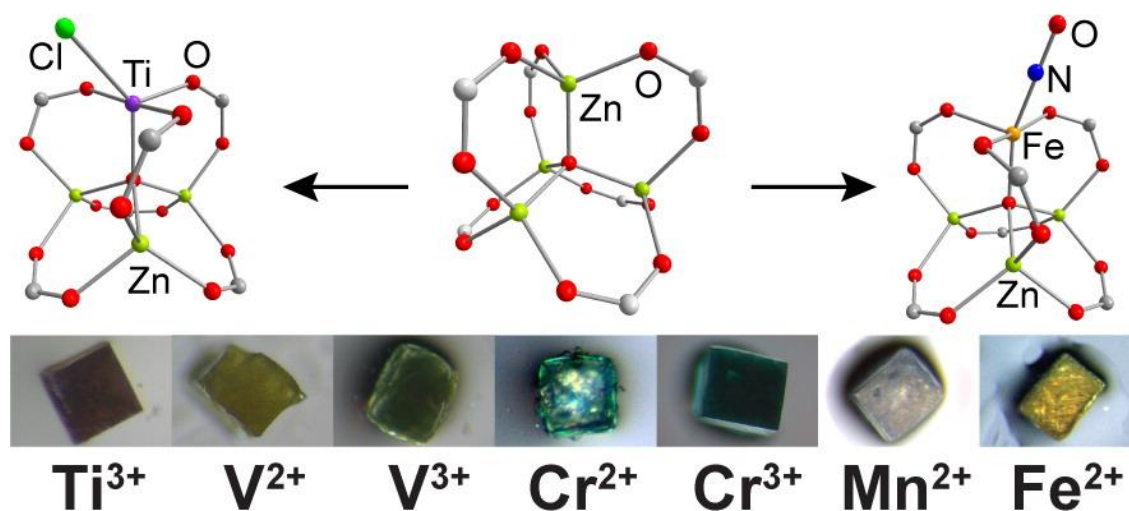


Figure 1.13. Various metal ions can be accessed and connected to the cluster of MOF-5 by post-synthetic metal exchange, producing MOF-5 analogues featuring multiple-metal oxide clusters.

During the PSME procedure, the PXRD patterns and shape of crystals were in consistence with MOF-5, indicating the metal ions substitution occurred in crystal-to-crystal manner rather than a dissolution-recrystallization mechanism. The resulting hetero-metal oxide clusters provide MOF-5 unique redox reactivity such as Cr^{2+} -MOF-5 could be converted to Cr^{3+} -MOF-5 by outer-sphere electron transfer, while Fe^{2+} -MOF-5 activated NO to produce an unusual Fe-nitrosyl complex more than any other MOF.

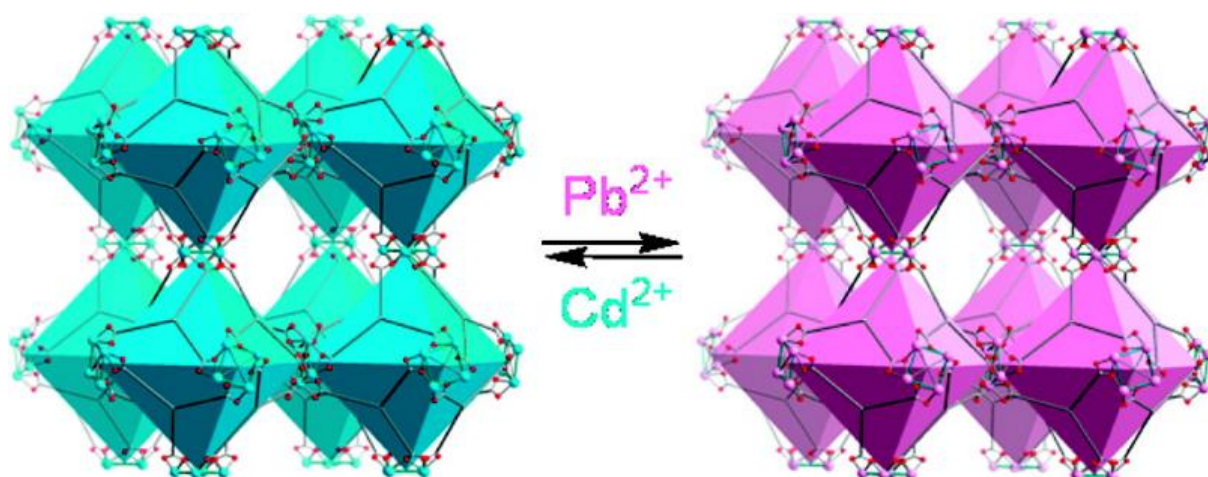


Figure 1.14. Complete and reversible metal ion exchange between crystalline Cd-MOF and Pd-MOF, while maintaining the crystal integrity.

Furthermore, Kim and coworkers reported stoichiometric metal-ions exchange of entire MOF clusters based on a crystalline cadmium MOF ($[\text{Cd}_{1.5}(\text{H}_2\text{O})_3][(\text{Cd}_3\text{O})_3(\text{hett})_8]6\text{H}_2\text{O}$], HETT = ethyl substituted truxene tricarboxylic acid). Each octahedron unit within the MOF consisted of six square-planar $\{\text{Cd}_4\text{O}\}$ as metal cluster and eight HETT linkers at the vertices and faces,

respectively. This type of connection provided the framework with exceptional stability and accessibility to the metal ions. As a result, metal ion exchange process was successfully achieved in a single-crystal-to-single-crystal manner (Figure 1.14).

1.3.1.3 Post-synthetic linker exchange (PSLE)

Cohen and coworkers early realized and studies post-synthetic linker exchange process on some structurally stable MOFs including UiO-66(Zr), MIL-53(Al), MIL-68(In) in both solid-liquid and solid-solid phase. The crystalline MOFs remained the coincident crystallinity with their parent ones after exchanging linkers. Normally, the carboxylate struts are inherently difficult for exchange due to their strong and complex bonding between the metal ions and carboxylate oxygens. UiO-66 is considered to possess high chemical stability and reported to be inert and robust to a variety of chemical conditions.⁷⁶ However, the PSLE were realized within UiO-66 MOFs both in solid-solid and solid-solvent manner.⁷⁷ Microcrystalline UiO-66-NH₂ and UiO-66-Br were physically mixed and suspended in chloroform, methanol and DMF (N,N-dimethylformamide), respectively. After incubation for five days at certain temperature, particle-to-particle ligand exchange was observed between solid MOF microcrystals in all the test solvent, and the particle size and chemical composition was analyzed by ATOFMS (aerosol time-of-flight mass spectrometry). Importantly, the particle size was not changing and crystallinity was well retained during the incubation period. Approximately more than half of the particles were modified, giving signals of bromine and nitrogen simultaneously. When suspended UiO-66 material in a solution of BDC-NH₂ or BDC-Br in water for 5 days incubation, the ligand exchange ratio for the total particles exceeded 50%. In addition, solvent plays quite important role and no ligand exchange is observed in the absence of solvent. By this PSLE approach, some thermally unstable or uncommon functionalities such as hydroxy or azide can be introduced into MOF crystals (Figure 1.15).

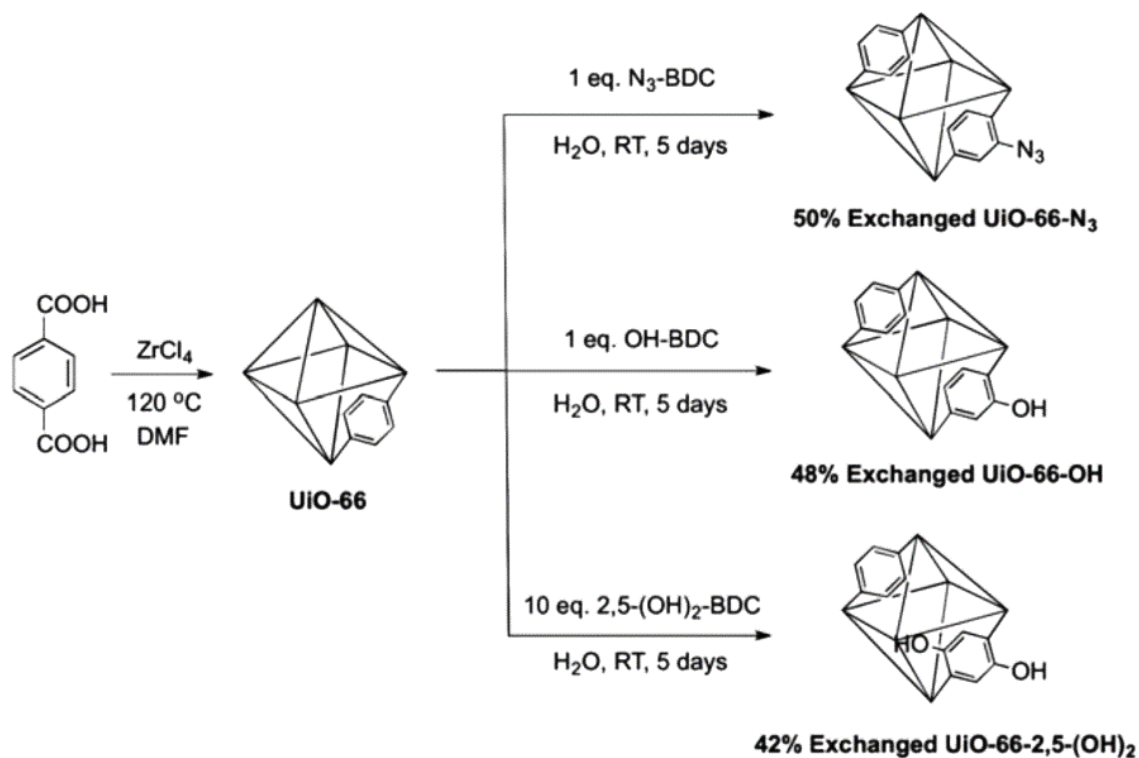


Figure 1.15. PSLE of UiO-66 to azido, hydroxyl, and dihydroxyl functionalized UiO-66 materials.

Some water-resistant MOFs such as MIL-53-Al and MIL-68-In can also undertake the PSLE phenomenon.⁷⁸ For instance, MIL-53(Al)-NH₂ and MIL-53(Al)-Br exchanged ligand in solid-solid reaction associated within water solvent. The exchanged MOF particles was characterized by ATOFMS and verified up to 56% particles containing both BDC-NH₂ and BDC-Br ligand. Exchanged MIL-68(In)-(NH₂)(Br) material was successfully obtained by the similar PSLE treatment in DMF solvent (Figure 1.16). As a comparison, no ligand exchange was detected in MIL-101-Cr under the similar PSLE treatment, due to the kinetically liability and inertness of the Cr(III) ions prevents the ligand exchange process.

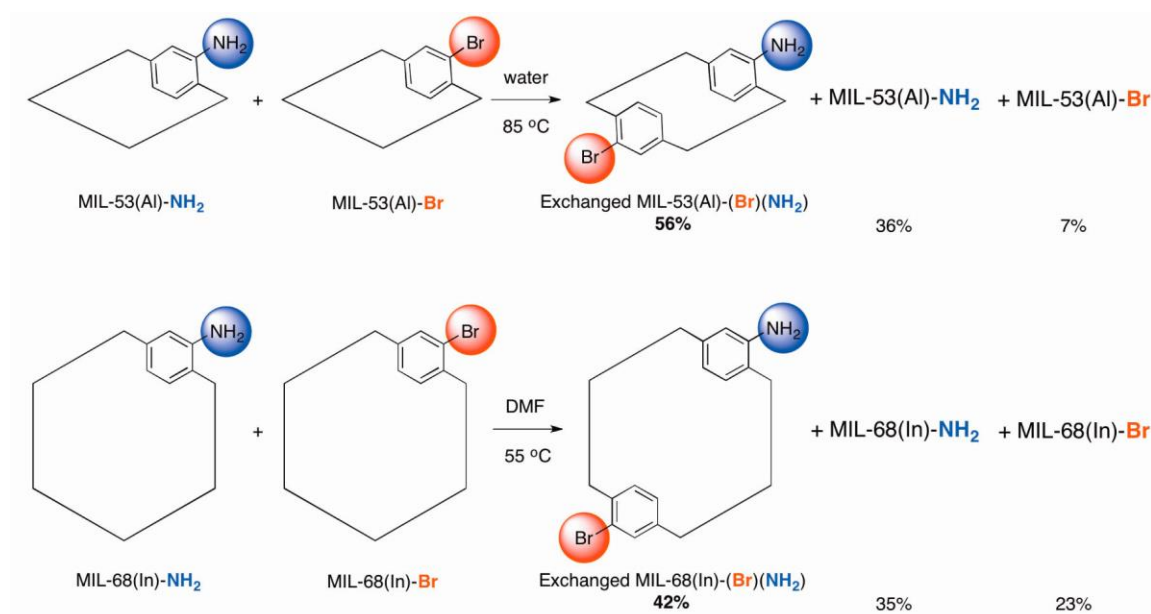


Figure 1.16. Post-synthetic ligand exchange process was carried out in MIL-53 and MIL-68 structures with solvent association.

Another impressive research work adapting the linker-exchange strategy to produce new MOF structures is of the preparation of BioMOF-100 ($[\text{Zn}_8(\text{adeninate})_4(\text{bpdc})_6\text{O}_2]$) isorecticular analogues. Bio-MOF-100 was reported by Rosi et al. and coworkers in 2011, using large metal-biomolecule zinc-adeninate clusters periodically linked with 4,4'-biphenyldicarboxylate (BPDC) to construct an exclusively mesoporous metal-organic frameworks. This structure adopts highly mesoporous channels along three directions and exhibiting high surface area, low crystal density and large pore volume (Figure 1.17).^{79,55} In order to increase the porosity of parent framework, researchers introduced extended linkers by replacing BPDC. However, it is known that direct synthesis of extremely porous framework with mixed organic linkers is not easy for MOFs.⁸⁰

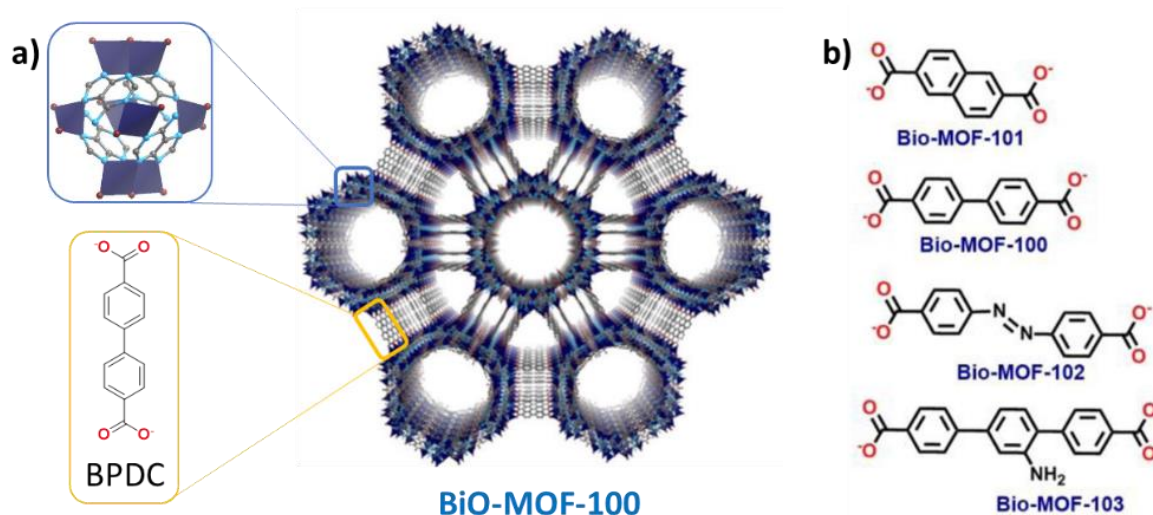


Figure 1.17. a) Direct synthesis MOF structures of BiO-MOF-100 consists of Zn-adeninate clusters ($\text{Zn}_8\text{Ad}_4\text{O}_2^{8+}$) and BPDC linker; b) corresponding ditopic linkers for constructing analogue frameworks of BiO-MOF-100.

Although the analogue of Bio-MOF-101 having shorter 2,6-naphthalenedicarboxylate (NDC) linkers was successfully prepared in direct solvothermal synthesis, other analogues with linkers longer than BPDC couldn't be obtained under the similar condition. Ligand exchange was employed to increase the pore dimensions of such MOF materials. By soaking the colorless BiO-MOF-100 crystals in azobenzene-4,4'-dicarboxylate (ABDC) and 2'-amino-1,1':4,1''-terphenyl-4,4''-dicarboxylate (NH_2 -TPDC) solutions, crystalline BiO-MOF-102 and BiO-MOF-103 were successfully obtained, which exhibit increased N_2 uptake and calculated pore volume of 4.36 and 4.31 cc/g, respectively.⁸¹ Interestingly, the pore expansion process via ligand exchange based on Bio-MOF-100 proceeds gradually in “outside-in” fashion within individual crystals. New intermediate MOFs can be produced by terminating the ligand exchange reaction prior to complete crystal conversion. These heterogeneous MOF crystals bear descending porosity gradients from crystal periphery to the crystal core, showing size-sensitive selectivity for some nanoclusters.⁸² These post-synthetic linker exchange approach provides a potential venue to introduce sensitive functions into robust MOF structures.

1.3.1.4 Post-synthetic insertion (PSI)

Recently, a new class of post-synthetic method has emerged in functionalization of MOFs termed as post-synthetic insertion (PSI).⁵⁷ Other nomenclature has been reported: Hupp and coworkers have used solvent-assisted linker incorporation (SALI),⁸³ and Zhou has termed

the phenomenon as sequential linker installation (SLI).⁸⁴ to describe this type of photosynthetic modification. The post-synthetic insertion usually refers to post-synthetically installation of organic ligands with suitable length or size into the existing MOF framework by taking advantage of the different coordination bonding strength between ligand and metal clusters.

One representative utility of post-synthetic insertion method for MOFs was the solvent-assisted linker incorporation established by Hupp, Farha and coworkers.⁸⁵ The zirconium-based NU-1000 was synthesized with 1,3,6,8-tetrakis(p-benzoic acid)pyrene (TBAPy) as platform to demonstrate post-modification reactions. The framework consisted of octahedral Zr₆ cluster connected by eight ligands, and eight terminal oriented -OH groups with four of which pointed to the mesoporous channel. Various perfluoroalkane carboxylates entities were introduced and coordinatively attached to the cluster nodes of NU-1000 by replacing the hydroxy/H₂O groups (Figure 1.18).

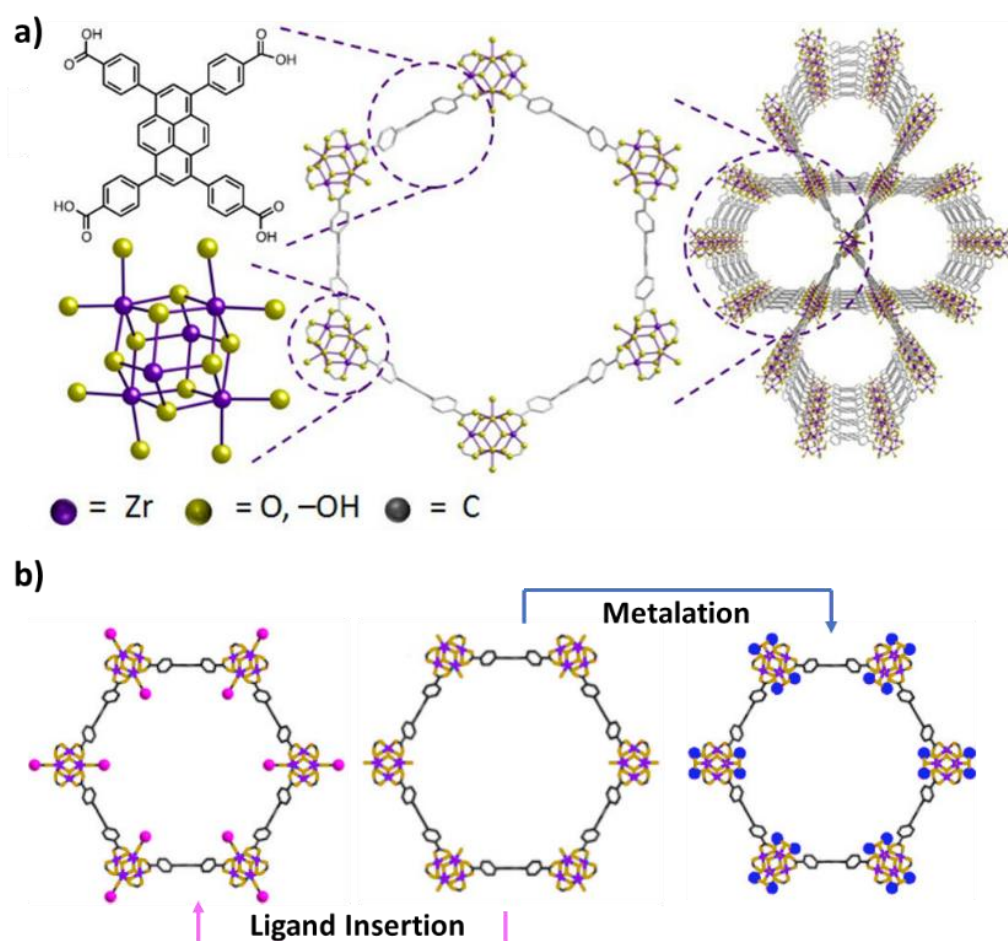


Figure 1.18. a) Molecular representation of NU-1000, and b) illustration of NU-1000 after post-synthetic ligand insertion (left) and metalation (right).

The resulted fluoroalkane-functionalized mesoporous MOFs achieved impressive enhancement for CO₂ uptake. Additionally, NU-1000 has great chemical generality and tolerance for installing many other carboxylate derivatives. The approach endowed the resulted MOF materials further chemical reactivity such as click chemistry, imine condensation and pyridine quaternization. Furthermore, reactive multiple metals could be formed within the framework by facile self-limiting metalation reaction when exposed the activated NU-1000 in vapor phase trimethylaluminum (AlMe₃) or diethylzinc (ZnEt₂) (Figure 18).⁸³ The metal-inserted MOF exhibited activity to Knoevenagel condensation reaction compared to inactive parent framework.

Another example for post-synthetic insertion of ligands to the framework was reported by Zhou and coworkers using PCN-700 as a prototype MOF.⁹⁰ In their study, a Zr-MOF with *bcu* network was synthesized with Me₂-BPDC ligand as the initial material. The space between two adjacent Zr-clusters forms a natural “pocket” in the equatorial plane, which is suitable for the accommodation of one linear dicarboxylic linker by replacing the terminal OH-/H₂O. The two pockets with different size (16.4 Å for A and 7.0 Å for B) make it possible to sequential linker installation. Subsequently, BDC and Me₂-TPDC (dimethylterphenyldicarboxylate) were selected as proper linkers to match the distance of the pockets. By exposing the PCN-700 crystals to solutions of BDC and Me₂-TPDC in DMF at 75 °C, three new frameworks PCN-701, 702, 703 were generated with post-synthetically installed BDC, Me₂-TPDC, BDC and Me₂-TPDC, respectively (Figure 1.19). It is worth noting that the sequence of linker insertion is crucial for the successful formation of PCN-703. The existence and position of different linkers was unambiguously determined in crystallography solved structure. Moreover, the crystallinity and porosity were well maintained after linker installation process. The excellent stability ensures the obtained functional MOF materials will be stable and usable under relatively harsh conditions.

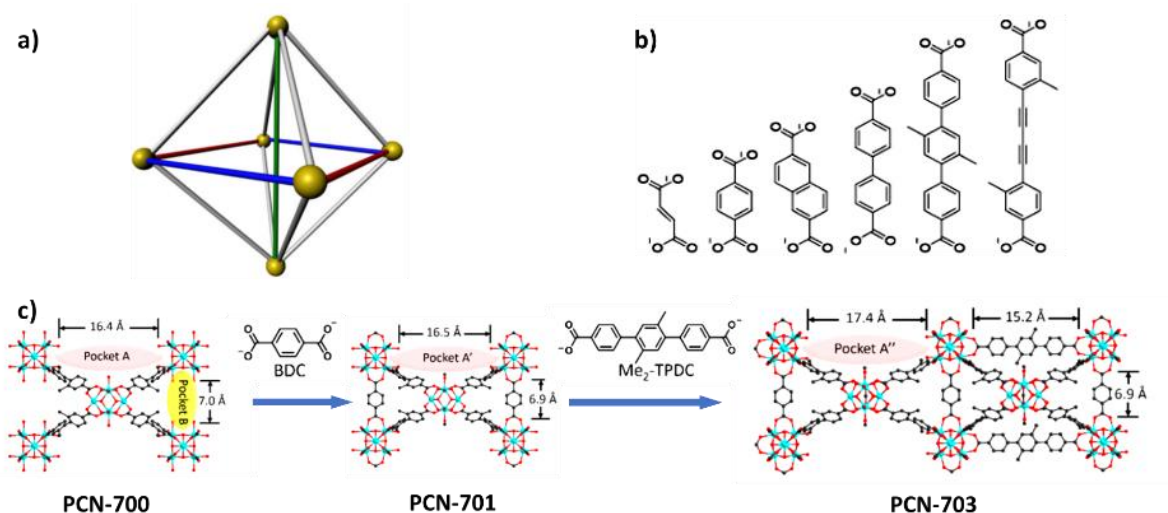


Figure 1.19. a) Illustration of PCN-700 showing ligand arrangement between SBUs (shown as gold spheres) and possible sites of PSI (blue, red, and green sticks). b) Ligands can be inserted into these sites. c) An example scheme of sequential post-synthetic ligand insertion to form PCN-701 and PCN-703.

Li group reported an interesting example for post-synthetic elimination followed by insertion involving both ligands and metal ions.⁸⁶ A MOF-5 analogue [Zn₄O(PyC)₃] (MOF 1, PyC = 4-pyrazolecarboxylate) was prepared by direct solvothermal synthesis with cubic network. The framework contains two distinct but similar metal clusters: the [Zn₄O(COO)₆] formed exclusively from the carboxylate side of PyC and the other [Zn₄ON₁₂] was self-organized from only the pyrazole end of PyC. When the MOF crystals were immersed in water, half of the ligand and a quarter of the Zn²⁺ ions (one from each SBU) were removed to generate a new porous MOF 2. Particularly, the transformation was performed in a SCSC manner, during which MOF 2 showed full retention of single crystallinity and possessed ordered ligand vacancies and metal vacancy sites (Figure 1.20). The resulted structure 2 constitutes rectangular channels with diagonal aperture up to 13 Å, which was accessed by the acridine red molecules (14.2 × 8.3 × 3.7 Å³) while no diffusion into the original MOF 1 was observed.

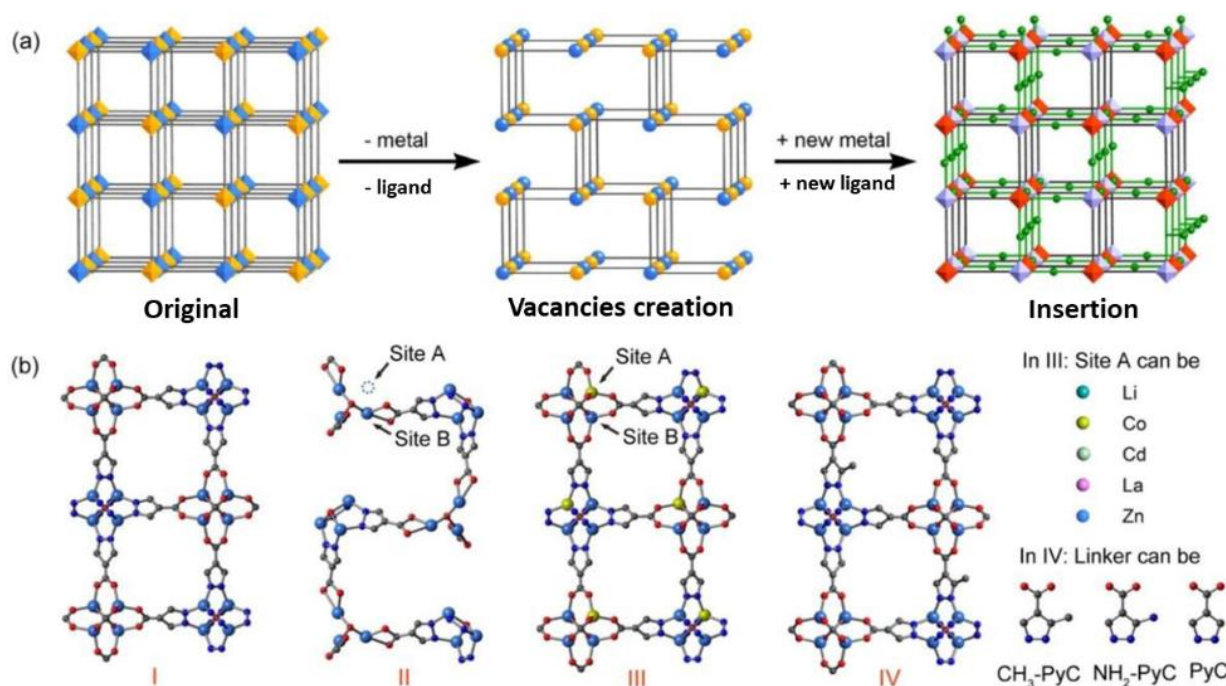


Figure 1.20. a) Schematic elimination of ligand and metal ions from original MOF to generate ordered vacancies followed by insertion of new metal and ligand into crystallographic defined position. b) Single-crystal structures of the MOFs without vacancies (I), with vacancies (II), and with new modules filled in the vacancies (III and IV).

Emersion of MOF 2 in solutions of various metal ions (Li^+ , Co^{2+} , Cd^{2+} , or La^{3+}) and/or different ligand derivatives of PyC ($\text{CH}_3\text{-PyC}$ and $\text{NH}_2\text{-PyC}$) allows incorporation of metals and/or ligands into the framework, resulting in new MOF materials with heterometallic or mixed-ligand or both heterometallic and mixed-ligand compositions. Moreover, this same MOFs (except structure 1) could not be produced neither by direct synthesis nor other post-modification reactions. Post-synthetic elimination and insertion reactions consecutively were performed within the same framework at high level of tunability and special control. This advancement will significantly elevate the importance of post-modification methods in generating more complex MOFs.

1.3.1.5 Post-synthetic elimination

For the posts-synthetic modification of MOFs, it is widely known that the terminal coordinated moieties can be removed or eliminated by evacuation and/or heating to generate open metal sites without compromising the integrity of framework.² As early as in 2000, Yaghi and coworkers reported the design of open metal sites in porous MOFs by post-synthetically removing the coordinated water from the Cu clusters of the framework.⁸⁷ In their work, a porous

MOF was firstly assembled with ATC (adamantane-1,3,5,7-tetracarboxylate) and Cu paddle wheel cluster. Each cluster contains two coordinated water in the perpendicular direction. By simple thermal treatment, all the guests in the channel together with the terminal bounded water molecules were removed completely from the immobilized Cu atoms, leaving a stable framework with periodic arrays of open metal sites (Figure 1.21). The open metal sites were identified by single-crystal X-ray diffraction and magnetic susceptibility data. This example could be regarded as an early post-synthetic elimination process to access open metal sites.

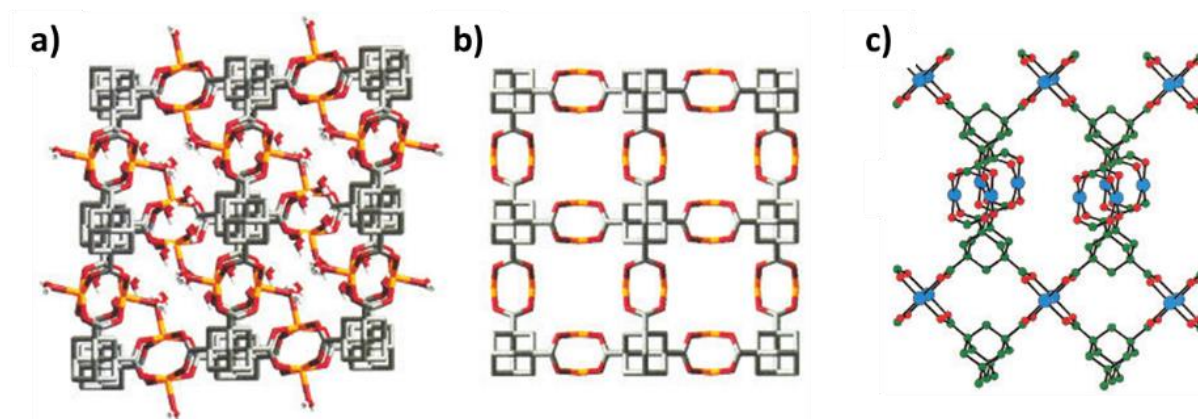


Figure 1.21. The single-crystal structures of a) as-synthesized $\text{Cu}_2(\text{ATC}), 6\text{H}_2\text{O}$ with coordinated water molecules, b) dehydrated MOF architecture shown in line representations, and c) open metal sites point into the pores

Besides thermal treatment, acid treatment is an efficient approach of eliminating linkers from the backbone, leading to active open sites. For example, De Vos and coworkers introduced additional Brønsted acid sites to the well-known MIL-100(Fe) structure by using acid treatment in a short time to tune the catalytic performance of MOFs.⁸⁸ The as-synthesized MIL-100(Fe) materials were immersed in the aqueous solution of HClO_4 or CF_3COOH varying concentrations, in which the carboxylate moieties got partially disconnected from the metal sites by deprotonation. After thoroughly washing with water, active sites were generated with coordinatively unsaturated metal nodes (Figure 1.22). The modified MOFs possessed two types of active sites: weak Brønsted acid sites and Lewis acid open metal sites, both of which were verified by the large increment of in CO-chemisorption experiments. In addition, the acid-treated MOFs strongly increased the Diels-Alder reaction of oxygenated dienophiles with 1,3-cyclohexadiene.

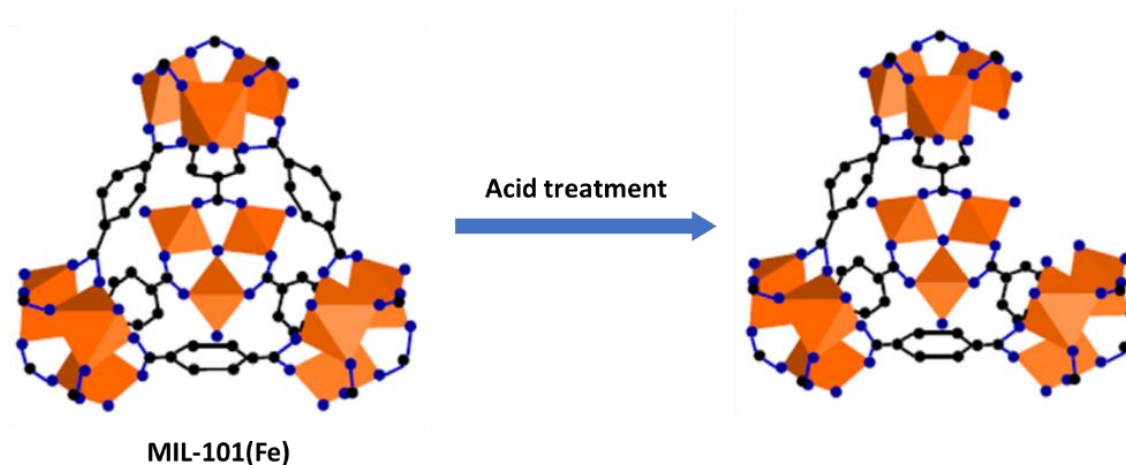


Figure 1.22. Illustrated creation of active sites in MIL-101(Fe) structure by post-synthetic elimination of coordinated species through acid treatment.

More recently, researchers start to extend the post-synthetic elimination method to create hierarchical micro/mesoporous MOFs. Kim and coworkers⁸⁹ reported an impressive work that they generated well-defined mesopores with high mesopore volume by controlling the acid etching process (Figure 1.23). The synthesized MIL-101(Fe) crystals were soaked in H₃PO₄ solution at room temperature and then heated at 70°C to accomplish the acid etching process. It is known that MIL-101(Fe) has two type of cages: the large one with hexagonal window open ($d = 0.89$ nm) and the smaller one with pentagonal window open ($d = 0.49$ nm).⁹⁰ Because the size of the H₃PO₄ molecule ($d = 0.61$ nm) is between the hexagonal and pentagonal window, the acid molecule selectively diffuses into the 3D tetrahedral channel of the large cage. During heating, the lattice of the large cage was gradually etched, resulting in the disassembly of the metal oxide nodes and ligands. The acid-etched MOF has a sponge-like morphology and much higher transparency compared with the pristine MIL-101(Fe). Scanning electron microscope (SEM) images also indicated the clearly regular enlargement of pore size on the crystal surface along with the increment of H₃PO₄ concentration. By N₂ sorption measurement, the mesopore sizes were calculated with gradually increment from 2.4 nm to 18 nm.

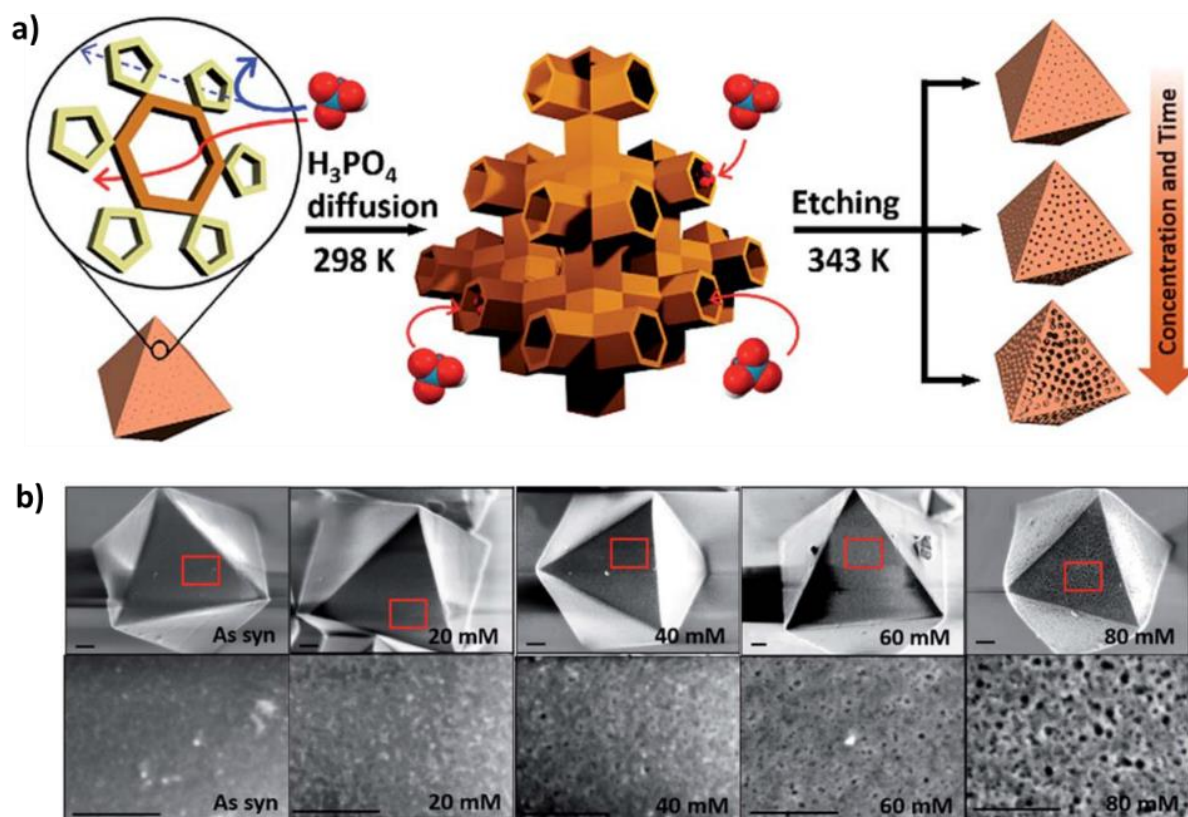


Figure 1.23. a) Illustration of the acid etching process for MIL-101(Fe) using phosphoric acid diffusion into the MOF channels through hexagonal windows. b) SEM images of pristine and acid-etched MIL-100(Fe) at different concentration of acid.

For the in-depth investigation, the authors employed H_2SO_4 and HCl as the etching agent to investigate the size selective acid diffusion of the etching process. The H_2SO_4 with comparable molecular size as H_3PO_4 could generate the hierarchical mesoporous MIL-101(Fe) in a controlled manner while the HCl only resulted in the collapse of the whole framework due to its small molecular dimension.

1.3.2 Solvent-less post-synthetic modification

1.3.2.1 Solid-solid phase post-synthetic modification

Attempt of implementing successful post-synthetic modification has given rise to a bunch of methods in order to immobilize various functionalities within MOF materials. Unfortunately, only few MOF samples could be modified because of the long PSM reaction time or the high temperature. Solvent-less post-synthetic modification has attracted much attention in recent years as a quick, simple and effective method in functionalization of MOFs. Hereafter, the discussion will focus on the post-synthetically covalent reaction between the reactant and MOF materials, without additional solvent.

A remarkable example of solid-solid post-synthetic modification is that of functionalization of a series of amino-tagged MOFs: MIL-53(Al)-NH₂, UiO-66(Zr)-NH₂, and MIL101(Al)-NH₂ reported by Wuttke and coworkers.⁹¹ In this work, carboxylic acids, acid anhydrides, and acid chlorides were employed to perform direct post-synthetic modification by incubating MOF materials with reactants. The influence of reactivity and size of the reactant on the PSM yield of these three MOF structures was also investigated. As a consequence, the amino-MOFs were post-functionalized quickly with the three acid reactants in high yielding. Especially, the solventless post-synthetic modification resulted in the highest reported PSM yield for acetic anhydride within 2 h of reaction (Figure 1.24).

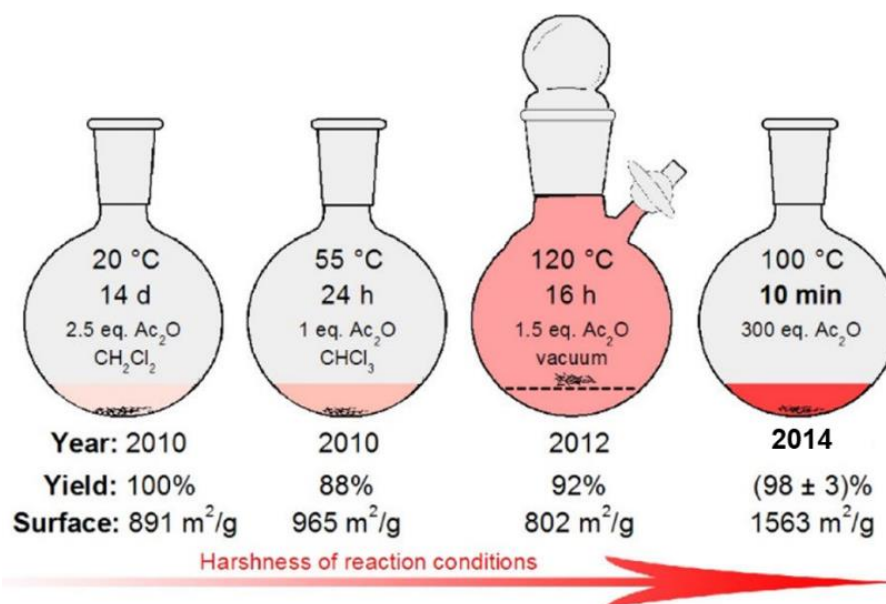


Figure 1.24. PSM conditions of UiO-66(Zr)-NH₂ with acetic anhydride (Ac₂O) referred to 1 equiv of MOF compared to PSM yields and Langmuir surface areas.

Another representative solvent-free post-synthetic method was reported recently by our group through spray-drying technique⁹² and photothermal effect of MOFs⁹³ that can perform covalent post-synthetic modification in drastically time-efficiency and acceptable yielding. Spray-drying technique has been demonstrated to be a useful, continuous and scalable method to synthesis of MOFs with reduced time regime and dried powder materials directly.⁹⁴ Also the spray-drying method can be extended to covalent post-synthetic modification of MOF crystals, such as UiO-66-NH₂ and ZIF-90 (Figure 1.25). Thus, either between discrete organic molecules or on the pore surfaces of MOFs, this solvent free method exhibited highly versatility and efficiency in post-functionalizing MOFs via Schiff-base condensations reactions in a very fast (1-2 s) and continuous way. Notably, the PSM cross-linking of aldehyde group tagged ZIF-90

via spray-drying even gave as much as 70% conversion with hexamethylenediamine in mere time, in comparison to the value of 25 - 42% conversion when butylamine was employed.

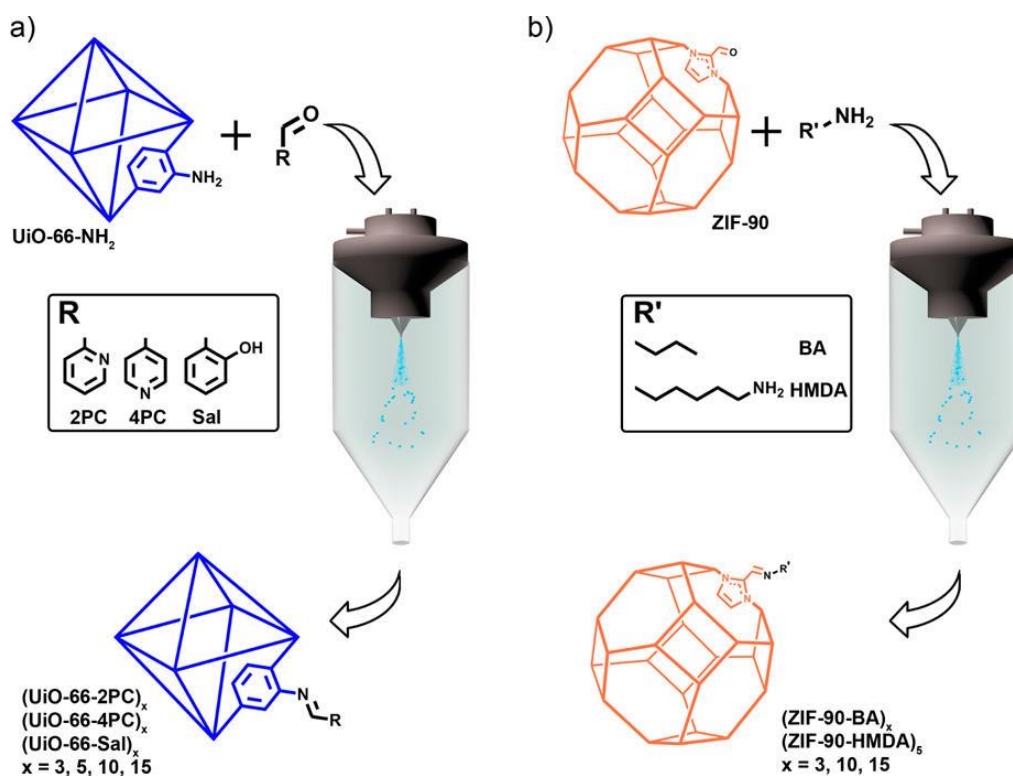


Figure 1.25. Solvent free spray-drying method used for covalent PSM of (a) UiO-66-NH₂ and (b) ZIF-90 MOF crystals.

In addition to that, interesting functionalized hybrid materials can be created by combining solventless post-synthetic method with polymerization. For example, Wang et al. reported a flexible stand-alone MOF membrane by consecutively use of covalent reaction and polymerization.⁹⁵ Direct synthesized UiO-66-NH₂ nanoparticles were firstly functionalized with methacrylic anhydride to form a polymerizable olefin groups decorated MOF material. Then under UV light irradiation, the modified MOF particles copolymerized with butyl methacrylate (BMA) monomers and photoinitiator, thus fabricating an elastic MOF/polymer hybrid membrane (Figure 1.26).

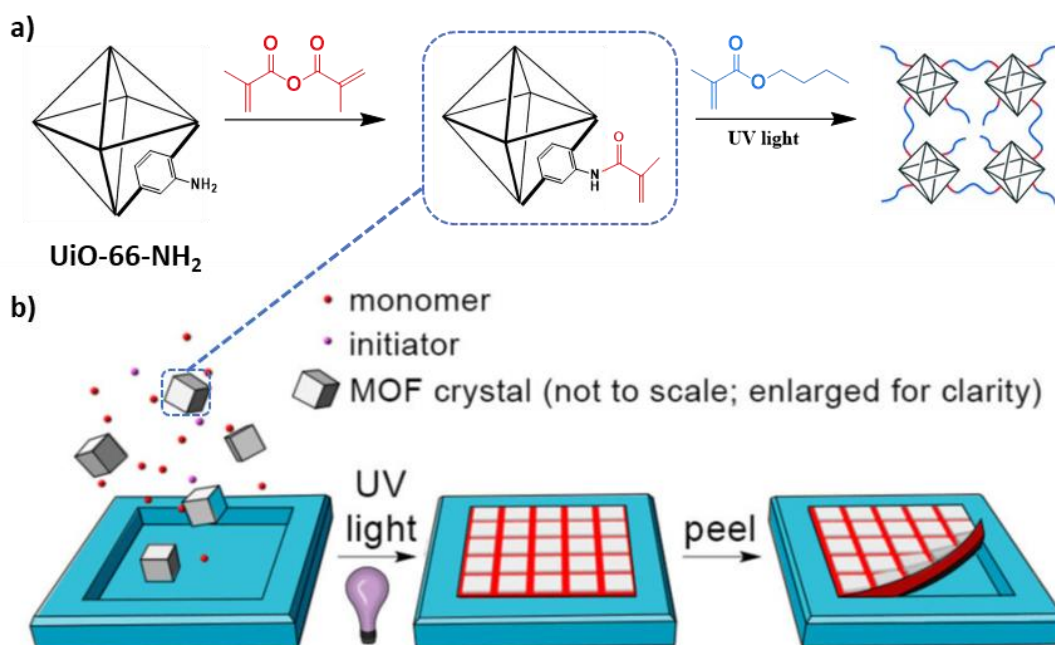


Figure 1.26. a) Schematic post-synthetic covalent modification of UiO-66-NH₂ followed by polymerization under irradiation of UV light. b) Illustrated preparation of PSP-derived membrane on a Teflon mold by photoinduced polymerization.

The result of CO₂ uptake measurement indicated the pores of UiO-66-NH-Met were not blocked by PBMA polymer after copolymerization, which was important for the application of the hybrid material. Indeed, separation capacity test of the PSM-derived MOF membrane showed impressive removal of Cr^{IV} ions from water.

Except that, photothermal effect of MOFs can be used as an effective way for conducting covalent post-synthetic modification of MOFs. In this work, the photothermal active UiO-66-NH₂ was mixed with anhydride reagents (e.g. maleic anhydride or benzoic anhydride) in solid state, then the solid mixture was transferred to a glass substrate and exposed under UV-Vis light irradiation. Photothermal effect caused the MOF to heat up, which in turn caused the organic reagent melt and subsequently react with the functional groups on the walls of MOF pores (Figure 1.27).

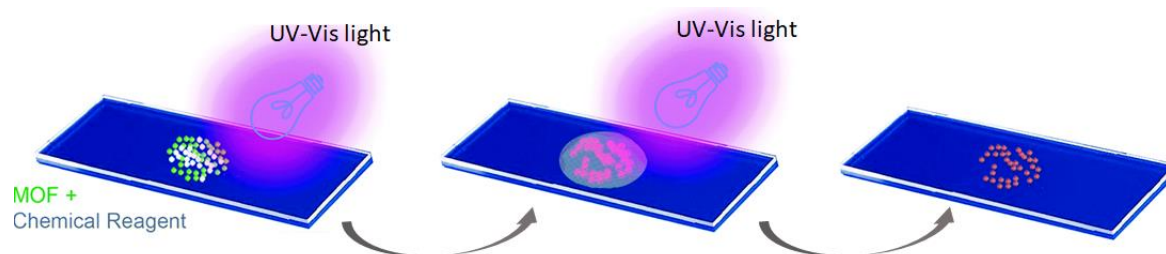


Figure 1.27. Illustration of the photo-mediated covalent PSM of MOFs. Under UV-Vis light irradiation, MOF particles will self-heat up and melt the organic anhydrides surrounded. Continuous irradiation in turn drives the reaction between the reagent with the functional groups on the pore walls of the MOF.

Highly conversion (> 83 %) for the modified MOFs can be achieved by only 30 minutes irradiation. Interestingly, the solid-phase covalent PSM approach can create an amide rather than imine just starting from an aldehyde (e.g. 4-bromobenzaldehyde) through a photo-induced cascade reaction. Therefore, this solid-solid PSM approach provides researchers with novel reactions to incorporate functionalities into MOFs.

1.3.2.2 Solid-gas phase post-synthetic modification

Solid-gas reaction, as a special type of heterogenous reaction, is of important in many industrial metallurgical and chemical process.⁶¹ Related to the solid-gas reaction, the gas behavior, diffusion kinetics and reaction mechanisms have been widely explored.^{96,97} The virtue of solid-gas reactivity has attracted much attention in recent years including but not limited to time saving, highly conversion, energy-efficient and environment benign. However, there is scant precedent in the solid-gas reactions with MOFs. Up to date, only several studies have been reported by vaporizing chemical agents to perform covalent post-synthetic modification.

An early exploration by Lee and coworkers^{98,99} above was reported through successfully introducing trifluoroacetic acid to functionalize a silver-based porous MOF. The framework was assembled from the linker 1,3,5-tris(4-ethynylbenzotrile)benzene with a pendent alcohol group on the 2-position, which served as the reactive feature of the porous material. Upon exposure of the porous MOF into vapors of trifluoroacetic acid for 1 h, ester-functionalized MOF was achieved with preservation of the crystallinity after quenching with benzyl alcohol to consume excess anhydride (Figure 1.28).

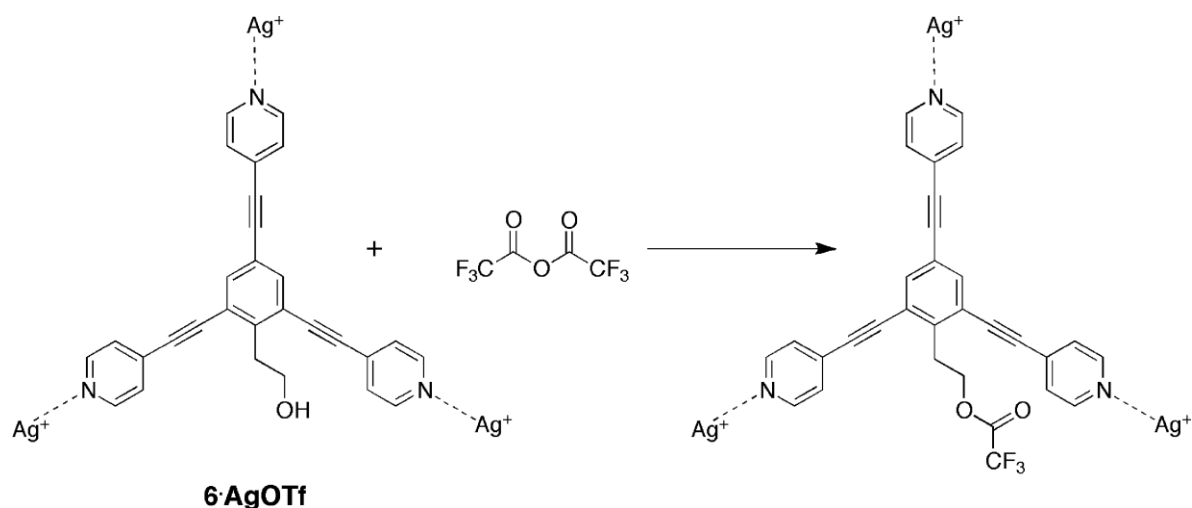


Figure 1.28. PSM of pendent alcohol group by exposure of silver-based MOF to vapors of trifluoroacetic anhydride.

Dissolved ^1H NMR and in situ FTIR unambiguously confirmed the chemical transformation of the alcohol to ester. The vapor-involved post-synthetic modification method provided a beautiful example for later post-functionalization of MOFs in vapor-solid manner.

Bokhoven and coworkers extended the PSM of UiO-66-NH₂ and IRMOF-3 with vapor acid anhydrides to investigate the flexibility of vapor phase reaction.⁹⁹ In this approach, the dried MOF crystals were placed onto a paper filter in a Schlenk tube containing salicylaldehyde or anhydrides. Subsequently the tube was left in a static vacuum at 100 °C to vaporize the reactant and the modification of MOFs was completed in direct vapor phase manner (Figure 1.29).

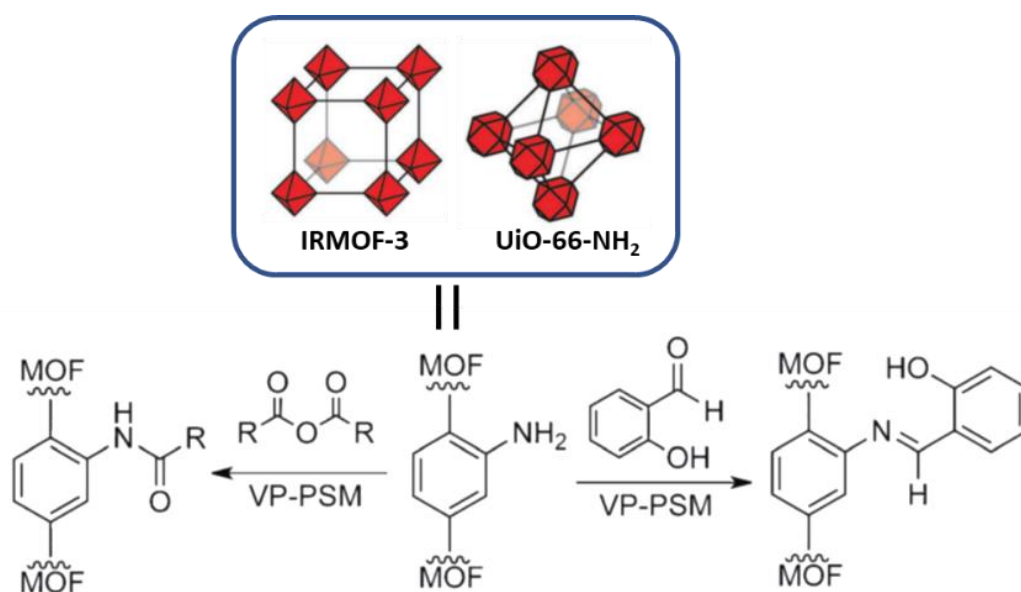


Figure 1.29. Schematic representation of vapor phase-PSM based on amino-tagged IRMOF-3 and UiO-66-NH₂.

The obtained functionalized MOF solid were analyzed by $^1\text{H-NMR}$ and conversion was calculated using the resulting integrals. The results indicated that the pending amino groups of MOF crystals were transformed into amides in reduced timescale and achieved very high conversion. For instance, the yield of the IRMOF-3 reaction with salicylaldehyde under VP-PSM conditions was $> 99\%$ while only 13% conversion was obtained by solution reaction in a previous report.¹⁰⁰ In the modification of UiO-66-NH₂ crystals with salicylaldehyde, VP-PSM showed significantly higher yield of 29% conversion after 16 h than that of 10% conversion produced by 7 days reaction under standard PSM condition in CH₂Cl₂. In addition, VP-PSM method exhibited good generality compared with standard PSM as it applied to UiO-66-NH₂ with anhydrides. The frameworks remained intact and high porous after smoothly proceeded vapor phase reaction. This vapor-phase PSM processing not only modified MOFs with in higher conversion and shorter reaction time, but also synthesize materials with homogeneous distribution of multifunctionalities.

In another notable example, Rosseinsky and coworkers made use of two steps of post-synthetic vapor-solid reaction to functionalize a N-diazenium diolate group within HKUST-1 framework, which could release NO under control in moisture.¹⁰¹ In their study, dehydrated HKUST-1 was exposed to the vapour of 4-(methylamino)pyridine (4-map) at 140 °C, and the strongly irreversible N-Cu binding led to successful incorporation of the 4-map into the framework. Particularly, the chemical loading process was implemented in a solid-gas fashion with quantitatively transformation of 4-map-Cu bound species achieved. Subsequent exposure of the 4-map-impregnated (60% percentage) HKUST-1 to NO at 25 °C for 72h, partial 4-map groups combined two NO molecules for each, transforming to N-diazenium diolate functionalities (Figure 1.30). Further investigation by exposure of the bimodified HUKST-1 to ambient atmosphere resulted in slowly NO release over 5 days. Unfortunately, the instability of HKUST-1 to H₂O severely limits the application of these materials toward NO delivery.

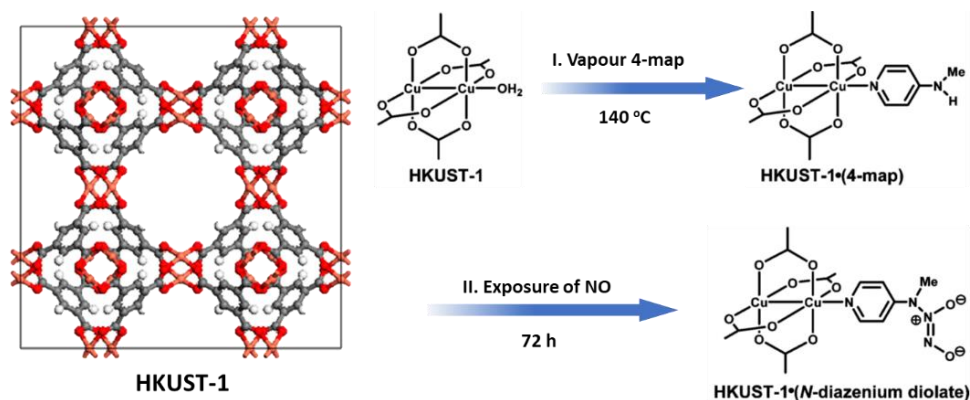


Figure 1.30. Preparation of H₂O-triggered functionalized HKUST-1 by two steps of solid-gas PSM.

Except direct reaction within MOFs, Fischer and coworkers¹²⁸ did the exploration of gas-phase loading of functionalities by chemical vapor deposition (CVD). Firstly, typical metal organic chemical vapor deposition (MOCVD) precursors (Pd, Cu and Au nanoparticle) were selected and absorbed in the MOF-5 cavities under vacuum condition (1 Pa and 343K), then metal nanoparticle loaded MOF-5 was achieved by reduction with hydrogen gas (Figure 1.31). Their catalytic performance of the resulting composites crystals verified the effective stabilization of nanoparticles by the MOF lattice.

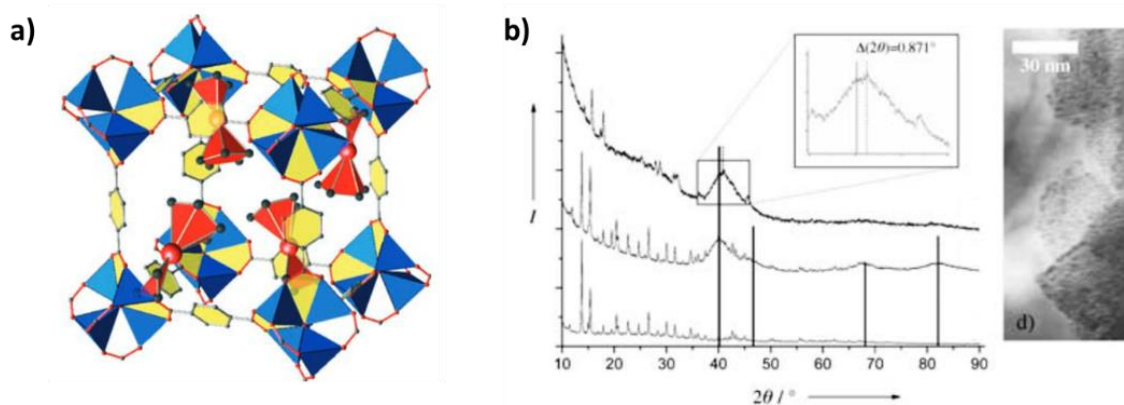


Figure 1.31. a) MOF-5 cage (blue/yellow) with four incorporated $[(\eta^5\text{-C}_5\text{H}_5)\text{Pd}(\eta^3\text{-C}_3\text{H}_5)]$ precursors. b) Powder diffraction patterns (bottom-up) of MOF-5, photolytically generated Pd@MOF-5, H₂ reduced Pd@MOF-5, respectively, with highlight of the palladium characteristics after vapor loading.

In-depth investigation indicated that the adsorption of precursors was highly size-selective and governed by the weak and reversible van der Waals forces with the MOF pore walls.¹⁰² This chemical vapor deposition approach was then extended to fabricate various nanoparticle@MOF composites by loading various organometallic molecules into porous MOFs, followed with hydrogenolysis or oxidative annealing treatment.^{103, 104} In another work from Fischer and coworkers,¹⁰⁵ Al(OH)(bdc)_n framework (MIL-53(Al)) was post-synthetically functionalized with the metallocene reagent 1,1'-ferrocenediyl-dimethylsilane by gas-phase loading approach. Here, the ferrocene compound was entrapped into the channel under reduced pressure and functionalized MIL-53 was achieved by a mild thermal treatment at 65 °C for 72h. Characterization of the resulted MOF material revealed that the ferrocene species were covalently coordinated to the hydroxy groups bridging two AlO₆ octahedra within the infinite one-dimensional chain (Figure 1.32). Interestingly, this process was found to proceed the

selective H-transfer from the hydroxyl group to the cyclopentadienyl ring of the ferrocene moiety, which was proved by ^2H labeling solid-state NMR studies.

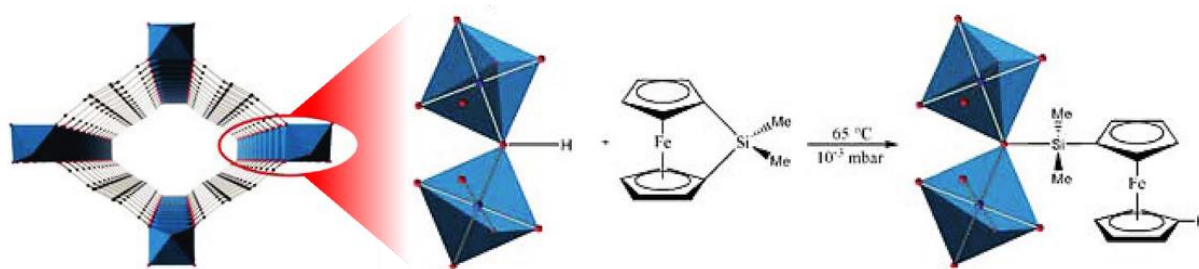


Figure 1.32. Partial crystal structure of MIL-53(Al) and after gas-phase loading, the organosilicon compound reacted with bridging HO-group between two AlO6 octahedra under thermal treatment.

In addition to the modification of metal oxide clusters, vapor-solid chemistry can be directly performed onto the organic linkers of the framework. For instance, zirconium or aluminum-based MOFs were often selected as chemically stable candidates for a platform to implement PSM by direct solid-gas reactions due to their impressive chemical resistance and highly thermal stability.

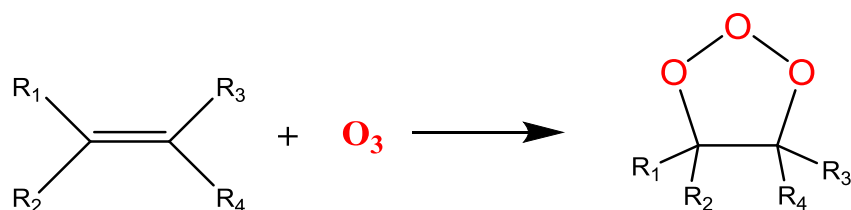
1.3.3 Post-synthetic modification by solid-gas ozonolysis

Ozone has been identified as a distinct chemical compound for almost two centuries. Since then the special gas with pungent smell has attracted great research interest for a long time.¹⁰⁶ Ozone is one of the most powerful oxidants and has many industrial applications related to oxidation.

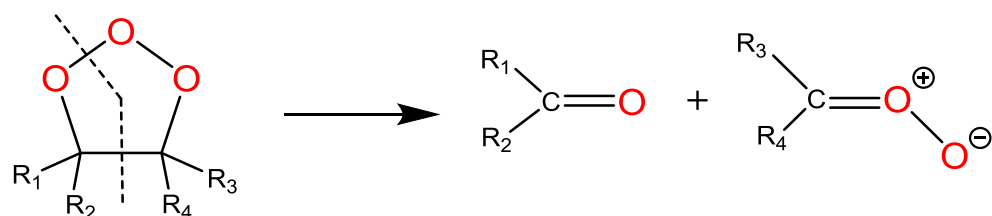
Ozonolysis refers to oxidative cleavage of unsaturated compounds with ozone, which is discovered and explored as an unusual type of oxidation reaction in many respects.¹⁰⁷ In atmospheric chemistry, ozonolysis of unsaturated bonds generates hydroxyl radicals upon O–O bond cleavage, which plays an important role in the oxidative degradation of pollutants.¹⁰⁸ In solution, a double bond was cleaved quantitatively and decomposed products can be harnessed purely by hydrolytical, reductive or oxidative work-up method.¹⁰⁹

The mechanism of an ozonolysis reaction has been thoroughly studied by Criegee and now the Criegee mechanism has been widely accepted.¹¹³ Typically, the ozonolysis of alkenes in solution follows the three-step mechanism through a [2+3] cycloaddition as shown below:

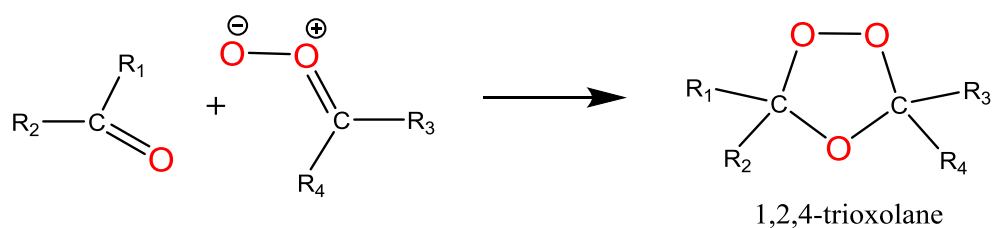
Reaction A: Formation of a “primary ozonide”



Reaction B: Decomposition of primary ozonide into carbonyl compound + “carbonyl oxide”

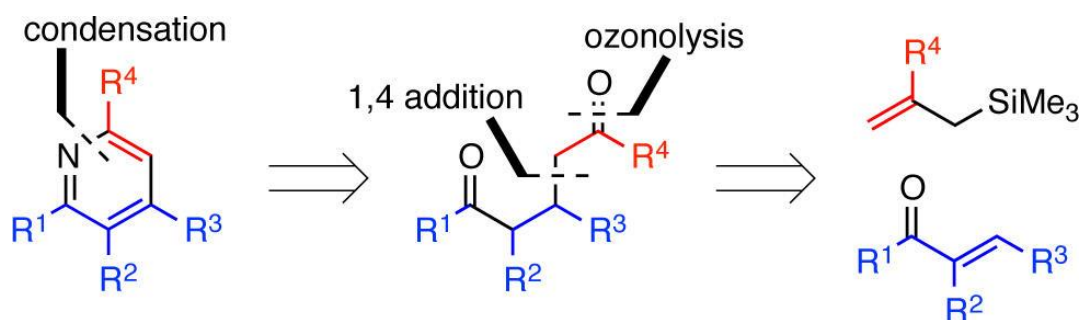


Reaction C: Addition of the “carbonyl oxide” to the carbonyl compound



Note that the heterocycle “primary ozonide” is unstable and instantly fragments into a carbonyl compound and a carbonyl oxide, also called Criegee intermediate, even under extremely mild conditions of below $-78\text{ }^\circ\text{C}$ in the absence of acid or base.

Ozonolysis chemistry has been used extensively in academic, research and industrial environments.¹¹⁰ Numerous examples have since been reported related to ozonolysis reactions, which is considered as an amiable, clean and effective choice by synthetic chemists for oxidative cleavage of double bonds. For example, Rychnovsky and coworkers achieved a reliable retrosynthesis to access substituted pyridines through a two-step Hosomi–Sakurai allylation/oxonolysis cleavage sequence (Scheme 1.2).¹¹¹ This approach allowed enones were first converted into 1,5-dicarbonyls and a diverse range of substituted pyridines were synthesized by this method.



Scheme 1.2. Retrosynthesis approach to pyridines with enone and allyl nucleophile components.

Indeed, ozone gas has been realized to be able to react with some organic crystals of unsaturated compounds in a solid-gas manner.¹¹² When exposed to ozone gas on a substrate for a few minutes, the single crystal of *trans*-stilbene rapidly liquefied into a mixture of benzaldehyde and benzoic acid. The trioxolane rings can be treated under mild reductive or oxidative conditions to form aldehyde moieties or carboxylic acids,¹⁰⁹ respectively.

Furthermore, the heterocycle trioxolane derivatives have the unique clinical applications. An extraordinary example of trioxolane derivatives for medical purpose was reported by Charman and coworkers.¹¹³ In this study, they synthesized a series of new selected 1,2,4-trioxolane compounds which showed highly efficient bioactivity for clinical antimalarial treatment (Figure 1.33).

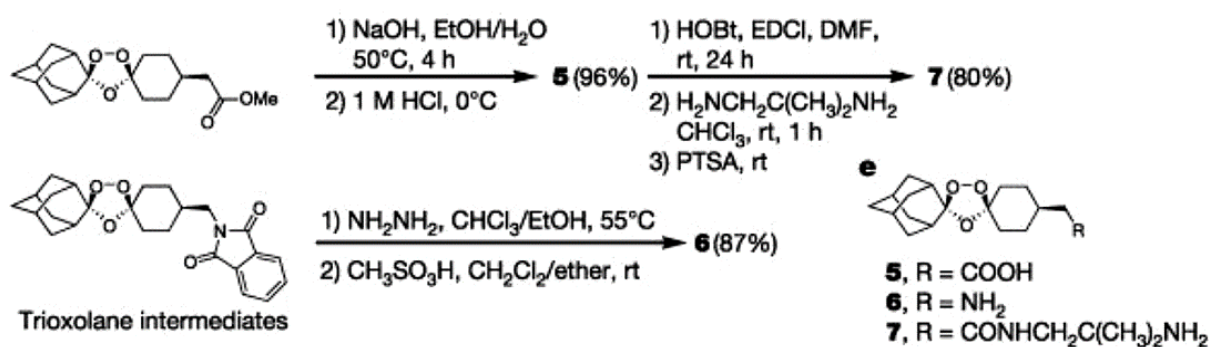


Figure 1.33. Synthesis of selected trioxolane compounds for the bioactive antimalarial drugs.

Subsequent tests by successive by rapid and interactive integration of antimalarial, physicochemical, metabolism, pharmacokinetic and toxicity data revealed their therapeutic potential. The selected 1,2,4-trioxolane drug development candidate exhibits structural simplicity, an economically feasible and scalable synthesis, superior antimalarial activity and an improved biopharmaceutical profile, in comparison to the conventional semi-synthetic drugs. These results provided successful treatment outcome for guiding the medicinal chemistry.

As illustrated above, ozonolysis of alkenes has been widely studied as a powerful tool to the oxidative cleavage. The trioxolane rings can be switchable controlled to form aldehyde or carboxylic acids. In addition, such compounds have been proven great therapeutically potential. All of these knowledges inspired us the attempt to explore the introduction of trioxolane into MOFs. Taking account of the reactivity of ozone gas and highly porosity of MOFs, solid-gas post-synthetic modification may probably be the best of all for achieving that.

1.4 Applications of metal-organic frameworks

Metal organic frameworks (MOFs) have emerged as one of the most promising porous materials owing to their remarkable characteristics including extremely high surface area, as well as tunable pore size and functionality. These prominent features make MOFs as one of the most promising materials beyond traditional porous materials such as zeolites or activated carbon, in a wide range of applications including but not limited to gas storage,³⁶ catalysis,^{114,115} chemical separation,^{116,117} proton conductivity¹¹⁸ and drug delivery.¹¹⁹⁻¹²¹ This section will touch on three representative applications of MOF materials: gas storage, molecular separation, and catalysis.

1.4.1 Gas storage

Hydrogen is considered as an ideal clean energy carrier containing 2.6 - 3 times more energy per unit mass than gasoline, which provide a promising clean alternative to traditional fossil-fuels.¹²² However, the challenges to achieve sufficient energy density on board storage at low temperature and high pressure of efficient hindered its application. MOF-based hydrogen storage has attract considerable attention because of their modular structures and large interior surface area. Great efforts have been dedicated to the exploration of various strategies to enhance hydrogen uptake in porous MOF materials.

A typical example of hydrogen storage of porous MOFs is MOF-5,¹²³ which has a remarkable maximal excess gravimetric uptake of 0.076kg/kg hydrogen at 77 K and 50 bar. Even though MOF-5 material has the Langmuir surface area of 4400 m²/g, it uptakes more hydrogen than highly porous MIL-101 (0.061 kg/kg)¹²⁴ and UMCM-2 (0.069 kg/kg)¹²⁵ which have much larger surface areas close to 6000 m²/g for both of them. In fact, the surface area is not the only factor to determine the hydrogen uptake capacity for a porous MOF. A screening investigation of MOFs from the Cambridge Structural Database allowed the compounds to be identified with high theoretical capacities and revealed that the relationship between gravimetric and volumetric H₂ density is not linear but has a maximal performance for surface areas of 3100–4800 m²/g.¹²⁶ For hydrogen adsorption, a tough problem is that at near ambient temperature, the storage capacity of MOFs decrease dramatically due to the weak physisorption and low interaction enthalpies between the gas molecules and framework. Long and coworkers synthesized a series of isomer structure to MOF-74 by modifying the linker dobdc (dobdc = 2,5-dioxido-1,4-benzenedicarboxylate) to a regioisomeric linker, resulting in highly density of coordinatively unsaturated metal sites within the adsorption sites within the framework.¹²⁷ The present highly

polarizing metal adsorption sites provide the porous MOFs large binding enthalpies and a dense of packing H₂ within the material at near-ambient temperature (Figure 1.34).

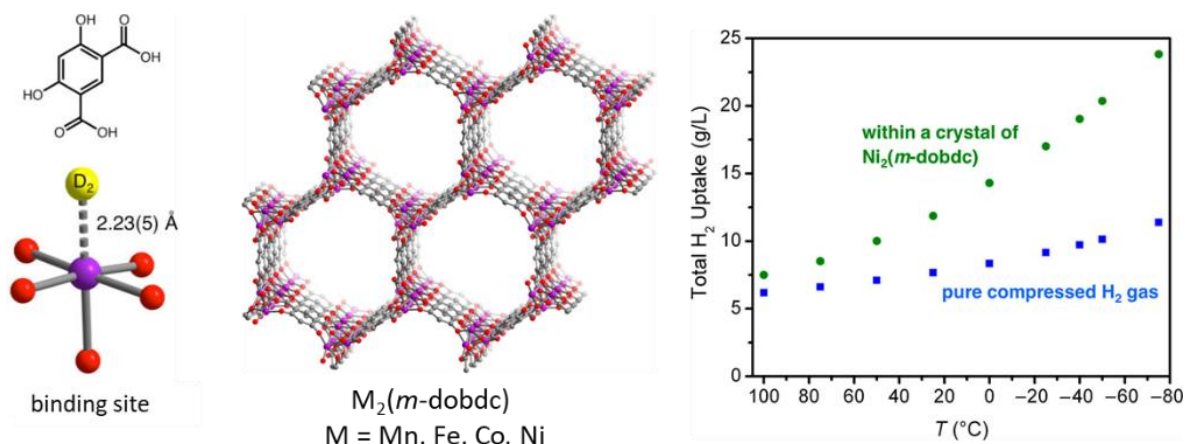


Figure 1.34. Illustration of structures $M_2(m\text{-dobdc})$ adopt similar framework as MOF-74 but exhibited enhanced charge density at the open metal sites, leading to very high and usable volumetric H₂ capacity at near-ambient temperature.

Methane is also another promising alternative to fossil fuels. Large number of MOFs have been explored for the CH₄ storage by scientists all over the world in the last decade. One of the representative porous MOF materials is the HKUST-1 that exhibits exceptional volumetric methane storage at room temperature. Farha and coworkers studied CH₄ storage of six promising existing MOFs (PCN-14, UTSA-20, HKUST-1, Ni₂(dobdc), NU-111, and NU-125) using a standardized measurement protocol. The adsorption results demonstrate that HKUST-1 shows a room-temperature volumetric methane uptake that exceeds any value reported at that time (Figure 1.35). The total CH₄ uptake of HKUST-1 is about 230 cm³/cm³ (STP) at 35 bar and 270 cm³/cm³ at 65 bar, which meets the new volumetric target recently set by the Department of Energy (DOE).¹²⁸ In depth structural analysis of HKUST-1 reveals that the right combination of binding sites and suitable pore size within HKUST-1 maximizes both the CH₄-framework and intermolecular interaction in the methane, promoting its capability for methane storage.¹²⁹

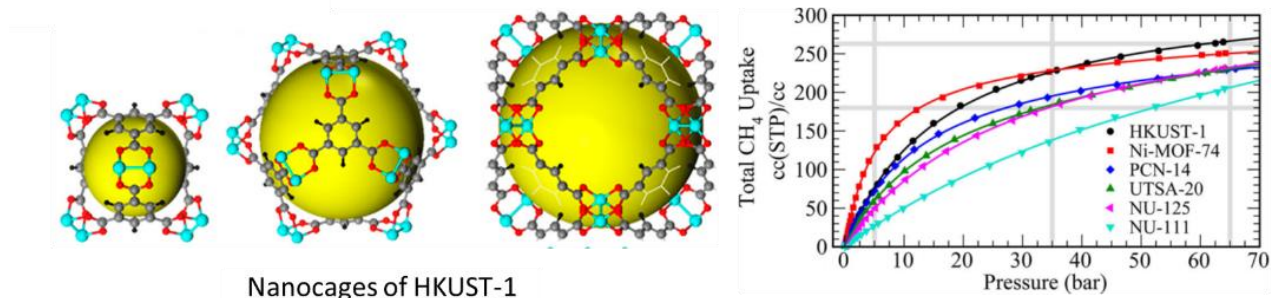


Figure 1.35. The nanocages and crystal structure of HKUST-1, which exhibits exceptional volumetric methane uptake at room temperature.

The stability of crystalline MOFs is also a major concern for practical application. Snurr and coworkers employed computational screening over 204 hypothetical MOF structures featuring $(Zr_6O_4)(OH)_4(CO_2)_n$ inorganic building blocks to find suitable Zr-MOF for CH₄ delivery. Among the hypothetical studies, the MOF with the *fcu* topological net (NU-800) based on the ditopic linker 1,4-benzenedipropynoic acid was predicted to have the best methane deliverable capacity. Subsequent CH₄ adsorption measurement based on successfully synthesized NU-800 exhibited the volumetric and gravimetric CH₄ deliverable capacities between 65 and 5 bar were 167 cm³/cm³ and 0.215 g/g, respectively. Stability tests verified no sample degradation over a large number of gas adsorption cycles, indicating the highly stable structures of zirconium-based MOFs.

Reducing the anthropogenic CO₂ emission associated with global climate change and global warming effects has become an important issue for humans. Developing efficient CO₂ capture and storage techniques featuring high uptake, selectivity, stability and reasonable cost is in high demand. As a new type of porous material, MOFs have received significant attention as promising sorbents for CO₂ capture and separation. For example, Feng and coworkers¹³⁰ developed a series of heterometallic MOF materials denoted CPM-200s with superior CO₂ uptake performance (Figure 1.36).

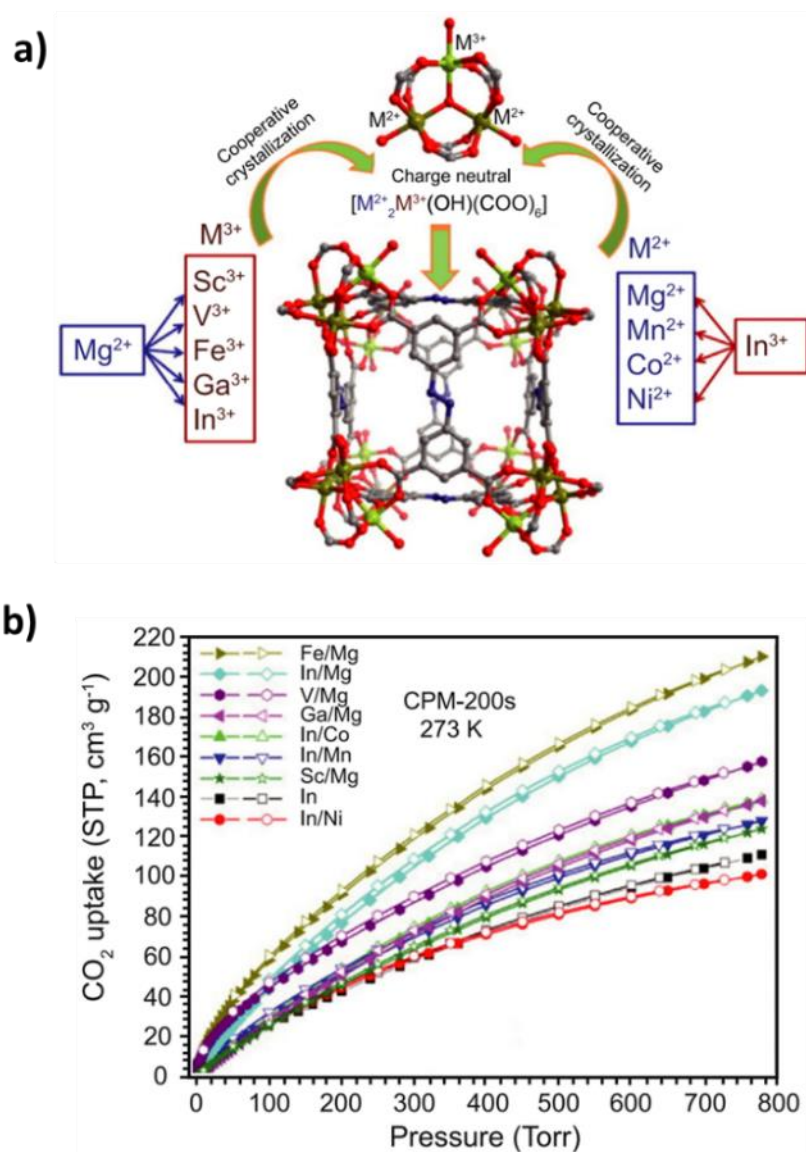


Figure 1.36. a) M^{2+} and M^{3+} combinations as heterometallic clusters for CPM-200s and b) CO_2 adsorption isotherms of CPM-200s at 273 K.

The combinations of trivalent and divalent metals provide these porous MOF crystals heterometallic clusters with various open metal sites. The CPM-200-Fe/Mg and CPM-200-In/Mg exhibited remarkable CO_2 uptakes up to 207.6 and 190.8 cm^3/g at 273K and 1 bar, which are close to the all-time record set by MOF-74-Mg (228 cm^3/g at 273K).¹³¹ It is interesting that CPM-200s show negligible N_2 uptake at 273K. The IAST (ideal adsorbed solution theory) selectivity of CPM-200-Fe/Mg for CO_2 (50%) and N_2 (50%) mixture reaches as high as 201 at 273K, which is attributed to the special interactions between gas molecules and open metal sites. The outperformance of CPM-200s indicate that they are promising materials for CO_2 capture.

1.4.2 Molecular separation

The separation of hydrocarbon mixtures has traditionally represented one of the most important chemical processes in the petrochemical industry. For example, both acetylene and ethylene are essential sources of organic chemicals for polymer products or other useful chemicals. High purity of starting materials is a prerequisite in the chemical industry. Separation by means of adsorption using porous materials is recognized as a promising strategy because they are environmentally benign and energy efficient. Benefiting from rational design and exquisite control over pore accessibility and pore surface, MOFs show great potential in the realm of hydrocarbon separation.

Chen and coworkers¹³² reported a microporous MOF material [Zn(dps)₂(SiF₆)] (UTSA-300) with two-dimensional channels of about 3.3 Å, well-matched for the molecular sizes of C₂H₂. The block crystals were synthesized from 4,4'-dipyridylsulfide (dps) with ZnSiF₆ in methanol at room temperature. After activation, the network was transformed to its closed-pore phase, UTSA-300a, with dispersed 0D cavities, accompanied by conformation change of the pyridyl ligand and rotation of SiF₆²⁻ pillars (Figure 1.37a, b). Interestingly, UTSA-300a takes up quite a large amount of C₂H₂ (76.4 cm³/g), while showing negligible C₂H₄ and CO₂ uptake under ambient conditions (Figure 1.37c). Subsequent neutron powder diffraction and molecular modeling studies clearly reveal that a C₂H₂ molecule primarily binds to two hexafluorosilicate F atoms in a head-on orientation, breaking the original intranetwork hydrogen bond and subsequently expanding to open-pore structure. Then unique pore chemistry and pore size associated with suitable pore aperture enable the IAST selectivities for the C₂H₂/CO₂ and C₂H₂/C₂H₄ binary equimolar mixtures to reach 743 and 104 at 298 K and 100 kPa, respectively. In addition, experimental breakthrough studies demonstrate that UTSA-300a exhibits highly efficient separation performance for C₂H₂/CO₂ and C₂H₂/C₂H₄ mixtures (Figure 1.37d). For both gas mixtures, only pure CO₂ or C₂H₄ (purity > 99.9%) was detected in the outlet effluent during initial purges, which indicates the molecular exclusion of CO₂ and C₂H₄ works well even under dynamic gas mixture flow.

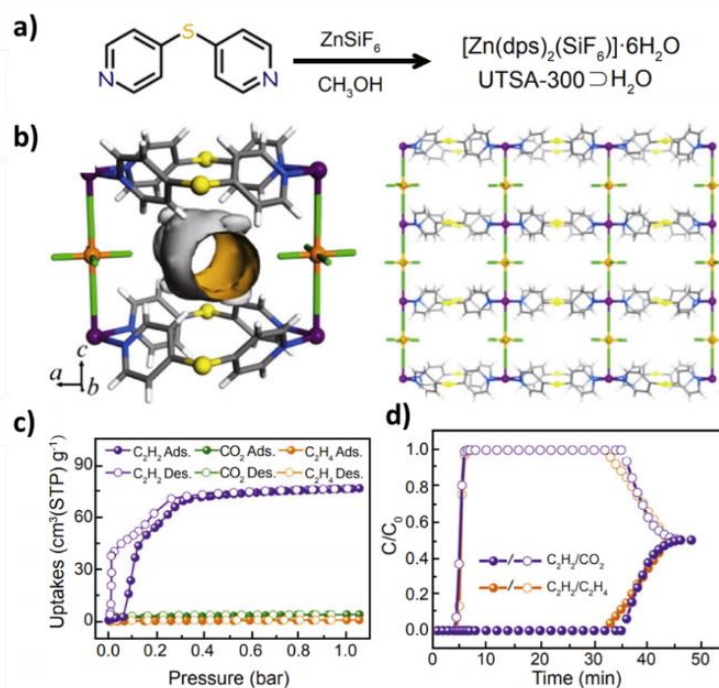


Figure 1.37. a) Schematic synthesis of $UTSA-300 \cdot 6H_2O$; b) perspective views of cage unit (left) and coordination layer (right) within $UTSA-300$; c) Sorption isotherms of C_2H_2 , CO_2 , and C_2H_4 for $UTSA-300a$ at 273 K; d) Experimental breakthrough curves for the 50/50 C_2H_2/CO_2 and C_2H_2/C_2H_4 gas mixtures at 298 K and 1 bar.

Beyond the excellent separation of gaseous chemical mixtures, MOF materials exhibit highly performance in separation of many organic compounds mixtures. Stoddart and coworkers fabricated a series of porous MOF materials from naturally available products as building blocks.¹³³ These extended porous framework, namely CD-MOF, are assembled by linking alkali metal ions (Na^+ , K^+ , Rb^+ , Cs^+) and α -cyclodextrin (α -CD), which can be prepared from entirely food-grade precursors and renewable.¹³⁴ Abundant of accessible free hydroxyl groups within the interior surface endow the CD-MOF material versatile functionalities, particularly in relation to molecular storage and separation sciences^{135, 136} Associated with the help of liquid-phase chromatographic technique, this porous material has been shown to facilitate the separation of a wide variety of mixtures, not only different alkylaromatic compounds into their pure components in both the liquid and gas phases, but also including ethylbenzene from styrene, haloaromatics, terpenes, pinenes and other chiral compounds at ambient temperature (Figure 1.38).

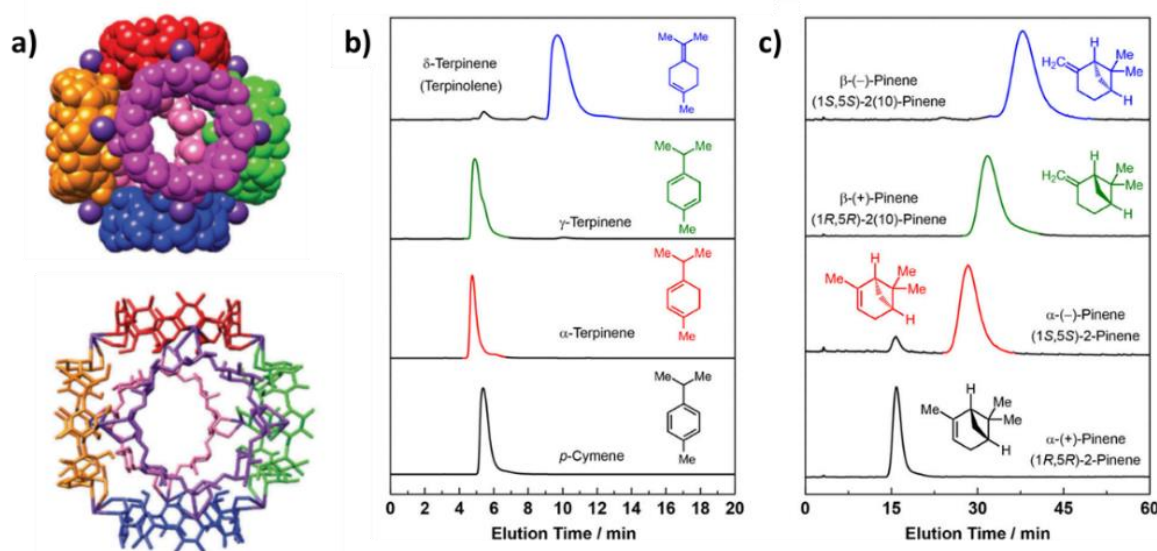


Figure 1.38. a) Space-filling and wireframe representations of (r-CD)₆ cube cage of CD-MOF showing the large cavity of 1.7 nm diameter. b) Liquid-phase HPLC traces illustrating the differences in retention of terpinene isomers and the aromatic analogue p-cymene, c) pinene isomers using HPLC-grade hexane as the mobile phase at a flow rate of 1 mL/min at 298K.

Moreover, the chirality of r-CD is maintained throughout the extended structure of CD-MOF, which is capable of enantiomeric recognition and the separation of racemic mixtures. The green, renewable CD-MOF materials and their energy-efficiently separation manner enable them significant implications for the petrochemical industry.

1.4.3 Catalysis

Due to the extremely large surface areas, highly ordered crystalline structures and tunable pore sizes and functionalities, MOFs have become promising candidates for heterogeneous catalyst in industrial applications. Some MOF materials exhibit remarkable intrinsic catalytic activities because of their appropriate pores and open metal sites that are catalytically accessible for reactants.

In the past decades, there have been many reports and reviews regarding MOFs as heterogeneous catalysts. For example, the MOF MIL-101 (Cr₃X(H₂O)₂O(bdc)₃; X = F, OH; bdc = benzene-1,4-dicarboxylate), reported by Férey and coworkers¹³ in 2005, showed a very high surface area and pore volume. Significantly, the large pore windows of MIL-101 give access for large reactant molecules diffusing into the pores and the chromium sites are accessible after simple dehydration. The highly catalytic activity of MIL-101 has been

demonstrated in several types of catalytic reactions. For instance, Mohammadpoor-Baltork and coworkers¹³⁸ demonstrated that the catalytic activity of porous MIL-101 materials in direct oxidation of alkenes into carboxylic acids, which is a valuable reaction in organic synthesis (Figure 1.39). Under mild conditions with H_2O_2 and CH_3CN refluxing, MIL-101 performed highly oxidative cleavage activity to a series of alkene compounds during three cycles, resulting in high yielding of corresponding carboxylic acid in moderate time. Moreover, the stable MIL-101 materials have been proved to be an efficient heterogeneous catalyst for the selective catalytic cyanosilylation of aldehydes¹³⁹ and oxidation of teterlin.¹⁴⁰

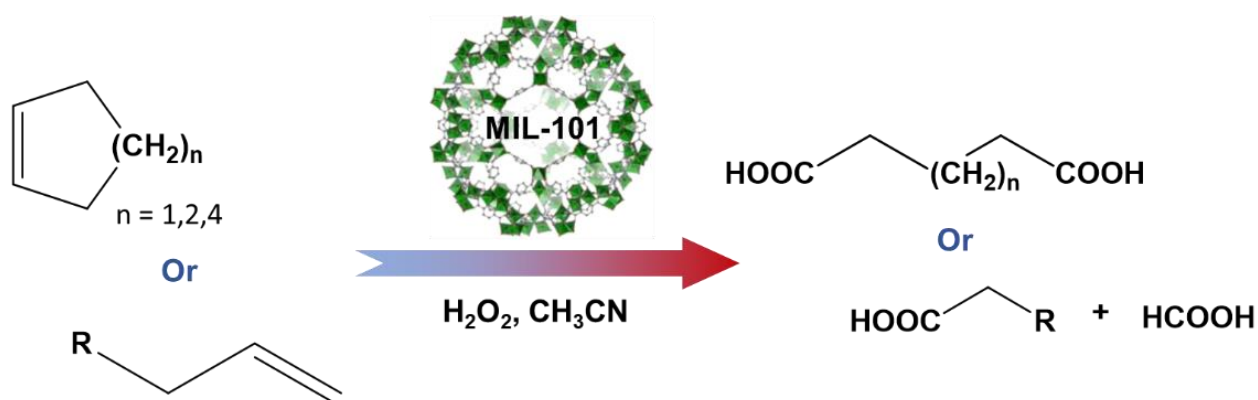


Figure 1.39. Oxidative cleavage of alkenes with H_2O_2 catalyzed by MIL-101 solid materials.

Except that, different types of catalytic sites are introduced into the MOF matrix and their properties as heterogeneous catalysts have been investigated in the past decade.¹⁴¹ Li and coworkers reported an amino-functionalized titanium MOF, $\text{NH}_2\text{-MIL-125(Ti)}$ could reduce CO_2 under visible light irradiation.¹⁴² In the presence of acetonitrile (MeCN) with triethanolamine (TEOA), the $\text{NH}_2\text{-MIL-125(Ti)}$ exhibits remarkable performance of CO_2 reduction to formate anion HCOO^- while parent MIL-125(Ti) shows negligible visible light photocatalytic activity under the similar condition. In addition, Cohen and coworkers¹⁴³ introduced mixed linker and titanium sites into the framework of UiO-66-derivative structures achieving effective photocatalyst for CO_2 reduction under visible light (Figure 1.40).

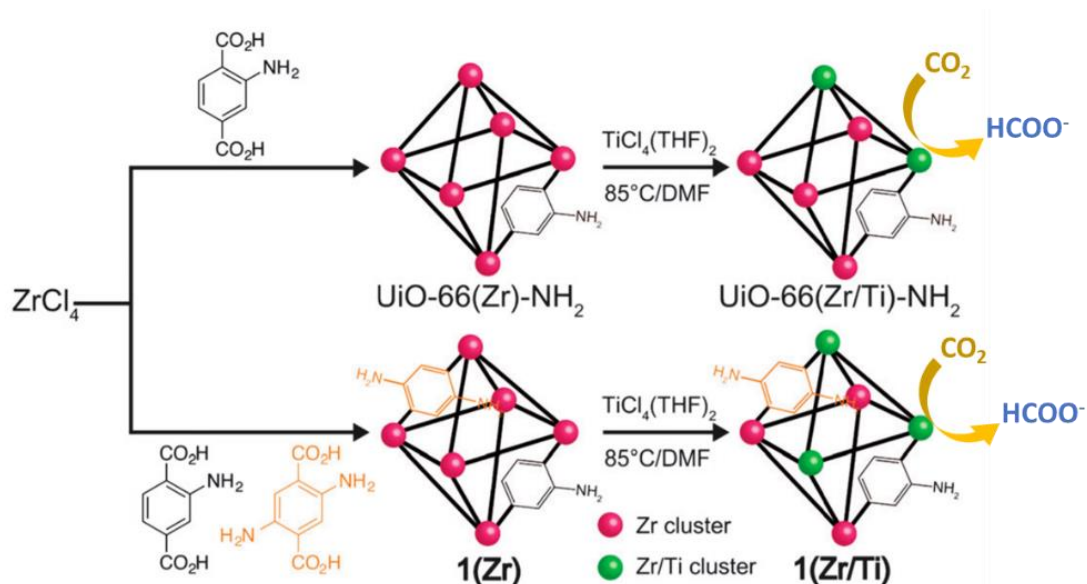


Figure 1.40. Synthesis of mixed-ligand MOF(Zr) and subsequent mixed-metal MOF(Zr/Ti) via PSM method to improve photocatalytic activity.

The resulted mixed metal MOF-Zr/Ti materials by post-synthetic exchange method exhibited much higher photocatalytic activity and improved visible light sensitivity comparing to the NH₂-MIL-125(Ti) and other non-MOF heterogenous photocatalysts. These results highlight the potential of MOF materials as high-efficient photocatalysts in application.

Another recent progress in practical catalytic applications of MOFs by controllable integration of other catalytic materials has received broad interest. For example, Farha and coworker¹⁴⁴ constructed a water-stable csq-net zirconium-based MOF, NU-1003, which was composed of interconnected hierarchical mesoporous and microporous channels. These existing mesoporous channels were suitable for encapsulate the large biological molecule OPAA (organophosphorus acid anhydrolase) (Figure 1.41), which was the important catalytic enzyme.

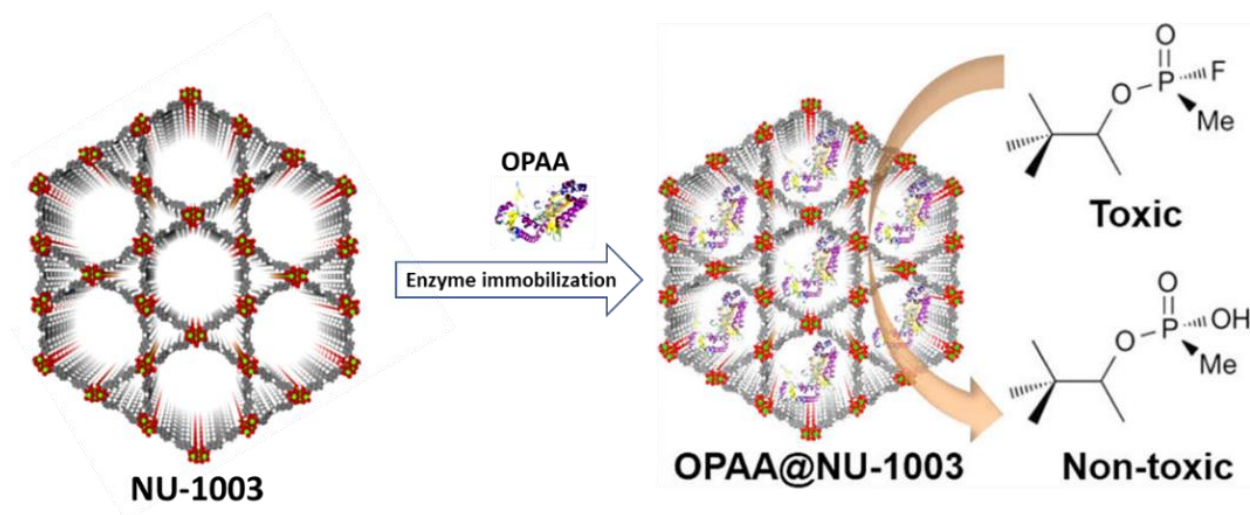


Figure 1.41. Representation of immobilization of OPAA in the mesoporous channels of NU-1003, which significantly improved the catalytic efficiency of the OPAA on nerve agent hydrolysis.

Subsequent test of the immobilized OPAA@NU-1003 showed significantly increased catalytic efficiency in the application of hydrolyzing nerve agents compared to that of free OPAA.

1.5 Reference

- (1) Hoskins, B. F.; Robson, R. *J. Am. Chem. Soc.* **1990**, *112*, 1546.
- (2) Hoskins, B. F.; Robson, R. *J. Am. Chem. Soc.* **1989**, *111*, 5962.
- (3) Yaghi, O. M.; Li, H. *J. Am. Chem. Soc.* **1995**, *117*, 10401.
- (4) Yaghi, O. M.; Li, G.; Li, H. *Nature* **1995**, *378*, 703.
- (5) Kondo, M.; Yoshitomi, T.; Seki, K.; Matsuzaka, H.; Kitagawa, S. *Angew. Chem., Int. Ed.* **1997**, *36*, 1725.
- (6) Li H., Eddaoudi M., O’Keeffe M., Yaghi O. M. *Nature* **1999**, *402*, 276.
- (7) Chui S. S.-Y.; Lo S. M.-F.; Charmant J. P. H., Orpen A. G., Williams I. D., *Science* **1999**, *283*, 1148.
- (8) Férey, G.; Mellot-Draznieks, C.; Serre, C.; Millange, F.; Dutour, J.; Surblé, S.; Margiolaki, I. *Science* **2005**, *309*, 2040.
- (9) Serre, C.; Millange, F.; Thouvenot, C.; Nogues, M.; Marsolier, G.; Louër, D.; Férey, G. *J. Am. Chem. Soc.* **2002**, *124*, 13519.
- (10) Barthelet, K.; Marrot, J.; Riou, D.; Férey, G. *Angew. Chem., Int. Ed.* **2002**, *41*, 281.
- (11) Furukawa, H.; Go, Y. B.; Ko, N.; Park, Y. K.; Uribe-Romo, F. J.; Kim, J.; O’Keeffe, M.; Yaghi, O. M. *Inorg. Chem.* **2011**, *50*, 9147.
- (12) Farha, O. K.; Yazaydin, A. O.; Eryazici, I.; Malliakas, C. D.; Hauser, B. G.; Kanatzidis, M. G.; Nguyen, S. T.; Snurr, R. Q.; Hupp, J. T. *Nat. Chem.* **2010**, *2*, 944.
- (13) Farha, O. K.; Eryazici, I.; Jeong, N. C.; Hauser, B. G.; Wilmer, C. E.; Sarjeant, A. A.; Snurr, R. Q.; Nguyen, S. T.; Yazaydin A. Ö.; Hupp J. T. *J. Am. Chem. Soc.* **2012**, *134*, 15016.
- (14) Cavka, J. H.; Jakobsen, S.; Olsbye, U.; Guillou, N.; Lamberti, C.; Bordiga, S.; Lillerud, K. *P. J. Am. Chem. Soc.* **2008**, *130*, 13850.
- (15) Ahnfeldt, T.; Guillou, N.; Gunzelmann, D.; Margiolaki, I.; Loiseau, T.; Férey, G.; Senker, J.; Stock, N. *Angew. Chem., Int. Ed.* **2009**, *48*, 5163.
- (16) Banerjee, R.; Phan, A.; Wang, B.; Knobler, C.; Furukawa, H.; O’Keeffe, M.; Yaghi, O. M. *Science* **2008**, *319*, 939.
- (17) Zhou, H.-C.; Kitagawa, S. *Chem. Soc. Rev.* **2014**, *43*, 5415.
- (18) Wang, Z.; Cohen, S. M. *Chem. Soc. Rev.* **2009**, *38*, 1315.
- (19) Tsuruoka, T.; Furukawa, S.; Takashima, Y.; Yoshida, K.; Isoda, S.; Kitagawa, S. *Angew. Chem., Int. Ed.* **2009**, *48*, 4739.
- (20) Deng, H.; Doonan, C. J.; Furukawa, H.; Ferreira, R. B.; Towne, J.; Knobler, C. B.; Wang, B.; Yaghi, O. M. *Science* **2010**, *327*, 846.

- (21) Eddaoudi, M.; Kim, J.; Rosi, N.; Vodak, D.; Wachter, J.; O’Keefe, M.; Yaghi, O. M. *Science* **2002**, *295*, 469.
- (22) Deng, H.; Grunder, S.; Cordova, K. E.; Valente, C.; Furukawa, H.; Hmadeh, M.; Gándara, F.; Whalley, A. C.; Liu, Z.; Asahina, S.; Kazumori, H.; O’Keeffe, M.; Terasaki, O.; Stoddart, J. F.; Yaghi, O. M. *Science* **2012**, *336*, 1018.
- (23) Furukawa H.; Yaghi O. M. *J. Am. Chem. Soc.* **2009**, *131*, 8875.
- (24) Xue, M.; Liu, Y.; Schaffino, R. M.; Xiang, S.; Zhao, X.; Zhu, G.-S.; Qiu, S.-L.; Chen, B. *Inorg. Chem.* **2009**, *48*, 4649.
- (25) Serre, C.; Millange, F.; Thouvenot, C.; Noguès, M.; Marsolier, G.; Louër, D.; Férey, G. *J. Am. Chem. Soc.* **2002**, *124*, 13519.
- (26) Férey, G.; Latroche, M.; Serre, C.; Millange, F.; Loiseau, T.; Percheron-Guegan, A. *Chem. Commun.* **2003**, 2976.
- (27) Llewellyn, P. L.; Horcajada, P.; Maurin, G.; Devic, T.; Rosenbach, N.; Bourrelly, S.; Serre, C.; Vincent, D.; Loera-Serna, S.; Filinchuk, Y.; Férey, G. *J. Am. Chem. Soc.* **2009**, *131*, 13002.
- (28) Mowat, J. P. S.; Miller, S. R.; Slawin, A. M. Z.; Seymour, V. R.; Ashbrook, S. E.; Wright, P. A. *Microporous Mesoporous Mater.* **2011**, *142*, 322.
- (29) Depauw, H.; Nevjestic, I.; Wang, G.B.; Leus, K.; Callens, F.; DeCanck, E.; De Buysser, K.; Vrielinck, H.; VanDer Voort, P. *J. Mater. Chem. A* **2017**, *5*, 24580.
- (30) Jiang, H.-L.; Makal, T. A.; Zhou, H.-C. *Coord. Chem. Rev.* **2013**, *257*, 2232.
- (31) Yoon M.; Srirambalaji R.; Kim K. *Chem. Rev.* **2012**, *112*, 1196.
- (32) Horcajada, P.; Gref, R.; Baati, T.; Allan, P. K.; Maurin, G.; Couvreur, P.; Férey, G.; Morris, R. E.; Serre, C. *Chem. Rev.* **2012**, *112*, 1232.
- (33) Horcajada, P.; Serre, C.; Maurin, G.; Ramsahye, N. A.; Balas, F.; Vallet-Regi, M.; Sebban, M.; Taulelle, F.; Férey, G. *J. Am. Chem. Soc.* **2008**, *130*, 6774.
- (34) Blatov, V. A.; Carlucci, L.; Ciani, G.; Proserpio D. M. *CrystEngComm* **2004**, *6*, 378.
- (35) M. Li, D. Li, M. O’Keeffe and O. M. Yaghi, *Chem. Rev.*, **2014**, *114*, 1343.
- (36) Caskey, S. R.; Wong-Foy, A. G.; Matzger, A. J. *J. Am. Chem. Soc.* **2008**, *130*, 10870.
- (37) Düren, T., Bae, Y.-S. & Snurr, R. Q. *Chem. Soc. Rev.* **2009**, *38*, 1237.
- (38) Fang, H., Demir, H., Kamakoti, P.; Sholl, D. S. *J. Mater. Chem. A* **2014**, *2*, 274.
- (39) Furukawa, H.; Ko, N.; Go, Y. B.; Aratani, N.; Choi, S. B.; Choi, E.; Yazaydin, A. O.; Snurr, R. Q.; O’Keeffe, M.; Kim, J.; Yaghi, O. M. *Science* **2010**, *329*, 424.

- (40) Qin, J.-S.; Yuan, S.; Wang, Q.; Alsalmeh, A.; Zhou, H.-C. *J. Mater. Chem. A* **2017**, *5*, 4280.
- (41) Yuan, S.; Qin, J. S.; Zou, L.; Chen, Y. P.; Wang, X.; Zhang, Q.; Zhou, H. C. *J. Am. Chem. Soc.*, **2016**, *138*, 6636.
- (42) Feng, L.; Yuan, S.; Zhang, L.-L.; Tan, K.; Li, J.-L.; Kirchon, A.; Liu, L.-M.; Zhang, P.; Han, Y.; Chabal, Y. J.; Zhou, H.-C. *J. Am. Chem. Soc.* **2018**, *140*, 2363.
- (43) Yuan, S.; Zou, L.; Qin, J.-S.; Li, J.; Huang, L.; Feng, L.; Wang, X.; Bosch, M.; Alsalmeh, A.; Cagin, T.; Zhou, H.-C. *Nat. Commun.* **2017**, *8*, 15356.
- (44) Bennett, T. D.; Cheetham, A. K. *Acc. Chem. Res.* **2014**, *47*, 1555.
- (45) Jiang, J.; Zhao, Y.; Yaghi, O. M. *J. Am. Chem. Soc.* **2016**, *138*, 3255.
- (46) Vermoortele, F.; Bueken, B.; Le Bars, G. I.; Van de Voorde, B.; Vandichel, M.; Houthoofd, K.; Vimont, A.; Daturi, M.; Waroquier, M.; Van Speybroeck, V.; Kirschhock, C.; De Vos, D. E. *J. Am. Chem. Soc.*, **2013**, *135*, 11465.
- (47) Tsuruoka, T.; Furukawa, S.; Takashima, Y.; Yoshida, K.; Isoda, S.; Kitagawa, S. *Angew. Chem., Int. Ed.* **2009**, *48*, 4739.
- (48) Umemura, A.; Diring, S.; Furukawa, S.; Uehara, H.; Tsuruoka, T.; Kitagawa, S. *J. Am. Chem. Soc.* **2011**, *133*, 15506.
- (49) Schaate, A.; Roy, P.; Godt, A.; Lippke, J.; Waltz, F.; Wiebcke, M.; Behrens, P. *Chem. - Eur. J.* **2011**, *17*, 6643.
- (50) McGuire C. V.; Forgan R. S. *Chem. Commun.*, **2015**, *51*, 5199.
- (51) Marshall, R. J.; Hobday, C. L.; Murphie, C. F.; Griffin, S. L.; Morrison, C. A.; Moggach, S. A.; Forgan, R. S. *J. Mater. Chem. A* **2016**, *4*, 6955.
- (52) Marshall, R. J.; Griffin, S. L.; Wilson, C.; Forgan, R. S. *J. Am. Chem. Soc.* **2015**, *137*, 9527.
- (53) Cohen S.M. *Chem. Rev.* **2012**, *112*, 970.
- (54) Goto, Y.; Sato, H.; Shinkai, S.; Sada, K. *J. Am. Chem. Soc.* **2008**, *130*, 14354.
- (55) Gadzikwa, T.; Farha, O. K.; Malliakas, C. D.; Kanatzidis, M. G.; Hupp, J. T.; Nguyen, S. T. *J. Am. Chem. Soc.* **2009**, *131*, 13613.
- (56) Kim M.; Cohen S. M. *CrystEngComm* **2012**, *14*, 4096.
- (57) Cohen S. M. *J. Am. Chem. Soc.* **2017**, *139*, 2855.
- (58) Tanabe, K. K.; Cohen, S. M. *Chem. Soc. Rev.* **2011**, *40*, 498.
- (59) Wang, Z.; Tanabe, K.; Cohen, S. M. *Chem. - Eur. J.* **2010**, *16*, 212.
- (60) Layer, R. W.; Lattimer, R. P. *Rubber Chem. Technol.* **1990**, *63*, 426.

- (61) Miki, N.; Maeno, M.; Maruhashi, K.; Nakagawa, Y.; Ohmi, T. *Corros. Sci.* **1990**, *31*, 69.
- (62) Harshé, G. *J. Mater. Eng. Perform.* **1992**, *1*, 83.
- (63) Jiang, J.; Zhao, Y.; Yaghi, O. M. *J. Am. Chem. Soc.* **2016**, *138*, 3255.
- (64) Wang, Z.; Cohen, S. M. *J. Am. Chem. Soc.* **2007**, *129*, 12368.
- (65) Wang Z.Q.; Cohen S.M. *Angew. Chem., Int. Ed.* **2008**, *47*, 4699.
- (66) DeCoste, J. B.; Peterson, G. W.; Jasuja, H.; Glover, T. G.; Huang, Y.; Walton, K. S. *J. Mater. Chem. A* **2013**, *1*, 5642.
- (67) Marshall, R. J.; Forgan, R. S. *Eur. J. Inorg. Chem.* **2016**, 4310.
- (68) Garibay S. J.; Cohen S. M. *Chem. Commun.* **2010**, 46, 7700.
- (69) Luan, Y.; Qi, Y.; Gao, H.; Andriamitantoa, R. S.; Zheng, N.; Wang, G.; Čejka, J.; Valenzano, L.; Lamberti, C.; Lillerud, K. P.; Bordigaa, S. *J. Mater. Chem. A* **2015**, *3*, 17320.
- (70) Kronast, A.; Eckstein, S.; Altenbuchner, P. T.; Hindelang, K.; Vagin, S. I.; Rieger, B. *Chem. - Eur. J.* **2016**, *22*, 12800.
- (71) Fracaroli, A. M.; Siman, P.; Nagib, D. A.; Suzuki, M.; Furukawa, H.; Toste, F. D.; Yaghi, O. M. *J. Am. Chem. Soc.* **2016**, *138*, 8352.
- (72) Townsend R.P.; Coker, E.N. *Stud. Surf. Sci. Catal.* **2001**, *137*, 467.
- (73) Brozek C. K.; Dincă M. *Chem. Soc. Rev.*, **2014**, *43*, 5456.
- (74) Lalonde, M.; Bury, W.; Karagiari, O.; Brown, Z.; Hupp, J. T.; Farha, O. K. *J. Mater. Chem. A* **2013**, *1*, 5453.
- (75) Dincă M.; Long J. R. *J. Am. Chem. Soc.*, **2007**, *129*, 11172.
- (76) Cavka, J. H.; Jakobsen, S.; Olsbye, U.; Guillou, N.; Lamberti, C.; Bordiga, S.; Lillerud, K. *P. J. Am. Chem. Soc.* **2008**, *130*, 13850.
- (77) Kim, M.; Cahill, J. F.; Su, Y. X.; Prather, K. A.; Cohen, S. M. *Chem. Sci.* **2012**, *3*, 126.
- (78) Kim, M.; Cahill, J. F.; Fei, H.; Prather, K. A.; Cohen, S. M. *J. Am. Chem. Soc.* **2012**, *134*, 18082.
- (79) Li, T.; Kozlowski, M. T.; Doud, E. A.; Blakely, M. N.; Rosi, N. L. *J. Am. Chem. Soc.* **2013**, *135*, 11688.
- (80) Yin, Z.; Zhou, Y.-L.; Zeng, M.-H.; Kurmoo, M. *Dalton Trans.* **2015**, *44*, 5258.
- (81) Liu, C.; Luo, T.-Y.; Feura, E. S.; Zhang, C.; Rosi, N. L. *J. Am. Chem. Soc.* **2015**, *137*, 10508.
- (82) Liu, C.; Zeng, C.; Luo, T.-Y.; Merg, A. D.; Jin, R.; Rosi, N. L. *J. Am. Chem. Soc.* **2016**, *138*, 12045.

- (83) Mondloch, J. E.; Bury, W.; Fairen-Jimenez, D.; Kwon, S.; DeMarco, E. J.; Weston, M. H.; Sarjeant, A. A.; Nguyen, S. T.; Stair, P.C.; Snurr, R. Q.; Farha, O. K.; Hupp, J. T. *J. Am. Chem. Soc.* **2013**, *135*, 10294.
- (84) Yuan, S.; Lu, W.; Chen, Y.-P.; Zhang, Q.; Liu, T.-F.; Feng, D.; Wang, X.; Qin, J.; Zhou, H.-C. *J. Am. Chem. Soc.* **2015**, *137*, 3177.
- (85) Deria, P.; Mondloch, J. E.; Tylianakis, E.; Ghosh, P.; Bury, W.; Snurr, R. Q.; Hupp, J. T.; Farha, O. K. *J. Am. Chem. Soc.* **2013**, *135*, 16801.
- (86) Tu, B.; Pang, Q.; Wu, D.; Song, Y.; Weng, L.; Li, Q. *J. Am. Chem. Soc.* **2014**, *136*, 14465.
- (87) Chen, B.; Eddaoudi, M.; Reineke, T. M.; Kampf, J. W.; O’Keeffe, M.; Yaghi, O. M. *J. Am. Chem. Soc.* **2000**, *122*, 11559.
- (88) Vermoortele, F.; Ameloot, R.; Alaerts, L.; Matthessen, R.; Carlier, B.; Fernandez, E. V. R.; Gascon, J.; Kapteijn, F.; De Vos, D. E. *J. Mater. Chem.* **2012**, *22*, 10313.
- (89) Koo, J.; Hwang, I. C.; Yu, X.; Saha, S.; Kim, Y.; Kim, K. *Chem. Sci.* **2017**, *8*, 6799.
- (90) Horcajada, P.; Surble, S.; Serre, C.; Hong, D. Y.; Seo, Y. K.; Chang, J. S.; Greneche, J. M.; Margiolaki, I.; Férey, G. *Chem. Commun.* **2007**, *27*, 2820.
- (91) Hintz H.; Wuttke, S. *Chem. Mater.* **2014**, *26*, 6722.
- (92) Garzón-Tovar, L.; Rodríguez-Hermida, S.; Imaz, I.; MasPOCH, D. *J. Am. Chem. Soc.*, **2017**, *139*, 897.
- (93) Espin, J.; Garzón-Tovar, L.; Boix, G.; Imaz, I.; MasPOCH, D. *Chem. Commun.*, **2018**, *54*, 4184.
- (94) Cárne-Sánchez, A.; Imaz, I.; Cano-Sarabia, M.; MasPOCH, D. *Nat. Chem.* **2013**, *5*, 203.
- (95) Zhang, Y. Y.; Feng, X.; Li, H. W.; Chen, Y. F.; Zhao, J. S.; Wang, S.; Wang, L.; Wang, B. *Angew. Chem., Int. Ed.* **2015**, *54*, 4259.
- (96) Szekely J.; Evans J. W. *Metall. Trans.*, **1971**, *2*, 1691.
- (97) Jamshidi E.; AleEbrahim H. *Chem. Eng. J.*, **1997**, *68*, 1.
- (98) Kiang, Y.-H.; Gardner, G. B.; Lee, S.; Xu, Z.; Lobkovsky, E. B. *J. Am. Chem. Soc.* **1999**, *121*, 8204.
- (99) Servalli M.; Ranocchiari, M. J.; Van Bokhoven A. *Chem. Commun.* **2012**, *48*, 1904.
- (100) Ingleson, M. J.; Perez Barrio, J.; Guilbaud, J. B.; Khimyak, Y. Z.; Rosseinsky, M. J. *Chem. Commun.* **2008**, 2680.
- (101) Ingleson, M. J.; Heck, R.; Gould, J. A.; Rosseinsky, M. J. *Inorg. Chem.* **2009**, *48*, 9986.
- (102) Hermes, S.; Schroder, F.; Amirjalayer, S.; Schmid, R.; Fischer, R. *J. Mater. Chem.* **2006**, *16*, 2464.

- (103) Müller, M.; Hermes, S.; Kähler, K.; van den Berg, M. W.; Muhler, M.; Fischer, R. A. *Chem. Mater.* **2008**, *20*, 4576.
- (104) Esken, D.; Noei, H.; Wang, Y.; Wiktor, W.; Turner, S.; Van Tendeloo, G.; Fischer, R. A. *J. Mater. Chem.* **2011**, *21*, 5907.
- (105) Meilikhov, M.; Yusenko, K.; Fischer, R. A. *J. Am. Chem. Soc.* **2009**, *131*, 9644.
- (106) Rubin, M. B. *Bull. Hist. Chem.* **2001**, *26*, 40.
- (107) Criegee R. *Angew. Chem., Int. Ed.* **1975**, *14*, 745.
- (108) Klusmann M. *Chem. Eur. J.* **2018**, *24*, 4480.
- (109) Willand-Charnley, R.; Fisher, T. J.; Johnson, B. M.; Dussault, P. H. *Org. Lett.* **2012**, *14*, 2242.
- (110) Van Ornum, S. G.; Champeau, R. M.; Pariza, R. *Chem. Rev.* **2006**, *106*, 2990.
- (111) Hilf, J. A.; Holzwarth, M. S.; Rychnovsky, S. D. *J. Org. Chem.* **2016**, *81*, 10376.
- (112) Desvergne, J.; Lapouyade, P. R.; Thomas J. M. *Cryst. Liq. Cryst.* **1976**, *32*, 143.
- (113) Vennerstrom, J. L.; Arbe-Barnes, S.; Brun, R.; Charman, S. A.; Chiu, F. C. K.; Chollet, J.; Dong, Y.; Dorn, A.; Hunziker, D.; Matile, H.; McIntosh, K.; Padmanilayam, M.; Santo Tomas, J.; Scheurer, C.; Scorneaux, B.; Tang, Y.; Urwyler, H.; Wittlin, S.; Charman, W. N. *Nature* **2004**, *430*, 900.
- (114) Corma, A.; García, H.; Llabrés i Xamena, F. X. *Chem. Rev.* **2010**, *110*, 4606.
- (115) Zeng, L.; Guo, X.; He, C.; Duan, C. *ACS Catal.* **2016**, *6*, 7935.
- (116) Bachman J. E.; Smith, Z. P.; Li, T.; Xu, T.; Long, J. R.; *Nat. Mater.* **2016**, *15*, 845.
- (117) Hartlieb, K. J.; Holcroft, J. M.; Moghadam, P. Z.; Vermeulen, N. A.; Algaradah, M. M.; Nassar, M. S.; Botros, Y. Y.; Snurr, R. Q.; Stoddart, J. F. *J. Am. Chem. Soc.* **2016**, *138*, 2292.
- (118) Kuppler, R.J.; Timmons, D.J.; Fang, Q.R.; Li, J.R.; Makal, T.A.; Young, M. D.; Yuan, D.; Zhao, D.; Zhang, W.; Zhou, H.-C. *Coord. Chem. Rev.* **2009**, *253*, 3042.
- (119) Levine, D. J.; Runcevski, T.; Kapelewski, M. T.; Keitz, B. K.; Oktawiec, J.; Reed, D. A.; Mason, J. A.; Jiang, H. Z. H.; Colwell, K. A.; Legendre, C. M.; FitzGerald, S. A.; Long, J. R. *J. Am. Chem. Soc.* **2016**, *138*, 10143.
- (120) Zhao, D.; Tan, S. W.; Yuan, D. Q.; Lu, W. G.; Rezenom, Y. H.; Jiang, H. L.; Wang, L. Q.; Zhou, H. C. *Adv. Mater.* **2011**, *23*, 90.
- (121) Carné, A.; Carbonell, C.; Imaz, I.; MasPOCH D. *Chem. Soc. Rev.* **2011**, *40*, 291.
- (122) Mazloomi, K.; Gomes, C. *Renewable Sustainable Energy Rev.* **2012**, *16*, 3024.

- (123) Rosi, N. L.; Eckert, J.; Eddaoudi, M.; Vodak, D. T.; Kim, J.; O'keeffe, M.; Yaghi, O. M. *Science* **2003**, *300*, 1127.
- (124) Latroche, M.; Surble, S.; Serre, C.; Mellot-Draznieks, C.; Llewellyn, P. L.; Chang, J. H.; Chang, J. S.; Jhung, S. H.; Férey, G. *Angew. Chem., Int. Ed.* **2006**, *45*, 8227.
- (125) Koh, K.; Wong-Foy, A. G.; Matzger, A. J. *J. Am. Chem. Soc.* **2009**, *131*, 4184.
- (126) Goldsmith, J.; Wong-Foy, A. G.; Cafarella, M. J.; Siegel, D. *J. Chem. Mater.* **2013**, *25*, 3373.
- (127) Kapelewski, M. T.; Geier, S. J.; Hudson, M. R.; Stück, D.; Mason, J. A.; Nelson, J. N.; Xiao, D. J.; Hulvey, Z.; Gilmour, E.; FitzGerald, S. A.; Head-Gordon, M.; Brown, C. M.; Long, J. R. *J. Am. Chem. Soc.* **2014**, *136*, 12119.
- (128) Peng, Y.; Krungleviciute, V.; Eryazici, I.; Hupp, J. T.; Farha, O. K.; Yildirim, T. *J. Am. Chem. Soc.* **2013**, *135*, 11887.
- (129) Hulvey, Z.; Vlaisavljevich, B.; Mason, J. A.; Tsivion, E.; Dougherty, T. P.; Bloch, E. D.; Head-Gordon, M.; Smit, B.; Long, J. R.; Brown, C. M. *J. Am. Chem. Soc.* **2015**, *137*, 10816.
- (130) Zhai, Q. G.; Bu, X. H.; Mao, C. Y.; Zhao, X.; Feng, P. Y. *J. Am. Chem. Soc.* **2016**, *138*, 2524.
- (131) Caskey, S.R.; Wong-Foy, A.G.; Matzger, A.J., *J. Am. Chem. Soc.* **2018**, *130*, 10870.
- (132) Lin, R.-B.; Li, L.; Wu, H.; Arman, H.; Li, B.; Lin, R.-G.; Zhou, W.; Chen, B. *J. Am. Chem. Soc.* **2017**, *139*, 8022.
- (133) Smaldone, R. A.; Forgan, R. S.; Furukawa, H.; Gassensmith, J. J.; Slawin, A. M. Z.; Yaghi, O. M.; Stoddart, J. F. *Angew. Chem., Int. Ed.* **2010**, *49*, 8630.
- (134) Smith, M. K.; Angle, S. R.; Northrop, B. H. *J. Chem. Educ.* **2015**, *92*, 368.
- (135) Holcroft, J. M.; Hartlieb, K. J.; Moghadam, P. Z.; Bell, J. G.; Barin, G.; Ferris, D. P.; Bloch, E. D.; Algaradah, M. M.; Nassar, M. S.; Botros, Y. Y.; Thomas, K. M.; Long, J. R.; Snurr, R. Q.; Stoddart, J. F. *J. Am. Chem. Soc.*, **2015**, *137*, 5706
- (136) Hartlieb, K. J.; Holcroft, J. M.; Moghadam, P. Z.; Vermeulen, N. A.; Algaradah, M. M.; Nassar, M. S.; Botros, Y. Y.; Snurr, R. Q.; Stoddart, J. F. *J. Am. Chem. Soc.* **2016**, *138*, 2292.
- (137) Corma, A.; Garcia, H.; Llabres i Xamena, F. X. L. I. *Chem. Rev.* **2010**, *110*, 4606.
- (138) Saedi, Z.; Tangestaninejad, S.; Moghadam, M.; Mirkhani, V.; Mohammadpoor-Baltork, I. *Catal. Commun.* **2012**, *17*, 18.
- (139) Henschel, A.; Gedrich, K.; Kraehnert, R.; Kaskel, S. *Chem. Commun.* **2008**, 4192.
- (140) Ramos-Fernandez, E.V. Garcia-Domingos, M. Juan-Alcáñiz J., Gascon, J. Kapteijn, F. *Applied Catalysis A: General* **2011**, *391*, 261.

- (141) Zhang, T.; Lin, W. *Chem. Soc. Rev.* **2014**, *43*, 5982.
- (142) Fu, Y.; Sun, D.; Chen, Y.; Huang, R.; Ding, Z.; Fu, X.; Li, Z. *Angew. Chem., Int. Ed.* **2012**, *51*, 3364.
- (143) Lee, Y.; Kim, S.; Kang J. K.; Cohen, S. M. *Chem. Commun.* **2015**, *51*, 5735.
- (144) Li, P.; Moon, S.-Y.; Guelta, M. A.; Lin, L.; Gómez-Gualdrón, D. A.; Snurr, R. Q.; Harvey, S. P.; Hupp, J. T.; Farha, O. K. *ACS Nano* **2016**, *10*, 9174.

Chapter 2

Objectives

Objective

Post-synthetic modification (PSM) has attracted much attention as a powerful tool to achieve specialized and sophisticated functionalities within metal-organic frameworks (MOFs).

As illustrated in **Chapter 1**, the merits of the unusual solid-gas post-synthetic modification encourage the conception of introducing unprecedented functionality by performing quick covalent chemistry on the surface of MOF frameworks in a solid-gas manner. Additionally, in our initial trial experiments, it was found that ozone gas reacted immediately with alkene compounds in solution-solid and gas-solid phase to form cleavage moieties. Based on literature retrieval and some initial trial results, our motivation arose from the context that the ozonolysis reaction can be implemented to functionalize and/or modify the interior surface of MOFs, resulting in interesting post-functional groups or frameworks. Following that, the objective of this THESIS is proposed.

- Develop a new solid-gas phase post-synthetic approach, by making use of the highly porosity of MOFs and rapid reactive property of ozonolysis, to functionalize the MOF materials without compromising framework integrity.
- Demonstrate the capability of solid-gas post-synthetic modification under optimized conditions. We anticipate a fancy single-crystal-to-single-crystal transformation through post-synthetically functionalizing a zirconium-based MOF with pendent olefin groups by utilizing our solid-gas system.
- Extend the solid-gas post-synthetic approach to modify other MOF systems. We aim to create hierarchically pores in exist MOF structures by taking advantage of the quick ozonolysis cleavage in solid-gas fashion.

Chapter 3

Single-Crystal-to-Single-Crystal Post-Synthetic Modification of a Metal–Organic Framework via Ozonolysis

This Chapter is based on the following publication:

Albalad, J.; **Xu, H.**; Gán ara, F.; Haouas, M.; Martineau-Corcos, C.; Mas-Ballesté, R.; Barnett, S. A.; Juanhuix, J.; Imaz, I.; Maspoch, D. *J. Am. Chem. Soc.* **2018**, *140*, 2028–2031.

3.1 Introduction

Metal–organic frameworks (MOFs) are crystalline materials that comprise organic linkers and metal ions/clusters. For the past two decades, they have attracted attention for their exceptional porosity and structural diversity.^{1,2} Beyond their inherent crystallinity and porosity, MOFs are an ideal platform for applications that entail incorporation of target chemical functionalities onto their pore walls.^{3–5} To date, several methodologies have been developed to introduce different chemical functionalities into preassembled MOFs. These include covalent modification of the organic linkers,^{6–9} ligand exchange processes^{10–12} and post-synthetic metalations.^{13,14} However, the synthetic conditions of post-synthetic covalent modifications typically require long reaction times and high temperatures that many MOFs cannot sustain; and for those MOFs that can resist such conditions, the yields are only low to moderate. This is partly because the methods are based on solid–liquid phase processes, whereby reaction progress is limited by the diffusion of reagents inside the porous frameworks to reach the target sites, especially for MOFs whose surfaces are already partially tagged, as the surface groups block access to the pores.¹⁵ Solvent-less reactivity, particularly solid–gas phase reactivity, is a widely explored approach in metallurgy and polymer science. Indeed, reactive gases (e.g., fluorine gas in the steel industry) have been used to quantitatively passivate, cleave, or switch the hydrophobic character of diverse materials.^{16–18} However, there is scant precedent on solid–gas phase reactions with MOFs.¹⁹ We reasoned that such an approach could be used to overcome the aforementioned limitations in post-synthetic functionalization of MOF pores.

As mentioned in “ozone chemistry” part of Chapter 1, ozone has proven to be a powerful oxidizing reagent for diverse chemistries under mild conditions.^{20,21} Of these reactions, ozonolysis of alkenes is arguably the most widely studied.^{22,23} Initially used for routine characterization of lipids and natural polymers, it is now employed for selective cleavage of olefinic bonds, as it enables regio-specific formation of aldehydes, ketones or carboxylic acids in mere minutes. This reaction involves the metastable intermediate 1,2,4-trioxolane. Due to their low stability, trioxolane rings are not easy to isolate; however, those that have been are strong antibacterial and therapeutic agents, especially in the form of ozonated oils or triglycerides. Moreover, trioxolane rings can be treated under mild reductive or oxidative conditions to form aldehyde moieties²⁴ or carboxylic acids,²¹ respectively.

In this chapter, the concept that post-synthetic functionalization of the porous olefin-tagged UiO-66-type MOF, ZrEBDC, using controlled, solid–gas phase ozonolysis will be

demonstrated. Through introduction of ozone gas under mild condition, we achieved the transformation of the olefin groups of a UiO-66-type MOF into 1,2,4-trioxolane rings in single-crystal to single-crystal fashion, which we then selectively converted into either aldehydes or carboxylic acids (Figure 3.1).

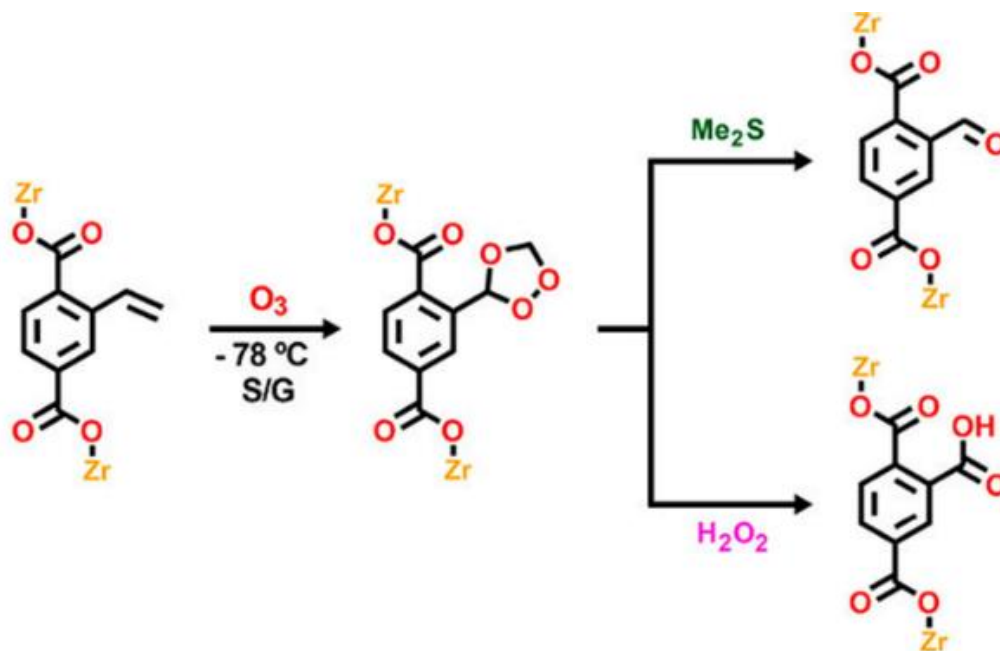


Figure 3.1 Illustrated post-synthetic modification of an olefin-substituted Zr-MOF via ozonolysis in solid-gas manner.

3.2 Results and discussion

3.2.1 Synthesis of zirconium-based MOF (ZrEBDC)

We selected zirconium-based MOFs as the porous platform to implement our concept because MOFs of this type exhibit high thermal and chemical stability and are resistant to aqueous and acidic conditions. Additionally, we chose 2-ethenylbenzene-1,4-dicarboxylic acid (H_2EBDC) as the organic ligand because it is a simple and robust linker with no reactive sites other than its olefin-tagged pendant arm (Figure 3.2).



Figure 3.2. Schematic synthesis of olefin substituted Zr-MOF in bulk crystalline powders by route ① and single crystals suitable for SCXRD by route ②.

Bulk **ZrEBDC** was synthesized by adding an equimolar mixture of H₂EBDC and ZrOCl₂·8H₂O into a mixture of DMF and formic acid and the resulting slurry was then heated at 120 °C. After 12 h, the crude solid was washed twice with DMF and acetone, filtered, and activated under vacuum prior to any ozonolysis test. Colorless octahedral crystals of **ZrEBDC** suitable for single-crystal X-ray diffraction (SCXRD) were obtained by dissolving the two reagents in a 3:1 mixture of DEF/formic acid, and then slowly heating the resulting solution from 25 to 135 °C (heating rate = 5 °C/min) for 72 h (more details see **Section 3.3**). After cooling down to room temperature, the crystals were carefully collected and washed with pure DMF for further analysis. The size of the obtained crystals was from 20 to 40 μm under scanning electron microscopy (SEM) images (Figure 3.3a). The crystal structure of **ZrEBDC** revealed the formation of the archetypical UiO-66-like backbone, in which the olefinic sidechains of the EBDC linkers point inward toward the pores, as shown in Figure 3.3b.

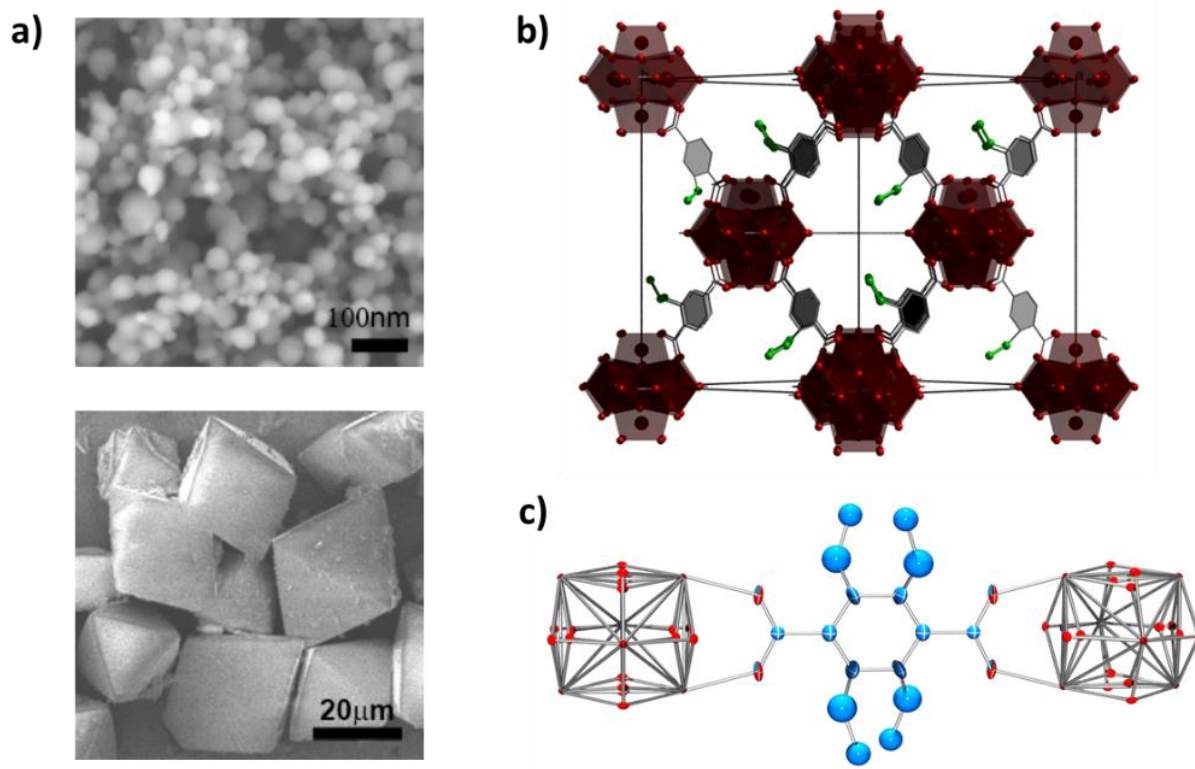


Figure 3.3. a) SEM images of the bulk crystalline powders (top) and octahedral single crystals (down) of as-synthesized ZrEBDC; b) Backbone illustration of single-crystal structure of ZrEBDC with the olefinic groups are highlighted in green, and c) ORTEP drawing of EBDC linker as found in the crystal structure of ZrEBDC, where the four equivalent ethenyl group positions are distorted in blue.

3.2.2 Establishment of set up for solid-gas ozonolysis

Solvent-assistant method. On the consideration that ozone has relative solubility in many different liquids such as water and aqueous solutions, acetone or chloroform, et al.²⁵ As proof of concept, in the very beginning, conventional PSM methods of ozonolysis was carried out in solvent-assistant manner, by bubbling the ozone gas into acetone containing ZrEBDC crystalline particles. In this way, ozone was expected to dissolve in the acetone, diffuse into the MOF cavities and accomplish the ozonolysis functionalization of all the MOF particles. Specifically, in a round-bottom flask filled with 50 mL acetone and 10 mg ZrEBDC crystalline particles, ozone gas was continuously bubbling through a glass pipette as the nozzle. The flask was kept at -78 °C to increase the ozone solubility and reduce their decomposition. After 2 h bubbling of ozone, the resulted MOF particles were collected and washed with acetone. The ozonolysis conversion was monitored by ¹H NMR measurement and crystallinity of MOF particles was characterized

by PXRD. As a result, on the basis of proton integration, only about 40 % MOF particles was ozonized although the crystallinity of MOFs still maintained (Figure 3.4). These results indicated the solvent-assistant method could not facilitate the ozonolysis process but the solvent molecules within MOF channels impeded ozone diffusion into the MOF internals.

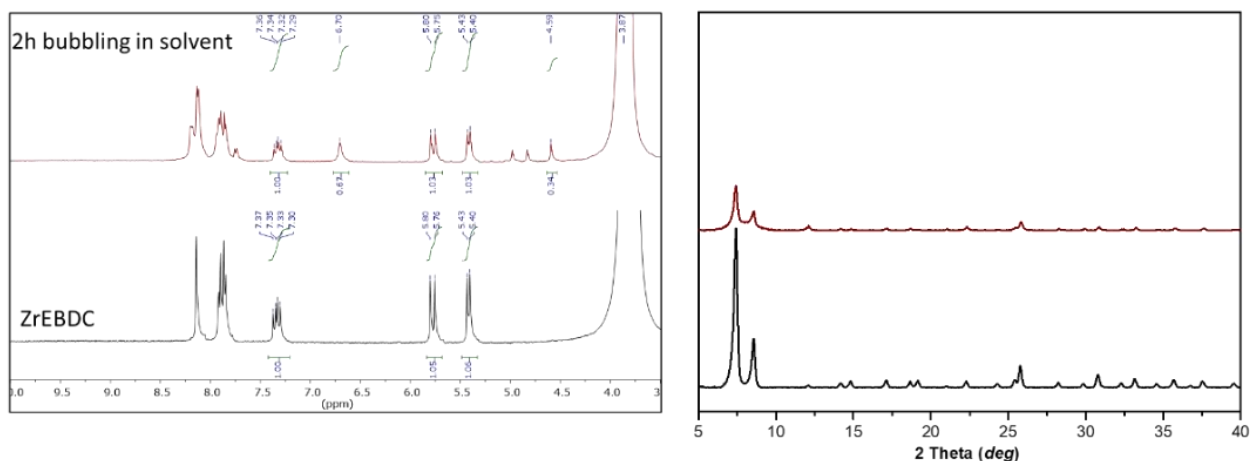


Figure 3.4. a) ^1H NMR spectrum and b) PXRD of the digested MOF particles after ozonolysis for 2 h in solid-solution manner (red) comparing with the as synthesized ZrEBDC (black).

Solid-gas method and ozonolysis set up. In contrast to the low efficient solvent-assistant reaction, ozone gas is capable of reacting with alkene compounds directly and instantly in solid-gas fashion, which provide an alternative way to realize the PSM functionalizing of MOFs.

In order to successfully achieve the solid-gas phase post-synthetic reaction between ozone gas and the olefin bonds within MOFs, the design of the setup should fulfill the following criteria, 1) ozone compatible materials should be applied in avoid of leaking and ozone corrosion; 2) a sealed set-up is necessary so that the PSM process can be controled under relatively low temperature. In this way the ozonolysis reaction can be conducted gently and decomposition of ozone gas will be inhibited; 3) the MOF particles can be purged out of air within the pores before introducing ozone gas in order to facilitate the diffusion of gas molecules into MOF internals; 4) the mixture gas need flow by MOF crystals continuously till all the olefin groups were ozonized. Based on these rules, a set up was organized for lab scale ozonolysis experiment (Figure 3.5).

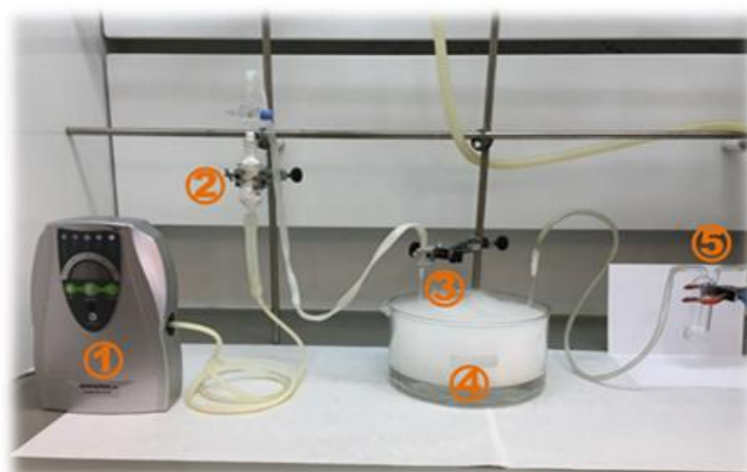
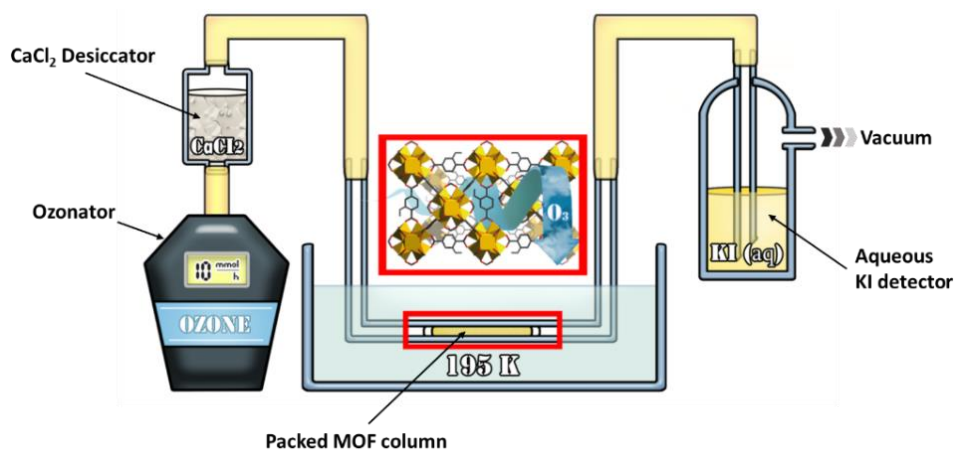


Figure 3.5 Schematic (top) and laboratory (down) set up applied for the ozonolysis of ZrEBDC. Laboratory set-up for performing ozonolysis experiments on MOF particles. ① Ozonator; ② Desiccator filled with granular CaCl₂; ③ U-shaped Pyrex tube containing the MOF column; ④ Basin keeping -78 °C with dry ice/acetone mixture; ⑤ Gas trap filled with aqueous KI solution.

3.2.3 Solid-gas ozonolysis of ZrEBDC

In a typical ozonolysis experiment, activated **ZrEBDC** (50 mg) was packed inside a 3.4 mm diameter Pyrex tube (Figure 3.5). Two cotton stoppers were added around the sample, and the tube was bent into a U-shape using a flame torch. One end was directly attached to an ozone generator, whereas the other was connected to vacuum. Before the reaction was started, the tube was immersed into a dry ice/acetone bath at -78 °C and purged under vacuum for 10 min. Under these conditions, ozone presents a moderate half-life and selectively reacts with unsaturated moieties. Excessive generation of ozone was avoided by adding an aqueous KI

detector to the end of the setup. Once the sample had reached the proper temperature, a constant stream of O_3 /air (10 mmol O_3 / h, dried through $CaCl_2$) was blown into the reaction from one end of the tube. The stream was maintained until the KI solution changed from colorless to bright yellow (after ~ 30 min), which indicated that all the olefins had been transformed. The ozone stream was then stopped immediately. It is worth to note that during the ozonolysis process at -78 °C, the sample column turned from white to blue color after 30 min, indicating excessive ozone aggregated around the sample and ozonolysis reaction was finished (Figure 3.6a). Besides, yellow color change was observed at 30 min ozonolysis under room temperature and kept the yellow color always, probably due to the high temperature caused unrecoverable oxidation of the sample (Figure 3.6b). Hereafter, the sample studied will only focus on the modified ones at -78 °C ozonolysis.

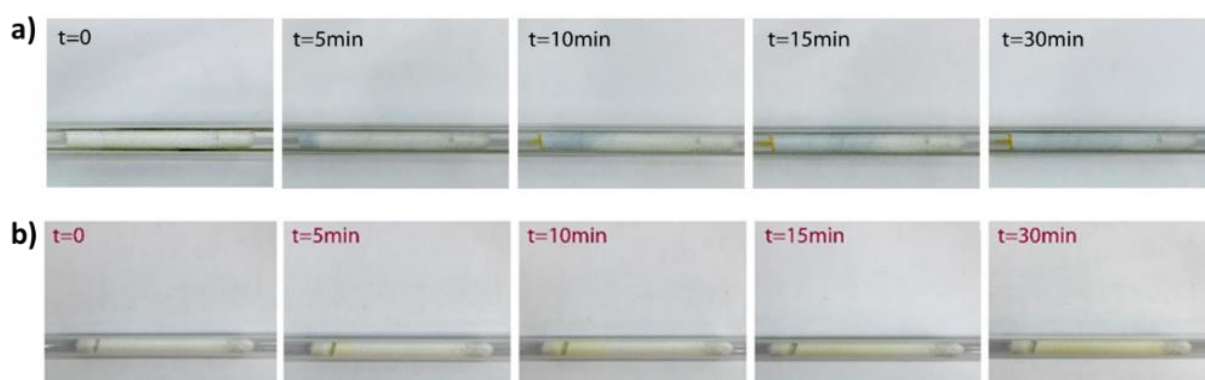


Figure 3.6. Photos of color change of the MOF column in tube at a) -78 °C and b) room temperature during solid-gas reaction.

After finishing ozonolysis, the sample column was left under vacuum for an additional 10 min to ensure that all the residual unreacted ozone was evacuated from inside the tube; after this, the sample became white again. When the tube recovered to room temperature, the ozonized MOF sample was carefully collected by breaking the tube and stock in a sealed vial.

3.3.4 Identification of SC-SC transformation

Identification of MOF frameworks by Powder X-Ray Diffraction (PXRD). The ozonized ZrEBDC particles with different ozonolysis treatment time were collected and send to PXRD scanning. Although ozonolysis reaction has been performed throughout the porous MOF particles, the resulting patterns confirmed that their crystallinity was in good agreement with the

MOF pristine (Figure 3.7), which proved the high stability of the zirconium framework within ozone atmosphere.

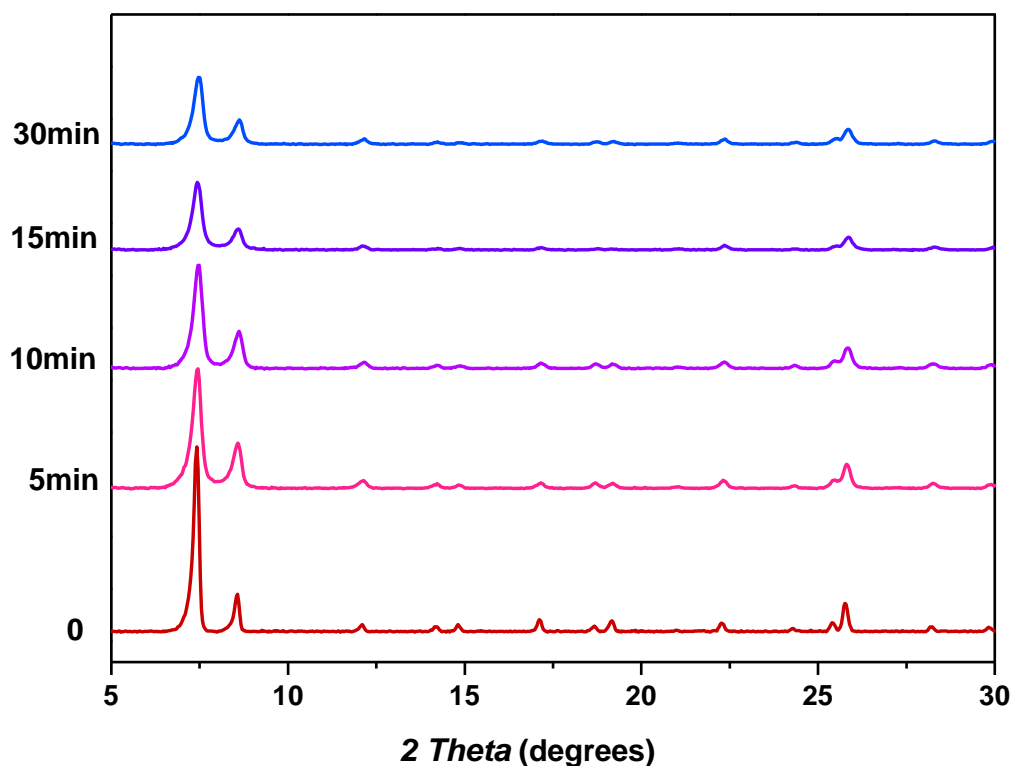


Figure 3.7. PXRD of ZrEBDC during the ozonolysis at $-78\text{ }^{\circ}\text{C}$, in function of the reaction time. (from red to blue: 0 min, 5 min, 10 min, 15 min and 30 min).

Single crystal analysis by Single-Crystal X-Ray Diffraction (SCXRD). We characterized the ozonolyzed crystals (hereafter called **ozo-ZrBDC**) by SCXRD, which confirmed that they had retained the crystallinity and the UiO-66 framework of the starting MOF (Figure 3.8a). Analysis of the difference Fourier maps revealed high electron-density within the pores of the framework, which we attributed to the 1,2,4-trioxolane. Due to the high symmetry of the framework, the positions of the 1,2,4-trioxolane groups were statistically disordered, which prevented us from refining their position in the cubic $Fm\bar{3}m$ space group of **ozo-ZrBDC** (Crystal data see Table 3.1). Nonetheless, upon refining the framework atoms (including the defect sites and adsorbed species),²⁶ we calculated a residual electron-density within the pores of 657 e^{-} per unit cell, using the program Squeeze.²⁷ This value is in good agreement with the calculated number of electrons corresponding to the presence of one 1,2,4-trioxolane per organic linker within the unit cell (653 e^{-}), which is the value obtained when 15% of the linker sites are considered to be defective (as suggested by our single-crystal refinement). To determine the orientation of the 1,2,4-trioxolane groups, we performed an additional single-crystal refinement in the monoclinic $C2$ -space group.

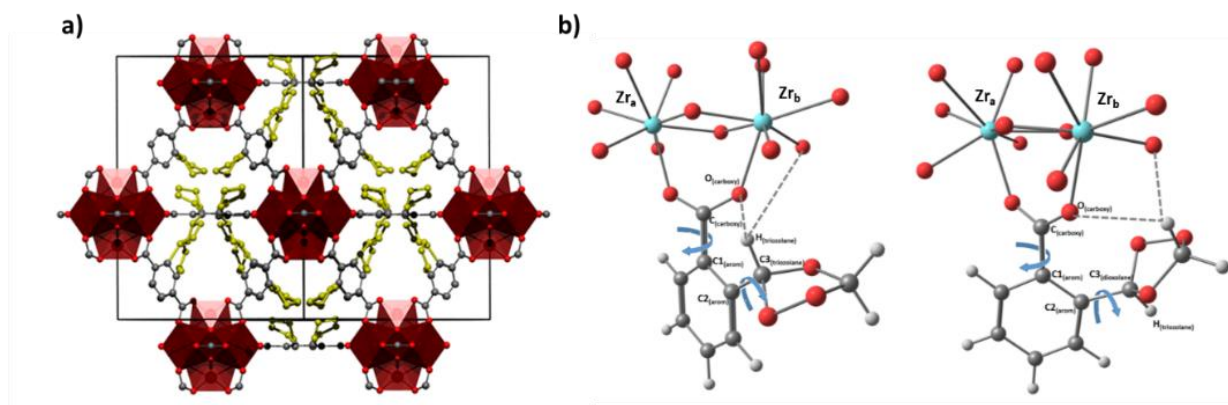


Figure 3.8 a) Illustration of the single-crystal structure of ozo-ZrBDC across the [110] direction, highlighting the disordered 1,2,4-trioxolane moieties (yellow). b) Simplified drawing of optimized structure geometries restricting to 180° the value of $Zr_a-Zr_b-C_{(carboxy)}-Cl_{(arom)}$ dihedral angle. Curve arrows indicate rotations found accounting for maximization of hydrogen bonding interactions (noted as dashed lines).

Due to the low partial occupancies of the 1,2,4- trioxolane and their positional disorder, rigid body restraints were employed, whereby the conformation of the 1,2,4-trioxolane moiety was obtained from DFT based calculations. The 1,2,4-trioxolane rings appeared to be rotated relative to the plane of their corresponding linker phenyl ring, and in all cases oriented toward the inorganic SBUs, at short-contact distances (range: 2.3 to 3.1 Å) between the 1,2,4-trioxolane atoms and the carboxylic groups of the adjacent linkers, in good agreement with DFT calculations (Figure 3.8b). Optimized structures with more detailed information by DFT calculation without and with any geometric restrictions can be found in **Annex part**.

Table 3.1. Crystal and structural refinement data for ZrEBDC, ozo-ZrBDC, ZrBDC-COOH.

Compound	ZrEBDC	ozo-ZrBDC ^a	ozo-ZrBDC ^b	ZrBDC-COOH
Empirical formula	C ₆₀ O ₄₀ Zr ₆	C _{40.8} O ₃₅ Zr ₆	C ₄₄ O _{44.5} H _{4.6} Zr ₆	Zr ₆ C _{45.6} O ₄₈
Formula weight	1907.92	1632.27	1792.40	1819.78
Crystal system	Cubic	Cubic	Monoclinic	Cubic
Space group	<i>Fm-3m</i>	<i>Fm-3m</i>	<i>C2</i>	<i>Fm-3m</i>
CCDC reference	1589286	1589288	1589287	1589289
Unit cell dimensions				
<i>a</i> (Å)	20.740(4)	20.720(2)	20.747(4)	20.740(4)
<i>b</i> (Å)	20.740(4)	20.720(2)	20.747(4)	20.740(4)
<i>c</i> (Å)	20.740(4)	20.720(2)	14.670(3)	20.740(4)
β (°)			135.00(3)	
<i>v</i> (Å ³)	8921.3(1)	8895.0(3)	4465(2)	8921.3(1)
<i>Z</i>	4	4	2	4
F(000)	6272	3155	1729.0	3533
θ range (°)	2.778 – 26.670	2.97 - 72.29	2.97 - 72.29	1.978 - 33.814
Tot., Uniq.Data,	28302, 513,	68423, 1636,	68694, 27598,	29683, 632,
R(int)	0.121	0.1208	0.1047	0.058
Final R indices [I/ sigma(I)>2]	R1 = 0.1012 wR2 = 0.2626	R1 = 0.0379 wR2 = 0.1129	R1 = 0.0616 wR2 = 0.1620	R1 = 0.0339 wR2 = 0.1482
Min. and Max. Resd.	-3.05, 1.34	-0.5, 1.29	-0.84, 3.19	-0.38, 1.24
Dens. [e/Å ³]				
GOF	1.243	1.137	1.1015	1.449

a: Data corresponding to refinement not including disorder model for the oxonale groups. Residual electron density in the cavities was accounted with the Platon Squeeze program. Details are copied below. *b*: Data corresponding to refinement carried out with a monoclinic cell in order to reduce the number of symmetry equivalent positions of the organic linkers. Note that due to the large correlation of the artificially generated independent positions of the framework atoms, a number of these were isotropically refined, also resulting in higher Rvalues.

Direct evidence by solid-state NMR and ligand exchange experiment. To further confirm the presence of the 1,2,4-trioxolane groups, we compared solid-state ^{13}C NMR spectra, recorded in cross-polarization under magic-angle spinning (CPMAS), of the starting **ZrEBDC** and the **ozo-ZrBDC**. The two ^{13}C -peaks of the ethenyl group in **ZrEBDC** appear at 115.6 and 131.0 ppm (Figure 2b, red spectrum). As expected, the spectrum of **ozo-ZrBDC** lacks these two peaks and shows two new ones, at 93.6 and 101.8 ppm (Figure 2b, blue spectrum), which indicated successful conversion of all the olefinic moieties. We then recorded CPMAS-NMR spectra of each product under Polarization Inversion (CPPI),²⁸ in order to differentiate between carbon sites coupled to protons with contrasted dipolar interaction. In the CPPI spectrum of **ozo-ZrBDC** (Figure 3.9a, orange spectrum), the resonance at 93.6 ppm is present, whereas that at 101.8 ppm is absent. These observations confirmed the formation of the 1,2,4-trioxalane ring, with the CH_2 peak located at 93.6 ppm and the CH peak, at 101.8 ppm; in agreement with literature data^{29,30} and the solution study is shown from Fig 3.12 to 3.18. We further confirmed this formation by performing a soft-ligand exchange experiment, from which two peaks in solution ^1H NMR corresponding to the CH and CH_2 groups of the 1,2,4-trioxolane ring ($\delta = 5.61$ and $\delta = 4.65$ ppm, integrating in a 1:2 ratio) were identified (Figure 3.9b).

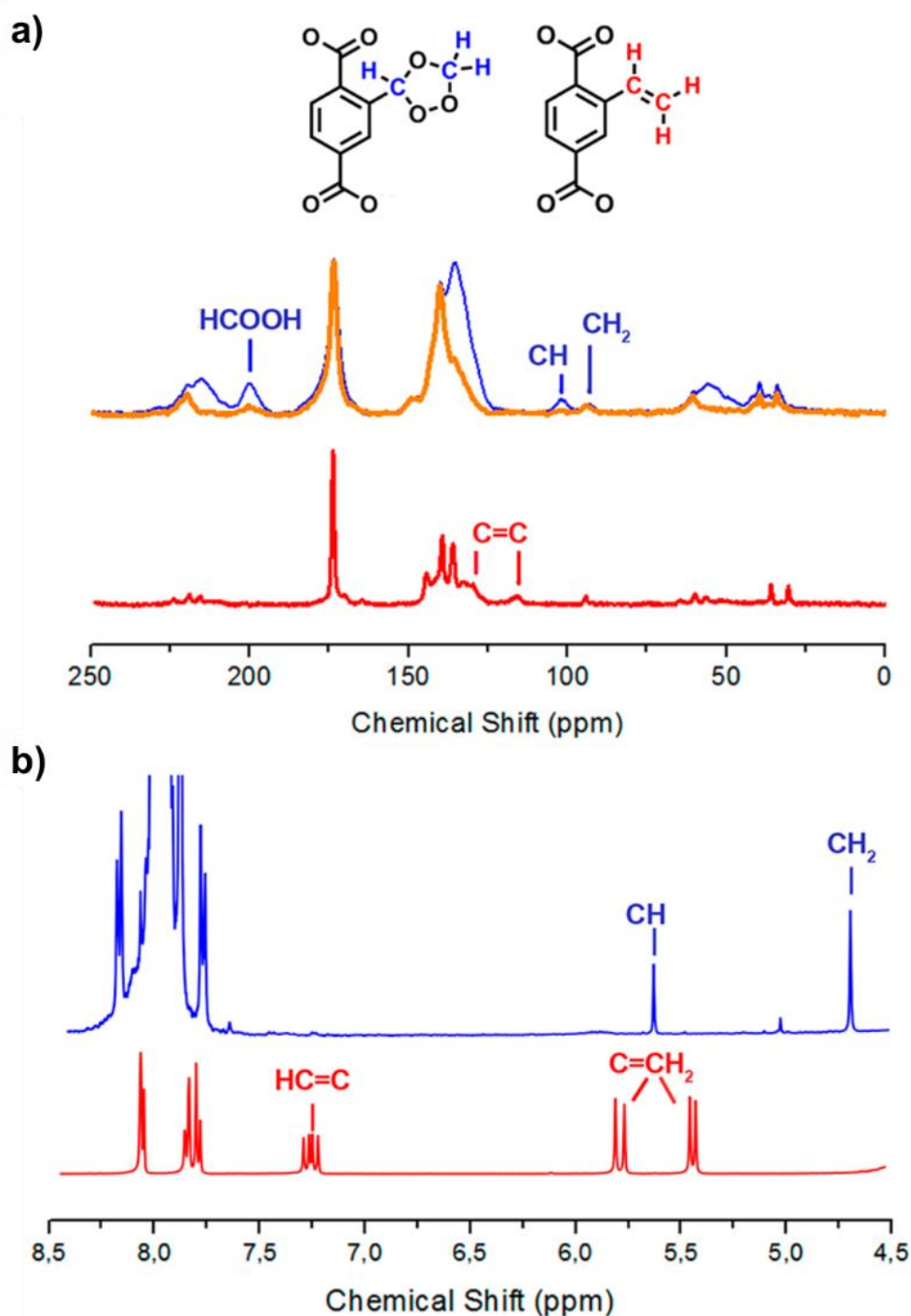
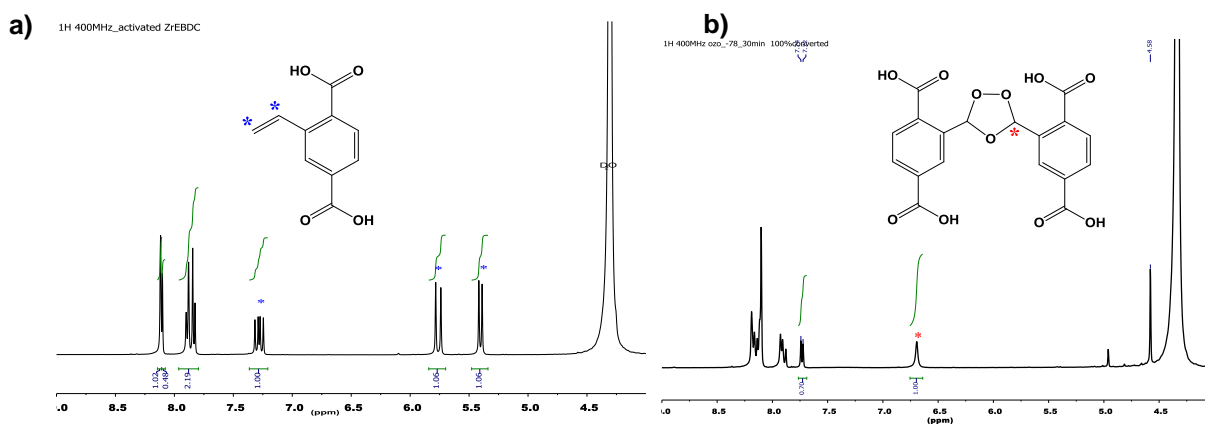


Figure 3.9. Solid-state ^{13}C NMR spectra of ZrEBDC (red: CPMAS) and ozo-ZrBDC (blue: CPMAS; orange: CPPI-MAS). ^1H NMR spectra after the ligand-exchange experiment (blue) and H_2EBDC (red).

Sophisticated study of the digested samples by nuclear magnetic resonance (NMR) spectroscopy. To gain further insight into the ozonolysis reaction, we systematically studied the ozonolysis process under various treatment times (5 min, 10 min, 15 min and 30 min) in order to

figure out the evolution of the new generated species. To this end, the degree of functionalization was monitored by recording the ^1H NMR spectra of the digested samples (5% HF/DMSO- d_6), then compared to that of the starting **ZrEBDC**. The digestion was done by adding 120 μL 5% HF in D_2O to 20 mg of dry **ZrEBDC** or **ozo-ZrBDC** powder in a 2 mL Eppendorf tube. The resulting mixture was sonicated for 5 min to afford a slurry, which was diluted with 0.5 mL DMSO- d_6 , sonicated for 5 more min and finally clear solution suitable for NMR analysis was obtained.

The ^1H NMR spectrum of the digested ZrEBDC showed the characteristic peaks of three nonequivalent olefinic protons at $\delta = 7.29$ ppm, $\delta = 5.77$ ppm and $\delta = 5.41$ ppm, integrating in a 1:1:1 ratio (Figure 3.10a). In contrast, the spectrum of the fully converted ozo-ZrBDC confirmed a quantitative fading of all the olefinic signals in approximately 30 min of solid-gas interaction, together with the appearance of new signals, including two peaks of interest, at $\delta = 6.70$ ppm and $\delta = 4.58$ ppm (Figure 3.10b). These latter signals fall within the typical range of chemical shifts for the expected trioxolane moiety,³¹ but their relative integration does not match the expected 1:2 ratio for the CH and CH_2 protons in the five-membered ring. However, the patterns of NMR spectra clearly showed the olefin groups vanished gradually depending on ozonolysis time and end up with fully conversion in 30 minutes (Figure 3.10c).



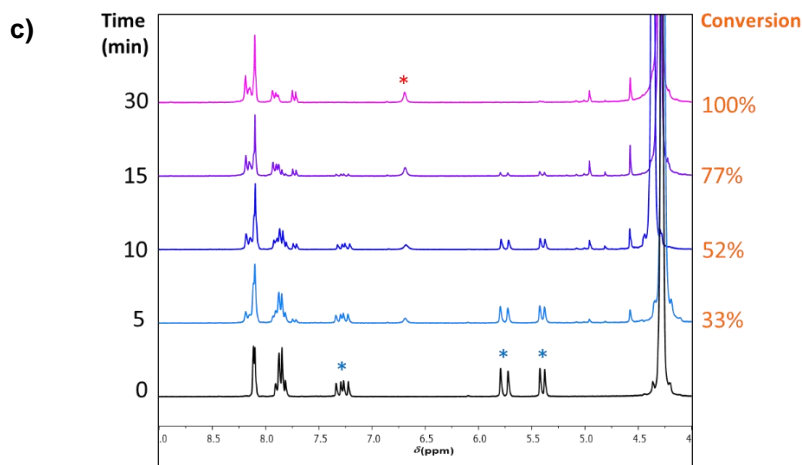


Figure 3.10. a) ^1H NMR spectrum of digested activated ZrEBDC. b) ^1H NMR spectrum of the digested ZrEBDC sample after ozonolysis for 30 min. Calculated integration of olefinic proton signals and newly generated proton signals indicated a conversion of 100%. c) ^1H NMR spectra of the digested sample at different ozonolysis time, which clearly indicated the fully conversion after 30 min treatment.

Due to the instability of trioxolane moiety under aggressive digestion conditions, the fully ozonized linker **1,2,4-trioxolane-BDC** was subjected to two different degradation pathways. To fully identify these species, the digested **ozo-ZrBDC** sample was further analyzed by 1D-NMR and 2D-NMR (NOESY, DOSY, DEPT135, HSQC and HMBC; see Figures 3.11-3.17). After an in-depth analysis of the digested product, four different entities were properly identified in the mixture (Figure 3.11). First, the two, symmetric **cross-ozonation** products of the target **trioxolane-BDC** were properly identified (**A'** and **A''**). Second, both products of the **acid-induced hydrolysis** of the initial trioxolane were identified (**B** and **C**). Further step-by-step identification of these moieties is presented hereafter, divided by the techniques used and employing the same nomenclature as in Figure 3.10, for clarity. Finally, the degree of conversion of the olefinic groups into 1,2,4-trioxolane rings was calculated by comparing the combined integration of two peaks, one at 7.73 ppm (corresponding to H3 of 1,2,4-benzenetricarboxylate) and one at 6.70 ppm (corresponding to H2 of the trioxolane-metathesis product **A'**), versus the olefinic peak at 5.77 ppm (corresponding to **EBCD**).

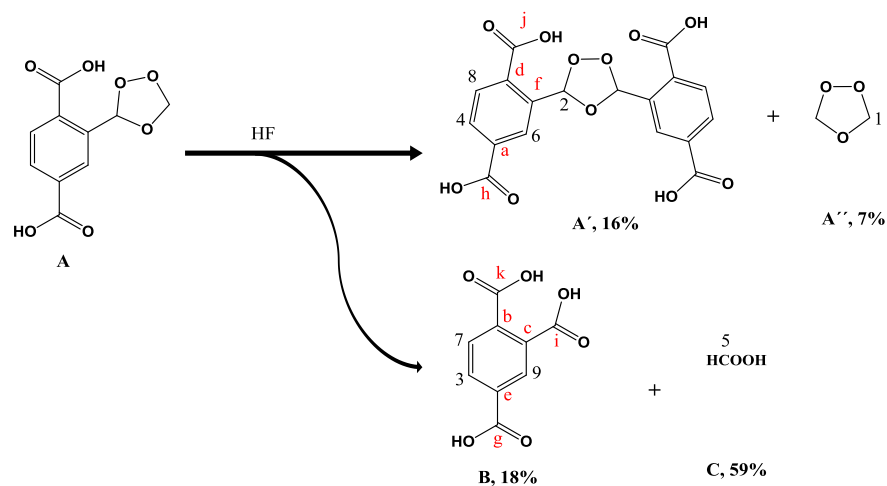


Figure 3.11. Representation of the species formed after digestion of ozo-ZrBDC with 5% HF in DMSO- d_6 . Carbon atoms with attached protons are labeled with black numbers (1-9) and quaternary carbon atoms, with red letters (a-k).

Hereafter, 1D-NMR and 2D-NMR spectra (^1H NMR, NOESY, DOSY, ^{13}C NMR, DEPT135, HSQC and HMBC) of digested **ozo-ZrBDC** sample are presented with briefly explanation of identification and/or components for each species.

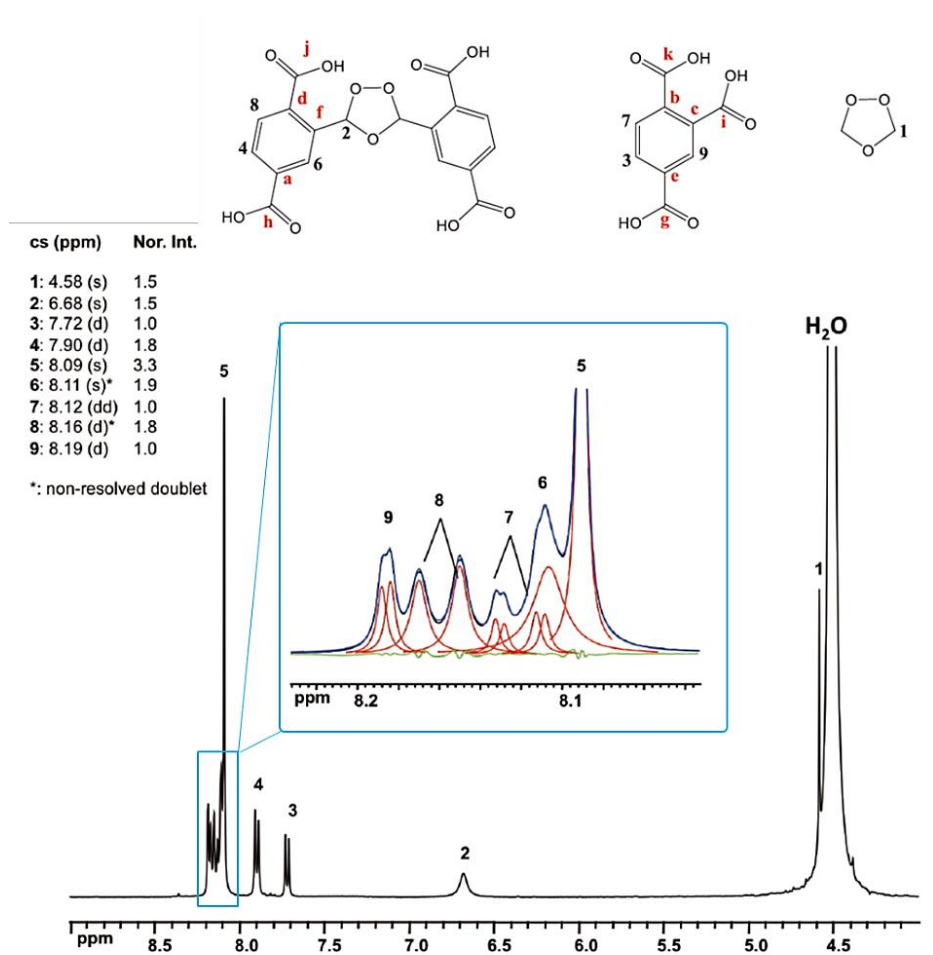


Figure 3.12. ^1H NMR spectrum of digested ozo-ZrBDC in HF/DMSO- d_6 , showing nine H resonances (labeled 1 to 9) that should correspond to the 1,2,4-trioxolane derivatives and their decompositions products. Insert: spectra (from 8.04 ppm to 8.23 ppm) focused on the aromatic region combined with fitted peaks (red lines).

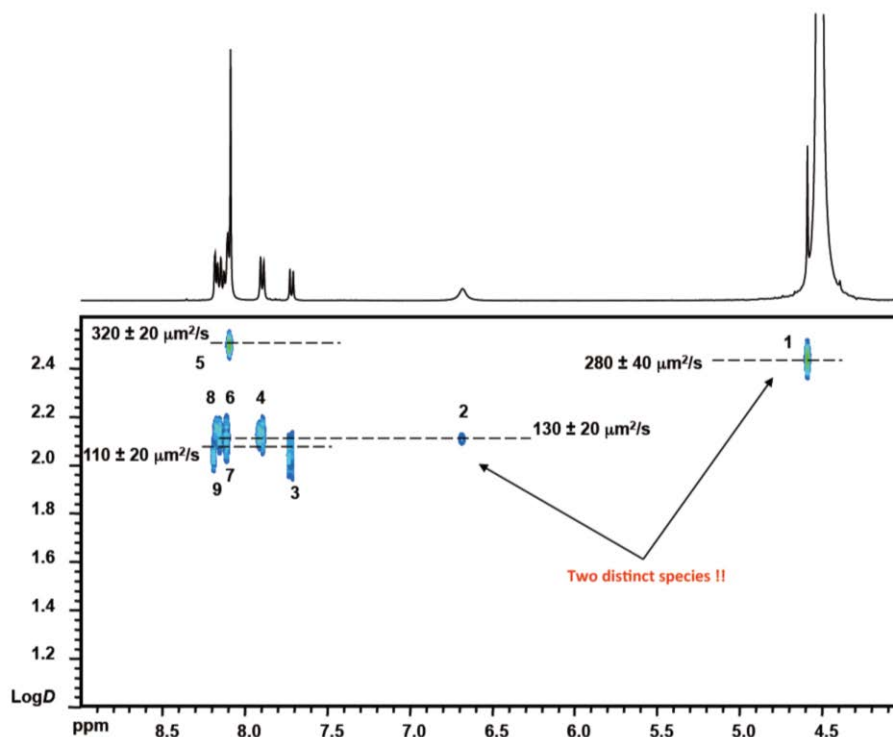


Figure 3.13. ^1H DOSY (Diffusion-Ordered Spectroscopy) spectrum of digested ozo-ZrBDC in HF/DMSO- d_6 , showing four ensembles of resonances with different diffusion coefficients. Note that signals 1 and 2, which appear in the range of trioxolane moieties, correspond to two distinct species.

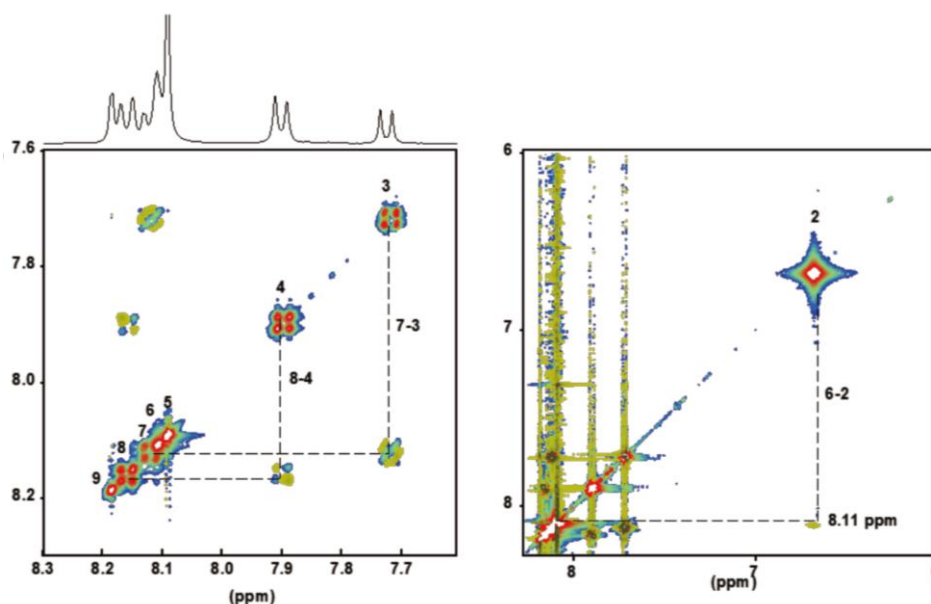


Figure 3.14. ^1H NOESY (Nuclear Overhauser Effect Spectroscopy) spectrum of digested ozo-ZrBDC in HF/DMSO- d_6 , showing the spatial proximities between: a) the adjacent aromatic protons (peaks 7 and 3; and peaks 8 and 4) and b) protons 2 and 6 over two neighboring bonds.

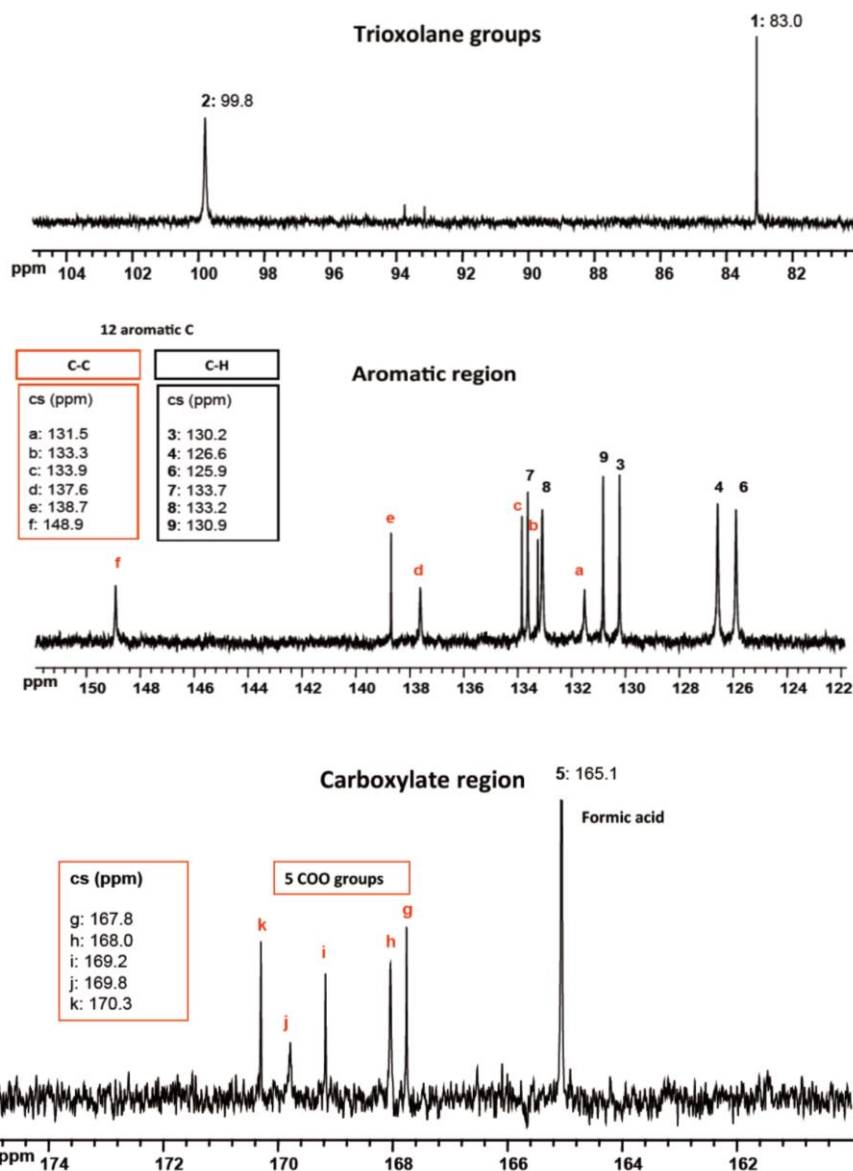


Figure 3.15. $^{13}\text{C}\{^1\text{H}\}$ NMR spectrum of digested ozo-ZrBDC in HF/DMSO- d_6 , showing the twenty different carbon atoms labeled 1-9 (attached to H) and a-k (attached to C and carbonyls). The two groups of resonances are differentiated by comparing DEPT135 and direct polarization experiments.

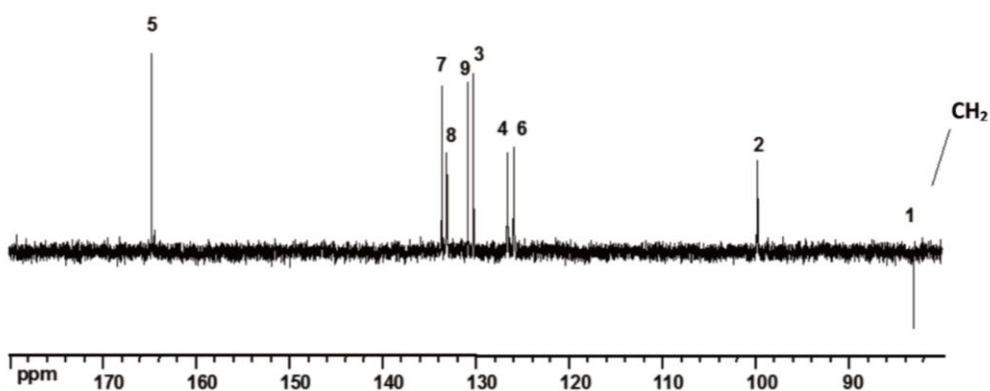


Figure 3.16. $^{13}\text{C}\{^1\text{H}\}$ DEPT135 NMR spectrum of digested ozo-ZrBDC in HF/DMSO- d_6 that enables differentiation of the CH groups from the CH₂ groups. Note that all the nine carbon atoms bear one proton, except for C1, which is attached to two protons.

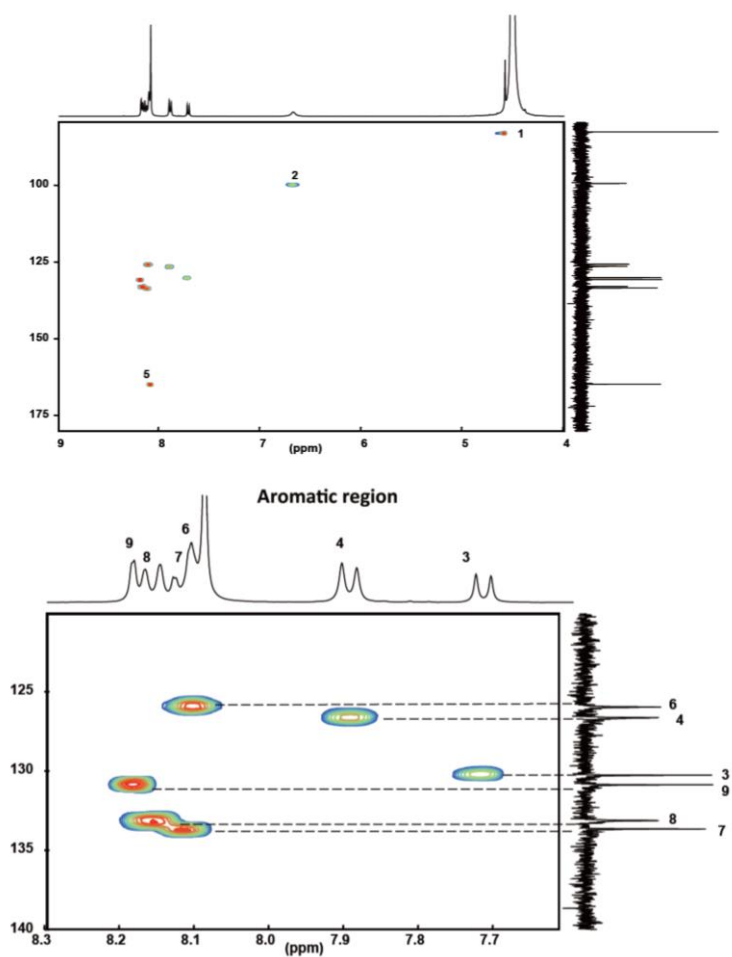


Figure 3.17. $^{13}\text{C}\{^1\text{H}\}$ HSQC NMR spectra of digested ozo-ZrBDC in HF/DMSO- d_6 , showing the nine hydrogen atoms attached to the nine carbon atoms (1-9).

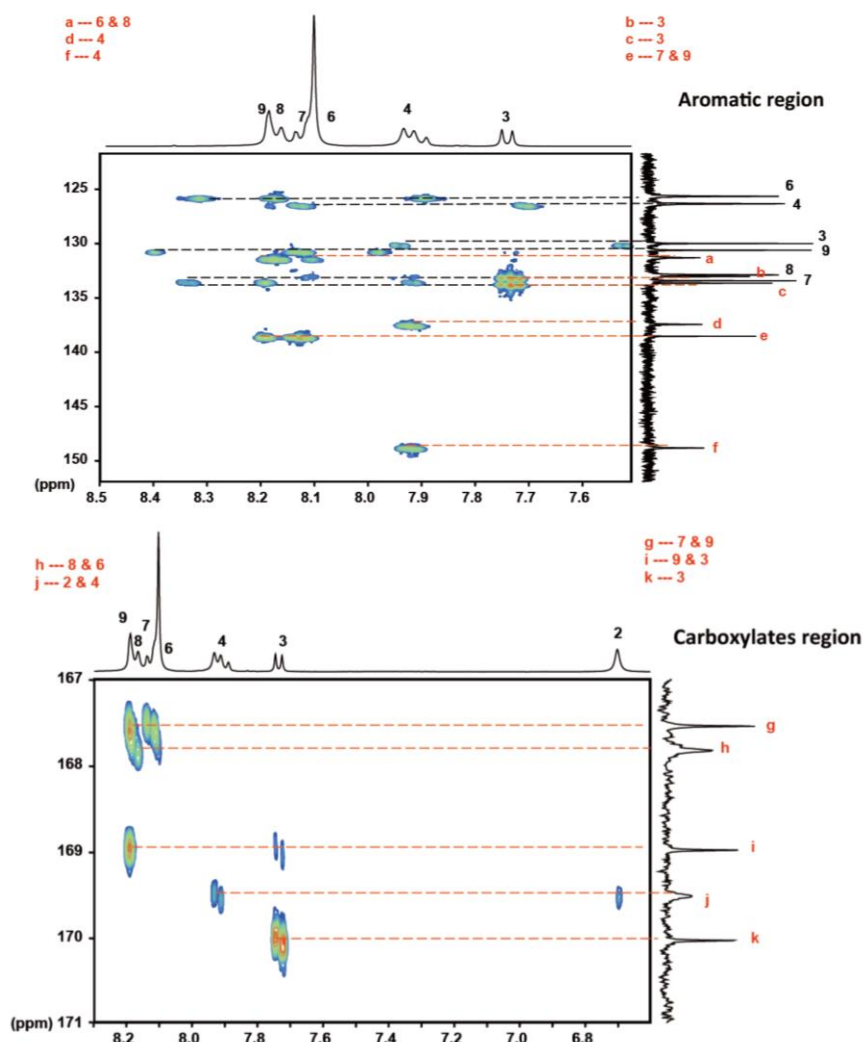


Figure 3.18. $^{13}\text{C}\{^1\text{H}\}$ HMBC NMR spectra of digested ozo-ZrBDC in HF/DMSO- d_6 , enabling the complete assignment of carbon resonances. The quaternary carbons could be identified based on long-range $J^2\text{CH}$ and $J^3\text{CH}$ couplings.

ESI-MS characterization of the digested samples. To further identify the existence of trioxolane species but exclude the possibility of other oxides (e.g. epoxides), we performed electrospray ionisation mass spectrometry (ESI-MS) measurement based on the digested samples. For the ZrEBDC particles, residue signals at m/z 191 $^{[1-]}$ and 147 $^{[1-]}$ match well with calculated ionized moieties from EBDC linker (Figure 3.18a). However, after the olefin groups were fully ozonized, residues corresponding to aldehyde (m/z 193 $^{[1-]}$ and 149 $^{[1-]}$) and carboxylic (m/z 209 $^{[1-]}$ and 165 $^{[1-]}$) moieties clearly revealed that they are generated from the cleavage of 1,2,4-triazolane-telephthalic under aggressive ionizing condition (Figure 3.19).

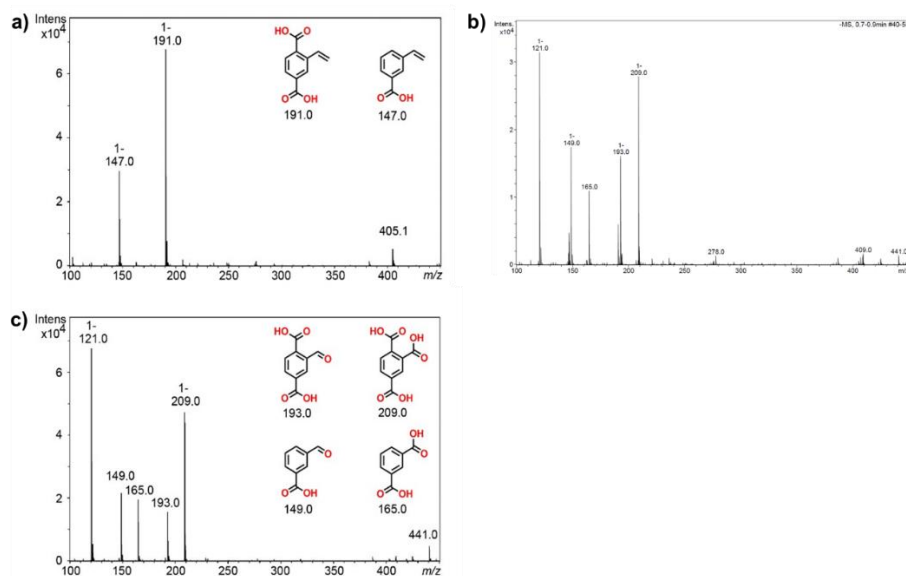


Fig. 3.19. ESI-MS spectrum of the digested microcrystalline a) ZrEBDC, b) 15min and c) 30min ozonized sample.

Porosity investigation by BET measurement. Samples exposed to different ozonation times were also subjected to standard conditions of MOF-activation (120 °C, 12 h), and their inner surface area was subsequently measured (Figure 3.20b). Compared to the initial S_{BET} value for ZrEBDC (1300 m^2/g ; Figure 3.20a), the ozonated samples exhibited decreasingly lower S_{BET} values in function of increasing ozonation time; the value for the fully converted ozo-ZrBDC was 685 m^2/g . Remarkably, this surface area is consistent with a previously reported value for a UiO-66-like MOF with imidazole moieties as pendant groups ($S_{\text{BET}} = 538 \text{ m}^2/\text{g}$).³²

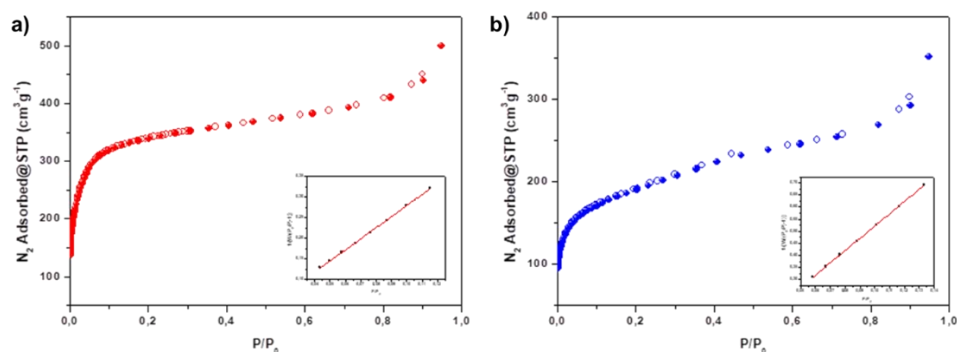


Figure 3.20. N_2 adsorption isotherm and BET liner fit for a) ZrEBDC and b) ozo-ZrBDC.

3.2.5 Selectively transformation to carboxylic or aldehyde.

Having demonstrated that ozonide rings can be stabilized inside a robust MOF, we next sought to explore the amenability of such rings in ozo-ZrBDC to be selectively reduced into aldehydes or oxidized into carboxylic acids (Figure 3.1). For the former, ozo-ZrBDC was soaked overnight, with stirring, in an acidic aqueous solution of dimethyl sulfide (Me_2S) as reducing agent, to convert the 1,2,4-trioxolane rings into aldehyde groups in a yield of 40% (Figure 3.21).

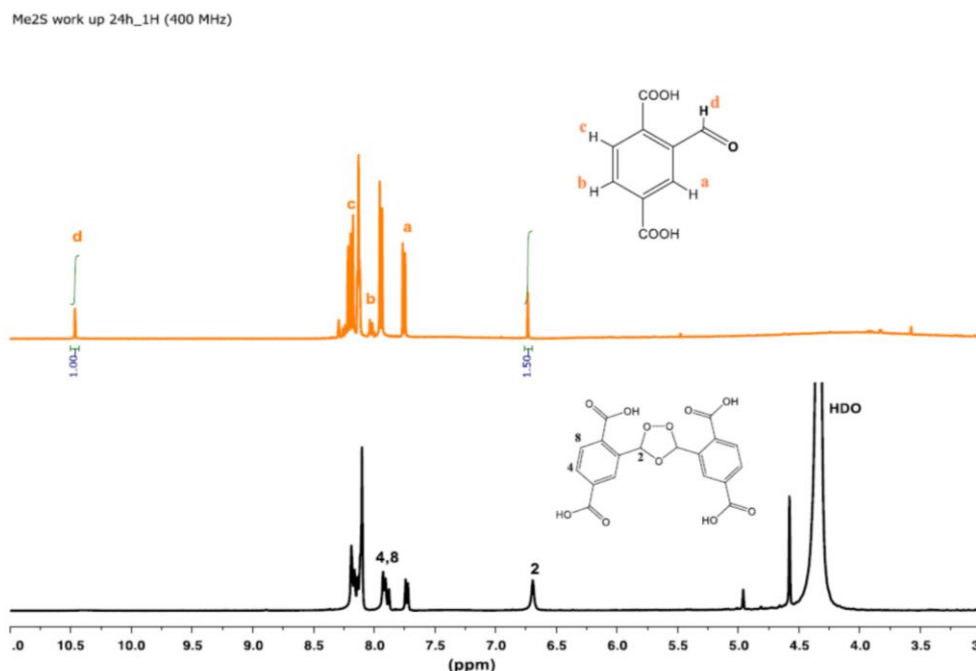


Figure 3.21. ^1H NMR spectrum of the digested CHO-functionalized ZrBDC resulting from soaking ozo-ZrBDC in Me_2S for 12 h (orange), compared to that of the digested ozo-ZrBDC (black). The degree of the conversion of the trioxolane ring into aldehyde groups (40%) was calculated by comparing the integration of the peak at 10.5 ppm to that of the peak at 6.7 ppm. Note that worked-up HF digested sample was dried before its dissolution in $\text{DMSO}-d_6$.

The mild conditions of the workup did not allow for quantitative conversion of the stabilized trioxolanes, and all attempts to make the reduction more aggressive resulted in undesired formation of carboxylate byproduct. The S_{BET} of this **ozo-ZrBDC** partially functionalized with aldehyde moieties was $960 \text{ m}^2/\text{g}$ (Figure 3.25a). Alternatively, soaking **ozo-ZrBDC** overnight, with stirring, in aq. hydrogen peroxide (H_2O_2) drove oxidative cleavage of the 1,2,4-trioxolane rings to the corresponding carboxylic acids. This transformation was quantitative, as confirmed by ^1H NMR analysis (Figure 3.22).

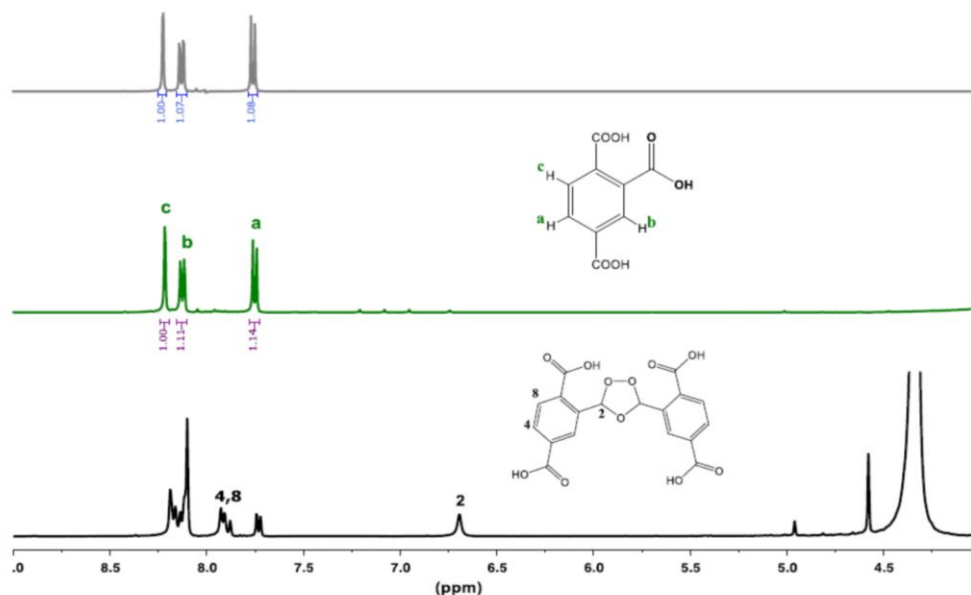


Figure 3.22. ^1H NMR spectrum of digested ZrBDC-COOH resulting from exposing ozo-ZrBDC in H_2O_2 (10% aq.) for 12 h (green), compared to that of the digested ozo-ZrBDC (black). Top: the spectrum of pure 1,2,4-benzenetricarboxylic acid (grey) is shown for reference. Note that worked-up HF digested sample was dried before its dissolution in $\text{DMSO-}d_6$.

In both the aldehyde and carboxylic acid products, the UiO-66-type framework was preserved, as confirmed by powder XRD patterns (Figure 3.23). Furthermore, SCXRD analysis of the crystals resulting from the aggressive oxidation confirmed that they also retained their single-crystal character. Remarkably, the position of the newly formed carboxylic acid groups could be determined through the refinement of the SCXRD data (Figure 3.24). In this case, the S_{BET} was found to be $301 \text{ m}^2/\text{g}$ (Figure 3.25b), which is in good agreement with those reported for this UiO-66-COOH ($S_{\text{BET}} = 350\text{--}400 \text{ m}^2/\text{g}$).³³

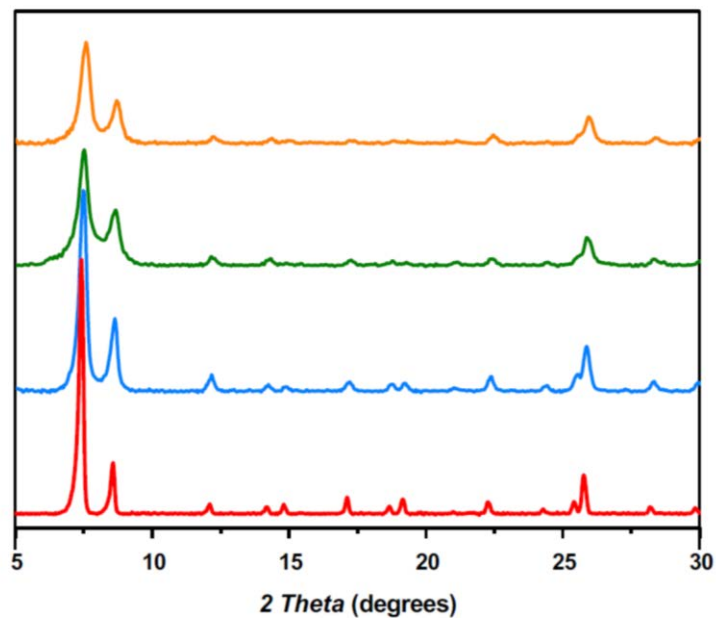


Figure 3.23. PXRD of ZrEBDC (red), ozo-ZrBDC (blue), ZrBDC-COOH (green) and ozo-ZrBDC partially functionalized with CHO groups (orange).

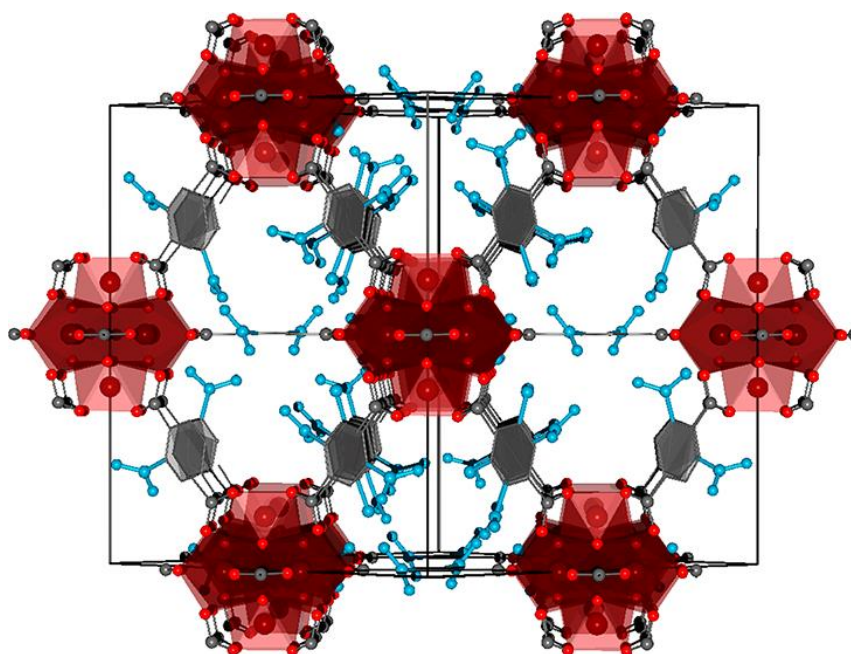


Figure 3.24. Illustration based on the single-crystal structure of ZrBDC-COOH across the [110] direction, highlighting the disordered -COOH moieties (blue).

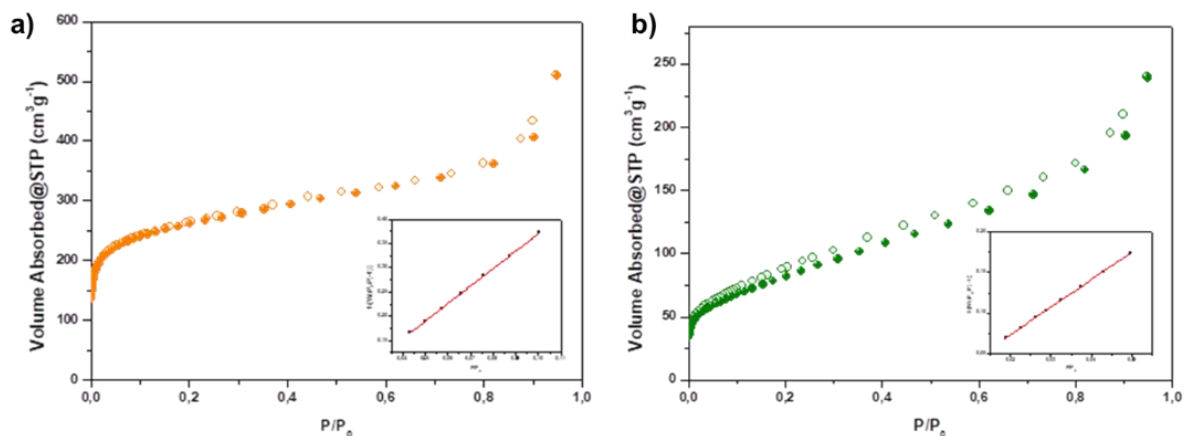


Figure 3.25. N₂ adsorption isotherm and BET liner fit for a) ozo-ZrBDC partially functionalized with CHO groups and b) ZrBDC-COOH by oxidative work up.

3.2.6 Extended application exploration: anti-virus investigation based on ozo-ZrBDC particles.

Up to date, many reports and literatures have demonstrated the uniqueness of the derivatives of 1,2,4-trioxolane used in biological applications, such as anti-inflammatory, antimicrobial and antiviral, et al.^{34,35} As a prove of concept, we investigated the antibacterial activity of the ozonized sample ozo-ZrBDC. In paralleled experiments, ZrEBDC together with UiO-66 samples were tested as contrast (Table 3.1).

Table 3.1 Antibacterial test with incubation time up to 6 hours.

Microorganism	MOF samples (5 mg)	Incubation Time (h)		
		0	4	6
Pseudomonas aeruginosa	UiO-66	9,7 E+06	8,5 E+07	4,3 E+08
	ZrEBDC	5,9 E+06	7,5 E+07	3,25 E+08
	Ozo-ZrBDC	6,7 E+06	4,5 E+07	1,85 E+08
	-	4,8 E+06	7,8 E+07	3,35 E+08
Staphylococcus aureus	UiO-66	1,2 E+07	7,5 E+08	> 3 E+08
	ZrEBDC	1,2 E+07	9,3 E+08	> 3 E+08
	Ozo-ZrBDC	1,2 E+07	1,1 E+09	> 3 E+08
	-	1 E+07	5,6 E+08	> 3 E+08

In *S. aureus* (Gram positive) up to 6 hours no antibacterial effect was observed. With respect to *P. aeruginosa* (Gram negative), the count in the present of ozo-ZrBDC was half than that in the cells alone or with the other two MOF materials after 6 h incubation. However, it is not significantly decrement because of the casual variation. Unfortunately, the crystalline ozo-ZrBDC sample didn't exhibit noticeable antibacterial activity probably due to the inward orientation of trioxolane groups and/or the limitation of the MOF pore aperture.

3.3 Conclusions

In summary, we have reported a solvent-less, solid-gas, single-crystal-to-single-crystal, post-synthetic functionalization of a MOF using ozone. Streaming of ozone gas through an olefin tagged UiO-66-type MOF at $-78\text{ }^{\circ}\text{C}$ provided quantitative transformation of the olefins into 1,2,4-trioxolane rings inside the robust MOF framework. When confined inside the MOF pores, this ring proved to be stable under standard heat and vacuum conditions for MOF activation,

unlike in solution. Finally, an optimized workup enabled further single-crystal-to single-crystal chemistry on these 1,2,4-trioxolane rings: reduction into the corresponding aldehyde or oxidation to the corresponding carboxylic acids, the latter in quantitative yield. We are confident that our methodology will offer new insight into how gas molecules might be exploited for MOF chemistry that transcends common physisorption phenomena.

3.4 Experimental Section

3.4.1 Materials and Characterization

Materials. Zirconium oxychloride octahydrate ($\text{ZrOCl}_2 \cdot 8\text{H}_2\text{O}$, purity $\geq 99.5\%$), formic acid (purity $> 98\%$), potassium iodide, *N,N*-diethylformamide (DEF) and anhydrous granular CaCl_2 (2-6 mm) were purchased from Sigma-Aldrich Co. *N,N*-dimethylformamide (DMF) and acetone were obtained from Fisher Chemical. 2-ethenylbenzene-1,4-dicarboxylic acid (purity $>97\%$) was obtained from iChemicals Co. All the reagents and solvents were used without further purification unless otherwise specified. Deionized water was obtained with a Milli-Q[®] system (18.2 M Ω ·cm). Pyrex tubes (out \varnothing 5mm x in \varnothing 3.4mm; length: 50 cm) were purchased from VIDRASA S.A. The tubes were bent into a U-shape with a flame torch prior to any ozonolysis process. A constant ozone flux was obtained using an ozone generator (model N1668A, 10.4 mmol/h O_3 at room temperature) purchased from Ozonotec.

Characterization. Powder X-Ray Diffraction (PXRD) patterns were recorded on an X'Pert PRO MPD analytical diffractometer (Panalytical) at 45 kV, 40 mA using $\text{CuK}\alpha$ radiation ($\lambda = 1.5419 \text{ \AA}$). Elemental Analysis measurements were performed on a Flash EA 2000 CHNS (Thermo Fisher Scientific) analyzer. Field-Emission Scanning Electron Microscopy (FE-SEM) images were collected on a FEI Magellan 400L scanning electron microscope at an acceleration voltage of 2.0 KV, using aluminum as support. ^{13}C NMR spectra were recorded on an Bruker Avance 500 NMR spectrometer (static magnetic field of 11.7 T) operating at Larmor frequencies of 500.1 MHz (^1H) or 125.8 MHz (^{13}C). The samples were packed in rotors (o.d.: 4 mm) and analyzed at 10 kHz MAS frequency. ^{13}C chemical shifts were referenced to the carbon signal in TMS at 0 ppm. The Cross-Polarization with Polarization Inversion (CPPI)³⁶ spectrum of **ozo-ZrBDC** was recorded using a pulse-inversion duration of 50 μs . ^1H step small-phase incremental alternation (SPINAL-64)³⁷ decoupling was applied during the ^{13}C signal acquisition ($\sim 80 \text{ kHz}$

RF field). Nitrogen adsorption and desorption measurements were done at 77 K using an Autosorb-IQ-AG analyser.

Crystallography. Single-Crystal X-Ray Diffraction (SCXRD) data of **ZrEBDC** and **ZrBDC-COOH** were collected at 100(2) K in BL13-XALOC beamline³⁸ at the ALBA synchrotron, on a single-axis goniometer with a Pilatus 6M detector using a monochromatic X-ray beam ($\lambda = 0.75253 \text{ \AA}$ and $\lambda = 0.82653 \text{ \AA}$, respectively). The data were indexed, integrated and scaled using the XDS program.³⁹ Absorption corrections were not applied. The **ZrEBDC** structure was solved by direct methods and subsequently refined by correction of F2 against all reflections, using SHELXS2013 and SHELXL2013 within the WinGX package and OLEX2.⁴⁰⁻⁴³ Single-crystal diffraction data for **ozoZrBDC** was collected in beamline I19-1 at Diamond Light Source, UK, on a fixed-chi goniometer with a Pilatus 2M detector (silicon (111) monochromatic radiation, $\lambda = 0.6889 \text{ \AA}$).⁴⁴ Data were processed using XiA.⁴⁵ Two different refinements were completed for this sample. In the first one, the S3 framework cubic symmetry was maintained, and the residual electron density corresponding to the trioxolane groups was accounted by means of the program Squeeze. In a second refinement, the crystal structure was refined in the C2 space group, in order to refine the position of the trioxolane groups, which were refined as rigid bodies with the use of the FRAG and EADP instructions. The position of the carbon atoms bound to the linker phenyl ring could be readily identified in the difference density maps, and used to set the position of rigid body fragments, whose conformation was obtained from DFT calculations.

Computational Details. All calculations were performed at the DFT level using the M06 functional^{46,47} with an ultrafine grid⁴⁸ as implemented in Gaussian09.⁴⁹ This functional accounts for dispersion interactions and has a good performance on inorganic systems.^{50,51} The Zr atom was described by means of an effective core potential SDD for the inner electron and its associated double- ζ basis set for the outer ones,⁵² complemented with a set of f-polarisation function.⁵³ The 6-31G basis set was used for the C atoms, 6-31G(d) for the O atoms and 6-31G(p,d), for H atoms.^{54,55} The two possible structures were fully optimized in gas phase. Both structures were identified as minimum points in the potential energy surface by determining the absence of imaginary frequencies in the Hessian matrix. All energy values correspond to Gibbs energies in kcal mol^{-1} . Structures optimized without any geometrical restriction resulted in folded geometry (Structures **A** and **B** in Figure S5a), which would impose a tension in the solid-state structure that could hardly allow the formation of crystalline samples. Therefore, an additional set of optimizations was carried out restricting to 180° the value of the dihedral angle described by the planes Zra-Zrb-Ca (Figure S5b) and Zrb-Ca-Cb. Although unrestricted re-

optimization always tends to the folded structure, the energetic difference between restricted and unrestricted was very small. In fact, frequency calculations in all restricted and unrestricted structures resulted only in positive values of frequencies. Therefore, the potential energy surface in the region of calculated geometries was very shallow and all structures found, both folded and straight, can be, as a matter of fact, considered as minimums of energy. The geometries relevant to elucidate the crystal structure are the ones that keep the dihedral angle Zra-Zrb-Ca-Cb value at 180° (Structures **C** and **D** in Figure S5b). Therefore, the following structural discussion is focused on such structures.

Structural Discussion of optimized geometries. The main structural feature distinctive of structures **C** and **D** is the interaction that triazolane cycle establishes with the $\{\text{Zr}_6(\text{RCOO})_{12}(\text{OH})_4\text{O}_4\}$ cluster. First, in structure **C** two H-bonding interactions can be described with the proton that corresponds to the fragment O-C(H)-O, one with a H \cdots O(benzoate) distance of 2.24 Å and the other one with a H \cdots O(formiate) distance of 2.41 Å. On the other hand, in structure **D** two H-bonding are established with one of the protons in the fragment O-C(H)₂-O, which can be discerned by a H \cdots O(benzoate) distance of 2.66 Å and a H \cdots O(formiate) distance of 2.37 Å. Such multiple supramolecular interactions orientate the triazolane cycle fixing two positions of the rotation trough the C(arom)-CH(triazolane) bond: one for structure **C** and another one for structure **D**. Such rotation positions, which can be defined by the S4 dihedral angle C1(arom)- C2(arom)-C3(triazolane)-H(triazolane) (Figure S5c; 23° for **C** and 162° for **D**), are two plausible conformations that could be found in the crystal structure. In fact, the crystal structure can be interpreted as a mixture of both situations, which can be found randomly in different positions of the structure. In addition, in order to maximize H-bonding interactions, phenyl groups also rotates around the C(carboxy)- C(arom) bond. This rotation can be described by the dihedral angle C1(arom)- C2(arom)-C(carboxy)-O(carboxy) (Figure S5c; 29° for **C** and 36° for **D**). This additional rotation, also associated to the interaction between the metallic cluster and the triazolane cycle, adds an additional uncertainty in the location of carbon atoms in of the phenyl group.

3.4.2. Synthesis

Synthesis of bulk ZrEBDC. Bulk **ZrEBDC** was prepared using an adapted version of a standard solvothermal synthesis.³ $\text{ZrOCl}_2 \cdot 8\text{H}_2\text{O}$ (2.5 g, 7.8 mmol) was added into a solvent mixture of DMF/formic acid (40 mL/15 mL) in a 100-mL screw-capped jar and sonicated for 15 min. 2-ethenylbenzene-1,4-dicarboxylic acid (**H₂EBDC**) 1.5g (7.8 mmol) was added to the

solution, which was further sonicated for 15 min. The jar was then transferred to a preheated oven and kept at 120 °C for 12 hours. A white crystalline material was collected and was washed three times with 50 mL of fresh DMF. The bulk particles were rinsed in 150 mL of acetone, which was replaced twice every 12 h. Finally, the solid powder was activated at 120 °C under vacuum for 12 h. (Yield: 2.2 g; 92% based on $\text{ZrOCl}_2 \cdot 8\text{H}_2\text{O}$). Elemental Analysis: Exp. C 32.77%, H 2.40%; Cal. C 32.61%, H 1.77%.

Synthesis of single crystals of ZrEBDC suitable for SCXRD. In a 100 mL Erlenmeyer flask, 240 mg (1.35 mmol) of $\text{ZrOCl}_2 \cdot 8\text{H}_2\text{O}$ and 250 mg (1.30 mmol) of H_2EBDC were dissolved in DEF (40 mL) under sonication. The resulting solution was divided into 20 scintillation vials, to each of which was added formic acid (2 mL). The samples were vortexed to homogenization and placed in an oven before being slowly heated to 135 °C (heating rate: 5 °C /min) for 72 h. Colorless octahedral crystals of **ZrEBDC** were harvested from the bottom and walls of the vials and treated as the bulk sample. (Yield: 110 mg; 20%).

3.4.3 Solid-gas phase procedure.

Activated bulk **ZrEBDC** (50 mg) was grinded to homogenous powder and mixed with single-crystal **ZrEBDC**, and the resulting mixture was packed inside of a Pyrex tube stoppered by cotton pellets at both ends. The tube was then bent into a U-shape. A 0.1M solution of KI was added at the end of the setup to provide a color-based indicator of ozonolysis progression (from colorless to yellow). Before solid-gas ozonolysis, the sample was vacuumed for 10 min to remove all the residual moisture/solvents. Then, ozone (dried through CaCl_2) was steamed into the setup until a deep yellow color in the KI trap indicated full conversion (*ca.* 30 min). The bulk column was kept under vacuum for a further 10 min to remove all the unreacted ozone.

3.4.4 Soft-ligand exchange experiment.

ozo-ZrBDC was immersed in a 0.2 M solution of 1,4-benzenedicarboxylic acid in DMF for one week. Afterwards, the supernatant was separated from the crystals by centrifugation and subsequently dried, and the resulting solid was dissolved in deuterated DMSO and analyzed by ^1H NMR.

3.4.5 Reduction and oxidation work up of Ozo-ZrBDC.

Fully-converted **ozo-ZrBDC** (80 mg) was soaked in Me_2S (5% in 0.1M HCl/acetone) and H_2O_2 (10% aq.) under stirring for 12 h.

3.5 Reference

- (1) Janiak, C. *Dalt. Trans.* **2003**, *14*, 2781.
- (2) Kitagawa, S.; Kitaura, R.; Noro, S. *Angew. Chem., Int. Ed.* **2004**, *43*, 2334.
- (3) Cohen, S. M. *Chem. Rev.* **2012**, *112*, 970.
- (4) Burrows, A. D.; Cohen, S. M. *CrystEngComm* **2012**, *14*, 4095.
- (5) Wang, Z.; Cohen, S. M.; Stern, C. L.; Hupp, J. T.; Li, J.; Uribe-Romo, F. J.; Chae, H. K.; O’Keeffe, M.; Yaghi, O. M.; Chaudret, B.; Fischer, R. A. *Chem. Soc. Rev.* **2009**, *38*, 1315.
- (6) Morris, W.; Doonan, C. J.; Furukawa, H.; Banerjee, R.; Yaghi, O. M. *J. Am. Chem. Soc.* **2008**, *130*, 12626.
- (7) Kim, M.; Cahill, J. F.; Prather, K. A.; Cohen, S. M. *Chem. Commun.* **2011**, *47*, 7629.
- (8) Morris, W.; Doonan, C. J.; Yaghi, O. M. *Inorg. Chem.* **2011**, *50*, 6853.
- (9) Luan, Y.; Qi, Y.; Gao, H.; Andriamitantsoa, R. S.; Zheng, N.; Wang, G.; Čejka, J.; Valenzano, L.; Lamberti, C.; Lillerud, K. P.; Bordigaa, S. *J. Mater. Chem. A* **2015**, *3*, 17320.
- (10) Boissonnault, J. A.; Wong-Foy, A. G.; Matzger, A. J. *J. Am. Chem. Soc.* **2017**, *139*, 14841.
- (11) Kim, M.; Cahill, J. F.; Su, Y.; Prather, K. A.; Cohen, S. M. *Chem. Sci.* **2012**, *3*, 126.
- (12) Liu, C.; Zeng, C.; Luo, T.-Y.; Merg, A. D.; Jin, R.; Rosi, N. L. *J. Am. Chem. Soc.* **2016**, *138*, 12045.
- (13) Bloch, W. M.; Burgun, A.; Coghlan, C. J.; Lee, R.; Coote, M. L.; Doonan, C. J.; Sumbly, C. J. *Nat. Chem.* **2014**, *6*, 906
- (14) Manna, K.; Zhang, T.; Lin, W. *J. Am. Chem. Soc.* **2014**, *136*, 6566.
- (15) Wang, Z.; Tanabe, K.; Cohen, S. M. *Chem. - Eur. J.* **2010**, *16*, 212.
- (16) Layer, R. W.; Lattimer, R. P. *Rubber Chem. Technol.* **1990**, *63*, 426.
- (17) Miki, N.; Maeno, M.; Maruhashi, K.; Nakagawa, Y.; Ohmi, T. *Corros. Sci.* **1990**, *31*, 69.
- (18) Harshé, G. *J. Mater. Eng. Perform.* **1992**, *1*, 83.
- (19) Servalli, M.; Ranocchiaro, M.; Van Bokhoven, J. A.; Long, J. R.; Lillerud, K. P.; Tilset, M.; Fischer, R. W.; Fischer, R. A. *Chem. Commun.* **2012**, *48*, 1904.
- (20) Schiaffo, C. E.; Dussault, P. H. *J. Org. Chem.* **2008**, *73*, 4688.
- (21) Cochran, B. *Synlett* **2016**, *27*, 245.
- (22) Criegee, R. *Angew. Chem., Int. Ed. Engl.* **1975**, *14*, 745.
- (23) Geletneky, C.; Berger, S. *Eur. J. Org. Chem.* **1998**, *1998*, 1625.
- (24) Willand-Charnley, R.; Fisher, T. J.; Johnson, B. M.; Dussault, P. H. *Org. Lett.* **2012**, *14*, 2242.
- (25) Biń, A. K. *Ozone: Sci. Engng.* **2006**, *28*, 67.
- (26) Trickett, C. A.; Gagnon, K. J.; Lee, S.; Gándara, F.; Bü gi, H.-B.; Yaghi, O. M. *Angew. Chem., Int. Ed.* **2015**, *54*, 11162.
- (27) Spek, A. L. *Acta Crystallogr., Sect. C: Struct. Chem.* **2015**, *71*, 9.
- (28) Wu, X.; Zilm, K. W. *J. Magn. Reson. Ser. A* **1993**, *102*, 205.

- (29) Soriano, N. U.; Migo, V. P.; Matsumura, M. *Chem. Phys. Lipids* **2003**, *126*, 133.
- (30) Sega, A.; Zanardi, I.; Chiasserini, L.; Gabbriellini, A.; Bocci, V.; Travagli, V. *Chem. Phys. Lipids* **2010**, *163*, 148.
- (31) Soriano, N. U.; Migo, V. P.; Matsumura, M. *Chem. Phys. Lipids* **2003**, *126*, 133.
- (32) Liang, J.; Chen, R.-P.; Wang, X.-Y.; Liu, T.-T.; Wang, X.-S.; Huang, Y.-B.; Cao, R. *Chem. Sci.* **2017**, *8*, 1570.
- (33) Ragon, F.; Campo, B.; Yang, Q.; Martineau, C.; Wiersum, A. D.; Lago, A.; Guillerm, V.; Hemsley, C.; Eubank, J. F.; Vishnuvarthan, M.; Taulelle, F.; Horcajada, P.; Vimont, A.; Llewellyn, P. L.; Daturi, M.; Devautour-Vinot, S.; Maurin, G.; Serre, C.; Devic, T.; Clet, G. *J. Mater. Chem. A* **2015**, *3*, 3294.
- (34) Ismail, H. M.; Barton, E.; Panchana, M.; Charoensutthivarakul, S.; Biagini, G. A.; Ward, S. A.; O'Neill, P. M. *Angew. Chem., Int. Ed.* **2016**, *55*, 6401.
- (35) Kazakova, O. B., Smirnova, I. E., Do Tkhi Tkhu, H., Tkhankh Tra Nguen, Apryshko, G. N., Zhukova, O. S., Medvedeva, N.I., Nazyrov, T. I., Tret'yakova, E.V., Chudov, I.V., Ismagilova, A.F., Suponitsky, K.Yu., Kazakov, D.V., Safarov, F.E., and Tolstikov, G.A., *Russ. J. Bioorg. Chem.* **2013**, *39*, 202.
- (36) Wu, X.; Zilm K.W. *J. Magn. Reson.* **1993**, *102*, 205.
- (37) Fung, B.M.; Khitritin, A. K.; Ermolaev, K., *J. Magn. Reson.* **2000**, *142*, 97.
- (38) Juanhuix, J.; Gil-Ortiz, F.; Cuní, G.; Colldelram, C.; Nicolás, J.; Lidón, J.; Boter, E.; Ruget, C.; Ferrer, S.; Benach, J. J. *Synchrotron Rad.* **2014**, *21*, 679.
- (39) Kissel, L.; Pratt, R.H. *Acta Cryst. Sec.A* **1990**, *46*, 170.
- (40) Sheldrick, G. M.; Dauter, Z.; Wilson, K.S.; Hope, H.; Sieker, L. C. *Acta Cryst.* **1993**, *D49*, 18.
- (41) Sheldrick, G. M. *Acta Cryst.* **2015**, *C71*, 3.
- (42) Farrugia, L. J.; *J. Appl. Cryst.* **2012**, *45*, 849.
- (43) Dolomanov, O.V.; Bourhis, L. J.; Gildea, R. J.; Howard, J. A. K.; Puschmann, H. J. *Appl. Cryst.* **2009**, *42*, 339.
- (44) Allan, D.; Nowell, H.; Barnett, S.; Warren, M.; Wilcox, A.; Christensen, J.; Saunders, L.; Peach, A.; Jooper, M.; Zaja, L.; Patel, S.; Cahill, L.; Marshall, R.; Trimmell, S.; Foster, A.; Bates, T.; Williams, M.; Hathaway, P.; Winter, G.; Gerstel, M.; Wooley, R. *Crystals* **2017**, *7*, 336.
- (45) Winter, G. *J. Appl. Crystallogr* **2010**, *43*, 186.
- (46) Cramer C. J.; Truhlar, D. G. *Phys. Chem. Chem. Phys.* **2009**, *11*, 10757.
- (47) Zhao Y.; Truhlar, D. G. *Theor. Chem. Acc.* **2008**, *120*, 215.
- (48) Wheeler, S. E.; Houk, K. N. *J. Chem. Theory Comput.* **2010**, *6*, 395.
- (49) Frisch, M. J.; Trucks, G. W.; Schlegel, H. B.; Scuseria, G. E.; Robb, M. A.; Cheeseman, J. R.; Scalmani, G.; Barone, V.; Petersson, G. A.; Nakatsuji, H.; Li, X.; Caricato, M.; Marenich, A.; Bloino, J.; Janesko, B. G.; Gomperts, R.; Mennucci, B.; Hratchian, H. P.; Ortiz, J. V.; Izmaylov, A. F.; Sonnenberg,

J. L.; Williams-Young, D.; Ding, F.; Lipparini, F.; Egidi, F.; Goings, J.; Peng, B.; Petrone, A.; Henderson, T.; Ranasinghe, D.; Zakrzewski, V. G.; Gao, J.; Rega, N.; Zheng, G.; Liang, W.; Hada, M.; Ehara, M.; Toyota, K.; Fukuda, R.; Hasegawa, J.; Ishida, M.; Nakajima, T.; Honda, Y.; Kitao, O.; Nakai, H.; Vreven, T.; Throssell, K.; Montgomery, J.A.; Peralta, J.E.; Ogliaro, F.; Bearpark, M.; Heyd, J.J.; Brothers, E.; Kudin, K.N.; Staroverov, V. N.; Keith, T.; Kobayashi, K.; Normand, J.; Raghavachari, K.; Rendell, A.; Burant, J. C.; Iyengar, S. S.; Tomasi, J.; Cossi, M.; Millam, J. M.; Klene, M.; Adamo, C.; Cammi, R.; Ochterski, J. W.; Martin, R. L.; Morokuma, K.; Farkas, O.; Foresman, J. B.; Fox, D. J. *Gaussian 09 (Revision D.01)*, Gaussian, Inc., Wallingford CT, **2011**.

(50) Zhao Y.; Truhlar, D. G. *Acc. Chem. Res.* **2008**, *41*, 157.

(51) Zhao Y.; Truhlar, D. G. *Chem. Phys. Lett.* **2011**, *502*, 1.

(52) Andrae, D.; Haeussermann, U.; Dolg, M.; Stoll, H; Preuss, H. *Theor. Chim. Acta* **1990**, *77*, 123.

(53) Ehlers, A. W.; Bohme, M.; Dapprich, S.; Gobbi, A.; Hollwarth, A.; Jonas, V.; Kohler, K. F.; Stegmann, R.; Veldkamp A.; Frenking, G. *Chem. Phys. Lett.* **1993**, *208*, 111.

(54) Hehre, W. J.; Ditchfield R.; Pople, J. A. *J. Chem. Phys.* **1972**, *56*, 2257.

(55) Francl, M. M.; Pietro, W. J.; Hehre, W. J.; Binkley, J. S.; Gordon, M. S.; DeFrees D. J.; Pople, J. A. *J. Chem. Phys.* **1982**, *77*, 3654.

Chapter 4

Post-Synthetic Selective Ligand Cleavage by Solid-Gas Phase Ozonolysis Fuses Micropores into Mesopores in Metal-Organic Frameworks

This Chapter is based on the following publication:

Guillerm, V., **Xu, H.**, Albalad, J, Imaz, I., Maspoch, D. *J. Am. Chem. Soc.* **2018**, *140*, 15022–15030.

4.1 Introduction

Since the advent of metal-organic frameworks (MOFs) in the late 1990's,¹⁻⁵ these porous materials have shown promise for critical applications⁶⁻⁸ such as gas storage,⁹⁻¹¹ catalysis,¹² drug delivery,¹³ thermal energy storage,¹⁴ sensors,¹⁵ etc. MOFs have become benchmark materials for adsorption, surpassing most traditional adsorbents for hydrogen storage,⁹ methane storage,¹⁰ CO₂/N₂ separation,¹⁶ etc. By marrying the advantages of the inorganic and organic chemistries, MOFs exhibit both polyfunctionality and a high degree of tunability, as well as the opportunity to post-functionalize them.¹⁷⁻²⁰ Among the main advantage of this tunability is the possibility to perform reticular chemistry^{4, 21-27} through ligand functionalization, length/width²⁷ variation, and/or metal ion substitution, which enables strategic design and synthesis of materials for specific applications.

A remaining challenge in MOF chemistry is the creation of mesoscale cavities, which are necessary for increased storage capacity, encapsulation of large molecules, etc. Reticular chemistry strategies to surpass previous limits on pore size and cavity diameter include increasing the distance between the organic molecular building blocks and using longer or wider organic ligands.^{25,28-31} However, many of the most well-known MOFs are associated to self-dual nets (**pcu**: MOF-5,³ IRMOFs (isoreticular metal-organic framework) series,⁴ MXFSIX MOFs^{32,33}) or nets that can easily interpenetrate upon ligand elongation (**tbo**: HKUST-1 (Hong Kong University of Science and Technology),^{5,34} **fcu**: UiO-66 (Universitetet I Oslo),^{35,36} **acs**: MIL-88's (Material Institute Lavoisier),^{37,38} etc.). To avoid this problem, researchers have developed platforms based on topologies that cannot interpenetrate, such as IRMOFs-74²⁵ and **rht**-MOFs³⁹, which, thanks to the design of very ambitious organic ligands, currently hold porosity records.^{25,29,31}

Regrettably, systematic access to MOFs exhibiting hierarchical porosity from the micro to the meso range remains a challenge, as it currently demands use of complex organic ligands that are not commercially available.^{28, 40-44} Although MOFs were initially considered as structurally ideal, defect-free materials, numerous recent studies have highlighted the non-negligible level of structural defects and irregularities in these materials, which strongly influence their porosity and catalytic properties.^{44,45-52} These findings suggest that access to hierarchically porous materials would require rational control over the structural defects within MOFs. Unfortunately, to date, only a few methods for generating and controlling such defects have emerged. One such strategy is to use large amounts of monotopic agents (known as *modulators*) in competition with the required polytopic ligand corresponding to the targeted

MOFs.^{36,53-57} Alternatively, rational design strategies such as transversal reticular chemistry also have proven invaluable for generating MOFs with ordered defects.²⁷ However, there are very few reports on engineering of defects and control of hierarchical porosity with commercially available and/or moderately sized ligands,^{44,49,58-66} and some of the existing methods require harsh chemical or thermal treatments.

Our group recently reported the first solid-gas phase post-synthetic modification of a MOF: under mild conditions, we achieved quantitative conversion of the constituent olefin groups in single crystals of UiO-66-like MOF into trioxolane moieties, aldehydes and/or carboxylates without compromising the crystallinity.⁶⁷ Encouraged by the stability of the MOFs under these conditions, we envisioned exploiting this solid-gas phase ozonolysis^{68,69} method to cleave and remove selected organic ligands within MOFs. We hypothesized and later confirmed (*vide supra*) that ligands containing non-terminal olefin groups could be split into several parts (Scheme S1). When implemented in MOFs, these ligands can be selectively broken and subsequently removed from the framework, to provide an original and controllable method for post-synthetic fusion of micropores into mesopores.

Herein we report application of our post-synthetic strategy to selectively and quantitatively cleave and remove the organic ligands in two multivariate (MTV)⁷⁰ Zr-**fcu**-MOFs (Figure 1), thereby affecting their adsorption performance in gas uptake. By controlling the ozone inert/active ratio of ligands in these MOFs, we were able to control the final number of defects in their structures.

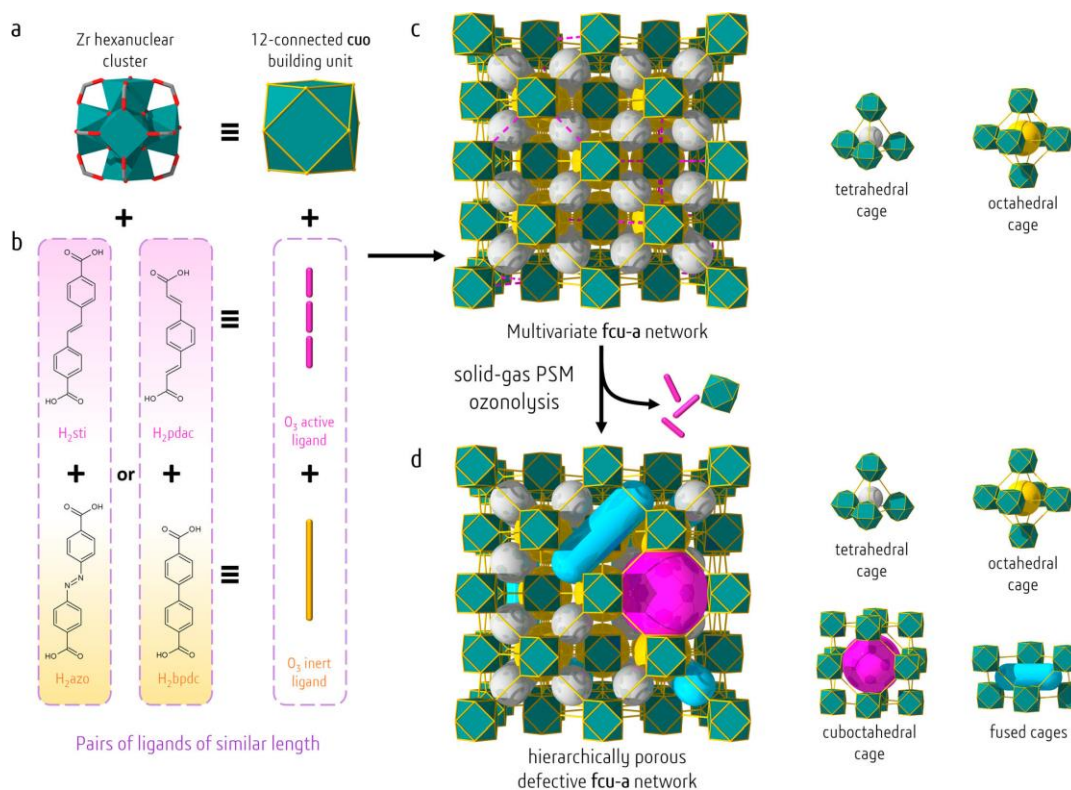


Figure 1. Post-synthetic modification of multivariate Zr-fcu-MOFs via solid-gas ozonolysis. Reaction of a) 12-connected hexanuclear clusters (cuo molecular building blocks) with b) pairs of organic ligands that are similar in length but show opposite reactivity to ozone (H₂sti and H₂azo or H₂pdac and H₂bpdc) yields. c) Multivariate MOFs with the fcu topology and two types of cages. Post-synthetic modification of the resultant MOFs through ligand cleavage by solid-gas ozonolysis results in d) Zr-fcu-MOFs with a defective network that exhibits hierarchical porosity generated upon fusion of micropores into larger pores (up to the mesoscale).

4.2 Results and discussion

4.2.1 Zr-fcu-azo/sti System

4.2.1.1 System Validation

Our ligand removal strategy is only amenable to MOFs based on ligand pairs that exhibit the following characteristics: similar shape and length; similar reactivity under given reaction conditions; and opposite reactivity to ozone (Figure 1b). To this end, we selected two dicarboxylic acids: 4,4'-azobenzene dicarboxylic acid (H₂azo) and 4,4'-stilbene dicarboxylic acid (H₂sti) (with lengths ≈ 13.3 Å). The reactivity of each ligand to ozone was initially tested in solution, in N, N'-dimethylformamide (DMF), which was used to avoid π - π stacking of the

their response to ozonolysis. Both MOFs were synthesized by suspending ZrCl_4 and the corresponding dicarboxylic ligand in DMF, in the presence of HCl and L-proline, and then heating the resulting mixture at 120 °C overnight in a scintillation vial. The resulting crystals (of Zr-**fcu**-azo or Zr-**fcu**-sti) were washed with DMF and then subjected to solvent exchange with acetone. When submitted to ozone treatment for 30 min, Zr-**fcu**-azo retained its crystallinity and porosity, whereas Zr-**fcu**-sti collapsed into an amorphous, nonporous solid due to cleavage of all the ligands of the framework (Figures 4.2).

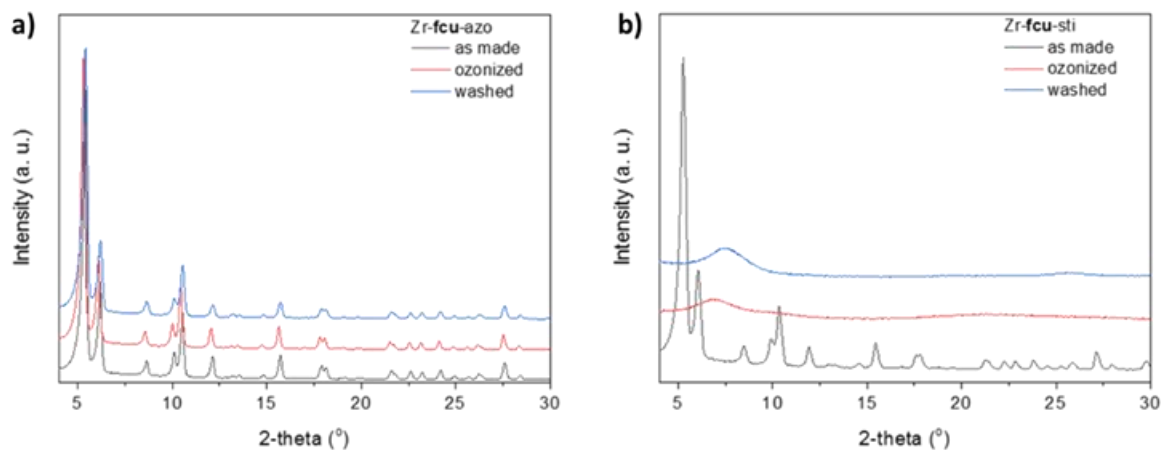


Figure 4.2. PXRD diagram ($\lambda_{\text{Cu}} = 1.5406 \text{ \AA}$) of as made, ozonized and washed Zr-**fcu**- sti in grey, red and blue, respectively.

As expected, N_2 sorption isotherms collected at 77 K confirmed comparable Brunauer–Emmett–Teller areas (A_{BET}) of $3025 \text{ m}^2/\text{g}$ for Zr-**fcu**-azo and $3065 \text{ m}^2/\text{g}$ for Zr-**fcu**-sti (Figure 4.3).

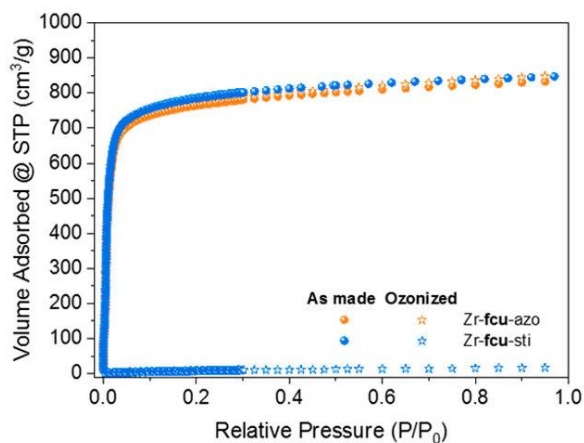


Figure 4.3. N_2 sorption isotherms for Zr-**fcu**-azo and Zr-**fcu**-sti before and after ozonolysis.

4.2.1.2 Synthesis and Porosity of Zr-fcu-azo/sti-X%

To prepare multivariate Zr-fcu-MOFs containing specific ratios of azo/sti (ranging from 90:10 to 40:60), we used similar synthetic conditions as for Zr-fcu-azo but partially replaced the H2azo with the appropriate amount of H2sti. The phase purity of the resulting single crystals of Zr-fcu-azo/sti-X% ($X \approx 10, 20, 30, 40, 50,$ or 60 stilbene molar percentage) was confirmed by powder X-ray diffraction (PXRD; Figure 4.4a).

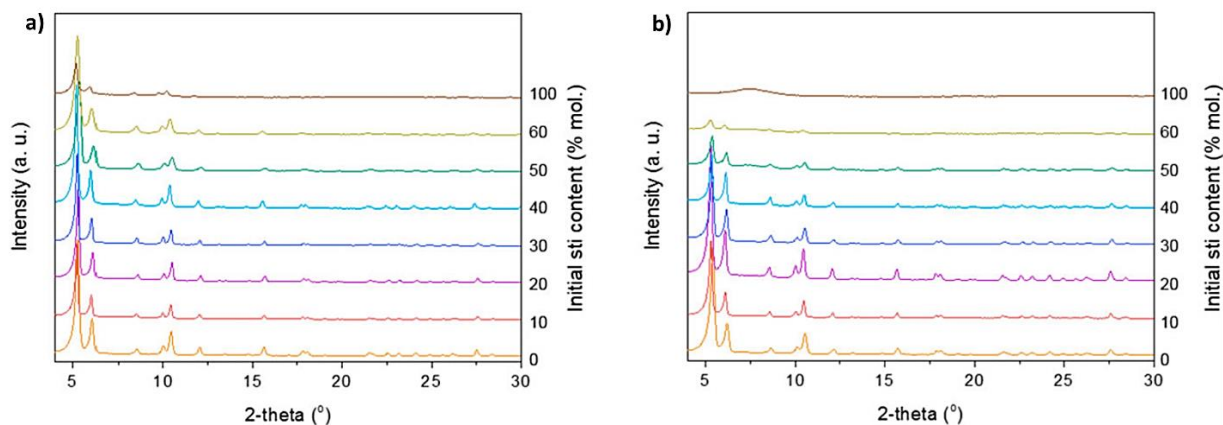


Figure 4.4. a) PXRD diagrams for Zr-fcu-azo/sti-X%. b) PXRD diagrams for ozonated (OZ), washed Zr-fcu-azo/sti-X%.

The synthesized crystals showed gradient color change from bright orange to colorless (Figure 4.5a) according to their constituent azo/sti ratio, which was confirmed by proton nuclear magnetic resonance (^1H NMR) of digested crystals (Figure 4.5b, see also Annex 3).

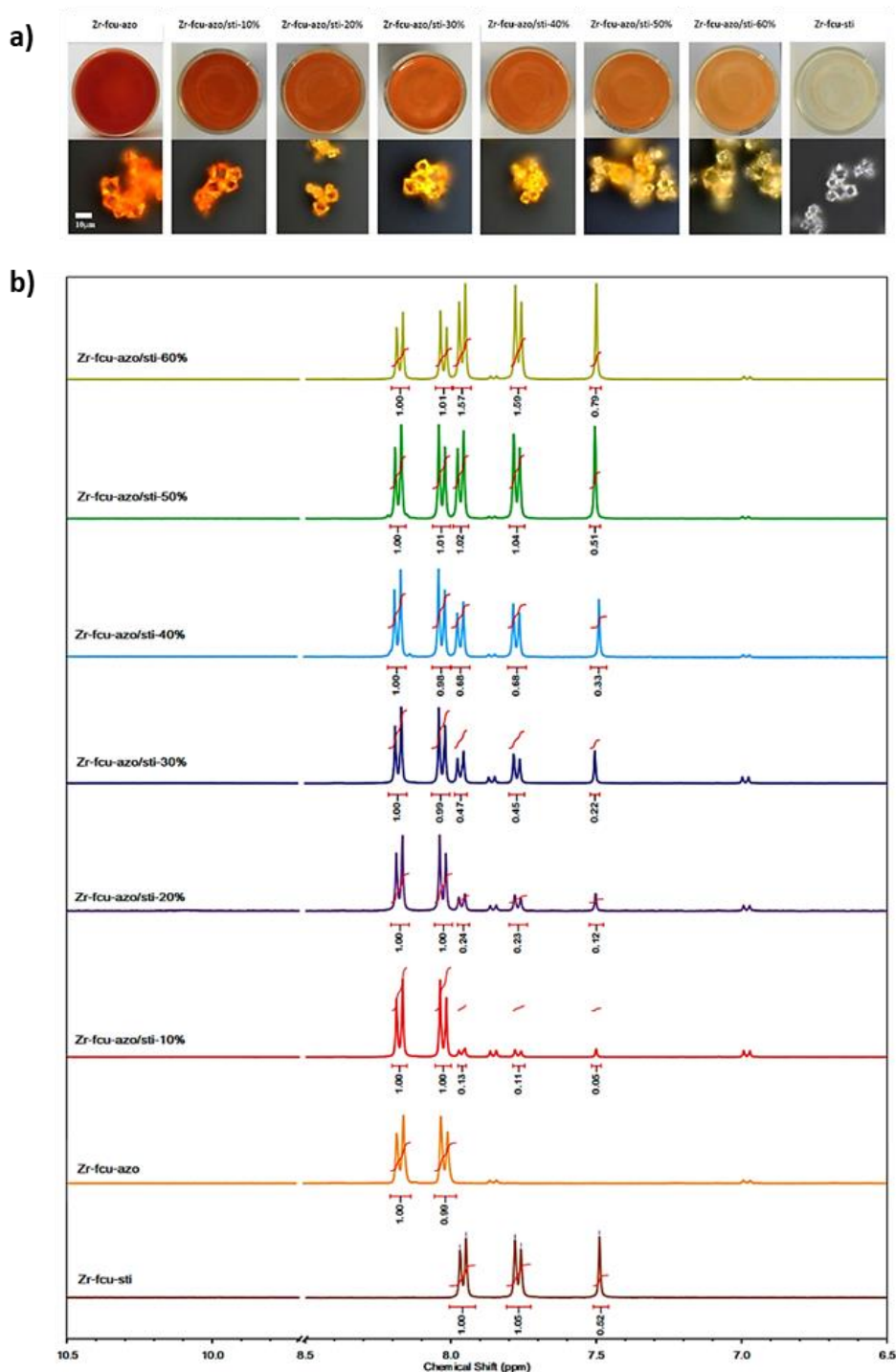


Figure 4.5. a) Optical images of Zr-fcu-azo/sti-X% samples. b) ¹H NMR spectra of digested Zr-fcu-azo/sti-X%.

Finally, N₂ sorption analysis performed at 77 K showed comparable uptake and type I isotherm for all different activated samples (Figure 4.6a). Indeed, all apparent A_{BET} values ranged from 3000 m²/g to 3065 m²/g, and total pore volumes ranged from 1.24 cm³/g to 1.28 cm³/g (Table 4.1). As expected, and similarly to reported values for comparable MOF systems,^{18e} the pore size distributions (PSD (pore size distribution), Figure 4.6b) of all Zr-fcu-azo/sti-X% are

comparable: with a main pore population of ca. 18.4 Å attributed to the intrinsic porosity of the framework and a minor population of larger pores of ca. 22.4 Å attributed to some modulator related defects.

Table 4.1. Apparent BET Area, Micropore Volume, and Total Pore Volume of Zr-fcu-azo/sti-X%, before and after Ozonolysis and Washing.

initial% sti	starting MOF			ozonated and washed MOF		
	A_{BET} (m^2/g)	V_{m}^{μ} (cm^3/g)	V_{t} (cm^3/g)	A_{BET} (m^2/g)	V_{m}^{μ} (cm^3/g)	V_{t} (cm^3/g)
0	3025	1.26	1.29	3030	1.24	1.27
10	3060	1.25	1.28	3115	1.27	1.32
20	3045	1.23	1.25	3130	1.31	1.38
30	3000	1.11	1.24	2680	1.17	1.38
40	3040	1.23	1.27	2580	1.10	1.44
50	3065	1.23	1.26	1860	0.79	1.36
60	3015	1.22	1.26	985	0.42	0.75
100	3065	1.26	1.31	nonporous		

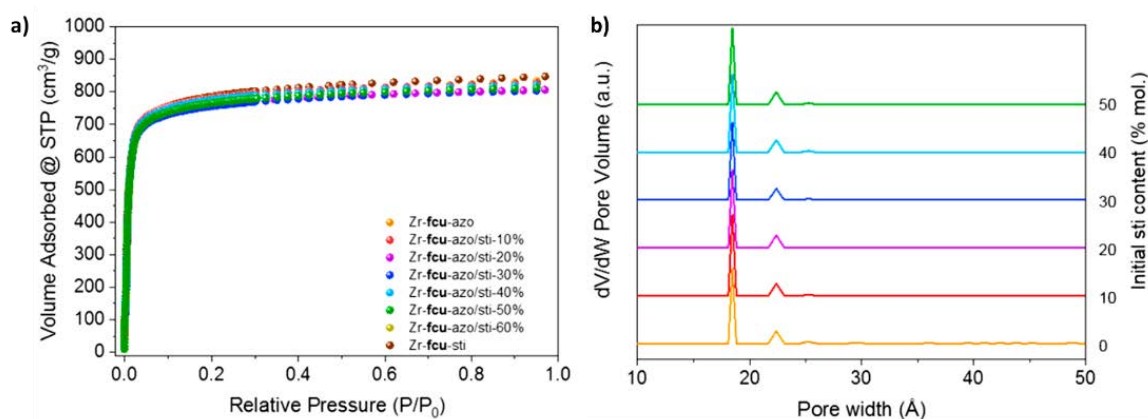


Figure 4.6. a) N_2 sorption isotherms (77 K) for Zr-fcu-azo/sti-X%. b) Pore size distribution estimated by DFT (density functional theory) for Zr-fcu-azo/sti-X%.

4.2.1.3 Ozonolysis of Zr-fcu-azo/sti-X%

To selectively break the sti ligands, we packed ca. 50 mg of Zr-fcu-azo/sti-X% into a L-shaped glass tube, connected on one side to the ozonator (through a CaCl_2 humidity trap) and, on the other side, to a vacuum pump (through a KI trap), to ensure a continuous flow of ozone through the column. The reaction was run at room temperature for 30 min. The ozonated Zr-fcu-azo/sti-X% materials maintained their high crystallinity after ozonolysis, as confirmed by PXRD

(Figure 4.4b, see also Annex 3). ^1H NMR of digested, Zr-**fcu**-azo/sti-X%_OZ confirmed the full conversion of sti into bdc and fba for all samples (Table 4.2, Figure 4.8). The 1:1 bdc/fba ratio observed for all Zr-**fcu**-azo/sti-X%_OZ also indicated the stoichiometric character of the reaction (Figures 4.7). As expected, based on our preliminary results with Zr**fcu**-azo, the content of azo ligand in the framework was not affected by ozonolysis, thus confirming its high selectivity toward olefin bonds.

Table 4.2. Organic moieties content from ^1H NMR for Zr-fcu**-azo/sti-X%_OZ.**

Material	% mol azo	% mol sti	% mol fba	% mol bdc
Zr- fcu -azo_OZ	100	0	0	0
Zr- fcu -azo/sti-10%_OZ	82	0	9	9
Zr- fcu -azo/sti-20%_OZ	68	0	16	16
Zr- fcu -azo/sti-30%_OZ	56	0	22	22
Zr- fcu -azo/sti-40%_OZ	43	0	26	31
Zr- fcu -azo/sti-50%_OZ	34	0	32	34
Zr- fcu -azo/sti-60%_OZ	24	0	37	39

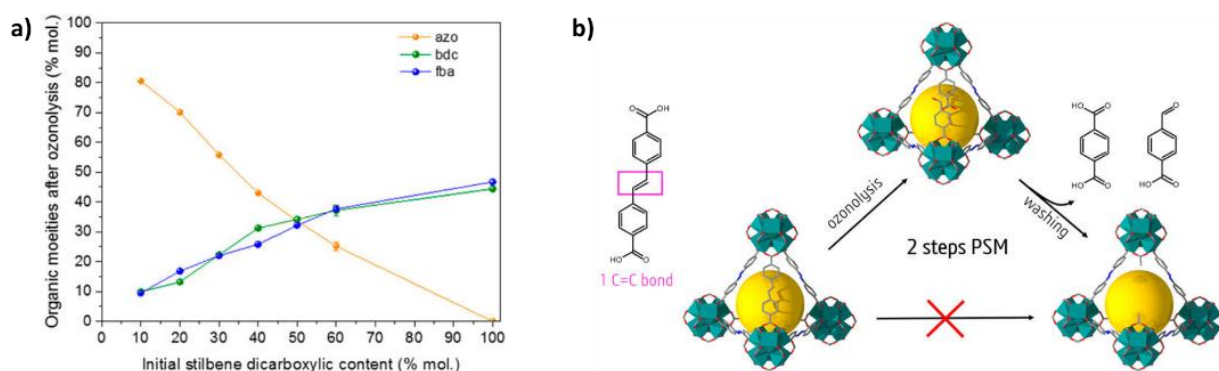


Figure 4.7. a) Remaining organic moieties in Zr-fcu**-azo/sti-X%_OZ, as derived from ^1H NMR spectra of digested samples. b) Post-synthetic generation of mesoporosity in MOFs in Zr-**fcu**-azo/sti MOFs, removal of the sti ligand requires two steps: ozonolysis (to break the ligand) and washing.**

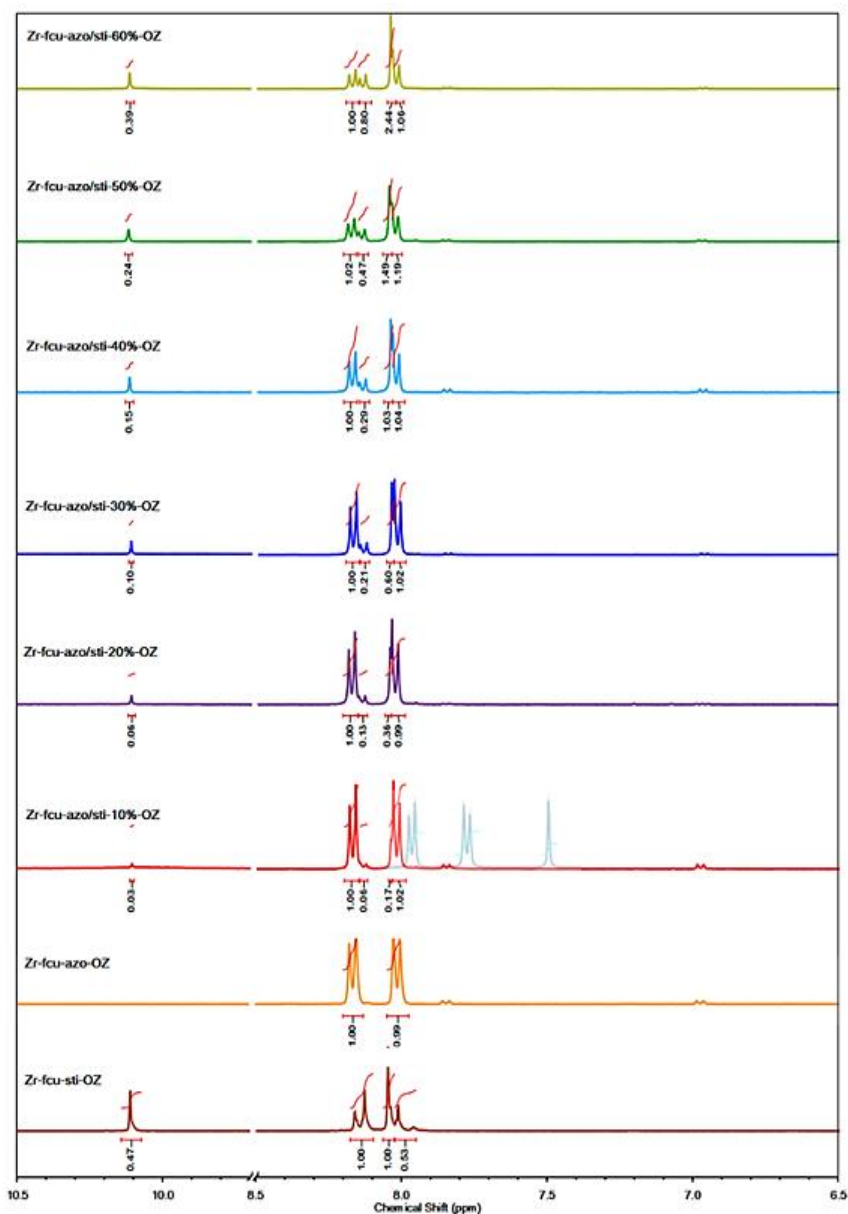


Figure 4.8. ^1H NMR spectra of digested Zr-fcu-azo/sti-X%_OZ showing the absence of H_2sti ligand (represented as “ghost spectrum” in Zr-fcu-azo/sti-10%_OZ).

4.2.1.4 Washing of Zr-fcu-azo/sti-X%_OZ

To remove the organic and inorganic fragments trapped in the pores of the Zr-fcu-azo/sti-X%_OZ, we washed the ozonated crude product in a 0.5 M solution of acetic acid in DMF. The washed samples did not exhibit any marked difference in crystallinity compared to the corresponding crude products, as confirmed by PXRD (Figure 4.9), with one exception: Zr-fcu-azo/sti-60%_OZ. The washing step revealed that the latter had indeed lost crystallinity, which we attributed to a partial collapse of its framework upon loss of 60% of its ligands via ozonolysis.

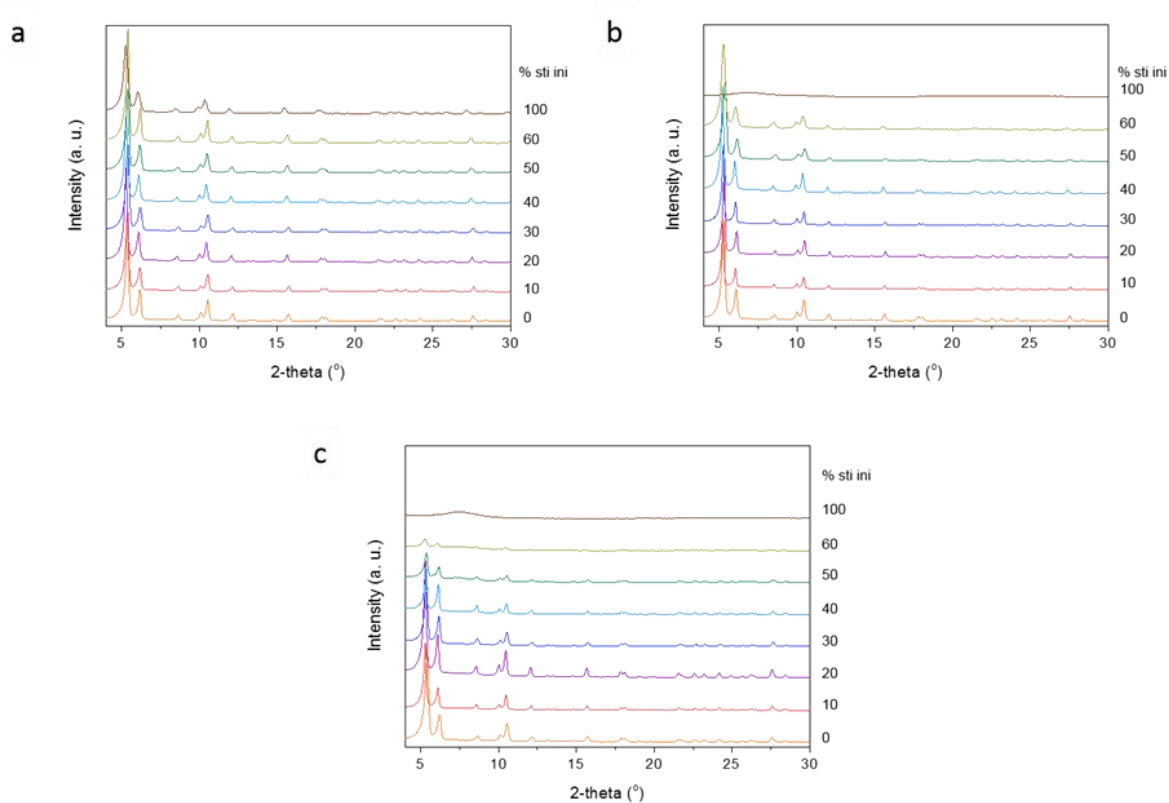


Figure 4.9. PXRD diagram ($\lambda_{\text{Cu}} = 1.5406 \text{ \AA}$) of as made (a), ozonized (b) and washed (c) Zr-fcu-azo/sti-X%.

In all cases, ^1H NMR (Figures 4.10 and Tables 4.3, see also Annex 3) of the washed Zr-fcu-azo/sti-X% revealed the absence of fba and the persistence of some bdc, which could not be fully removed (repeated washing did not remove any additional bdc).

Table 4.3. Organic moieties content from ^1H NMR for Zr-fcu-azo/sti-X%_W.

Material	% mol azo	% mol sti	% mol fba	% mol bdc
Zr-fcu-azo_W	100	0	0	0
Zr-fcu-azo/sti-10%_W	100	0	0	0
Zr-fcu-azo/sti-20%_W	91.7	0	0	8.3
Zr-fcu-azo/sti-30%_W	87.0	0	0	13.0
Zr-fcu-azo/sti-40%_W	74.6	0	0	25.4
Zr-fcu-azo/sti-50%_W	66.7	0	0	33.3
Zr-fcu-azo/sti-60%_W	59.2	0	0	40.8

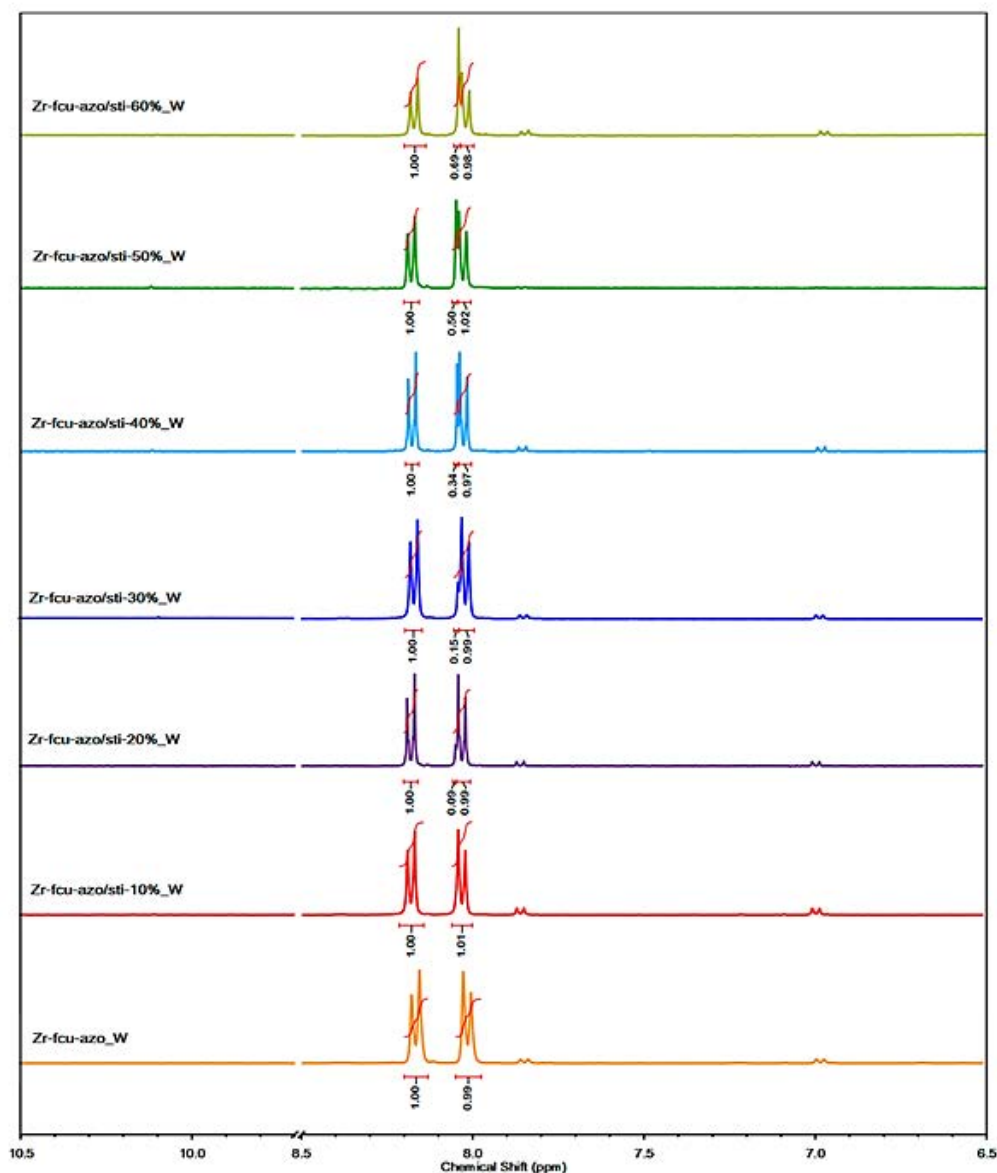


Figure 4.10. ^1H NMR spectra of digested Zr-fcu-azo/sti-X%_W showing the absence of fba and remaining traces of bdc ligands.

4.2.1.5. Porosity Properties of Washed, Ozonated Zr-fcu-azo/sti-X%

After confirming that in the washed, ozonated Zr-fcu-azo/sti-X%, all the sti ligands had been broken (Figure 4.8), most of the resulting organic fragments had washed out (Figure 4.10), and the high crystallinity had remained (Figure 4.9c), we submitted these materials to N_2 sorption tests at 77 K (Figure 11a, Table 4.1). As expected, Zr-fcu-azo/sti-10% performed very similarly to the preozonated material, showing only slightly higher values for apparent A_{BET} ($3115 \text{ m}^2/\text{g}$ vs $3060 \text{ m}^2/\text{g}$) and total pore volume ($1.32 \text{ cm}^3/\text{g}$ vs $1.28 \text{ cm}^3/\text{g}$). Based on the Dubinin–Radushkevich (DR) equation,⁷⁶ the relative proportion of microporosity to the total pore volume was estimated to be 96% (Figure 4.11b).

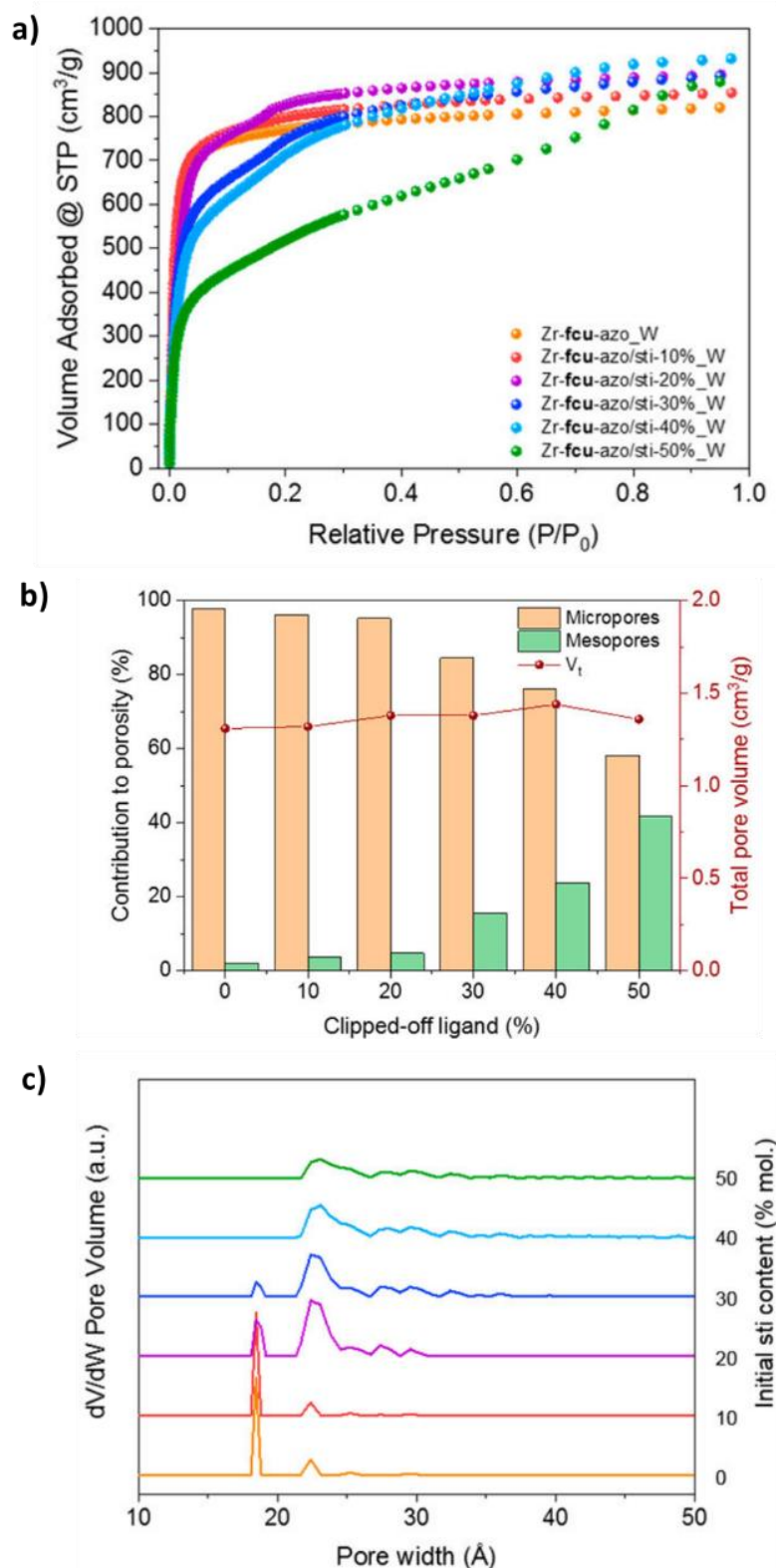


Figure 4.11. a) N₂ sorption isotherms (77 K) for ozonated Zr-fcu-azo/sti-X % after washing (denoted here by “_W”). b) Change in total pore volume and in the relative contribution of microporosity and mesoporosity to total uptake, in Zr-fcu-azo/sti-X%_{OZ} after washing, as calculated with the Dubinin–Radushkevich equation. c) Pore size distribution estimated by DFT for ozonated, washed Zr-fcu-azo/sti-X%.

Although the washed ozonated Zr-**fcu**-azo/sti-20% showed a nearly identical value for this parameter (95%), its isotherm exhibited a shoulder/ step characteristic from bigger pores, giving insights into the modified nature of the microporosity. The isotherms for the washed ozonated Zr-**fcu**-azo/sti-30% and Zr-**fcu**-azo/sti-40% did not show the type I shape of the isotherms of the corresponding starting MOFs, but rather they exhibited a small hysteresis on the desorption branch, characteristic of mesoporosity (Figure 4.12).

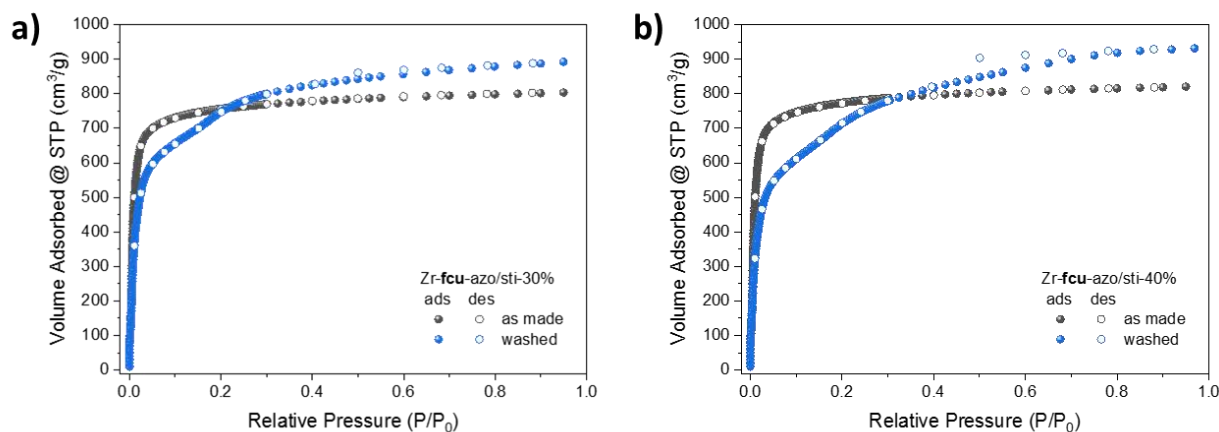


Figure 4.12. N₂ sorption isotherms (77 K) of as made and ozonized-washed a) Zr-**fcu**-azo/sti-30% and b) Zr-**fcu**-azo/sti-30% in grey and blue, respectively.

Notably, ozonolysis treatment reduced the apparent A_{BET} : for the washed ozonated Zr**fcu**-azo/sti-30%, 2680 m²/g (vs 3000 m²/g) and for the washed ozonated Zr-**fcu**-azo/sti-40%, 2580 m²/g (vs 3040 m²/g) (Table 4.1). However, in both cases, this decrease was offset by a major increase in the proportion of pores with mesoscale dimensions, as derived from the DR equation (Figure 4.11b and Table 4.4): for the washed ozonated Zr-**fcu**-azo/sti-30%, 15% (vs 2%) and for the washed ozonated Zr-**fcu**-azo/sti-40%, 24% (vs 3%).

Table 4.4. Contribution of microporosity vs mesoporosity extracted from the DR equation in Zr-fcu-azo/sti-X%_W.

Material	V_{μ} (cm ³ /g)	V_t (cm ³ /g)	Microporosity (%)	Mesoporosity (%)
Zr-fcu-azo_W	1.24	1.27	98	2
Zr-fcu-azo/sti-10%_W	1.27	1.32	96	4
Zr-fcu-azo/sti-20%_W	1.31	1.38	95	5
Zr-fcu-azo/sti-30%_W	1.17	1.38	85	15
Zr-fcu-azo/sti-40%_W	1.10	1.44	76	24
Zr-fcu-azo/sti-50%_W	0.79	1.36	58	42
Zr-fcu-azo/sti-60%_W	0.42	0.75	56	44

Likewise, the total pore volume also increased in both cases: for the washed ozonated Zr-fcu-azo/sti-30%, 1.36 cm³/g (vs 1.24 cm³/g) and for the washed ozonated Zr-fcu-azo/sti-40%, 1.44 cm³/g (vs 1.27 cm³/g). Similar results were observed in the washed ozonated Zr-fcu-azo/sti-50%, which exhibited the most extreme change relative to the corresponding starting MOF: the contribution of the mesoporosity reached 42% of the total porosity (Figure 4.11b and Table 4.4), and the hysteresis characteristic from mesoporosity was clearly visible (Figure 4.13a); consequently, its A_{BET} was only 1860 m²/g (vs 3065 m²/g). Note that additional washing treatment did not affect the sorption properties (Figure 13b), excluding the hypothesis of structural etching sometimes observed through chemical treatment.^{49,77}

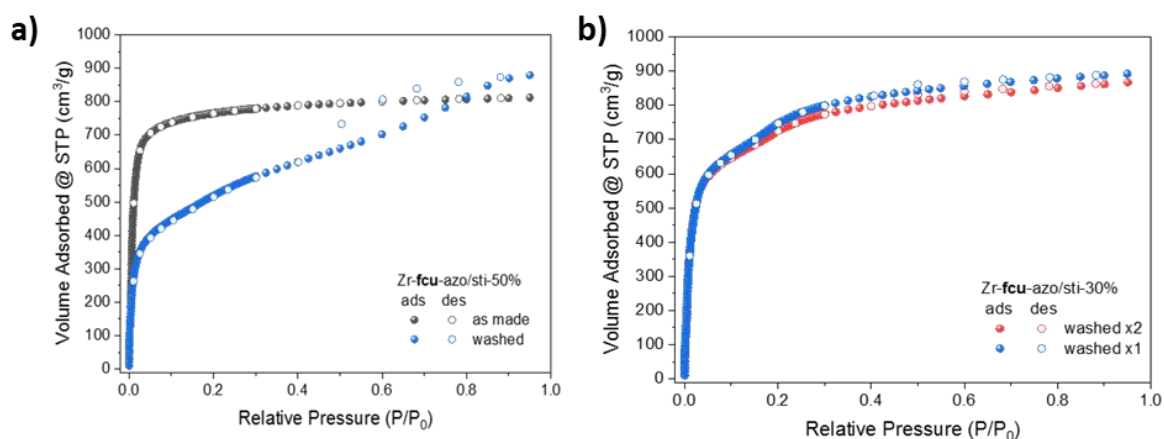


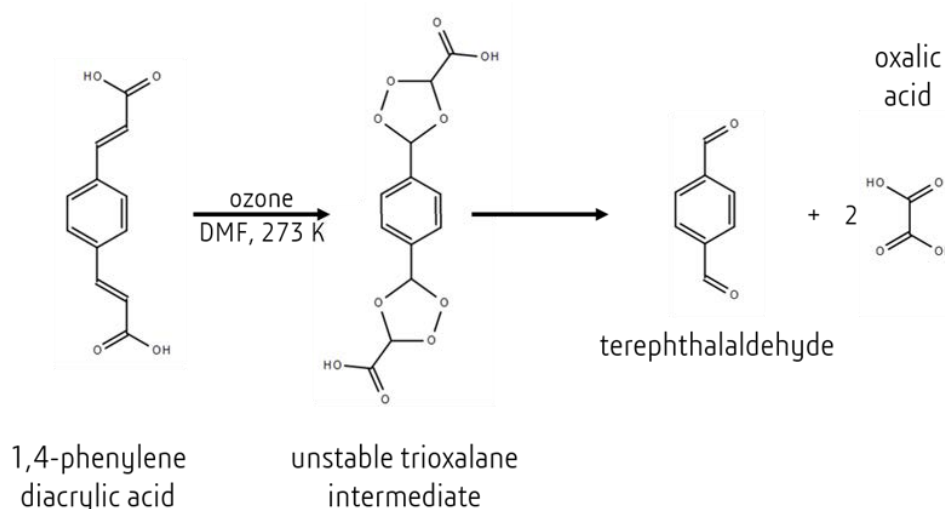
Figure 4.13. a) N₂ sorption isotherms (77 K) of as made and ozonized-washed Zr-fcu-azo/sti-50% in grey and blue, respectively. b) N₂ sorption isotherms (77 K) of Zr-fcu-azo/sti-30% after ozonolysis followed by one (blue) and two washing treatments.

The modification of the micro- vs mesoporosity ratio was also reflected by studying the PSD (Figure 4.11c). If no noticeable change was observed for the washed ozonated Zr-fcu-azo, a subtle appearance of pores of ca. 25 Å and above was noted for the washed ozonated Zr-fcu-

azo/sti-10%. The washed ozonated Zr-**fcu**-azo/sti-20% and -30% showed a clear decrease of the initial main pore size of ca. 18.4 Å and an increase of the second population at ca. 22.4 Å, confirming that micropores are merged into wider pores. For these two samples, the formation of pores bigger than 25 Å was also visible. Finally, the initial main pores of ca. 18.4 Å completely vanished in washed and ozonated Zr-**fcu**-azo/sti-40% and -50%. In these cases, the pores were mainly observed at ca. 22.4 Å and spread over a wide range up to 50 Å. Albeit nonobserved through PXRD, the pore population centered at 22.4 Å could be attributed to the existence of nonordered reo motifs, resulting from the removal of inorganic clusters, as hypothesized in some comparable systems.⁴⁹

4.2.2 Zr-**fcu**-bpdc/pdac System

Based on these pioneering results, we envisioned extending our method to a more challenging system. We considered that 4,4'-biphenyldicarboxylic acid (H₂bpdc) and 1,4-phenylenediacyrylic acid (H₂pdac), found in the two Zr-**fcu**-MOFs UiO-67 and NU-801, would be a suitable ligand pair, given their geometric (length ≈ 11.3 Å) and chemical properties (vide supra). A particularity of H₂pdac is its two olefin bonds (Scheme 4.3), which we reasoned would enable cutting of the ligand into three distinct parts, rather than two, as in H₂sti (Scheme 4.1, Figure 4.1).



Scheme 4.2. Ozonolysis of H₂pdac into terephthalaldehyde and oxalic acid.

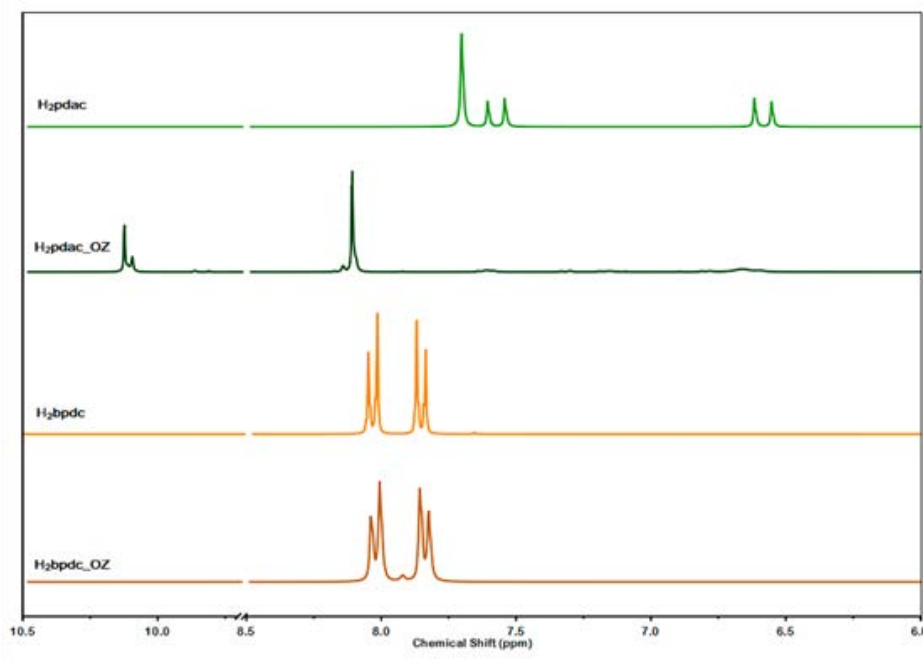
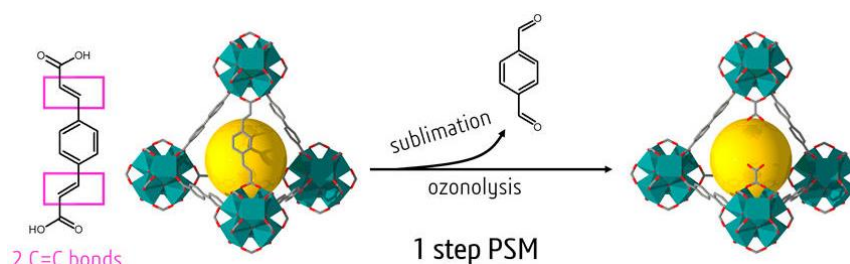


Figure 4.14. ^1H NMR spectra of H2bpdc, H2pdac before and after ozonolysis treatment in DMF at $0\text{ }^\circ\text{C}$.

In addition, we hypothesized that removal of the central part of the ligand could generate terephthalaldehyde, which could be sublimated under vacuum at moderate temperature -for example, during ozonolysis and/or during a classical presorption activation procedure (Scheme 4.3). That turned out to be correct and, by obviating the washing step, represented a major improvement to our method.



Scheme 4.3. Proposal of post-synthetic generation of mesoporosity in Zrfcu- bpdc/pdac MOFs, removal of the pdac ligand requires only one step: ozonolysis (to break the ligand) and concomitant sublimation (to remove the central core). This is made possible by the two olefin groups in this ligand.

4.2.2.1 Synthesis of Zr-fcu-bpdc/pdac-X%

Multivariate Zr-fcu-MOFs containing specific ratios of bpdc/pdac, from 100:0 (UiO-67)⁷⁸ to 0:100 (NU-801)^{54,79} were prepared from mixtures of ZrCl₄, H₂bpdc, and H₂pdac dissolved in DMF in the presence of trifluoroacetic acid (tfa) and heated at 120 °C for 72 h in a scintillation vial. The samples were washed with DMF overnight and then soaked in toluene for 3 days. The phase purity of the single crystals of Zr-fcu-bpdc/pdac-X% (X ≈ 10, 20, 30, 40% pdac molar percentage) was confirmed by PXRD (Figure 4.15a), ¹H NMR of digested crystals (Figure 4.16, See also Annex 3), and N₂ sorption analysis performed at 77 K (Figure 4.15b and Table 4.5).

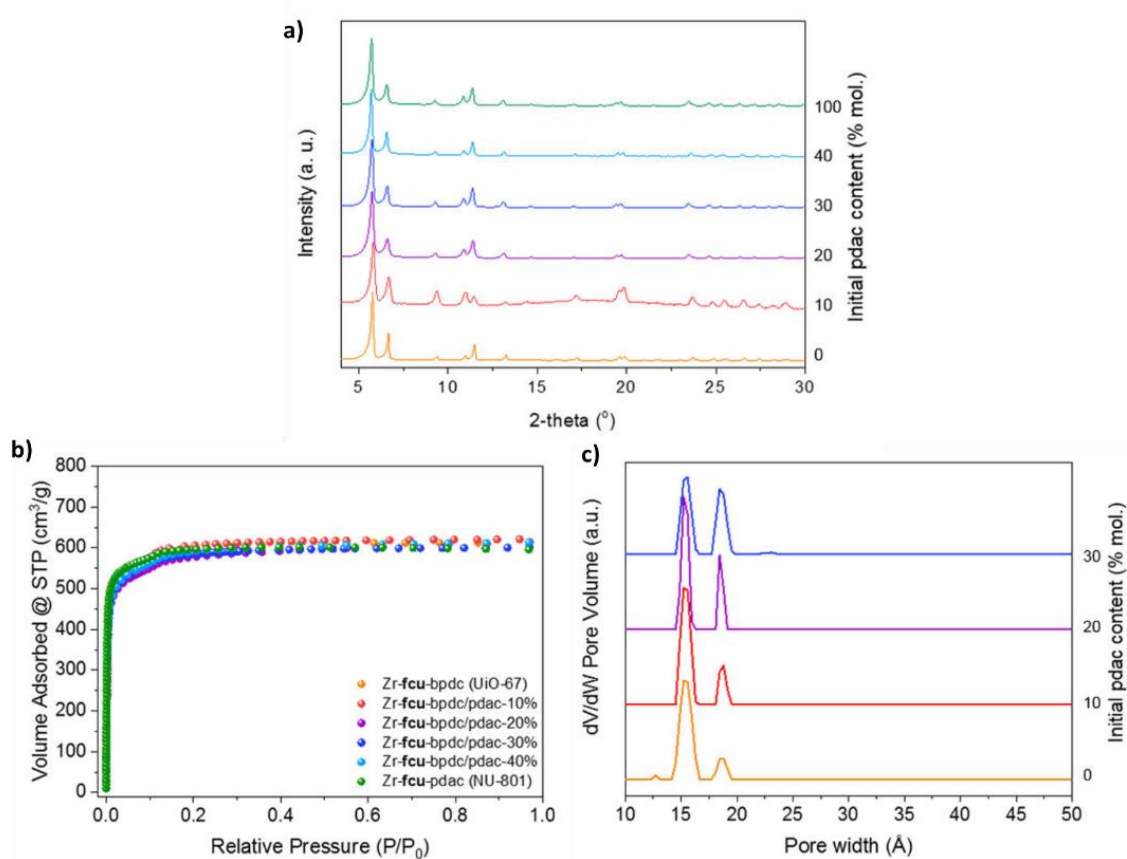


Figure 4.15. a) PXRD diagrams for Zr-fcu-bpdc/pdac-X%. b) N₂ sorption isotherms (77 K) for Zr-fcu-bpdc/pdac-X%. c) Pore size distribution estimated by DFT for Zr-fcu-bpdc/pdac-X%.

Table 4.5. Apparent BET Area, Microporous, and Total Pore volume of Zr-fcu-bpdc/pdac-X%, before and after Ozonolysis.

% pdac initial	starting MOF			ozonated MOF		
	A_{BET} (m ² /g)	V_{t} (cm ³ /g)	V_{t} (cm ³ /g)	A_{BET} (m ² /g)	V_{t} (cm ³ /g)	V_{t} (cm ³ /g)
0	2250	0.91	0.93	2305	0.92	0.95
10	2295	0.95	0.96	2400	0.97	1.09
20	2210	0.91	0.95	1870	0.73	0.99
30	2245	0.93	0.94	1730	0.65	1.05
40	2265	0.93	0.95		nonporous	
100	2310	0.92	0.92		nonporous	

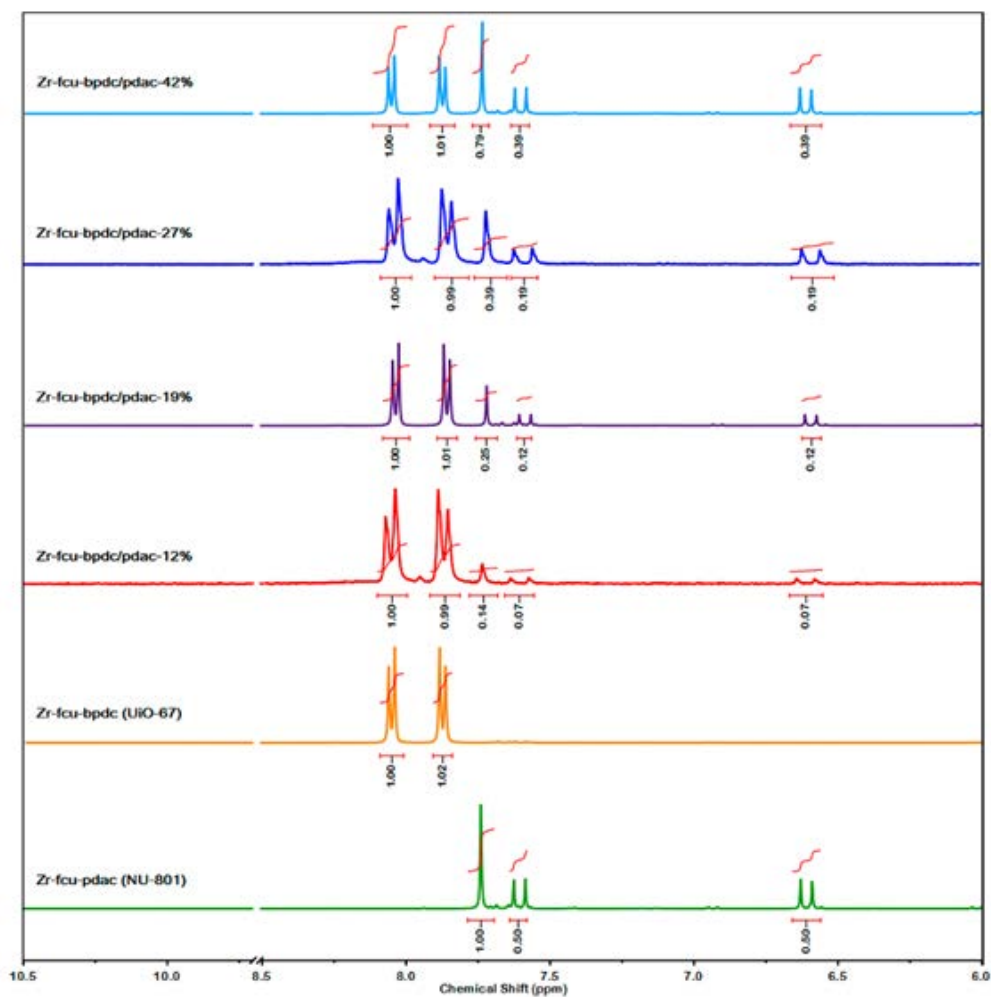


Figure 4.16. ^1H NMR spectra of digested Zr-fcu-bpdc/pdac-X%.

The sorption isotherms for Zr-fcu-bpdc/ pdac-X% were comparable ($2210 \text{ m}^2/\text{g} < A_{\text{BET}} < 2310 \text{ m}^2/\text{g}$ and $0.92 \text{ cm}^3/\text{g} < V_t < 0.96 \text{ cm}^3/\text{g}$). We observed a slight shoulder at a P/P₀ value of ca. 0.1, which we attributed to a higher number of initial defects in the structure, likely due to our use of a slightly different synthetic procedure than for Zr-fcu- azo/sti-X%. This is in fact reflected by the estimation of the PSD (Figure 4.15c), in which all samples presented two main contributions at ca. 15.2 and 18.4 Å; the bigger size being attributed (similarly as for Zr-fcu- azo/sti system, vide supra) to modulator-related defects.

4.2.2.2 Ozonolysis of Zr-fcu-bpdc/pdac-X%

Analogously to the previous MOF pair (vide supra), the crystallinity and porosity of UiO-67 were unaffected by ozonolysis (Figure 4.17a, b), but cleavage of the pdac ligands in NU-801 led to collapse of its framework and loss of its crystallinity and porosity (Figures 4.17a, c).

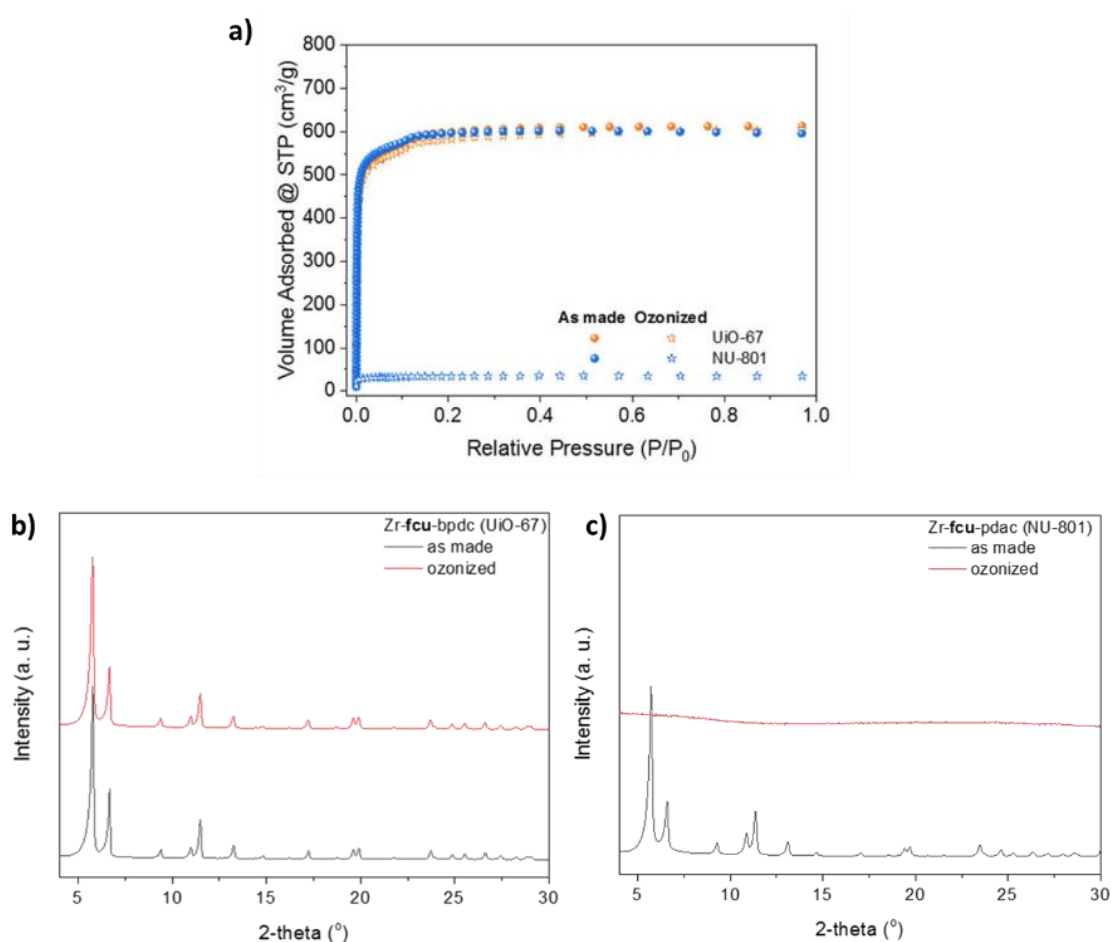


Figure 4.17. PXRD diagram ($\lambda_{\text{Cu}} = 1.5406 \text{ \AA}$) of as made and ozonized a) Zr-fcu-bpdc (UiO-67) and Zr-fcu-pdac (NU-801) in grey and red, respectively.

Having demonstrated this, we proceeded with ozonolysis of the Zr-**fcu**-bpdc/pdac-X% MOFs. ^1H NMR of all Zr-**fcu**bpdc/ pdac-X%_OZ highlighted the absence of any remaining pdac ligand (Figures 4.18, Table 4.6). Moreover, after the Zr**fcu**-bpdc/pdac-X%_OZ were activated at 85 °C, a white solid was recovered in the cold trap (77 K) placed between the MOFs and the pump. This solid was confirmed by ^1H NMR to be terephthalaldehyde (Figure 4.19), which, after cleavage of pdac, we were able to directly extract from the framework via sublimation, as anticipated.

Table 4.6. Organic moieties content from ^1H NMR for Zr-**fcu**-bpdc/pdac-X%_OZ.

Material	% mol bpdc	% mol pdac	% mol terephthalaldehyde
Zr- fcu -bpdc_OZ (UiO-67_OZ)	100	0	0
Zr- fcu -bpdc/pdac-10%_OZ	100	0	0
Zr- fcu -bpdc/pdac-20%_OZ	100	0	0
Zr- fcu -bpdc/pdac-30%_OZ	100	0	0
Zr- fcu -bpdc/pdac-40%_OZ	100	0	0

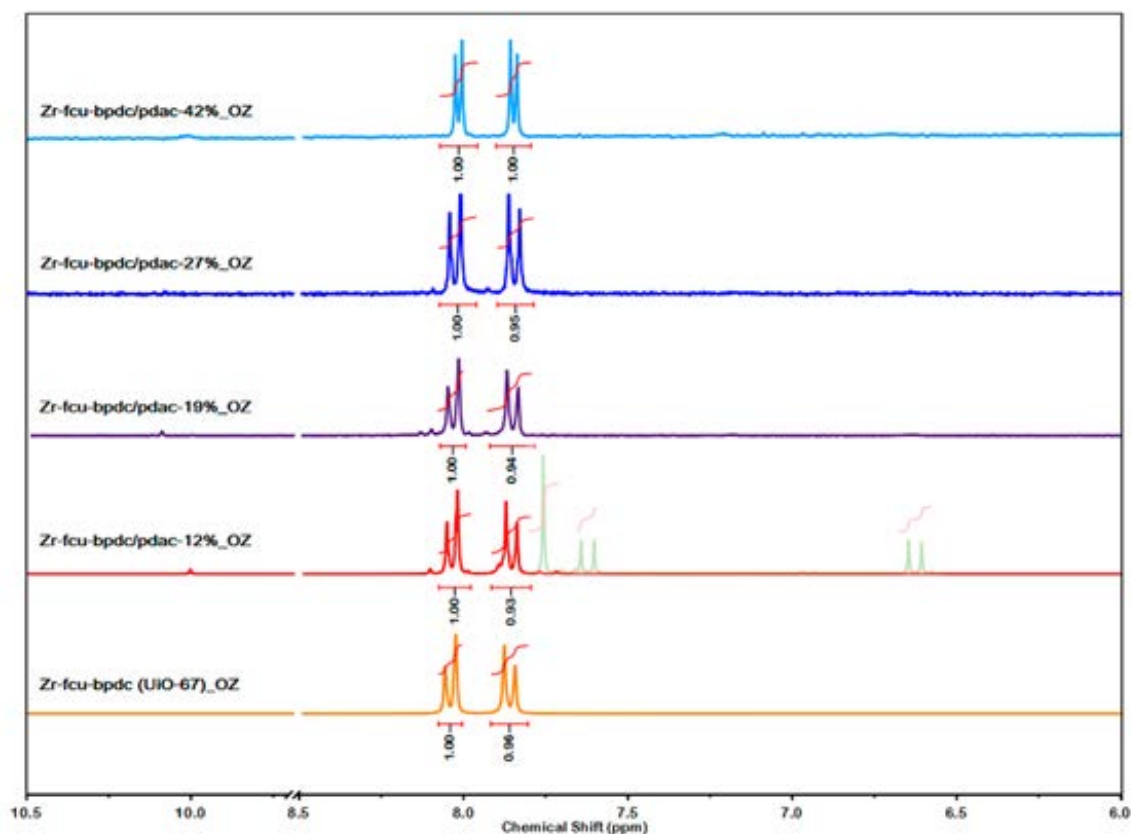


Figure 4.18. ^1H NMR spectra of digested Zr-fcu-bpdc/pdac-X%_OZ showing the absence of H2pdac ligand (represented as “ghost spectrum” in Zr-fcu-bpdc/pdac-10%_OZ).

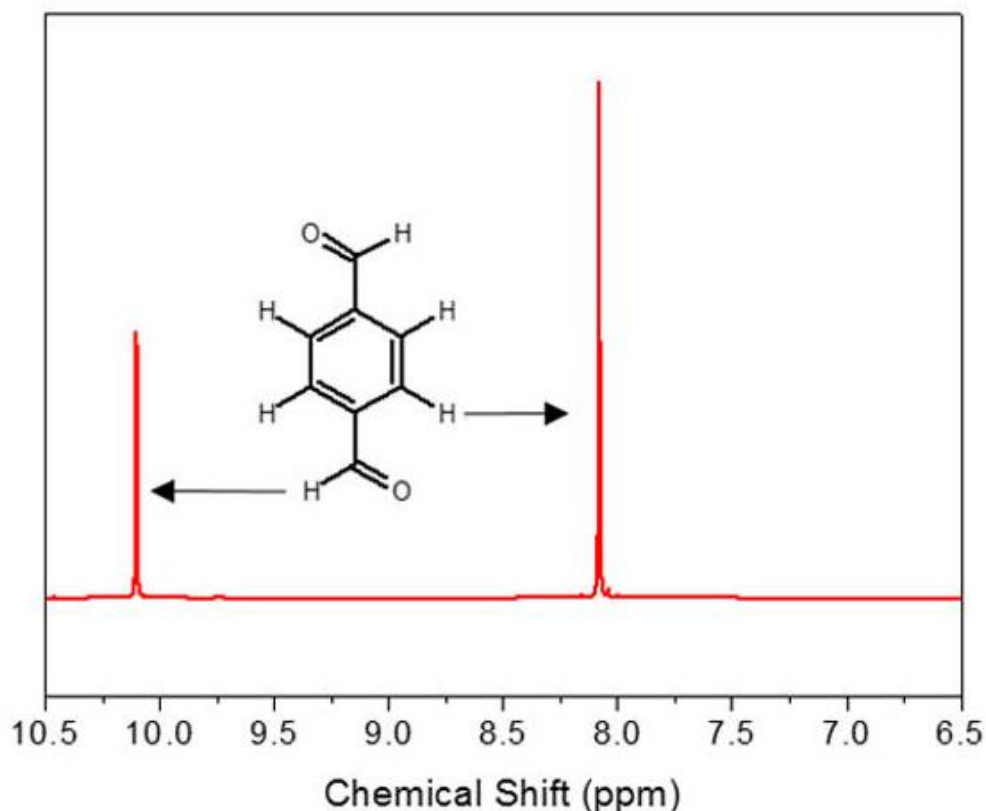


Figure 4.19. ^1H NMR spectra of the sublimated terephthalaldehyde recovered by heating at 85 °C under vacuum after ozonolysis.

4.2.2.3 Porosity of Zr-fcu-bpdc/pdac-X%_OZ

To investigate the effects of removing the central core of pdac on the porosity of the Zr-fcu-bpdc/pdac-X%_OZ, we performed N_2 sorption experiments on these MOFs (Figure 4.20a, Table 4.6). Upon extracting terephthalaldehyde from the backbone of Zr-fcu-bpdc/pdac-10%, the porosity was enhanced, as demonstrated by an increase in the apparent A_{BET} (from 2295 m^2/g to 2400 m^2/g). In this sample, besides the evolution of microporous pore volume (V_{μ}) (from 0.95 cm^3/g to 0.97 cm^3/g) not being significant, a more pronounced shoulder in the isotherm reflected a transformation of the microporosity. The emergence of some mesoporosity was revealed by the DR equation, with a contribution of 11% (vs 1%) to the total porosity. In contrast, upon further removal of pdac pillars, from Zr-fcu-bpdc/pdac-20%_OZ and Zr-fcu-bpdc/pdac-30%_OZ, the apparent A_{BET} decreased sharply: for Zr-fcu-bpdc/pdac-20%_OZ ($A_{\text{BET}} = 1870 \text{ m}^2/\text{g}$ vs 2210 m^2/g) and for Zr-fcu-bpdc/pdac-30%_OZ ($A_{\text{BET}} = 1730 \text{ m}^2/\text{g}$ vs 2245 m^2/g). The loss in

microporosity for Zr-**fcu**-bpdc/pdac-20%_OZ ($V_{\mu} = 0.73 \text{ cm}^3/\text{g}$ vs $0.91 \text{ cm}^3/\text{g}$) and for Zr-**fcu**-bpdc/pdac-30%_OZ ($V_{\mu} = 0.65 \text{ cm}^3/\text{g}$ vs $0.93 \text{ cm}^3/\text{g}$) was offset by a major increase in the proportion of pores with mesoscale dimensions, as derived from the DR equation (Figure 4.20b, Table 4.7): for Zr-**fcu**-bpdc/pdac-20%_OZ, 26% (vs 4%) and for Zr-**fcu**-bpdc/pdac-30%_OZ, 38% (vs 1%). Likewise, the total pore volume also slightly increased in both cases: for Zr-**fcu**-bpdc/pdac-20%_OZ, $0.99 \text{ cm}^3/\text{g}$ (vs $0.95 \text{ cm}^3/\text{g}$) and for Zr-**fcu**-bpdc/pdac-30%_OZ, $1.05 \text{ cm}^3/\text{g}$ (vs $0.94 \text{ cm}^3/\text{g}$).

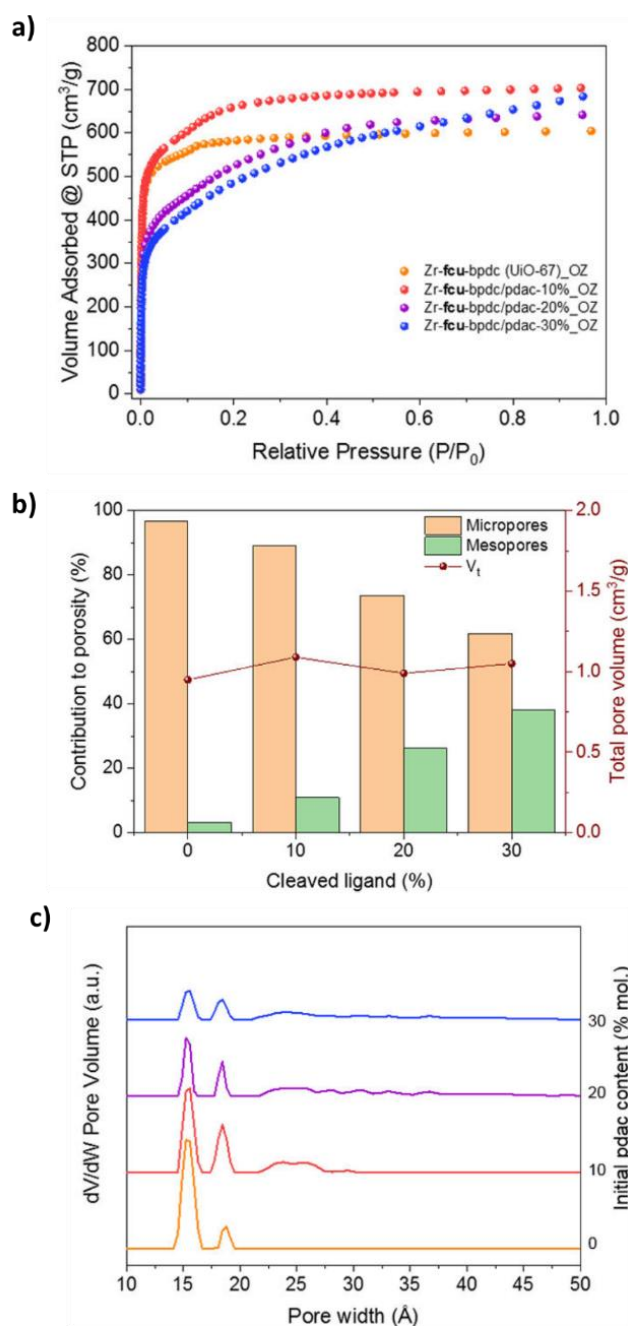


Figure 4.20. a) N₂ sorption isotherms (77 K) for Zr-**fcu**-bpdc/pdac-X%_OZ. b) Plot showing the overall stability of the total pore volume and evolution of the relative contribution of mesoporosity

vs microporosity to total uptake, in Zr-fcu-bpdc/pdac-X%_OZ, as calculated with the Dubinin–Radushkevich equation. c) Pore size distribution estimated by DFT for Zr-fcu-bpdc/pdac-X_OZ%.

Table 4.7. Contribution of microporosity vs mesoporosity extracted from the DR equation in Zr-fcu-bpdc/pdac-X%_OZ.

Material	V_{μ} (cm^3/g)	V_t (cm^3/g)	Microporosity (%)	Mesoporosity (%)
Zr-fcu-bpdc_OZ (UiO-67)	0.92	0.95	97	3
Zr-fcu-bpdc/pdac-10%_OZ	0.97	1.09	89	11
Zr-fcu-bpdc/pdac-20%_OZ	0.73	0.99	74	26
Zr-fcu-bpdc/pdac-30%_OZ	0.65	1.05	62	38

As expected, Zr-fcubpdc/pdac-40%, which, upon ozonation, lost its crystallinity (Figure 4.21) due to structural collapse caused by removal of 40% of its ligands, was nonporous.

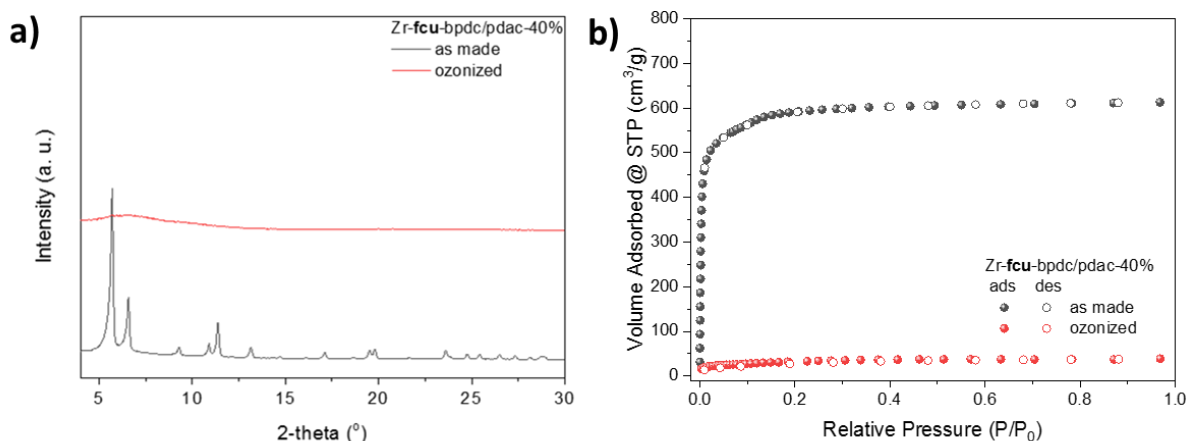


Figure 4.21. a) PXRD diagram ($\lambda_{\text{Cu}} = 1.5406 \text{ \AA}$) of as made and ozonized Zr-fcu-bpdc/pdac-40% in grey and red; b) N_2 sorption isotherms (77 K) of as made and ozonized Zr-fcu-bpdc/pdac-40% in grey and red, respectively.

Overall, the change in the porosity in Zr-fcu-bpdc/pdac-X% paralleled that of Zr-fcu-azo/sti-X%. However, in the former, these changes occurred at lower percentages of ligand removal—presumably due to a greater number of defects in the starting MOFs. The estimation of the PSD in this system also confirmed the evolution of the porosity toward mesopores (Figure 4.20c). While ozonolysis of UiO-67 did not affect the pore system of the pristine MOF, the appearance of pores distributed between 21.6 and 27.4 \AA was clearly visible for the ozonated Zr-fcu-bpdc/pdac-10%, -20%, and -30%. In addition, the two initial main pore populations decreased in ozonated Zr-fcu-bpdc/pdac-20% and Zr-fcu-bpdc/pdac-30%. In these two last

samples, the porosity population was extended up to ca. 50 Å, further confirming the fusion of micropores into novel mesopores.

4.3 Conclusions

In conclusion, we have developed a selective and quantitative method for post-synthetic modification of MOF porosity via ozonolysis. Through removal of organic ligands, our approach causes micropores to fuse into larger (mesoscale) pores in a controlled fashion and without any loss in total porosity. It selectively breaks the olefin bonds in organic ligands without affecting other organic moieties and can be applied for short reaction times (ca. 30 min) under mild conditions (room temperature). Moreover, we have demonstrated that ozonolysis can be used as a novel tool to selectively remove, and recover, specific fragments of molecules/frameworks through solid–gas manipulation.

4.4 Experimental section

4.4.1 Materials and Instruments.

Reagents. 4,4'-Stilbenedicarboxylic acid (H_2sti), 4,4'-biphenyldicarboxylic (H_2bpd), and azobenzene-4,4'-dicarboxylic acid (H_2azo) were purchased from TCI Europe. Acetic acid, 1,4-phenylenediacrylic acid (H_2pdac), trifluoroacetic acid (tfa), zirconium chloride ($ZrCl_4$), L-proline, hydrochloric acid, potassium iodide, and anhydrous granular $CaCl_2$ (2–6 mm) were purchased from Sigma-Aldrich (Merck). N, N-Dimethylformamide (DMF) and acetone were obtained from Fisher Chemical. Toluene was purchased from Acros Organics. All the reagents and solvents were used as received. Pyrex tubes (ext $\varnothing = 7$ mm; in $\varnothing = 5$ mm; length = 150 mm) were purchased from Vidrasa S.A. The tubes were bent into an L-shape with a flame torch.

Instruments. Optical Microscopy images were captured by a Zeiss Axio Observer Z1m optical microscope. PXRD diagrams were recorded on an X'Pert PRO MPD analytical diffractometer (Panalytical) at 45 kV, 40 mA using $CuK\alpha$ radiation ($\lambda = 1.5406 \text{ \AA}$). 1H NMR spectra were recorded on a Bruker Avance 400 NMR spectrometer (static magnetic field: 11.7 T) operating at Larmor frequencies of 400 MHz (1H). Ozonolysis treatment was performed using an ozone generator (N1668A from Ozonotec) generating a constant flow of 10.4 mmol/h at room temperature. Volumetric N_2 sorption isotherms were collected at 77 K (N_2) using an ASAP 2020 HD (Micromeritics). Temperature was controlled by using a liquid nitrogen bath. Total pore volume (V_t) was calculated at $P/P_0 = 0.95$, and microporous volume (V_μ) was calculated using the Dubinin–Radushkevich equation. Pore size distribution was estimated using a density functional theory (DFT) model (N_2 – cylindrical pores–oxide surface) implemented in the Microactive 4.00 software with a regularization factor of 0.01.

4.4.2 Synthesis and Activation of MOFs

Synthesis of Zr-fcu-azo/sti-X%. 4,4'-Stilbenedicarboxylic acid (H_2sti , 0.44-x mmol) and azobenzene-4,4'-dicarboxylic acid (H_2azo , x mmol) were suspended in 10 mL of DMF and sonicated for 30 min in a 23 mL scintillation vial. Then 5 mL of a DMF solution of $ZrCl_4$ (105 mg, 0.45 mmol), L-proline (250 mg, 2.17 mmol), and 45 μL of conc. HCl was transferred into the vial and vortexed for 1 min. After heating at 120 °C for 16 h, the reaction afforded orange octahedral crystals of Zr-fcu-azo/sti-X% (see the Annex 3 for more details about the $H_2azo:H_2sti$ ratio in this synthesis).

Synthesis of Zr-fcu-bpdc/pdac-X%. ZrCl₄ (200 mg, 0.86 mmol), 1,4-phenylenediacrylic acid (H₂pdac, x mmol), and biphenyl-4,4'-dicarboxylic acid (H₂bpdc, y mmol) were dissolved by sonication in 10 mL of DMF in the presence of tfa (1 mL) in a 23 mL scintillation vial. After heating at 120 °C for 72 h, colorless octahedral crystals of Zr-fcu-bpdc/pdac-X% were obtained (see the Annex 3 for more details about the H₂bpdc/H₂pdac ratio in the synthesis).

Sample Activation.

Activation of Zr-fcu-azo/sti-X%. Crystals of Zr-fcu-azo/sti-X% were soaked in 15 mL of DMF (refreshed after 4 h) and then subjected to solvent exchange in 15 mL of acetone (refreshed after 4 h). The supernatant was removed after decantation, and the crystals were dried at 65 °C. Sample purity was verified by PXRD, and experimental azo/sti ratios were analyzed by ¹H NMR of the digested samples. Crystals of Zr-fcu-azo/sti-X% were then transferred into a glass sorption cell and activated under dynamic vacuum at 85 °C prior to sorption experiments.

Activation of Zr-fcu-bpdc/pdac-X%. Crystals of Zr-fcu-bpdc/pdac-X% were soaked in 10 mL of DMF for 24 h and then subjected to solvent exchange for 72 h in 20 mL of toluene (refreshed twice per day). The supernatant was removed by filtration. The sample purity was verified by PXRD, and the experimental bpdc/pdac ratios were analyzed by ¹H NMR of the digested samples. Crystals of Zr-fcu-bpdc/pdac-X% were then transferred into a glass sorption cell and activated under dynamic vacuum at 85 °C prior to sorption experiments.

4.4.3 Solid-gas Ozonolysis Treatment.

Ozonolysis of the Organic Ligands. In a typical procedure, 30 mg of the H₂azo, H₂sti, H₂bpdc, or H₂pdac was dissolved/dispersed in 20 mL of DMF. The solution was then transferred to a 50 mL three-necked round-bottom flask and was cooled to 0 °C using an ice-water bath. A constant ozone flux was blown into the solution through a glass pipet for 30 min under stirring. The crude reaction was then allowed to warm up to room temperature, and the solvent was removed in vacuo. The crude residue was collected and analyzed by ¹H NMR. ¹H NMR analysis confirmed the inert character of H₂azo and H₂bpdc, while revealing complete conversion, within 30 min, of the active linkers H₂sti and H₂pdac (See Annex 3).

Ozonolysis of Zr-fcu-azo/sti-X% and Zr-fcu-bpdc/pdac-X%. A column of Zr-fcu-azo/sti-X% or Zr-fcu-azo/sti-X% (50 mg to 100 mg) was loaded over a cotton stopper in an L-shaped Pyrex tube. The glass tube was connected to the solid-gas post-synthetic modification setup and purged under vacuum for 5 min. The ozone gas flow (10.4 mmol/h) was passed through the MOF column for 30 min. After 1–2 min, the aqueous potassium iodide solution turned yellow,

indicating the whole MOF column had been exposed to oz1 atm. The recovered Zr-**fcu**-azo/sti-X%_OZ or Zr-**fcu**-bpdc/pdac-X%_OZ samples were further characterized by PXRD and ¹H NMR (see Annex 3).

Acetic Acid Wash.

About 50 mg of Zr-**fcu**-azo/sti-X%_OZ was vortexed for a few seconds in 20 mL of a 0.5 M acetic acid solution in DMF and left at room temperature for 24 h. The supernatant was removed and analyzed by ¹H NMR after decantation. The crystals were washed twice with 20 mL of acetone. The acetone was removed after decantation, and the crystals were dried at 65 °C. The sample purity was verified by PXRD, and the experimental organic content was analyzed by ¹H NMR of the digested samples. Crystals of washed ozonated Zr-**fcu**-azo/sti-X% were then transferred into a glass sorption cell and activated under dynamic vacuum at 85 °C prior to the sorption experiments. Note that the Zr-**fcu**-bpdc/pdac-X% samples did not require this additional treatment to reveal their tuned porosity potential.

HF-Digestion.

Methodology. In a typical procedure, 10 mg of MOF was placed in an Eppendorf tube, to which 120 μL of a 5% aq. HF solution was added. The mixture was sonicated for 15 min, and then the slurry was placed in a 110 °C sand bath inside a fume hood to evaporate overnight. The crude solid samples were highly soluble in DMSO-*d*₆ without any need for addition of acid. Note that attempts with standard digestion methodologies were not successful, even when using the same quantities of HF and solvent. Therefore, the evaporation step is crucial for proper sample digestion. Moreover, the digested solutions obtained with our methodology did not require any specific (e.g., HF-resistant) PTFE NMR tubes.

4.5 Reference

- (1) Subramanian, S.; Zaworotko, M. J. *Angew. Chem., Int. Ed. Engl.* **1995**, *34*, 2127.
- (2) Kondo, M.; Yoshitomi, T.; Matsuzaka, H.; Kitagawa, S.; Seki, K. *Angew. Chem., Int. Ed. Engl.* **1997**, *36*, 1725.
- (3) Li, H.; Eddaoudi, M.; O’Keeffe, M.; Yaghi, O. M. *Nature* **1999**, *402*, 276.
- (4) Eddaoudi, M.; Kim, J.; Rosi, N.; Vodak, D.; Wachter, J.; O’Keeffe, M.; Yaghi, O. M. *Science* **2002**, *295*, 469.
- (5) Chui, S. S. Y.; Lo, S. M. F.; Charmant, J. P. H.; Orpen, A. G.; Williams, I. D. *Science* **1999**, *283*, 1148.
- (6) Themed issue: Metal-Organic Frameworks: *Chem. Soc. Rev.* Zhou, H. C., Kitagawa, S., Eds.; **2014**, *43*, 5415.
- (7) Themed issue: Metal-Organic Frameworks: *Chem. Soc. Rev.* Zhou, H. C., Long, J. R., Yaghi, O. M., Eds.; **2012**, *112*, 673.
- (8) Themed issue: Metal-Organic Frameworks: *Chem. Soc. Rev.* Long, J. R., Yaghi, O. M., Eds.; **2009**, *38*, 1201.
- (9) Suh, M. P.; Park, H. J.; Prasad, T. K.; Lim, D.-W. *Chem. Rev.* **2012**, *112*, 782.
- (10) He, Y.; Zhou, W.; Qian, G.; Chen, B. *Chem. Soc. Rev.* **2014**, *43*, 5657.
- (11) Sumida, K.; Rogow, D. L.; Mason, J. A.; McDonald, T. M.; Bloch, E. D.; Herm, Z. R.; Bae, T.-H.; Long, J. R. *Chem. Rev.* **2012**, *112*, 724.
- (12) Farrusseng, D.; Aguado, S.; Pinel, C. *Angew. Chem., Int. Ed.* **2009**, *48*, 7502.
- (13) Horcajada, P.; Gref, R.; Baati, T.; Allan, P. K.; Maurin, G.; Couvreur, P.; Férey, G.; Morris, R. E.; Serre, C. *Chem. Rev.* **2012**, *112*, 1232.
- (14) de Lange, M. F.; Verouden, K. J. F. M.; Vlugt, T. J. H.; Gascon, J.; Kapteijn, F. *Chem. Rev.* **2015**, *115*, 12205.
- (15) Kreno, L. E.; Leong, K.; Farha, O. K.; Allendorf, M.; Van Duyne, R. P.; Hupp, J. T. *Chem. Rev.* **2012**, *112*, 1105.
- (16) Belmabkhout, Y.; Guillerm, V.; Eddaoudi, M. *Chem. Eng. J.* **2016**, *296*, 386.
- (17) Cohen, S. M. *Chem. Rev.* **2012**, *112*, 970.
- (18) Kim, M.; Cohen, S. M. *CrystEngComm* **2012**, *14*, 4096.
- (19) Bloch, W. M.; Burgun, A.; Coghlan, C. J.; Lee, R.; Coote, M. L.; Doonan, C. J.; Sumby, C. J. *Nat. Chem.* **2014**, *6*, 906.
- (20) Garibay, S. J.; Cohen, S. M. *Chem. Commun.* **2010**, *46*, 7700.

- (21) Yaghi, O. M.; O’Keeffe, M.; Ockwig, N. W.; Chae, H. K.; Eddaoudi, M.; Kim, J. *Nature* **2003**, *423*, 705.
- (22) Chae, H. K.; Eddaoudi, M.; Kim, J.; Hauck, S. I.; Hartwig, J. F.; O’Keeffe, M.; Yaghi, O. M. *J. Am. Chem. Soc.* **2001**, *123*, 11482.
- (23) Eddaoudi, M.; Moler, D. B.; Li, H. L.; Chen, B. L.; Reineke, T. M.; O’Keeffe, M.; Yaghi, O. M. *Acc. Chem. Res.* **2001**, *34*, 319.
- (24) Eddaoudi, M.; Kim, J.; O’Keeffe, M.; Yaghi, O. M. *J. Am. Chem. Soc.* **2002**, *124*, 376.
- (25) Deng, H.; Grunder, S.; Cordova, K. E.; Valente, C.; Furukawa, H.; Hmadeh, M.; Gándara, F.; Whalley, A. C.; Liu, Z.; Asahina, S.; Kazumori, H.; O’Keeffe, M.; Terasaki, O.; Stoddart, J. F.; Yaghi, O. M. *Science* **2012**, *336*, 1018.
- (26) Furukawa, H.; Cordova, K. E.; O’Keeffe, M.; Yaghi, O. M. *Science* **2013**, *341*, 1230444.
- (27) Guillerm, V.; Grancha, T.; Imaz, I.; Juanhuix, J.; MasPOCH, D. *J. Am. Chem. Soc.* **2018**, *140*, 10153.
- (28) Li, P.; Vermeulen, N. A.; Malliakas, C. D.; Gómez-Gualdrón, D. A.; Howarth, A. J.; Mehdi, B. L.; Dohnalkova, A.; Browning, N. D.; O’Keeffe, M.; Farha, O. K. *Science* **2017**, *356*, 624.
- (29) Farha, O. K.; Eryazici, I.; Jeong, N. C.; Hauser, B. G.; Wilmer, C. E.; Sarjeant, A. A.; Snurr, R. Q.; Nguyen, S. T.; Yazaydin, A. O.; Hu p, J. T. *J. Am. Chem. Soc.* **2012**, *134*, 15016.
- (30) Férey, G.; Mellot-Draznieks, C.; Serre, C.; Millange, F.; Dutour, J.; Surblé, S.; Margiolaki, I. *Science* **2005**, *309*, 2040.
- (31) Guillerm, V.; Weseliński, Ł. J.; Belmabkhout, Y.; Cairns, A. J.; D’Elia, V.; Wojtas, Ł.; Adil, K.; Eddaoudi, M. *Nat. Chem.* **2014**, *6*, 673.
- (32) Seki, K.; Takamizawa, S.; Mori, W. *Chem. Lett.* **2001**, *30*, 332.
- (33) Nugent, P.; Belmabkhout, Y.; Burd, S. D.; Cairns, A. J.; Luebke, R.; Forrest, K.; Pham, T.; Ma, S.; Space, B.; Wojtas, Ł.; Eddaoudi, M.; Zaworotko, M. J. *Nature* **2013**, *49*, 580.
- (34) Sun, D.; Ma, S.; Ke, Y.; Collins, D. J.; Zhou, H.-C. *J. Am. Chem. Soc.* **2006**, *128*, 3896.
- (35) Cavka, J. H.; Jakobsen, S.; Olsbye, U.; Guillou, N.; Lamberti, C.; Bordiga, S.; Lillerud, K. P. *J. Am. Chem. Soc.* **2008**, *130*, 13850.
- (36) Schaate, A.; Roy, P.; Godt, A.; Lippke, J.; Waltz, F.; Wiebcke, M.; Behrens, P. *Chem. - Eur. J.* **2011**, *17*, 6643.
- (37) Serre, C.; Mellot-Draznieks, C.; Surblé, S.; Audebrand, N.; Filinchuk, Y.; Férey, G. *Science* **2007**, *315*, 1828.

- (38) Dan-Hardi, M.; Chevreau, H.; Devic, T.; Horcajada, P.; Maurin, G.; Férey, G.; Popov, D.; Riekkel, C.; Wuttke, S.; Lavalley, J.-C.; Vimont, A.; Boudewijns, T.; de Vos, D.; Serre, C. *Chem. Mater.* **2012**, *24* (13), 2486–2492.
- (39) Eubank, J. F.; Nouar, F.; Luebke, R.; Cairns, A. J.; Wojtas, L.; Alkordi, M.; Bousquet, T.; Hight, M. R.; Eckert, J.; Embs, J. P.; Georgiev, P. A.; Eddaoudi, M. *Angew. Chem., Int. Ed.* **2012**, *51*, 10099.
- (40) Sonnauer, A.; Hoffmann, F.; Froeba, M.; Kienle, L.; Duppel, V.; Thommes, M.; Serre, C.; Férey, G.; Stock, N. *Angew. Chem., Int. Ed.* **2009**, *48*, 3791.
- (41) Koh, K.; Wong-Foy, A. G.; Matzger, A. J. *Angew. Chem., Int. Ed.* **2008**, *47*, 677.
- (42) Feng, D.; Wang, K.; Su, J.; Liu, T.-F.; Park, J.; Wei, Z.; Bosch, M.; Yakovenko, A.; Zou, X.; Zhou, H.-C. *Angew. Chem., Int. Ed.* **2015**, *54*, 149.
- (43) Serra-Crespo, P.; Ramos-Fernandez, E. V.; Gascon, J.; Kapteijn, F. *Chem. Mater.* **2011**, *23*, 2565.
- (44) Feng, L.; Yuan, S.; Zhang, L.-L.; Tan, K.; Li, J.-L.; Kirchon, A.; Liu, L.-M.; Zhang, P.; Han, Y.; Chabal, Y. J.; Zhou, H.-C. *J. Am. Chem. Soc.* **2018**, *140*, 2363.
- (45) Cliffe, M. J.; Wan, W.; Zou, X.; Chater, P. A.; Kleppe, A. K.; Tucker, M. G.; Wilhelm, H.; Funnell, N. P.; Coudert, F.-X.; Goodwin, A. L. *Nat. Commun.* **2014**, *5*, 4176.
- (46) Bunck, D. N.; Dichtel, W. R. *Chem. -Eur. J.* **2013**, *19*, 818.
- (47) Park, J.; Wang, Z. U.; Sun, L.-B.; Chen, Y.-P.; Zhou, H.-C. *J. Am. Chem. Soc.* **2012**, *134*, 20110.
- (48) Choi, K. M.; Jeon, H. J.; Kang, J. K.; Yaghi, O. M. *J. Am. Chem. Soc.* **2011**, *133*, 11920.
- (49) Yuan, S.; Zou, L.; Qin, J.-S.; Li, J.; Huang, L.; Feng, L.; Wang, X.; Bosch, M.; Alsalme, A.; Cagin, T.; Zhou, H.-C. *Nat. Commun.* **2017**, *8*, 15356.
- (50) Fang, Z.; Bueken, B.; De Vos, D. E.; Fischer, R. A. *Angew. Chem., Int. Ed.* **2015**, *54*, 7234.
- (51) Bradshaw, D.; El-Hankari, S.; Lupica-Spagnolo, L. *Chem. Soc. Rev.* **2014**, *43*, 5431.
- (52) Liang, W.; Coghlan, C. J.; Ragon, F.; Rubio-Martinez, M.; D'Alessandro, D. M.; Babarao, R. *Dalton Trans.* **2016**, *45*, 4496.
- (53) Wißmann, G.; Schaate, A.; Lilienthal, S.; Bremer, I.; Schneider, A. M.; Behrens, P. *Microporous Mesoporous Mater.* **2012**, *152*, 64.
- (54) Gutov, O. V.; Molina, S.; Escudero-Adán, E. C.; Shafir, A. *Chem. - Eur. J.* **2016**, *22*, 13582.
- (55) Marshall, R. J.; Hobday, C. L.; Murphie, C. F.; Griffin, S. L.; Morrison, C. A.; Moggach, S. A.; Forgan, R. S. *J. Mater. Chem. A* **2016**, *4*, 6955.

- (56) Øien, S.; Wragg, D.; Reinsch, H.; Svelle, S.; Bordiga, S.; Lamberti, C.; Lillerud, K. P. *Cryst. Growth Des.* **2014**, *14*, 5370.
- (57) Trickett, C. A.; Gagnon, K. J.; Lee, S.; Gándara, F.; Bügi, H.-B.; Yaghi, O. M. *Angew. Chem., Int. Ed.* **2015**, *54*, 11162.
- (58) Yue, Y.; Qiao, Z.-A.; Fulvio, P. F.; Binder, A. J.; Tian, C.; Chen, J.; Nelson, K. M.; Zhu, X.; Dai, S. *J. Am. Chem. Soc.* **2013**, *135*, 9572.
- (59) Yue, Y.; Fulvio, P. F.; Dai, S. *Acc. Chem. Res.* **2015**, *48*, 3044.
- (60) Sun, L.-B.; Li, J.-R.; Park, J.; Zhou, H.-C. *J. Am. Chem. Soc.* **2012**, *134*, 126.
- (61) Huang, H.; Li, J.-R.; Wang, K.; Han, T.; Tong, M.; Li, L.; Xie, Y.; Yang, Q.; Liu, D.; Zhong, C. *Nat. Commun.* **2015**, *6*, 8847.
- (62) Qiu, L.-G.; Xu, T.; Li, Z.-Q.; Wang, W.; Wu, Y.; Jiang, X.; Tian, X.-Y.; Zhang, L.-D. *Angew. Chem., Int. Ed.* **2008**, *47*, 9487.
- (63) Zhao, Y.; Zhang, J.; Han, B.; Song, J.; Li, J.; Wang, Q. *Angew. Chem., Int. Ed.* **2011**, *50*, 636.
- (64) Cao, S.; Gody, G.; Zhao, W.; Perrier, S.; Peng, X.; Ducati, C.; Zhao, D.; Cheetham, A. K. *Chem. Sci.* **2013**, *4*, 3573.
- (65) Wee, L. H.; Wiktor, C.; Turner, S.; Vanderlinden, W.; Janssens, N.; Bajpe, S. R.; Houthoofd, K.; Van Tendeloo, G.; De Feyter, S.; Kirschhock, C. E. A.; Martens, J. A. *J. Am. Chem. Soc.* **2012**, *134*, 10911.
- (66) Shen, K.; Zhang, L.; Chen, X.; Liu, L.; Zhang, D.; Han, Y.; Chen, J.; Long, J.; Luque, R.; Li, Y.; Chen, B. *Science* **2018**, *359*, 206.
- (67) Albalad, J.; Xu, H.; Gándara, F.; Haouas, M.; Martineau-Corcós, C.; Mas-Ballesté, R.; Barnett, S. A.; Juanhuix, J.; Imaz, I.; MasPOCH, D. *J. Am. Chem. Soc.* **2018**, *140*, 2028.
- (68) Geletneky, C.; Berger, S. *Eur. J. Org. Chem.* **1998**, *1998*, 1625.
- (69) Criegee, R. *Angew. Chem., Int. Ed. Engl.* **1975**, *14*, 745.
- (70) Deng, H.; Doonan, C. J.; Furukawa, H.; Ferreira, R. B.; Towne, J.; Knobler, C. B.; Wang, B.; Yaghi, O. M. *Science* **2010**, *327*, 846.
- (71) Marshall, R. J.; Forgan, R. S. *Eur. J. Inorg. Chem.* **2016**, *2016*, 4310.
- (72) Ragon, F.; Campo, B.; Yang, Q.; Martineau, C.; Wiersum, A. D.; Lago, A.; Guillerm, V.; Hemsley, C.; Eubank, J. F.; Vishnuvarthan, M.; Taulelle, F.; Horcajada, P.; Vimont, A.; Llewellyn, P. L.; Daturi, M.; Devautour-Vinot, S.; Maurin, G.; Serre, C.; Devic, T.; Clet, G. *J. Mater. Chem. A* **2015**, *3*, 3294.

- (73) Yang, Q.; Guillerm, V.; Ragon, F.; Wiersum, A. D.; Llewellyn, P. L.; Zhong, C.; Devic, T.; Serre, C.; Maurin, G. *Chem. Commun.* **2012**, *48*, 9831.
- (74) Hobday, C. L.; Marshall, R. J.; Murphie, C. F.; Sotelo, J.; Richards, T.; Allan, D. R.; Dü en, T.; Coudert, F.-X.; Forgan, R. S.; Morrison, C. A.; Moggach, S. A.; Bennett, T. D. *Angew. Chem., Int. Ed.* **2016**, *55*, 2401.
- (75) Marshall, R. J.; Richards, T.; Hobday, C. L.; Murphie, C. F.; Wilson, C.; Moggach, S. A.; Bennett, T. D.; Forgan, R. S. *Dalton Trans.* **2016**, *45*, 4132.
- (76) Dubinin, M. M.; Zaverina, E. D.; Radushkevich, L. V.; Sorbtsiya, I. *Zh. Fiz. Khim.* **1947**, *21*, 1351.
- (77) Avci, C.; Ariñez-Soriano, J.; Carné-Sánchez, A.; Guillerm, V.; Carbonell, C.; Imaz, I.; Maspoch, D. *Angew. Chem., Int. Ed.* **2015**, *54*, 14417.
- (78) Guillerm, V.; Ragon, F.; Dan-Hardi, M.; Devic, T.; Vishnuvarthan, M.; Campo, B.; Vimont, A.; Clet, G.; Yang, Q.; Maurin, G.; Férey, G.; Vittadini, A.; Gross, S.; Serre, C. *Angew. Chem., Int. Ed.* **2012**, *51*, 9267.
- (79) Gomez-Gualdron, D. A.; Gutov, O. V.; Krungleviciute, V.; Borah, B.; Mondloch, J. E.; Hupp, J. T.; Yildirim, T.; Farha, O. K.; Snurr, R. Q. *Chem. Mater.* **2014**, *26*, 5632.

Conclusions

The efforts of this Thesis were dedicated to develop a novel post-synthetic method based on solid-gas ozonolysis for the functionalization of MOFs.

Firstly, we have successfully established a new set-up for suitably practicing the solid-gas ozonolysis reaction in efficient and safe ways. With the new set-up, a solvent-less, solid-gas, single-crystal-to-single-crystal, post-synthetic functionalization of a MOF using ozone was achieved. Streaming of ozone gas through an olefin tagged UiO-66-type MOF at $-78\text{ }^{\circ}\text{C}$ provided quantitative transformation of the olefins into 1,2,4-trioxolane rings inside the robust MOF framework. When confined inside the MOF pores, this ring proved to be stable under standard heat and vacuum conditions for MOF activation, unlike in solution. Finally, an optimized workup enabled further single-crystal-to single-crystal chemistry on these 1,2,4-trioxolane rings: reduction into the corresponding aldehyde or oxidation to the corresponding carboxylic acids, the latter in quantitative yield. We are confident that our methodology will offer new insight into how gas molecules might be exploited for MOF chemistry that transcends common physisorption phenomena.

Once the potential of the solid-gas post-synthetic method has been demonstrated, we explored to extend its capabilities to construct hierarchically porous MOFs. To this end, we developed a selective and quantitative method for post-synthetic modification of MOF porosity via ozonolysis. Through removal of organic ligands, our approach causes micropores to fuse into larger (mesoscale) pores in a controlled fashion and without any loss in total porosity. It selectively breaks the olefin bonds in organic ligands without affecting other organic moieties and can be applied for short reaction times (ca. 30 min) under mild conditions (room temperature). Moreover, we have demonstrated that ozonolysis can be used as a novel tool to selectively remove, and recover, specific fragments of molecules/frameworks through solid-gas manipulation.

Annex 1

Optimized structures in Chapter 3

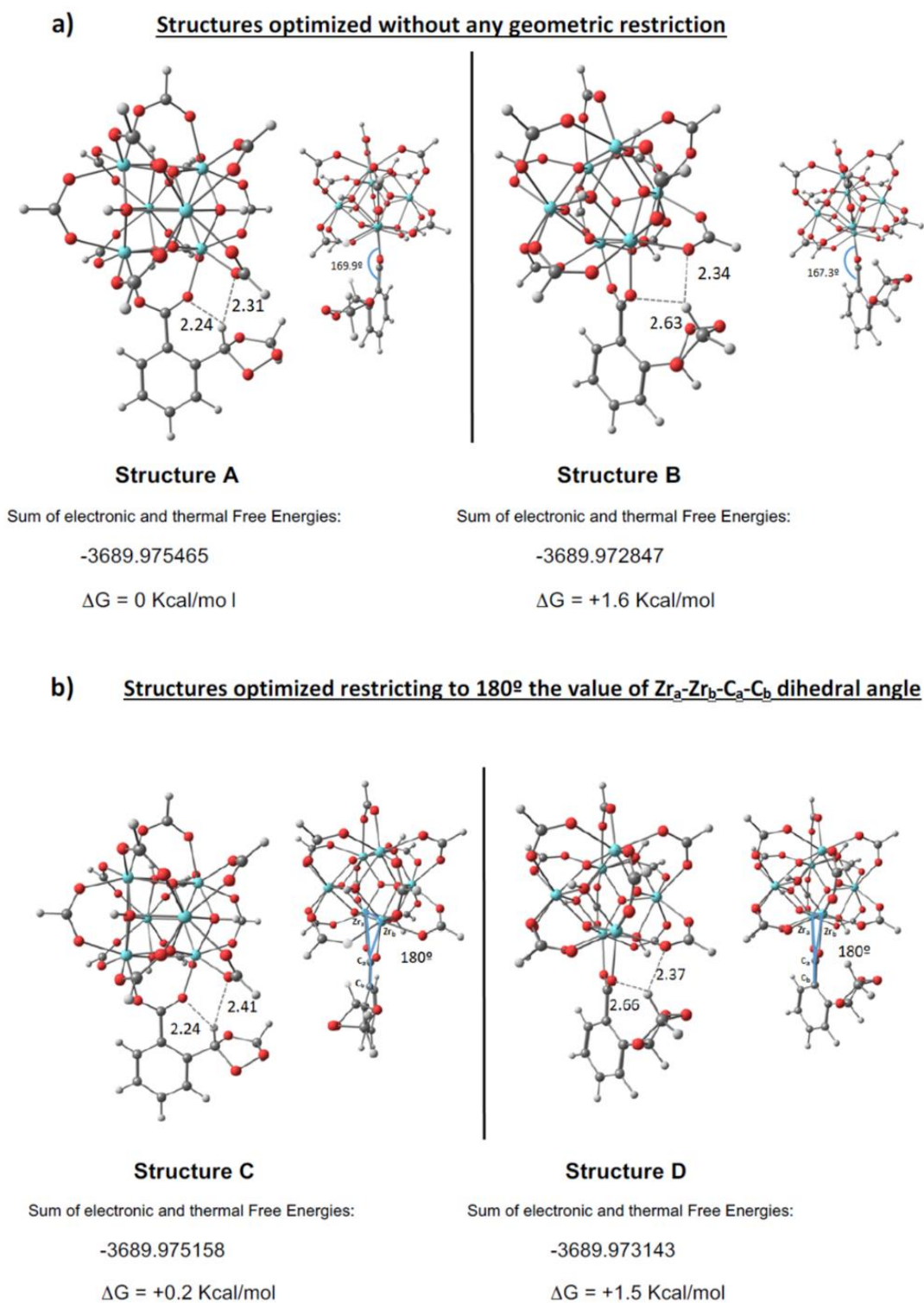


Figure 1. Optimized structures a) without and b) with geometric restriction

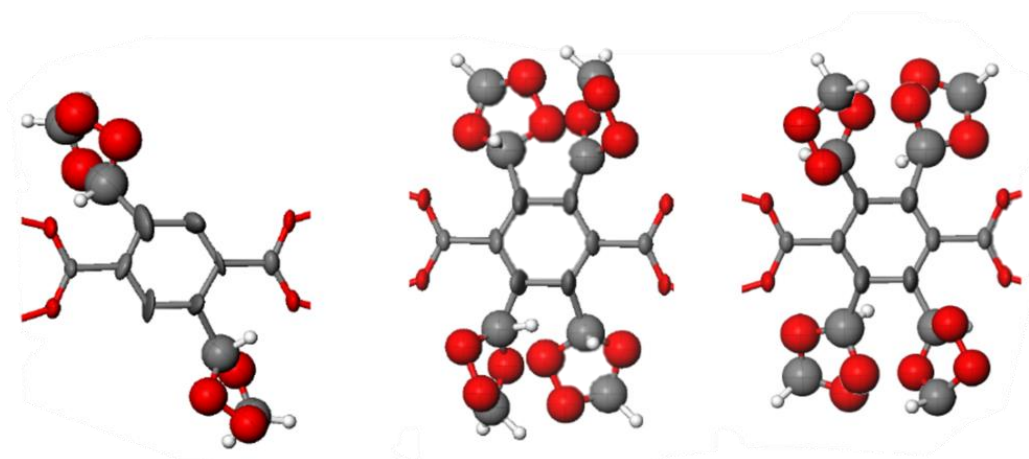


Figure 2. ORTEP drawing of **ozo-BDC** linker as found in the crystal structure of **ozo-ZrBDC**.

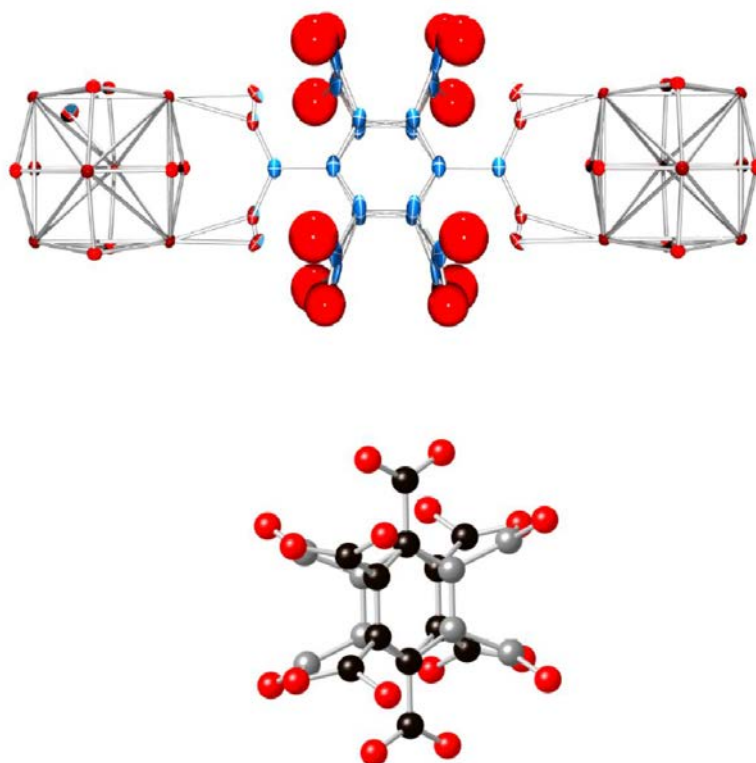


Figure 3. Top: ORTEP drawing BDC-COOH linker as found in the crystal structure of ZrBDC-COOH after oxidative work up, showing the disorder of the phenyl ring and the carboxylic group. Bottom: Disorder model in the organic linker in ZrBDC-COOH: Two orientations are defined for the phenyl ring and the corresponding pending carboxylate C atom, represented in black and grey color, respectively. The position of one of the oxygen atoms of the pending carboxylate groups is shared for the two possible orientations.

Squeeze details of Ozo-ZrBDC:

Summary and Remarks: N = NOTE, W = WARNING, E = ERROR

N: Maximum Residue Number Reduced (Round ARU to 0.1 units)

N: No S.U.'s (esd) on observed/calculated parameters.

N: Maximum allowed number of residues reduced

N: DISORDERED structure - ATOMS with Pop. .LT. 1.0 are not moved or as a group.

N: No-Hydrogen atoms in this structure

N: Number of moved primary input atoms: 9

W: Number of (Carbon) Atoms with no sp(x) assignment 1

N: Number of Ignored Lines on INPUT 4

of which blank in column 1 4

N: Number of modified (= #) ATOM labels 2

W: Number of unusual anisotropic displacement parameters 1

N: Total Potential Solvent Accessible Void Vol (SOLV-Map Value) ... 3466 Ang³

N: Electron Count Voids / Cell = 657

Annex 2

Spectroscopic characterization and sorption isotherms in Chapter 4

Table 1. Additional details for the synthesis of Zr-fcu-azo/sti-X%

Material	ZrCl ₄		H ₂ azo		H ₂ sti		% mol azo theo	% mol sti theo	% mol azo exp	% mol sti exp	Proline		HCl		DMF
	mmol	mg	mmol	mg	mmol	mg					mmol	mg	mmol	μL	mL
Zr-fcu-azo	0.45	105	0.44	120	0	0	100 %	0 %	100 %	0 %	2.17	250	0.54	45	15
Zr-fcu-azo/sti-10%	0.45	105	0.40	108	0.04	12	90 %	20 %	90 %	10 %	2.17	250	0.54	45	15
Zr-fcu-azo/sti-20%	0.45	105	0.36	96	0.09	24	80 %	20 %	79 %	21 %	2.17	250	0.54	45	15
Zr-fcu-azo/sti-30%	0.45	105	0.31	84	0.13	36	70 %	30 %	70 %	30 %	2.17	250	0.54	45	15
Zr-fcu-azo/sti-40%	0.45	105	0.27	72	0.18	48	60 %	40 %	59 %	41 %	2.17	250	0.54	45	15
Zr-fcu-azo/sti-50%	0.45	105	0.22	60	0.22	60	50 %	50 %	49 %	51 %	2.17	250	0.54	45	15
Zr-fcu-azo/sti-60%	0.45	105	0.18	48	0.26	72	40 %	60 %	38 %	62 %	2.17	250	0.54	45	15
Zr-fcu-sti	0.45	105	0	0	0.44	120	0 %	100 %	0 %	100 %	2.17	250	0.54	45	15

Synthesis time	12 h
Synthesis temperature	120 °C

Table 2. Additional details for the synthesis of Zr-fcu-bpdc/pdac-X%

Material	ZrCl ₄		H ₂ bpdc		H ₂ pdac		% mol bpdc theo	% mol pdac theo	% mol bpdc exp	% mol pdac exp	tfa	DMF
	mmol	mg	mmol	mg	mmol	mg					mL	mL
Zr-fcu-bpdc (UiO-67)	0.86	200	0.37	90	0	0	100 %	0 %	100 %	0 %	1	10
Zr-fcu-bpdc/pdac-10%	0.86	200	0.28	67.5	0.08	20.3	77 %	23 %	88 %	12 %	1	10
Zr-fcu-bpdc/pdac-20%	0.86	200	0.22	54	0.13	32.4	63 %	37 %	81 %	19 %	1	10
Zr-fcu-bpdc/pdac-30%	0.86	200	0.20	49.5	0.15	36.5	58 %	42 %	73 %	27 %	1	10
Zr-fcu-bpdc/pdac-40%	0.86	200	0.15	36	0.20	48.6	43 %	57 %	58 %	42 %	1	10
Zr-fcu-pdac (NU-801)	0.86	200	0	0	0.33	81	0 %	100 %	0 %	100 %	1	10

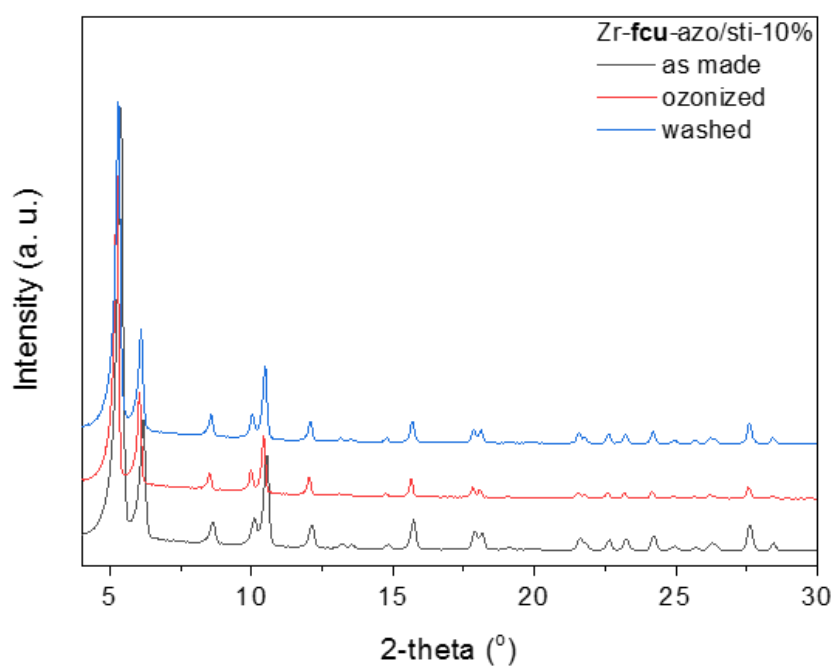
Synthesis time	72 h
Synthesis temperature	120 °C

Table 3. Organic ligand content from ¹H NMR for Zr-fcu-azo/sti-X%.

Material	% mol azo exp	% mol sti exp
Zr-fcu-azo	100	0
Zr-fcu-azo/sti-10%	90	10
Zr-fcu-azo/sti-20%	79	21
Zr-fcu-azo/sti-30%	70	30
Zr-fcu-azo/sti-40%	59	41
Zr-fcu-azo/sti-50%	49	51
Zr-fcu-azo/sti-60%	38	62
Zr-fcu-sti	0	100

Table 4. Organic moieties content from ^1H NMR for Zr-fcu-bpdc/pdac-X%.

Material	% mol bpdc	% mol pdac
Zr-fcu-bpdc (UiO-67)	100	0
Zr-fcu-bpdc/pdac-10%	77	23
Zr-fcu-bpdc/pdac-20%	63	38
Zr-fcu-bpdc/pdac-30%	58	42
Zr-fcu-bpdc/pdac-40%	43	57
Zr-fcu-pdac (NU-801)	0	100

**Figure 3.** PXRD diagram ($\lambda_{\text{Cu}} = 1.5406 \text{ \AA}$) of as made, ozonized and washed Zr-fcu-azo/sti-10% in grey, red and blue, respectively.

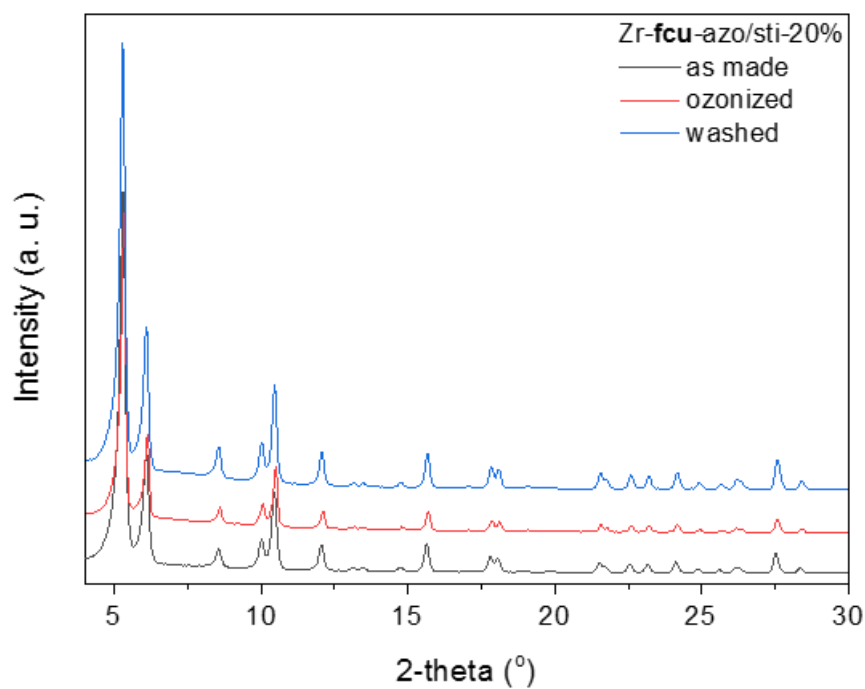


Figure 4. PXRD diagram ($\lambda_{\text{Cu}} = 1.5406 \text{ \AA}$) of as made, ozonized and washed Zr-fcu-azo/sti-20% in grey, red and blue, respectively.

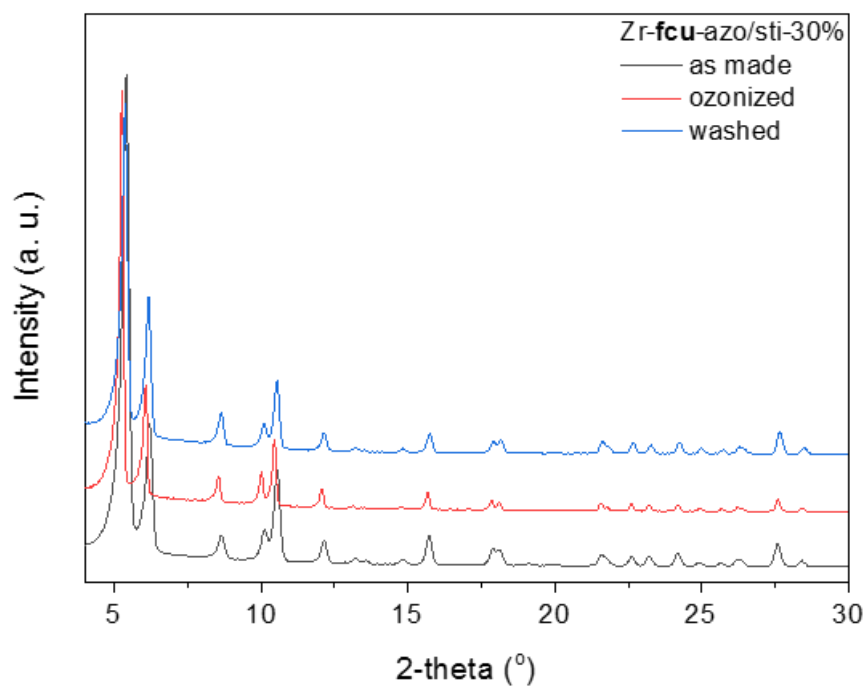


Figure 5. PXRD diagram ($\lambda_{\text{Cu}} = 1.5406 \text{ \AA}$) of as made, ozonized and washed Zr-fcu-azo/sti-30% in grey, red and blue, respectively.

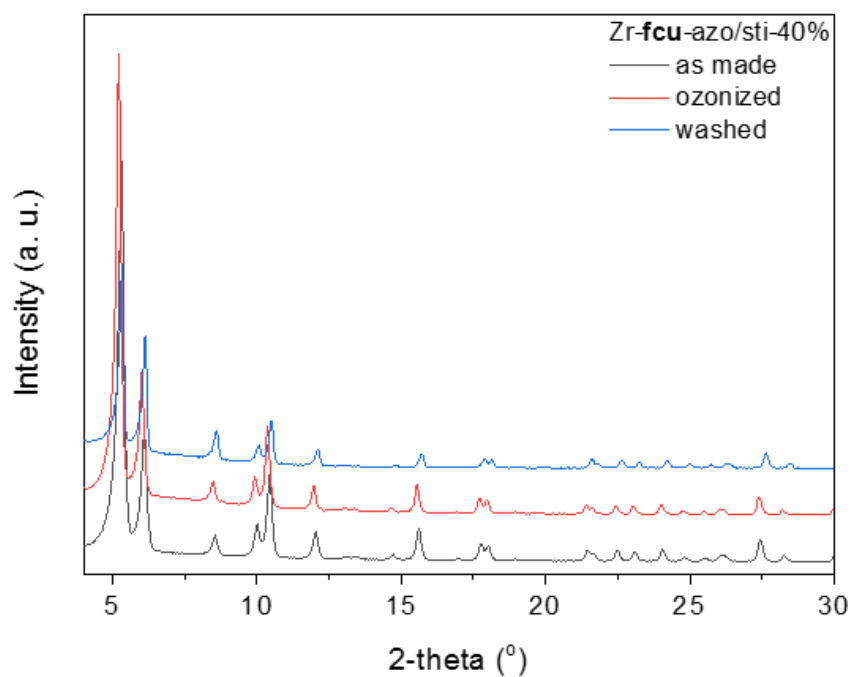


Figure 6. PXR diagram ($\lambda_{\text{Cu}} = 1.5406 \text{ \AA}$) of as made, ozonized and washed Zr-fcu-azo/sti-40% in grey, red and blue, respectively.

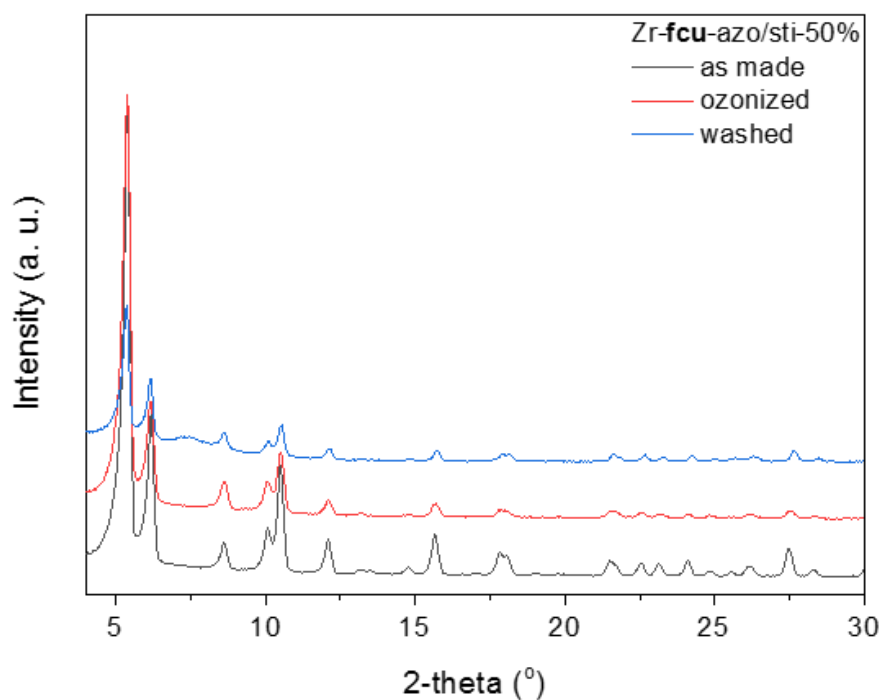


Figure 7. PXR diagram ($\lambda_{\text{Cu}} = 1.5406 \text{ \AA}$) of as made, ozonized and washed Zr-fcu-azo/sti-50% in grey, red and blue, respectively.

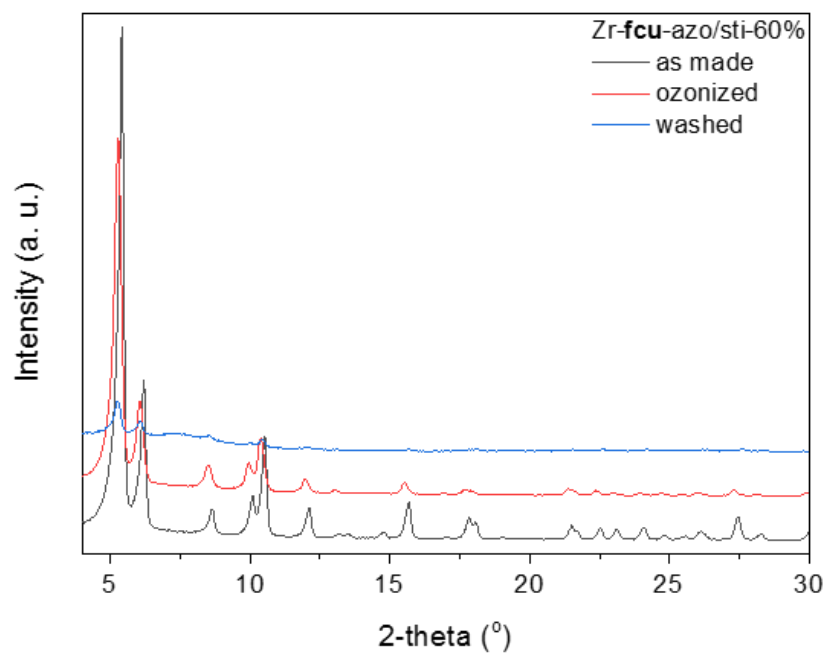


Figure 8. PXRD diagram ($\lambda_{\text{Cu}} = 1.5406 \text{ \AA}$) of as made, ozonized and washed Zr-fcu-azo/sti-60% in grey, red and blue, respectively.

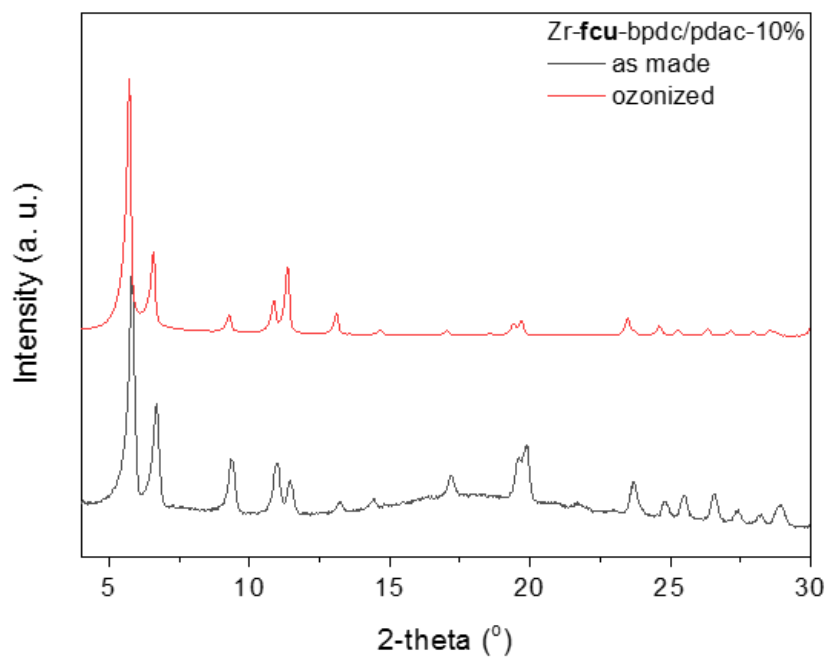


Figure 9. PXRD diagram ($\lambda_{\text{Cu}} = 1.5406 \text{ \AA}$) of as made and ozonized Zr-fcu-bpdc/pdac-10% in grey and red, respectively.

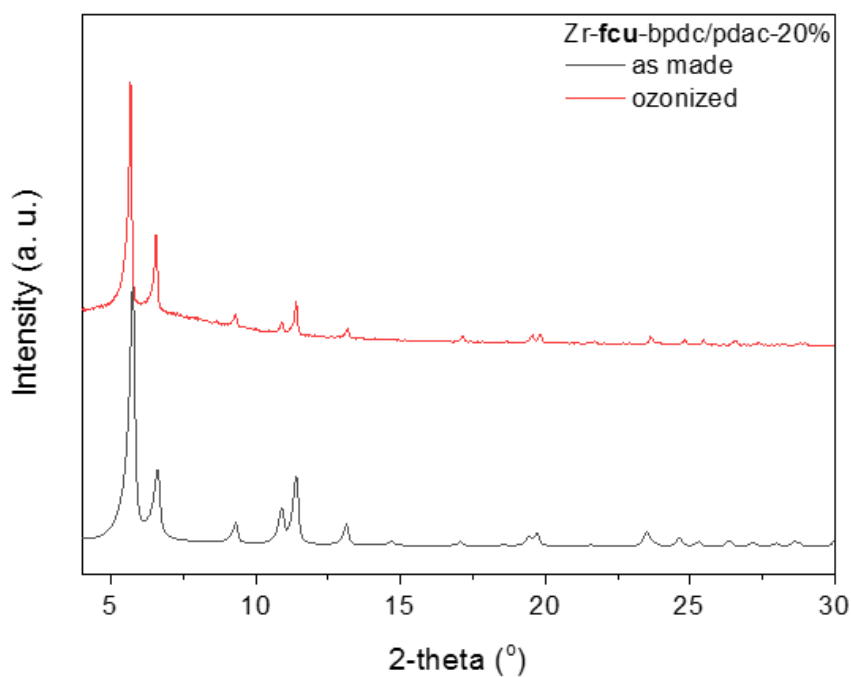


Figure 10. PXRD diagram ($\lambda_{\text{Cu}} = 1.5406 \text{ \AA}$) of as made and ozonized Zr-fcu-bpdc/pdac-20% in grey and red, respectively.

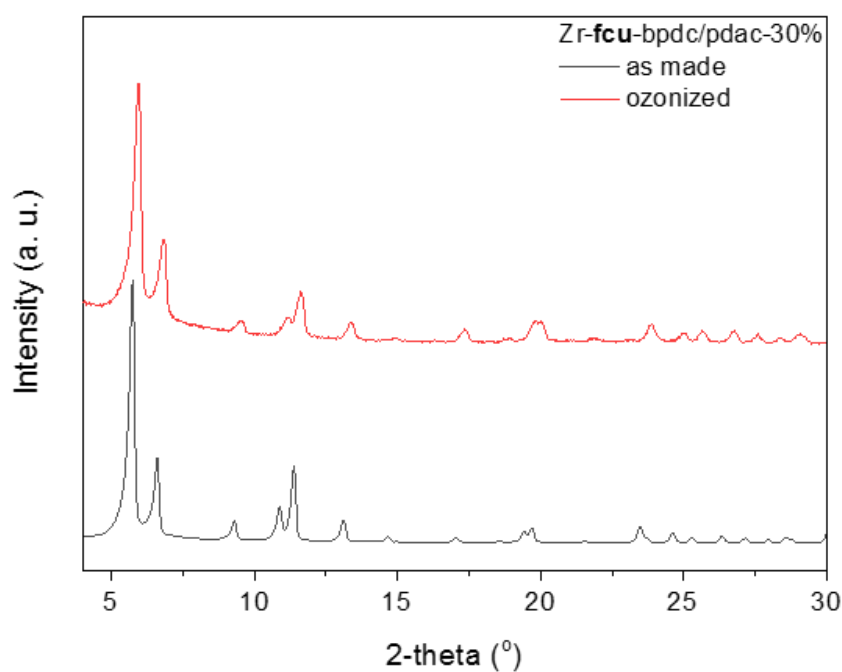


Figure 11. PXRD diagram ($\lambda_{\text{Cu}} = 1.5406 \text{ \AA}$) of as made and ozonized Zr-fcu-bpdc/pdac-30% in grey and red, respectively.

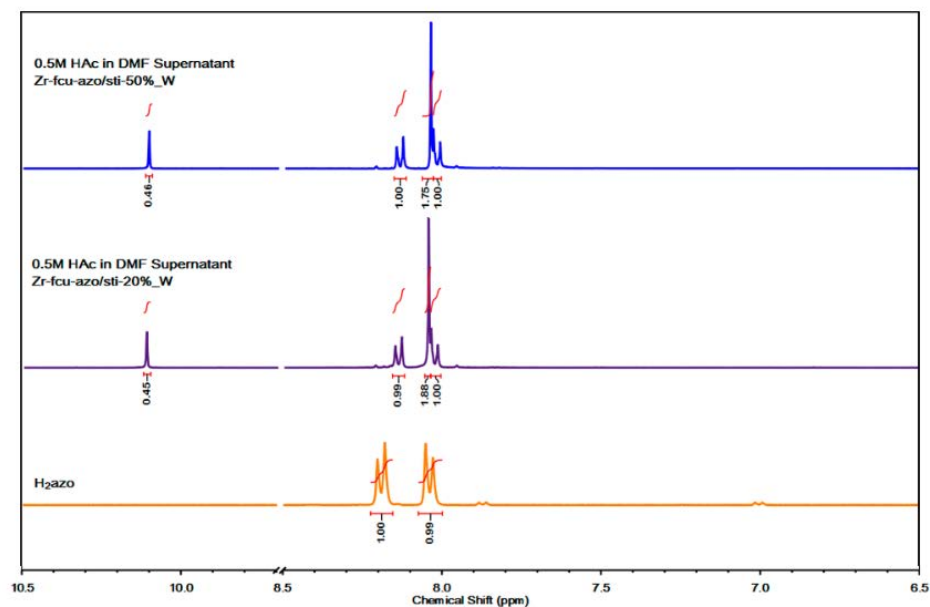


Figure 12. ^1H NMR spectra of washing solution (0.5 M acetic acid in DMF) of Zr-**fcu**-azo/sti-20% and Zr-**fcu**-azo/sti-50% showing the presence of fba and bdc.

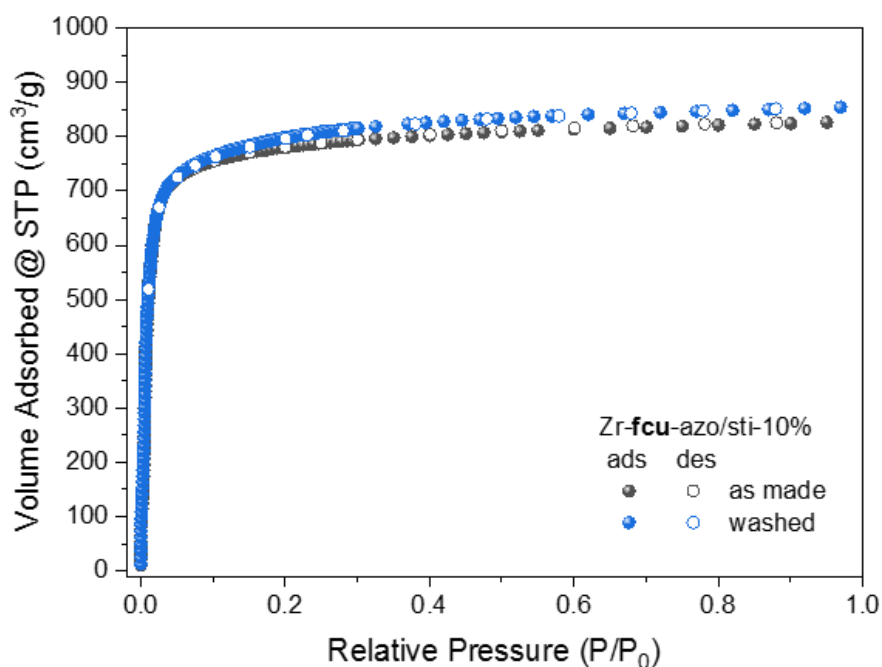


Figure 13. N_2 sorption isotherms (77 K) of as made and ozonized-washed Zr-**fcu**-azo/sti-10% in grey and blue, respectively.

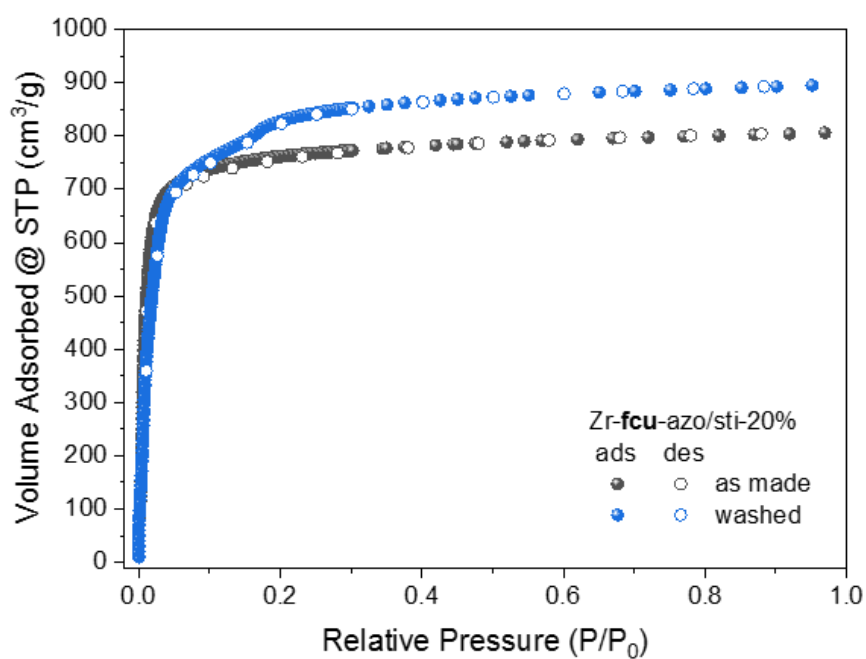


Figure 14. N₂ sorption isotherms (77 K) of as made and ozonized-washed Zr-fcu-azo/sti-20% in grey and blue, respectively.

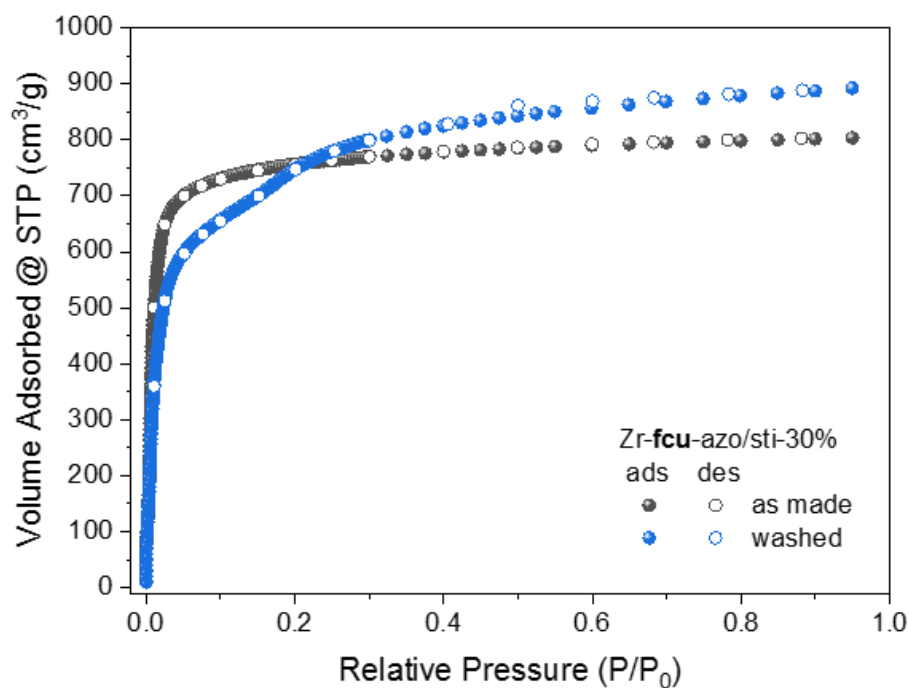


Figure 15. N₂ sorption isotherms (77 K) of as made and ozonized-washed Zr-fcu-azo/sti-30% in grey and blue, respectively.

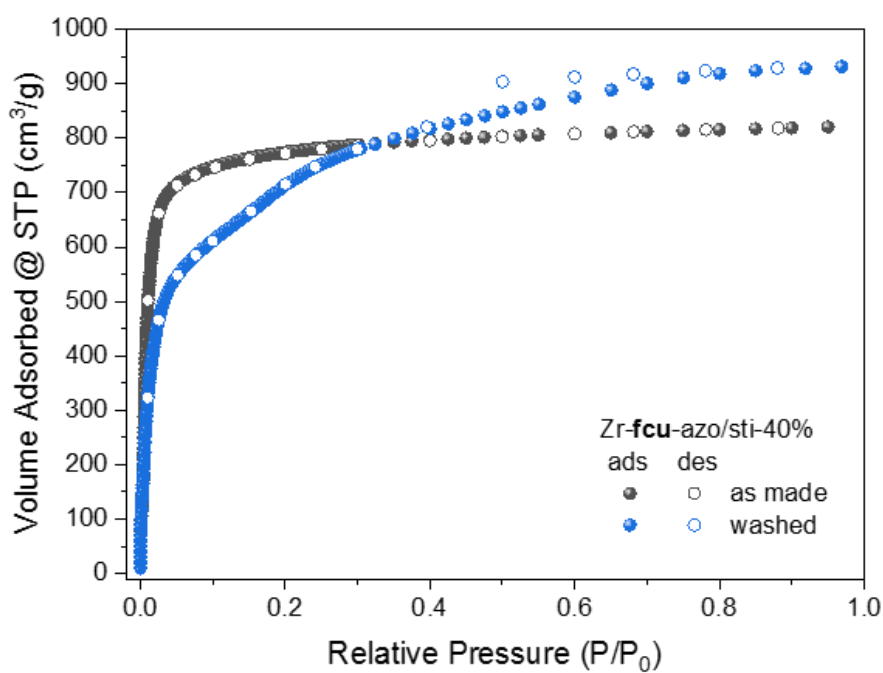


Figure 16. N₂ sorption isotherms (77 K) of as made and ozonized-washed Zr-fcu-azo/sti-40% in grey and blue, respectively.

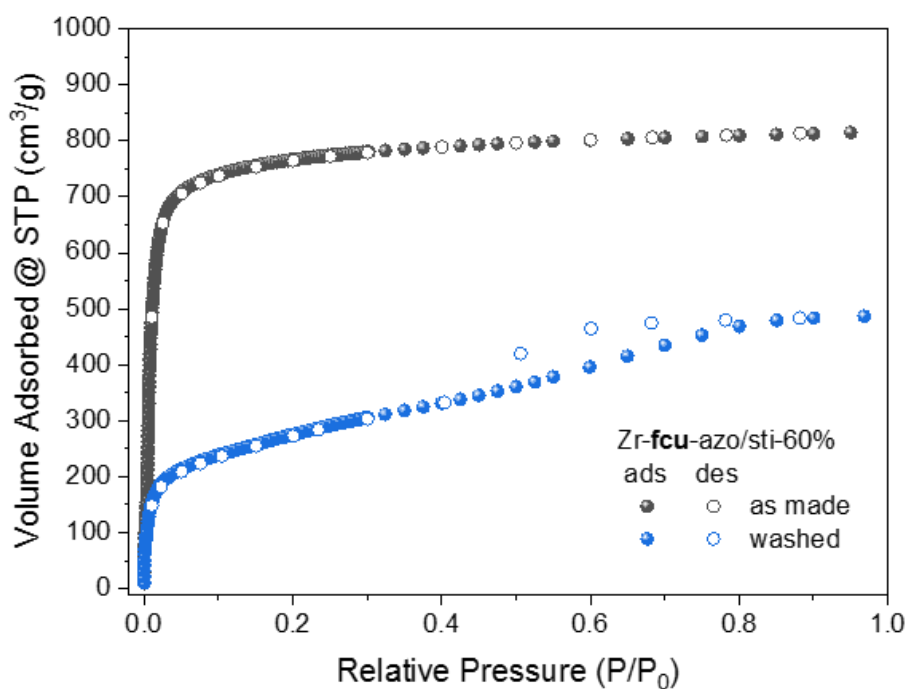


Figure 17. N₂ sorption isotherms (77 K) of as made and ozonized-washed Zr-fcu-azo/sti-60% in grey and blue, respectively.

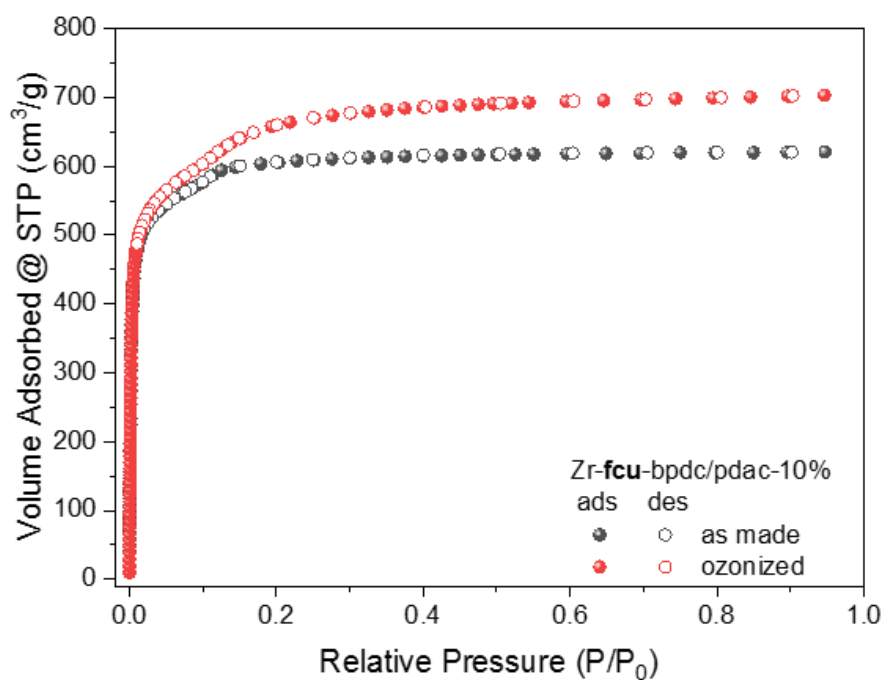


Figure 18. N₂ sorption isotherms (77 K) of as made and ozonized Zr-fcu-bpdc/pdac-10% in grey and red, respectively.

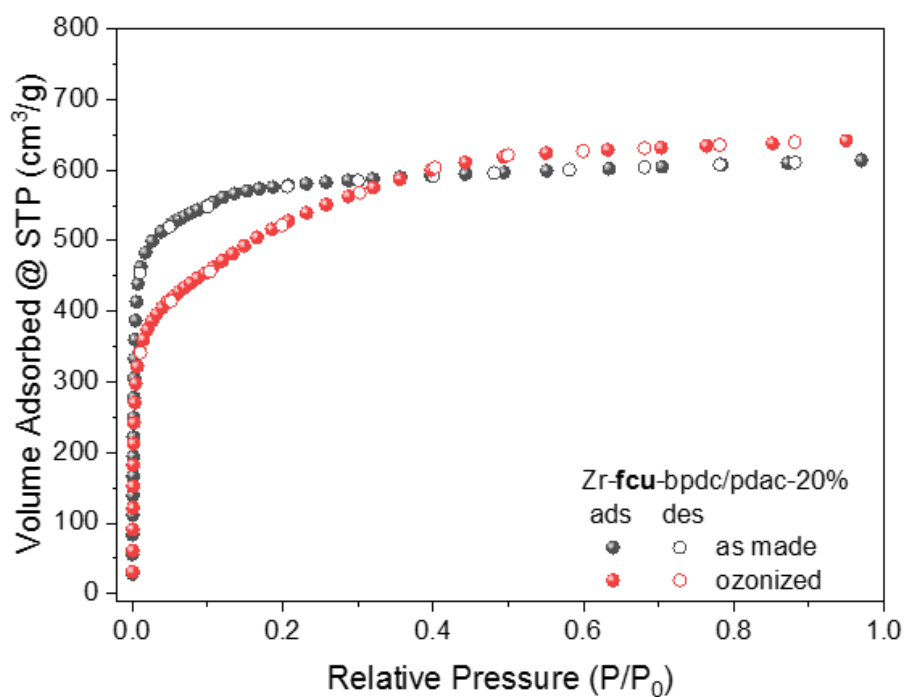


Figure 19. N₂ sorption isotherms (77 K) of as made and ozonized Zr-fcu-bpdc/pdac-20% in grey and red, respectively.

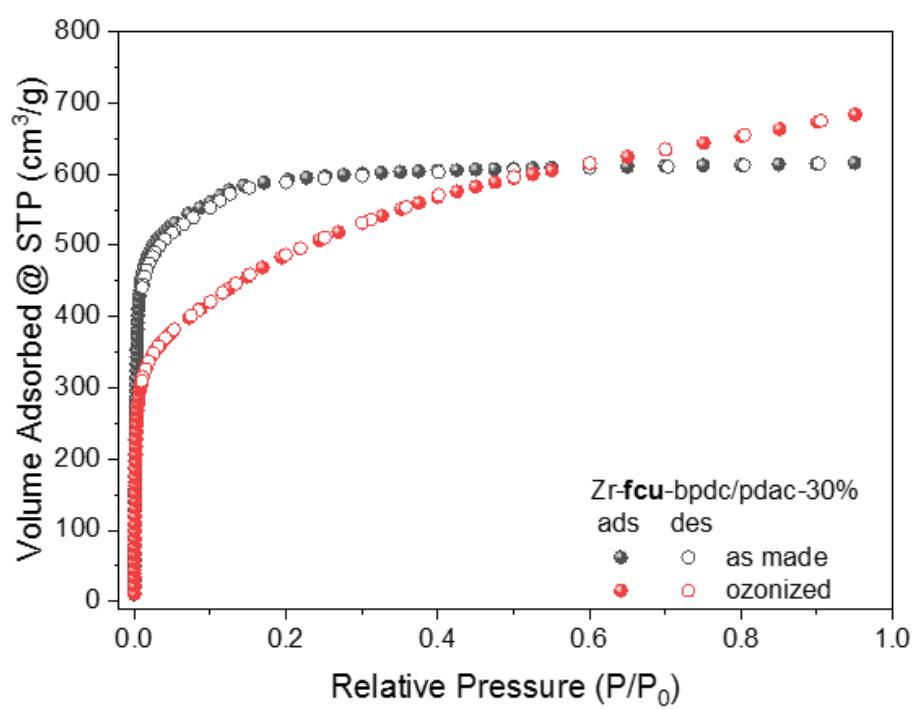


Figure 20. N₂ sorption isotherms (77 K) of as made and ozonized Zr-fcu-bpdc/pdac-30% in grey and red, respectively.

Single-Crystal-to-Single-Crystal Postsynthetic Modification of a Metal–Organic Framework via Ozonolysis

Jorge Albalad,^{†,‡} Heng Xu,^{†,‡} Felipe Gándara,^{‡,§} Mohamed Haouas,[§] Charlotte Martineau-Corcós,^{§,||} Rubén Mas-Balleste,^{‡,¶} Sarah A. Barnett,[⊥] Judith Juanhuix,[¶] Inhar Imaz,^{*,†,Ⓢ} and Daniel Maspoch^{*,†,Ⓢ}

[†]Catalan Institute of Nanoscience and Nanotechnology (ICN2), CSIC and The Barcelona Institute of Science and Technology, Campus UAB, Bellaterra, 08193 Barcelona, Spain

[‡]Materials Science Factory, Instituto de Ciencia de Materiales de Madrid (ICMM), Consejo Superior de Investigaciones Científicas (CSIC), Calle Sor Juana Inés de la Cruz, 3, 28049 Madrid, Spain

[§]Institut Lavoisier de Versailles, CNRS, UVSQ, Université Paris-Saclay, 45 Avenue des Etats-Unis, 78035 Versailles Cedex, France

^{||}CNRS, CEMHTI UPR3079, Université d'Orléans, F-45071 Orléans, France

[¶]Inorganic Chemistry Department, Universidad Autónoma de Madrid, Madrid 28049, Spain

[⊥]Diamond Light Source, Harwell Science and Innovation Campus, Didcot, Oxfordshire OX11 0DE, United Kingdom

[¶]ALBA Synchrotron, Cerdanyola del Vallès, 08290 Barcelona, Spain

[Ⓢ]ICREA, Pg. Lluís Companys 23, 08010 Barcelona, Spain

Supporting Information

ABSTRACT: We describe solid–gas phase, single-crystal-to-single-crystal, postsynthetic modifications of a metal–organic framework (MOF). Using ozone, we quantitatively transformed the olefin groups of a UiO-66-type MOF into 1,2,4-trioxolane rings, which we then selectively converted into either aldehydes or carboxylic acids.

Metal–organic frameworks (MOFs) are crystalline materials that comprise organic linkers and metal ions/clusters. For the past two decades, they have attracted attention for their exceptional porosity and structural diversity.¹ Beyond their inherent crystallinity and porosity, MOFs are an ideal platform for applications that entail incorporation of target chemical functionalities onto their pore walls.^{2–4} To date, several methodologies have been developed to introduce different chemical functionalities into preassembled MOFs. These include covalent modification of the organic linkers,⁵ ligand exchange processes⁶ and postsynthetic metalations.^{7,8} However, the synthetic conditions of postsynthetic covalent modifications typically require long reaction times and high temperatures that many MOFs cannot sustain; and for those MOFs that can resist such conditions, the yields are only low to moderate. This is partly because the methods are based on solid–liquid phase processes, whereby reaction progress is limited by the diffusion of reagents inside the porous frameworks to reach the target sites, especially for MOFs whose surfaces are already partially tagged, as the surface groups block access to the pores.⁹

Solvent-less reactivity, particularly solid–gas phase reactivity, is a widely explored approach in metallurgy and polymer science. Indeed, reactive gases (e.g., fluorine gas in the steel industry) have been used to quantitatively passivate, cleave, or switch the hydrophobic character of diverse materials.¹⁰ However, there is scant precedent on solid–gas phase reactions

with MOFs.¹¹ We reasoned that such an approach could be used to overcome the aforementioned limitations in post-synthetic functionalization of MOF pores. Here, we demonstrate this concept by reporting transformation of the olefin groups of a UiO-66-type MOF into 1,2,4-trioxolane rings, which we then selectively converted into either aldehydes or carboxylic acids.

Ozone has proven to be a powerful oxidizing reagent for diverse chemistries under mild conditions.^{12,13} Of these reactions, ozonolysis of alkenes is arguably the most widely studied.^{14,15} Initially used for routine characterization of lipids and natural polymers, it is now employed for selective cleavage of olefinic bonds, as it enables regio-specific formation of aldehydes, ketones or carboxylic acids in mere minutes. This reaction involves the metastable intermediate 1,2,4-trioxolane. Due to their low stability, trioxolane rings are not easy to isolate; however, those that have been are strong antibacterial and therapeutic agents, especially in the form of ozonated oils or triglycerides. Moreover, trioxolane rings can be treated under mild reductive or oxidative conditions to form aldehyde moieties¹⁶ or carboxylic acids,¹² respectively.

Here, we report postsynthetic functionalization of the porous olefin-tagged UiO-66-type MOF, ZrEBDC, using controlled, solid–gas phase ozonolysis. We selected it because MOFs of this type exhibit high thermal and chemical stability and are resistant to aqueous and acidic conditions. Additionally, we chose 2-ethenylbenzene-1,4-dicarboxylic acid (H₂EBDC) as the organic ligand because it is a simple and robust linker with no reactive sites other than its olefin-tagged pendant arm (Figure 1a). We demonstrate that, by constantly streaming ozone through ZrEBDC, the pendant alkene groups can be quantitatively transformed into stable 1,2,4-trioxolane moieties on the pore walls, with no loss of single-crystallinity. Moreover,

Received: December 6, 2017

Published: January 24, 2018

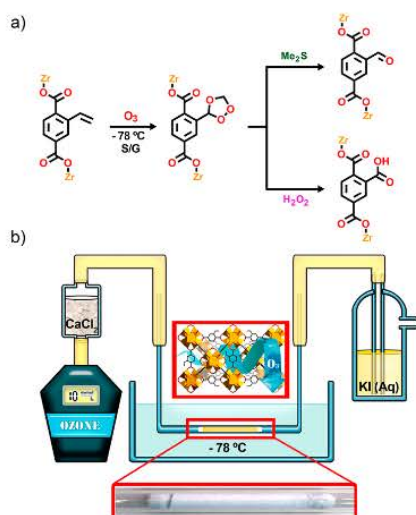


Figure 1. (a) Scheme of the postsynthetic modifications performed with ZrEBDC. (b) Scheme of the setup used for the ozonolysis of ZrEBDC. Bottom: photo of the tube containing the crystals.

optimized workup conditions enabled cleavage of these 1,2,4-trioxolane rings to selectively form aldehydes or carboxylic acids (Figure 1a).

Bulk ZrEBDC was synthesized by adding an equimolar mixture of H₂EBDC and ZrOCl₂·8H₂O into a mixture of DMF and formic acid, and the resulting slurry was then heated at 120 °C. After 12 h, the crude solid was washed twice with DMF and acetone, filtered, and activated under vacuum prior to any ozonolysis test. Colorless octahedral crystals of ZrEBDC suitable for single-crystal X-ray diffraction (SCXRD) were obtained by dissolving the two reagents in a 3:1 mixture of DEF/formic acid, and then heating the resulting solution from 25 to 135 °C (heating rate = 5 °C/min) for 72 h (Figure S2). The crystal structure of ZrEBDC revealed the formation of the archetypical UiO-66-like backbone, in which the olefinic side-chains of the EBDC linkers point inward toward the pores (Figures S3, S4).

In a typical ozonolysis experiment, activated ZrEBDC (50 mg) was packed inside a 3.4 mm diameter Pyrex tube (Figure 1b, Figure S1). Two cotton stoppers were added around the sample, and the tube was bent into a U-shape using a flame torch. One end was directly attached to an ozone generator, whereas the other was connected to vacuum. Before the reaction was started, the tube was immersed into a dry ice/acetone bath at -78 °C and purged under vacuum for 10 min. Under these conditions, ozone presents a moderate half-life and selectively reacts with unsaturated moieties. Excessive generation of ozone was avoided by adding an aqueous KI detector to the end of the setup. Once the sample had reached the proper temperature, a constant stream of O₃/air (10 mmol O₃/h, dried through CaCl₂) was blown into the reaction from one end of the tube. The stream was maintained until the KI solution changed from colorless to bright yellow (after ~30 min), which indicated that all the olefins had been transformed. The ozone stream was then stopped immediately. The sample, which showed a blue color, was left under vacuum for an additional 10 min to ensure that all the residual unreacted ozone was evacuated from inside the tube; after this, the sample became white again.

We characterized the ozonolyzed crystals (hereafter called **ozo-ZrBDC**) by SCXRD, which confirmed that they had retained the crystallinity and the UiO-66 framework of the starting MOF (Figure 2a). Analysis of the difference Fourier

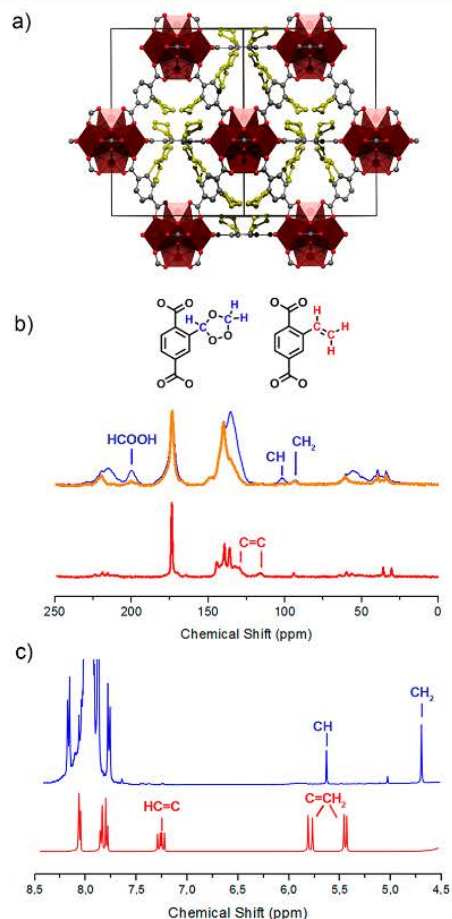


Figure 2. (a) Illustration of the single-crystal structure of **ozo-ZrBDC** across the [110] direction, highlighting the disordered 1,2,4-trioxolane moieties (yellow). (b) Solid-state ¹³C NMR spectra of ZrEBDC (red: CPMAS) and **ozo-ZrBDC** (blue: CPMAS; orange: CPPI-MAS). (c) ¹H NMR spectra after the ligand-exchange experiment (blue) and H₂EBDC (red).

maps revealed high electron-density within the pores of the framework, which we attributed to the 1,2,4-trioxolane groups, which we attributed to the 1,2,4-trioxolane groups. Due to the high symmetry of the framework, the positions of the 1,2,4-trioxolane groups were statistically disordered, which prevented us from refining their position in the cubic *Fm* $\bar{3}$ *m* space group of **ozo-ZrBDC**. Nonetheless, upon refining the framework atoms (including the defect sites and adsorbed species),¹⁷ we calculated a residual electron-density within the pores of 657 e⁻ per unit cell, using the program Squeeze.¹⁸ This value is in good agreement with the calculated number of electrons corresponding to the presence of one 1,2,4-trioxolane per organic linker within the unit cell (653 e⁻), which is the value obtained when 15% of the linker sites are considered to be defective (as suggested by our single-crystal refinement). To determine the orientation of the 1,2,4-trioxolane groups, we performed an additional single-crystal refinement in the monoclinic *C2*-space

group. Due to the low partial occupancies of the 1,2,4-trioxolane and their positional disorder, rigid body restraints were employed, whereby the conformation of the 1,2,4-trioxolane moiety was obtained from DFT based calculations. The 1,2,4-trioxolane rings appeared to be rotated relative to the plane of their corresponding linker phenyl ring, and in all cases oriented toward the inorganic SBUs, at short-contact distances (range: 2.3 to 3.1 Å) between the 1,2,4-trioxolane atoms and the carboxylic groups of the adjacent linkers, in good agreement with DFT calculations (Figure 2a).

To further confirm the presence of the 1,2,4-trioxolane groups, we compared solid-state ^{13}C NMR spectra, recorded in cross-polarization under magic-angle spinning (CPMAS), of the starting ZrEBDC and the ozo-ZrBDC. The two ^{13}C -peaks of the ethenyl group in ZrEBDC appear at 115.6 and 131.0 ppm (Figure 2b, red spectrum). As expected, the spectrum of ozo-ZrBDC lacks these two peaks and shows two new ones, at 93.6 and 101.8 ppm (Figure 2b, blue spectrum), which indicated successful conversion of all the olefinic moieties. We then recorded CPMAS-NMR spectra of each product under Polarization Inversion (CPPI),¹⁹ in order to differentiate between carbon sites coupled to protons with contrasted dipolar interaction. In the CPPI spectrum of ozo-ZrBDC (Figure 2b, orange spectrum), the resonance at 93.6 ppm is present, whereas that at 101.8 ppm is absent. These observations confirmed the formation of the 1,2,4-trioxolane ring, with the CH_2 peak located at 93.6 ppm and the CH peak, at 101.8 ppm; in agreement with literature data²⁰ and the solution study shown in the Supporting Information. We further confirmed this formation by performing a soft-ligand exchange experiment (Supporting Information), from which two peaks in solution ^1H NMR corresponding to the CH and CH_2 groups of the 1,2,4-trioxolane ring ($\delta = 5.61$ and $\delta = 4.65$ ppm, integrating in a 1:2 ratio) were identified (Figure 2c).

To gain further insight into the ozonolysis reaction, we systematically studied it using various reaction times (5, 10, 15, and 30 min). To this end, the degree of conversion of the olefinic groups into 1,2,4-trioxolane rings was monitored by measuring the ^1H NMR spectra of the digested samples (5% HF/DMSO- d_6), and then compared to that of the starting ZrEBDC (Section S4). The spectrum of the digested ZrEBDC showed the characteristic peaks of three nonequivalent olefinic protons at $\delta = 7.29$, 5.77, and 5.41 ppm, integrating in a 1:1:1 ratio. In contrast, the spectrum of the fully converted ozo-ZrBDC confirmed a quantitative fading of these olefinic signals in approximately 30 min of solid-gas interaction. It also confirmed the formation of four byproducts (two symmetric trioxolane-metathesis products, 1,2,4-benzenetricarboxylate, and formic acid; Scheme S1) in solution coming from exposing the released 1,2,4-trioxolane-containing linker under aggressive acidic conditions.¹⁴ The results at intermediate reaction times confirmed a direct correlation between the disappearance of the olefinic signals and the appearance of the new ones: with conversions of 33% at 5 min; 52% at 10 min; 78% at 15 min; and 100% at 30 min (as previously confirmed by CPMAS- ^{13}C NMR).

Samples exposed to different ozonation times were also subjected to standard conditions of MOF-activation (120 °C, 12 h), and their inner surface area was subsequently measured (Figure S25). Compared to the initial S_{BET} value for ZrEBDC (1300 m^2/g ; Figure S24), the ozonated samples exhibited decreasingly lower S_{BET} values in function of increasing ozonation time; the value for the fully converted ozo-ZrBDC

was 685 m^2/g . Remarkably, this surface area is consistent with a previously reported value for a UiO-66-like MOF with imidazole moieties as pendant groups ($S_{\text{BET}} = 538 \text{ m}^2/\text{g}$).²¹

Having demonstrated that ozonide rings can be stabilized inside a robust MOF, we next sought to explore the amenability of such rings in ozo-ZrBDC to be selectively reduced into aldehydes or oxidized into carboxylic acids (Figure 1a). For the former, ozo-ZrBDC was soaked overnight, with stirring, in an acidic aq. solution of dimethyl sulfide (Me_2S) as reducing agent, to convert the 1,2,4-trioxolane rings into aldehyde groups in a yield of 40% (Figure S20). The mild conditions of the workup did not allow for quantitative conversion of the stabilized trioxolanes, and all attempts to make the reduction more aggressive resulted in undesired formation of carboxylate byproduct. The S_{BET} of this ozo-ZrBDC partially functionalized with aldehyde moieties was 960 m^2/g (Figure S26). Alternatively, soaking ozo-ZrBDC overnight, with stirring, in aq. hydrogen peroxide (H_2O_2) drove oxidative cleavage of the 1,2,4-trioxolane rings to the corresponding carboxylic acids. This transformation was quantitative, as confirmed by ^1H NMR analysis (Figure S21). In both the aldehyde and carboxylic acid products, the UiO-66-type framework was preserved, as confirmed by powder XRD (Figure S23). Furthermore, SCXRD analysis of the crystals resulting from the aggressive oxidation confirmed that they also retained their single-crystal character. Remarkably, the position of the newly formed carboxylic acid groups could be determined through the refinement of the SCXRD data (Figure 3). In this case, the S_{BET} was found to be 301 m^2/g (Figure S27), which is in good agreement with those reported for this UiO-66-COOH ($S_{\text{BET}} = 350\text{--}400 \text{ m}^2/\text{g}$).²²

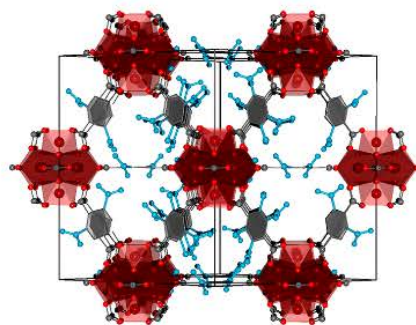


Figure 3. Illustration based on the single-crystal structure of ZrBDC-COOH across the [110] direction, highlighting the disordered -COOH moieties (blue).

In summary, we have reported a solvent-less, solid-gas, single-crystal-to-single-crystal, postsynthetic functionalization of a MOF using ozone. Streaming of ozone gas through an olefin-tagged UiO-66-type MOF at -78 °C provided quantitative transformation of the olefins into 1,2,4-trioxolane rings inside the robust MOF framework. When confined inside the MOF pores, this ring proved to be stable under standard heat and vacuum conditions for MOF activation, unlike in solution. Finally, an optimized workup enabled further single-crystal-to-single-crystal chemistry on these 1,2,4-trioxolane rings: reduction into the corresponding aldehyde or oxidation to the corresponding carboxylic acids, the latter in quantitative yield. We are confident that our methodology will offer new

insight into how gas molecules might be exploited for MOF chemistry that transcends common physisorption phenomena.

■ ASSOCIATED CONTENT

■ Supporting Information

The Supporting Information is available free of charge on the ACS Publications website at DOI: 10.1021/jacs.7b12913.

Experimental details, DFT calculations, NMR spectra and crystal structures (PDF)

Data for 0.25(C₂₀₄O_{123.2}Zr₂₄), 2.67(O₃) (CIF)

Data for 0.5(C_{81.6}O₆₄Zr₁₂), 1.98(O₃) (CIF)

Data for 0.5(C₈₈H₉₂O_{73.6}Zr₁₂), 2.57(O₃) (CIF)

Data for 0.25(C_{182.4}O_{171.3}Zr₂₄), 47.62(O_{0.11}) (CIF)

■ AUTHOR INFORMATION

Corresponding Authors

*inhar.imaz@icn2.cat

*daniel.maspocho@icn2.cat

ORCID

Felipe Gándara: 0000-0002-1671-6260

Charlotte Martineau-Corcós: 0000-0003-1887-1042

Rubén Mas-Ballesté: 0000-0003-1988-8700

Inhar Imaz: 0000-0002-0278-1141

Daniel Maspocho: 0000-0003-1325-9161

Author Contributions

[†]J.A. and H.X. contributed equally.

Notes

The authors declare no competing financial interest.

■ ACKNOWLEDGMENTS

This work was supported by EU-FP7-ERC-Co-615954, the Spanish MINECO (projects PN MAT2015-65354-C2-1-R and CTQ2015-64561-R), and the Catalan AGAUR (project 2014 SGR 80). It was also funded by the CERCA Program/Generalitat de Catalunya. J.A. and H.X. acknowledge the Generalitat de Catalunya for FI fellowships. C.M.C. thanks the Institut Universitaire de France (IUF) for financial support. We also thank for the award of beamtime at Diamond through rapid access mode, visit number mt18409-1, and for the allocation of computer time at the Centro de Computación Científica at the Universidad Autónoma de Madrid (CCC-UAM). ICN2 acknowledges the support of MINECO through the Severo Ochoa Centers of Excellence Program, under Grant SEV-2013-0295.

■ REFERENCES

- (1) (a) Janiak, C. *Dalt. Trans.* **2003**, *14*, 2781. (b) Kitagawa, S.; Kitaura, R.; Noro, S. *Angew. Chem., Int. Ed.* **2004**, *43*, 2334.
- (2) Wang, Z.; Cohen, S. M.; Stern, C. L.; Hupp, J. T.; Li, J.; Uribe-Romo, F. J.; Chae, H. K.; O'Keeffe, M.; Yaghi, O. M.; Chaudret, B.; Fischer, R. A. *Chem. Soc. Rev.* **2009**, *38*, 1315.
- (3) Burrows, A. D.; Cohen, S. M. *CrystEngComm* **2012**, *14*, 4095.
- (4) Cohen, S. M. *Chem. Rev.* **2012**, *112*, 970.
- (5) (a) Morris, W.; Doonan, C. J.; Furukawa, H.; Banerjee, R.; Yaghi, O. M. *J. Am. Chem. Soc.* **2008**, *130*, 12626. (b) Kim, M.; Cahill, J. F.; Prather, K. A.; Cohen, S. M. *Chem. Commun.* **2011**, *47*, 7629. (c) Morris, W.; Doonan, C. J.; Yaghi, O. M. *Inorg. Chem.* **2011**, *50*, 6853. (d) Luan, Y.; Qi, Y.; Gao, H.; Andriamantsoa, R. S.; Zheng, N.; Wang, G.; Čejka, J.; Valenzano, L.; Lamberti, C.; Lillerud, K. P.; Bordiga, S. *J. Mater. Chem. A* **2015**, *3*, 17320.
- (6) (a) Boissonault, J. A.; Wong-Foy, A. G.; Matzger, A. J. *J. Am. Chem. Soc.* **2017**, *139*, 14841. (b) Kim, M.; Cahill, J. F.; Su, Y.; Prather,

- (c) Liu, C.; Zeng, C.; Luo, T.-Y.; Merg, A. D.; Jin, R.; Rosi, N. L. *J. Am. Chem. Soc.* **2016**, *138*, 12045.
- (7) Bloch, W. M.; Burgun, A.; Coghlan, C. J.; Lee, R.; Coote, M. L.; Doonan, C. J.; Sumby, C. J. *Nat. Chem.* **2014**, *6*, 906.
- (8) Manna, K.; Zhang, T.; Lin, W. *J. Am. Chem. Soc.* **2014**, *136*, 6566.
- (9) Wang, Z.; Tanabe, K.; Cohen, S. M. *Chem. - Eur. J.* **2010**, *16*, 212.
- (10) (a) Layer, R. W.; Lattimer, R. P. *Rubber Chem. Technol.* **1990**, *63*, 426. (b) Miki, N.; Maeno, M.; Maruhashi, K.; Nakagawa, Y.; Ohmi, T. *Corros. Sci.* **1990**, *31*, 69. (c) Harshé, G. *J. Mater. Eng. Perform.* **1992**, *1*, 83.
- (11) Servalli, M.; Ranocchiaro, M.; Van Bokhoven, J. A.; Long, J. R.; Lillerud, K. P.; Tilset, M.; Fischer, R. W.; Fischer, R. A. *Chem. Commun.* **2012**, *48*, 1904.
- (12) Cochran, B. *Synlett* **2016**, *27*, 245.
- (13) Schiaffo, C. E.; Dussault, P. H. *J. Org. Chem.* **2008**, *73*, 4688.
- (14) Criegee, R. *Angew. Chem., Int. Ed. Engl.* **1975**, *14*, 745.
- (15) Geletneky, C.; Berger, S. *Eur. J. Org. Chem.* **1998**, *1998*, 1625.
- (16) Willand-Charnley, R.; Fisher, T. J.; Johnson, B. M.; Dussault, P. H. *Org. Lett.* **2012**, *14*, 2242.
- (17) Trickett, C. A.; Gagnon, K. J.; Lee, S.; Gándara, F.; Bürgi, H.-B.; Yaghi, O. M. *Angew. Chem., Int. Ed.* **2015**, *54*, 11162.
- (18) Spek, A. L. *Acta Crystallogr., Sect. C: Struct. Chem.* **2015**, *71*, 9.
- (19) Wu, X.; Zilm, K. W. *J. Magn. Reson., Ser. A* **1993**, *102*, 205.
- (20) (a) Soriano, N. U.; Migo, V. P.; Matsumura, M. *Chem. Phys. Lipids* **2003**, *126*, 133. (b) Segar, A.; Zanardi, I.; Chiasserini, L.; Gabbriellini, A.; Bocci, V.; Travagli, V. *Chem. Phys. Lipids* **2010**, *163*, 148.
- (21) Liang, J.; Chen, R.-P.; Wang, X.-Y.; Liu, T.-T.; Wang, X.-S.; Huang, Y.-B.; Cao, R. *Chem. Sci.* **2017**, *8*, 1570.
- (22) Ragon, F.; Campo, B.; Yang, Q.; Martineau, C.; Wiersum, A. D.; Lago, A.; Guillerme, V.; Hemsley, C.; Eubank, J. F.; Vishnuvarthan, M.; Taulelle, F.; Horcajada, P.; Vimont, A.; Llewellyn, P. L.; Daturi, M.; Devautour-Vinot, S.; Maurin, G.; Serre, C.; Devic, T.; Clet, G. *J. Mater. Chem. A* **2015**, *3*, 3294.

Postsynthetic Selective Ligand Cleavage by Solid–Gas Phase Ozonolysis Fuses Micropores into Mesopores in Metal–Organic Frameworks

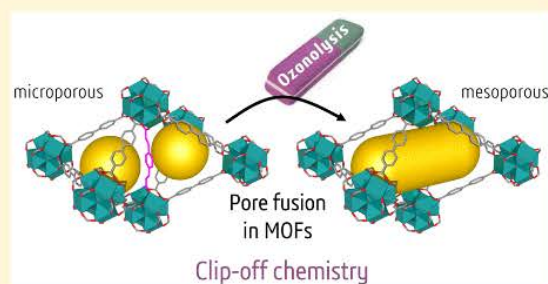
Vincent Guillerm,[†] Heng Xu,[†] Jorge Albalad,[†] Inhar Imaz,^{*,†} and Daniel Maspoch^{*,†,§}

[†]Catalan Institute of Nanoscience and Nanotechnology (ICN2), CSIC and The Barcelona Institute of Science and Technology, Campus UAB, Bellaterra, 08193 Barcelona, Spain

[§]ICREA, Pg. Lluís Companys 23, 08010 Barcelona, Spain

S Supporting Information

ABSTRACT: Herein we report a novel, ozone-based method for postsynthetic generation of mesoporosity in metal–organic frameworks (MOFs). By carefully selecting mixed-ligand Zr-fcu-MOFs based on organic ligand pairs in which one ligand has ozone-cleavable olefin bonds and the other ligand is ozone-resistant, we were able to selectively break the cleavable ligand via ozonolysis to trigger fusion of micropores into mesopores within the MOF framework. This solid–gas phase method is performed at room-temperature, and, depending on the cleavable ligand used, the resultant ligand-fragments can be removed from the ozonated MOF by either washing or sublimation. Compared to the corresponding highly microporous starting MOFs, the highly mesoporous product MOFs exhibit radically distinct gas sorption properties.



INTRODUCTION

Since the advent of metal–organic frameworks (MOFs) in the late 1990s,¹ these porous materials have shown promise for critical applications² such as gas storage,³ catalysis,⁴ drug delivery,⁵ thermal energy storage,⁶ sensors,⁷ etc. MOFs have become benchmark materials for adsorption, surpassing most traditional adsorbents for hydrogen storage,^{3a} methane storage,^{3b} CO₂/N₂ separation,⁸ etc. By marrying the advantages of the inorganic and organic chemistries, MOFs exhibit both polyfunctionality and a high degree of tunability, as well as the opportunity to postfunctionalize them.⁹ Among the main advantage of this tunability is the possibility to perform reticular chemistry^{1,4,10} through ligand functionalization, length/width^{10g} variation, and/or metal ion substitution, which enables strategic design and synthesis of materials for specific applications.

A remaining challenge in MOF chemistry is the creation of mesoscale cavities, which are necessary for increased storage capacity, encapsulation of large molecules, etc. Reticular chemistry strategies to surpass previous limits on pore size and cavity diameter include increasing the distance between the organic molecular building blocks and using longer or wider organic ligands.^{10c,11} However, many of the most well-known MOFs are associated with self-dual nets (*pcu*: MOF-5,^{1c} IRMOFs (isoreticular metal-organic framework) series,^{1d} MXFSIX MOFs¹²) or nets that can easily interpenetrate upon ligand elongation (*tbo*: HKUST-1 (Hong Kong University of Science and Technology),^{1e,13} *fcu*: UiO-66 (Universitetet i

Oslo),¹⁴ *acs*: MIL-88's (Material Institute Lavoisier),¹⁵ etc.). To avoid this problem, researchers have developed platforms based on topologies that cannot interpenetrate, such as IRMOFs-74^{10c} and *rht*-MOFs,¹⁶ which, thanks to the design of very ambitious organic ligands, currently hold porosity records.^{10e,11b,d}

Regrettably, systematic access to MOFs exhibiting hierarchical porosity from the micro- to the mesorange remains a challenge, as it currently demands use of complex organic ligands that are not commercially available.^{11c,17} Although MOFs were initially considered as structurally ideal, defect-free materials, numerous recent studies have highlighted the non-negligible level of structural defects and irregularities in these materials, which strongly influence their porosity and catalytic properties.^{17e,18} These findings suggest that access to hierarchically porous materials would require rational control over the structural defects within MOFs. Unfortunately, to date, only a few methods for generating and controlling such defects have emerged. One such strategy is to use large amounts of monotopic agents (known as *modulators*) in competition with the required polytopic ligand corresponding to the targeted MOFs.^{14b,19} Alternatively, rational design strategies such as transversal reticular chemistry also have proven invaluable for generating MOFs with ordered defects.^{10g} However, there are very few reports on engineering of defects and control of

Received: September 7, 2018

Published: October 13, 2018

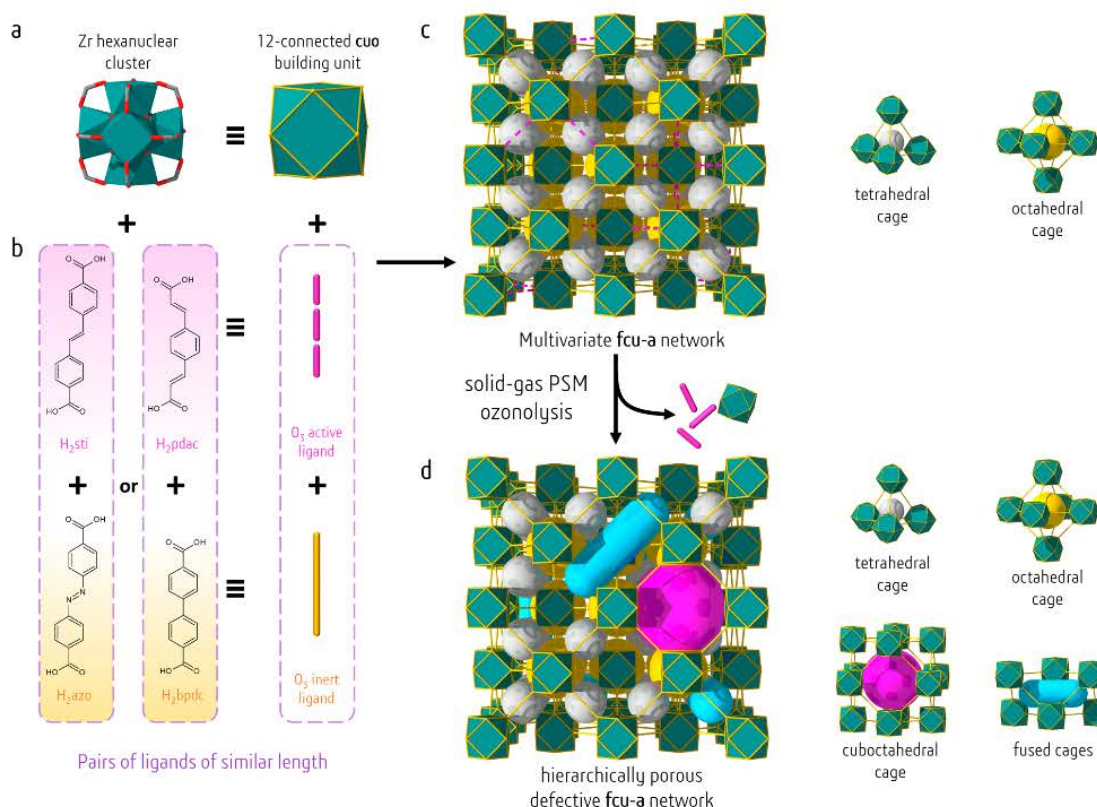


Figure 1. Postsynthetic modification of multivariate Zr-fcu-MOFs via solid–gas ozonolysis. Reaction of a) 12-connected hexanuclear clusters (cuo molecular building blocks) with b) pairs of organic ligands that are similar in length but show opposite reactivity to ozone (H₂sti and H₂azo or H₂pdc and H₂bpdc) yields. c) Multivariate MOFs with the fcu topology and two types of cages. Postsynthetic modification of the resultant MOFs through ligand cleavage by solid–gas ozonolysis results in d) Zr-fcu-MOFs with a defective network that exhibits hierarchical porosity generated upon fusion of micropores into larger pores (up to the mesoscale).

hierarchical porosity with commercially available and/or moderately sized ligands,^{17e,18e,20} and some of the existing methods require harsh chemical or thermal treatments.

Our group recently reported the first solid–gas phase covalent postsynthetic modification of a MOF: under mild conditions, we achieved quantitative conversion of the constituent olefin groups in single crystals of UiO-66-like MOF into trioxolane moieties, aldehydes, and/or carboxylates without compromising the crystallinity.²¹ Encouraged by the stability of the MOFs under these conditions, we envisioned exploiting this solid–gas phase ozonolysis²² method to cleave and remove selected organic ligands within MOFs. We hypothesized and later confirmed (*vide infra*) that ligands containing nonterminal olefin groups could be split into several parts (Scheme S1). When implemented in MOFs, these ligands can be selectively broken and subsequently removed from the framework, to provide an original and controllable method for postsynthetic fusion of micropores into mesopores.

Herein we report application of our postsynthetic strategy to selectively and quantitatively cleave and remove the organic ligands in two multivariate (MTV)²³ Zr-fcu-MOFs (Figure 1), thereby affecting their adsorption performance in gas uptake. By controlling the ozone inert/active ratio of ligands in these MOFs, we were able to control the final number of defects in their structures.

RESULTS AND DISCUSSION

Zr-fcu-azo/sti System. System Validation. Our ligand-removal strategy is only amenable to MOFs based on ligand pairs that exhibit the following characteristics: similar shape and length; similar reactivity under given reaction conditions; and opposite reactivity to ozone (Figure 1b). To this end, we selected two dicarboxylic acids: 4,4'-azobenzene dicarboxylic acid (H₂azo) and 4,4'-stilbene dicarboxylic acid (H₂sti) (with lengths ≈ 13.3 Å). The reactivity of each ligand to ozone was initially tested in solution, in *N,N'*-dimethylformamide (DMF), which was used to avoid π – π stacking of the ligands and to facilitate access of the ozone molecules to the olefin groups. Interestingly, the two acids showed diametric responses to ozone: H₂azo was unreactive, whereas H₂sti was fully converted into terephthalic acid (H₂bdc) and formylbenzoic acid (Hfba) (Scheme S1, Figure S18).

Having confirmed the suitability of H₂azo and H₂sti as a ligand pair, we then decided to choose an appropriate MOF for testing. We selected the robust Zr-fcu-MOF platform, which had already proven amenable to postsynthetic modification and ozone resistant.^{9b,d,21,24} Thus, we embarked on the synthesis of the resultant MOFs (Zr-fcu-azo²⁵ and Zr-fcu-sti²⁶) and testing of their response to ozonolysis. Both MOFs were synthesized by suspending ZrCl₄ and the corresponding

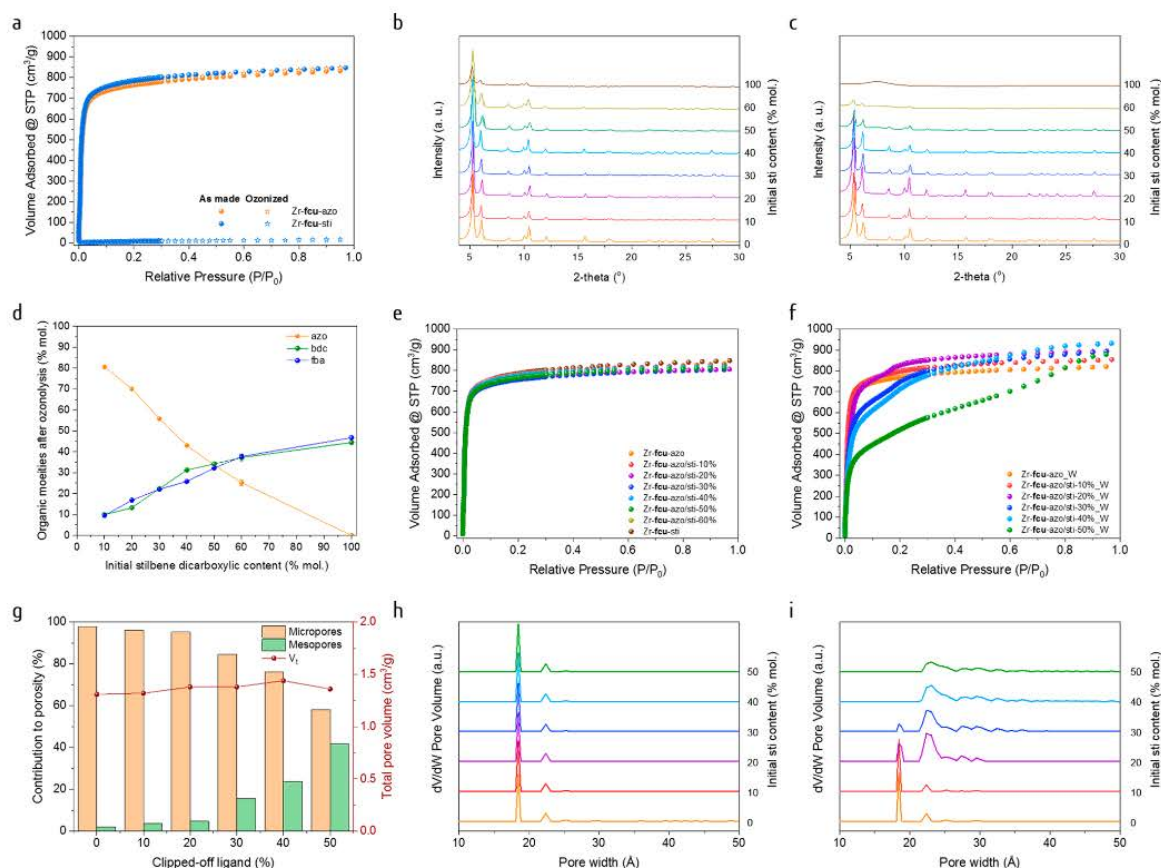


Figure 2. a) N_2 sorption isotherms for Zr-fcu-azo and Zr-fcu-sti before and after ozonolysis. b) PXRD diagrams for Zr-fcu-azo/sti-X%. c) PXRD diagrams for ozonated (OZ), washed Zr-fcu-azo/sti-X%. d) Remaining organic moieties in Zr-fcu-azo/sti-X% OZ, as derived from ¹H NMR spectra of digested samples. e) N_2 sorption isotherms (77 K) for Zr-fcu-azo/sti-X% OZ. f) N_2 sorption isotherms (77 K) for ozonated Zr-fcu-azo/sti-X% after washing (denoted here by "_W"). g) Change in total pore volume and in the relative contribution of microporosity and mesoporosity to total uptake, in Zr-fcu-azo/sti-X% OZ after washing, as calculated with the Dubinin–Radushkevich equation. h) Pore size distribution estimated by DFT (density functional theory) for Zr-fcu-azo/sti-X%. i) Pore size distribution estimated by DFT for ozonated, washed Zr-fcu-azo/sti-X%.

dicarboxylic ligand in DMF, in the presence of HCl and L-proline, and then heating the resulting mixture at 120 °C overnight in a scintillation vial. The resulting crystals (of Zr-fcu-azo or Zr-fcu-sti) were washed with DMF and then subjected to solvent exchange with acetone. As expected, N_2 sorption isotherms collected at 77 K confirmed comparable Brunauer–Emmett–Teller areas (A_{BET}) of 3025 m²/g for Zr-fcu-azo and 3065 m²/g for Zr-fcu-sti (Figure 2a). When submitted to ozone treatment for 30 min, Zr-fcu-azo retained its crystallinity and porosity, whereas Zr-fcu-sti collapsed into an amorphous, nonporous solid due to cleavage of all the ligands of the framework (Figures 2a, S2, S9).

Synthesis and Porosity of Zr-fcu-azo/sti-X%. To prepare multivariate Zr-fcu-MOFs containing specific ratios of azo/sti (ranging from 90:10 to 40:60), we used similar synthetic conditions as for Zr-fcu-azo but partially replaced the H₂azo with the appropriate amount of H₂sti. The phase purity of the resulting single crystals of Zr-fcu-azo/sti-X% ($X \approx 10, 20, 30, 40, 50, \text{ or } 60$ stilbene molar percentage) was confirmed by powder X-ray diffraction (PXRD; Figure 2b). The crystals varied in color from bright orange to colorless (Figure S1)

according to their constituent azo/sti ratio, which was confirmed by proton nuclear magnetic resonance (¹H NMR) of digested crystals (Figure S19, Tables S1, S3). Finally, N_2 sorption analysis performed at 77 K showed comparable uptake and type I isotherm for all different activated samples (Figure 2e). Indeed, all apparent A_{BET} values ranged from 3000 m²/g to 3065 m²/g, and total pore volumes ranged from 1.24 cm³/g to 1.28 cm³/g (Table 1). As expected, and similarly to reported values for comparable MOF systems,^{18e} the pore size distributions (PSD (pore size distribution), Figure 2h) of all Zr-fcu-azo/sti-X% are comparable: with a main pore population of ca. 18.4 Å attributed to the intrinsic porosity of the framework and a minor population of larger pores of ca. 22.4 Å attributed to some modulator related defects.

Ozonolysis of Zr-fcu-azo/sti-X%. To selectively break the sti ligands, we packed ca. 50 mg of Zr-fcu-azo/sti-X% into a L-shaped glass tube, connected on one side to the ozonator (through a CaCl₂ humidity trap) and, on the other side, to a vacuum pump (through a KI trap), to ensure a continuous flow of ozone through the column. The reaction was run at room temperature for 30 min. The ozonated Zr-fcu-azo/sti-X%

Table 1. Apparent BET Area, Micropore Volume, and Total Pore Volume of Zr-fcu-azo/sti-X%, before and after Ozonolysis and Washing

initial% sti	starting MOF			ozonated and washed MOF		
	A_{BET} (m^2/g)	$V_{\text{p}}^{\text{mic}}$ (cm^3/g)	$V_{\text{p}}^{\text{tot}}$ (cm^3/g)	A_{BET} (m^2/g)	$V_{\text{p}}^{\text{mic}}$ (cm^3/g)	$V_{\text{p}}^{\text{tot}}$ (cm^3/g)
0	3025	1.26	1.29	3030	1.24	1.27
10	3060	1.25	1.28	3115	1.27	1.32
20	3045	1.23	1.25	3130	1.31	1.38
30	3000	1.11	1.24	2680	1.17	1.38
40	3040	1.23	1.27	2580	1.10	1.44
50	3065	1.23	1.26	1860	0.79	1.36
60	3015	1.22	1.26	985	0.42	0.75
100	3065	1.26	1.31	nonporous		

materials maintained their high crystallinity after ozonolysis, as confirmed by PXRD (Figures S2–S10). ^1H NMR of digested, Zr-fcu-azo/sti-X%_{OZ} confirmed the full conversion of sti into bdc and fba for all samples (Figure S20, Table S4). The 1:1 bdc/fba ratio observed for all Zr-fcu-azo/sti-X%_{OZ} also indicated the stoichiometric character of the reaction (Figures 2d, 3a). As expected, based on our preliminary results with Zr-

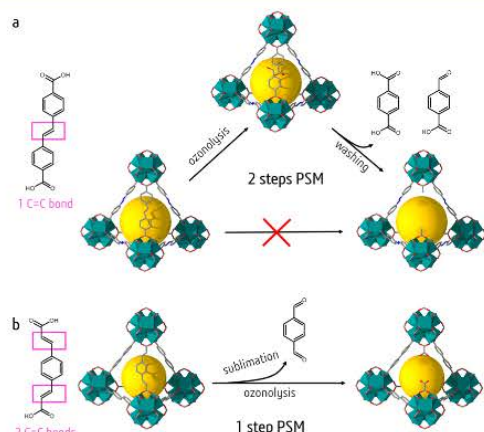


Figure 3. Postsynthetic generation of mesoporosity in MOFs. a) In Zr-fcu-azo/sti MOFs, removal of the sti ligand requires two steps: ozonolysis (to break the ligand) and washing. b) In contrast, in Zr-fcu-bpdc/pdac MOFs, removal of the pdac ligand requires only one step: ozonolysis (to break the ligand) and concomitant sublimation (to remove the central core). This is made possible by the two olefin groups in this ligand.

fcu-azo, the content of azo ligand in the framework was not affected by ozonolysis, thus confirming its high selectivity toward olefin bonds.

Washing of Zr-fcu-azo/sti-X%_{OZ}. To remove the organic and inorganic fragments trapped in the pores of the Zr-fcu-azo/sti-X%_{OZ}, we washed the ozonated crude product in a 0.5 M solution of acetic acid in DMF. The washed samples did not exhibit any marked difference in crystallinity compared to the corresponding crude products, as confirmed by PXRD (Figure S10), with one exception: Zr-fcu-azo/sti-60%_{OZ}. The washing step revealed that the latter had indeed lost crystallinity, which we attributed to a partial collapse of its framework upon loss of 60% of its ligands via ozonolysis. In all cases, ^1H NMR (Figures S21, S22 and Tables S5, S6) of the

washed Zr-fcu-azo/sti-X% revealed the absence of fba and the persistence of some bdc, which could not be fully removed (repeated washing did not remove any additional bdc).

Porosity Properties of Washed, Ozonated Zr-fcu-azo/sti-X%. After confirming that in the washed, ozonated Zr-fcu-azo/sti-X%, all the sti ligands had been broken (Figure S20), most of the resulting organic fragments had washed out (Figure S21), and the high crystallinity had remained (Figure S10c), we submitted these materials to N_2 sorption tests at 77 K (Figure 2f, Table 1). As expected, Zr-fcu-azo/sti-10% performed very similarly to the preozonated material, showing only slightly higher values for apparent A_{BET} ($3115 \text{ m}^2/\text{g}$ vs $3060 \text{ m}^2/\text{g}$) and total pore volume ($1.32 \text{ cm}^3/\text{g}$ vs $1.28 \text{ cm}^3/\text{g}$). Based on the Dubinin–Radushkevich (DR) equation,²⁷ the relative proportion of microporosity to the total pore volume was estimated to be 96% (Figure 2g). Although the washed ozonated Zr-fcu-azo/sti-20% showed a nearly identical value for this parameter (95%), its isotherm exhibited a shoulder/step characteristic from bigger pores, giving insights into the modified nature of the microporosity. The isotherms for the washed ozonated Zr-fcu-azo/sti-30% and Zr-fcu-azo/sti-40% did not show the type I shape of the isotherms of the corresponding starting MOFs, but rather they exhibited a small hysteresis on the desorption branch, characteristic of mesoporosity (Figures S29, S30). Notably, ozonolysis treatment reduced the apparent A_{BET} : for the washed ozonated Zr-fcu-azo/sti-30%, $2680 \text{ m}^2/\text{g}$ (vs $3000 \text{ m}^2/\text{g}$) and for the washed ozonated Zr-fcu-azo/sti-40%, $2580 \text{ m}^2/\text{g}$ (vs $3040 \text{ m}^2/\text{g}$) (Table 1). However, in both cases, this decrease was offset by a major increase in the proportion of pores with mesoscale dimensions, as derived from the DR equation (Figure 2g and Table S9): for the washed ozonated Zr-fcu-azo/sti-30%, 15% (vs 2%) and for the washed ozonated Zr-fcu-azo/sti-40%, 24% (vs 3%). Likewise, the total pore volume also increased in both cases: for the washed ozonated Zr-fcu-azo/sti-30%, $1.36 \text{ cm}^3/\text{g}$ (vs $1.24 \text{ cm}^3/\text{g}$) and for the washed ozonated Zr-fcu-azo/sti-40%, $1.44 \text{ cm}^3/\text{g}$ (vs $1.27 \text{ cm}^3/\text{g}$). Similar results were observed in the washed ozonated Zr-fcu-azo/sti-50%, which exhibited the most extreme change relative to the corresponding starting MOF: the contribution of the mesoporosity reached 42% of the total porosity (Figure 2g and Table S9), and the hysteresis characteristic from mesoporosity was clearly visible (Figure S31); consequently, its A_{BET} was only $1860 \text{ m}^2/\text{g}$ (vs $3065 \text{ m}^2/\text{g}$). Note that additional washing treatment did not affect the sorption properties (Figure S40a), excluding the hypothesis of structural etching sometimes observed through chemical treatment.^{18c,28}

The modification of the micro- vs mesoporosity ratio was also reflected by studying the PSD (Figure 2i). If no noticeable change was observed for the washed ozonated Zr-fcu-azo, a subtle appearance of pores of ca. 25 Å and above was noted for the washed ozonated Zr-fcu-azo/sti-10%. The washed ozonated Zr-fcu-azo/sti-20% and -30% showed a clear decrease of the initial main pore size of ca. 18.4 Å and an increase of the second population at ca. 22.4 Å, confirming that micropores are merged into wider pores. For these two samples, the formation of pores bigger than 25 Å was also visible. Finally, the initial main pores of ca. 18.4 Å completely vanished in washed and ozonated Zr-fcu-azo/sti-40% and -50%. In these cases, the pores were mainly observed at ca. 22.4 Å and spread over a wide range up to 50 Å. Albeit nonobserved through PXRD, the pore population centered at 22.4 Å could be attributed to the existence of nonordered reo

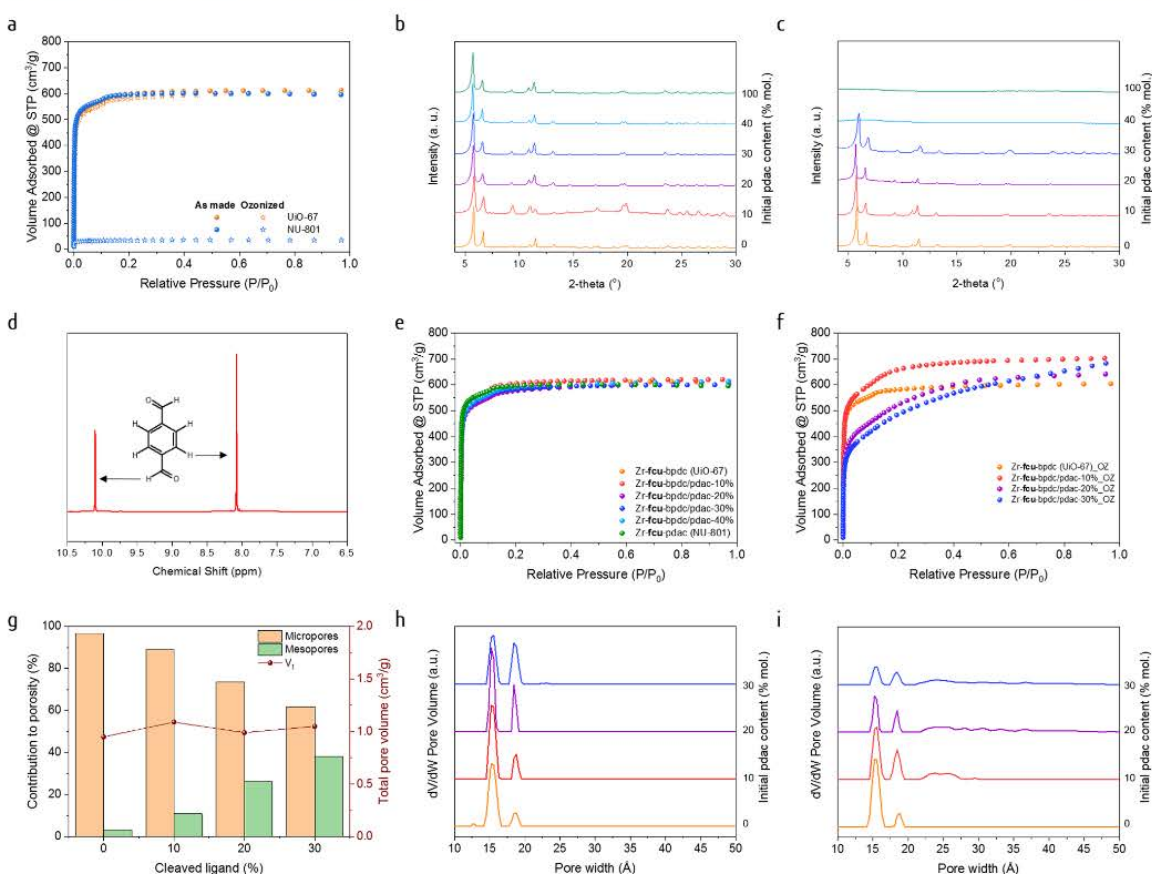


Figure 4. a) N_2 sorption isotherms for UiO-67 and NU-801 before and after ozonolysis. b) PXRD diagrams for Zr-fcu-bpdc/pdac-X%. c) PXRD diagrams for Zr-fcu-bpdc/pdac-X%_OZ. d) 1H NMR spectra of the sublimated terephthalaldehyde recovered by heating at 85 °C under vacuum after ozonolysis. e) N_2 sorption isotherms (77 K) for Zr-fcu-bpdc/pdac-X%. f) N_2 sorption isotherms (77 K) for Zr-fcu-bpdc/pdac-X%_OZ. g) Plot showing the overall stability of the total pore volume and evolution of the relative contribution of mesoporosity vs microporosity to total uptake, in Zr-fcu-bpdc/pdac-X%_OZ, as calculated with the Dubinin–Radushkevich equation. h) Pore size distribution estimated by DFT for Zr-fcu-bpdc/pdac-X%. i) Pore size distribution estimated by DFT for Zr-fcu-bpdc/pdac-X%_OZ.

motifs, resulting from the removal of inorganic clusters, as hypothesized in some comparable systems.^{18c}

Zr-fcu-bpdc/pdac System. Based on these pioneering results, we envisioned extending our method to a more challenging system. We considered that 4,4'-biphenyldicarboxylic acid (H_2 bpdc) and 1,4-phenylenediacrylic acid (H_2 pdac), found in the two Zr-fcu-MOFs UiO-67 and NU-801, would be a suitable ligand pair, given their geometric (length ≈ 11.3 Å) and chemical properties (*vide supra*). A particularity of H_2 pdac is its two olefin bonds (Figure 3b), which we reasoned would enable cutting of the ligand into three distinct parts, rather than two, as in H_2 sti (Scheme S2, Figure S23). In addition, we hypothesized that removal of the central part of the ligand could generate terephthalaldehyde, which could be sublimated under vacuum at moderate temperature -for example, during ozonolysis and/or during a classical presorption activation procedure (Figure 3). That turned out to be correct and, by obviating the washing step, represented a major improvement to our method.

Synthesis of Zr-fcu-bpdc/pdac-X%. Multivariate Zr-fcu-MOFs containing specific ratios of bpdc/pdac, from 100:0

(UiO-67)^{14,29} to 0:100 (NU-801),^{19b,30} were prepared from mixtures of $ZrCl_4$, H_2 bpdc, and H_2 pdac dissolved in DMF in the presence of trifluoroacetic acid (tfa) and heated at 120 °C for 72 h in a scintillation vial. The samples were washed with DMF overnight and then soaked in toluene for 3 days. The phase purity of the single crystals of Zr-fcu-bpdc/pdac-X% ($X \approx 10, 20, 30, 40\%$ pdac molar percentage) was confirmed by PXRD (Figure 4b), 1H NMR of digested crystals (Figure S24, Table S7), and N_2 sorption analysis performed at 77 K (Figure 4e and Table 2). The sorption isotherms for Zr-fcu-bpdc/pdac-X% were comparable ($2210 \text{ m}^2/\text{g} < A_{\text{BET}} < 2310 \text{ m}^2/\text{g}$ and $0.92 \text{ cm}^3/\text{g} < V_t < 0.96 \text{ cm}^3/\text{g}$). We observed a slight shoulder at a P/P_0 value of ca. 0.1, which we attributed to a higher number of initial defects in the structure, likely due to our use of a slightly different synthetic procedure than for Zr-fcu-azo/sti-X%. This is in fact reflected by the estimation of the PSD (Figure 4h), in which all samples presented two main contributions at ca. 15.2 and 18.4 Å; the bigger size being attributed (similarly as for Zr-fcu-azo/sti system, *vide supra*) to modulator-related defects.

Table 2. Apparent BET Area, Microporous, and Total Pore Volume of Zr-fcu-bpdc/pdac-*X*%, before and after Ozonolysis

% pdac initial	starting MOF			ozonated MOF		
	A_{BET} (m ² /g)	V_{μ} (cm ³ /g)	V_{t} (cm ³ /g)	A_{BET} (m ² /g)	V_{μ} (cm ³ /g)	V_{t} (cm ³ /g)
0	2250	0.91	0.93	2305	0.92	0.95
10	2295	0.95	0.96	2400	0.97	1.09
20	2210	0.91	0.95	1870	0.73	0.99
30	2245	0.93	0.94	1730	0.65	1.05
40	2265	0.93	0.95	nonporous		
100	2310	0.92	0.92	nonporous		

Ozonolysis of Zr-fcu-bpdc/pdac-*X*%. Analogously to the previous MOF pair (*vide supra*), the crystallinity and porosity of UiO-67 were unaffected by ozonolysis (Figures 4a, S11), but cleavage of the pdac ligands in NU-801 led to collapse of its framework and loss of its crystallinity and porosity (Figures 4a, S16). Having demonstrated this, we proceeded with ozonolysis of the Zr-fcu-bpdc/pdac-*X*% MOFs. ¹H NMR of all Zr-fcu-bpdc/pdac-*X*%_OZ highlighted the absence of any remaining pdac ligand (Figures S25, Table S8). Moreover, after the Zr-fcu-bpdc/pdac-*X*%_OZ were activated at 85 °C, a white solid was recovered in the cold trap (77 K) placed between the MOFs and the pump. This solid was confirmed by ¹H NMR to be terephthalaldehyde (Figure 4d), which, after cleavage of pdac, we were able to directly extract from the framework via sublimation, as anticipated.

Porosity of Zr-fcu-bpdc/pdac-*X*%_OZ. To investigate the effects of removing the central core of pdac on the porosity of the Zr-fcu-bpdc/pdac-*X*%_OZ, we performed N₂ sorption experiments on these MOFs (Figure 4f, Table 2). Upon extracting terephthalaldehyde from the backbone of Zr-fcu-bpdc/pdac-10%, the porosity was enhanced, as demonstrated by an increase in the apparent A_{BET} (from 2295 m²/g to 2400 m²/g). In this sample, besides the evolution of microporous pore volume (V_{μ}) (from 0.95 cm³/g to 0.97 cm³/g) not being significant, a more pronounced shoulder in the isotherm reflected a transformation of the microporosity. The emergence of some mesoporosity was revealed by the DR equation, with a contribution of 11% (vs 1%) to the total porosity. In contrast, upon further removal of pdac pillars, from Zr-fcu-bpdc/pdac-20%_OZ and Zr-fcu-bpdc/pdac-30%_OZ, the apparent A_{BET} decreased sharply: for Zr-fcu-bpdc/pdac-20%_OZ (A_{BET} = 1870 m²/g vs 2210 m²/g) and for Zr-fcu-bpdc/pdac-30%_OZ (A_{BET} = 1730 m²/g vs 2245 m²/g). The loss in microporosity for Zr-fcu-bpdc/pdac-20%_OZ (V_{μ} = 0.73 cm³/g vs 0.91 cm³/g) and for Zr-fcu-bpdc/pdac-30%_OZ (V_{μ} = 0.65 cm³/g vs 0.93 cm³/g) was offset by a major increase in the proportion of pores with mesoscale dimensions, as derived from the DR equation (Figure 4g, Table S10): for Zr-fcu-bpdc/pdac-20%_OZ, 26% (vs 4%) and for Zr-fcu-bpdc/pdac-30%_OZ, 38% (vs 1%). Likewise, the total pore volume also slightly increased in both cases: for Zr-fcu-bpdc/pdac-20%_OZ, 0.99 cm³/g (vs 0.95 cm³/g) and for Zr-fcu-bpdc/pdac-30%_OZ, 1.05 cm³/g (vs 0.94 cm³/g). As expected, Zr-fcu-bpdc/pdac-40%, which, upon ozonation, lost its crystallinity (Figure S15) due to structural collapse caused by removal of 40% of its ligands, was nonporous. Overall, the change in the porosity in Zr-fcu-bpdc/pdac-*X*% paralleled that of Zr-fcu-azo/sti-*X*%. However, in the former, these changes occurred at

lower percentages of ligand removal—presumably due to a greater number of defects in the starting MOFs.

The estimation of the PSD in this system also confirmed the evolution of the porosity toward mesopores (Figure 4i). While ozonolysis of UiO-67 did not affect the pore system of the pristine MOF, the appearance of pores distributed between 21.6 and 27.4 Å was clearly visible for the ozonated Zr-fcu-bpdc/pdac-10%, -20%, and -30%. In addition, the two initial main pore populations decreased in ozonated Zr-fcu-bpdc/pdac-20% and Zr-fcu-bpdc/pdac-30%. In these two last samples, the porosity population was extended up to ca. 50 Å, further confirming the fusion of micropores into novel mesopores.

CONCLUSIONS

In conclusion, we have developed a selective and quantitative method for postsynthetic modification of MOF porosity via ozonolysis. Through removal of organic ligands, our approach causes micropores to fuse into larger (mesoscale) pores in a controlled fashion and without any loss in total porosity. It selectively breaks the olefin bonds in organic ligands without affecting other organic moieties and can be applied for short reaction times (ca. 30 min) under mild conditions (room temperature). Moreover, we have demonstrated that ozonolysis can be used as a novel tool to selectively remove, and recover, specific fragments of molecules/frameworks through solid–gas manipulation.

EXPERIMENTAL SECTION

Materials and Instruments. *Reagents.* 4,4'-Stilbenedicarboxylic acid (H₂sti), 4,4'-biphenyldicarboxylic acid (H₂bpdc), and azobenzene-4,4'-dicarboxylic acid (H₂azo) were purchased from TCI Europe. Acetic acid, 1,4-phenylenediacrylic acid (H₂pdac), trifluoroacetic acid (tfa), zirconium chloride (ZrCl₄), L-proline, hydrochloric acid, potassium iodide, and anhydrous granular CaCl₂ (2–6 mm) were purchased from Sigma-Aldrich (Merck). *N,N*-Dimethylformamide (DMF) and acetone were obtained from Fisher Chemical. Toluene was purchased from Acros Organics. All the reagents and solvents were used as received. Pyrex tubes (ext Ø = 7 mm; in Ø = 5.5 mm; length = 150 mm) were purchased from Vidrasa S.A. The tubes were bent into an L-shape with a flame torch.

Optical Microscopy images were captured by a Zeiss Axio Observer Z1m optical microscope.

PXRD diagrams were recorded on an X'Pert PRO MPD analytical diffractometer (Panalytical) at 45 kV, 40 mA using CuK α radiation (λ = 1.5406 Å).

¹H NMR spectra were recorded on a Bruker Avance 400 NMR spectrometer (static magnetic field: 11.7 T) operating at Larmor frequencies of 400 MHz (¹H).

Ozonolysis treatment was performed using an ozone generator (N1668A from Ozonotec) generating a constant flow of 10.4 mmol/h at room temperature.

Volumetric N₂ sorption isotherms were collected at 77 K (N₂) using an ASAP 2020 HD (Micromeritics). Temperature was controlled by using a liquid nitrogen bath. Total pore volume (V_{t}) was calculated at P/P_0 = 0.95, and microporous volume (V_{μ}) was calculated using the Dubinin–Radushkevich equation. Pore size distribution was estimated using a density functional theory (DFT) model (N₂ – cylindrical pores–oxide surface) implemented in the Microactive 4.00 software with a regularization factor of 0.01.

Synthesis. *Synthesis of Zr-fcu-azo/sti-*X*%.* 4,4'-Stilbenedicarboxylic acid (H₂sti, 0.44-*x* mmol) and azobenzene-4,4'-dicarboxylic acid (H₂azo, *x* mmol) were suspended in 10 mL of DMF and sonicated for 30 min in a 23 mL scintillation vial. Then 5 mL of a DMF solution of ZrCl₄ (105 mg, 0.45 mmol), L-proline (250 mg, 2.17 mmol), and 45 μ L of conc. HCl was transferred into the vial and vortexed for 1 min.

After heating at 120 °C for 16 h, the reaction afforded orange octahedral crystals of Zr-fcu-azo/sti-X% (see the [Supporting Information](#) for more details about the H₂azo:H₂sti ratio in this synthesis).

Synthesis of Zr-fcu-bpdc/pdac-X%. ZrCl₄ (200 mg, 0.86 mmol), 1,4-phenylenediacrylic acid (H₂pdac, *x* mmol), and biphenyl-4,4'-dicarboxylic acid (H₂bpdc, *y* mmol) were dissolved by sonication in 10 mL of DMF in the presence of tfa (1 mL) in a 23 mL scintillation vial. After heating at 120 °C for 72 h, colorless octahedral crystals of Zr-fcu-bpdc/pdac-X% were obtained (see the [Supporting Information](#) for more details about the H₂bpdc/H₂pdac ratio in the synthesis).

Sample Activation. Activation of Zr-fcu-azo/sti-X%. Crystals of Zr-fcu-azo/sti-X% were soaked in 15 mL of DMF (refreshed after 4 h) and then subjected to solvent exchange in 15 mL of acetone (refreshed after 4 h). The supernatant was removed after decantation, and the crystals were dried at 65 °C. Sample purity was verified by PXRD (Figure 2b), and experimental azo/sti ratios were analyzed by ¹H NMR of the digested samples (Figure S19, Table S3). Crystals of Zr-fcu-azo/sti-X% were then transferred into a glass sorption cell and activated under dynamic vacuum at 85 °C prior to sorption experiments.

Activation of Zr-fcu-bpdc/pdac-X%. Crystals of Zr-fcu-bpdc/pdac-X% were soaked in 10 mL of DMF for 24 h and then subjected to solvent exchange for 72 h in 20 mL of toluene (refreshed twice per day). The supernatant was removed by filtration. The sample purity was verified by PXRD (Figure 4b), and the experimental bpdc/pdac ratios were analyzed by ¹H NMR of the digested samples (Figure S24, Table S7). Crystals of Zr-fcu-bpdc/pdac-X% were then transferred into a glass sorption cell and activated under dynamic vacuum at 85 °C prior to sorption experiments.

Ozonolysis Treatment. Ozonolysis of the Organic Ligands. In a typical procedure, 30 mg of the H₂azo, H₂sti, H₂bpdc, or H₂pdac was dissolved/dispersed in 20 mL of DMF. The solution was then transferred to a 50 mL three-necked round-bottom flask and was cooled to 0 °C using an ice–water bath. A constant ozone flux was blown into the solution through a glass pipet for 30 min under stirring. The crude reaction was then allowed to warm up to room temperature, and the solvent was removed *in vacuo*. The crude residue was collected and analyzed by ¹H NMR. ¹H NMR analysis confirmed the inert character of H₂azo and H₂bpdc, while revealing complete conversion, within 30 min, of the active linkers H₂sti and H₂pdac.

Ozonolysis of Zr-fcu-azo/sti-X% and Zr-fcu-bpdc/pdac-X%. A column of Zr-fcu-azo/sti-X% or Zr-fcu-bpdc/pdac-X% (50 mg to 100 mg) was loaded over a cotton stopper in an L-shaped Pyrex tube. The glass tube was connected to the solid–gas postsynthetic modification setup and purged under vacuum for 5 min. The ozone gas flow (10.4 mmol/h) was passed through the MOF column for 30 min. After 1–2 min, the aqueous potassium iodide solution turned yellow, indicating the whole MOF column had been exposed to oz1 atm. The recovered Zr-fcu-azo/sti-X%_OZ or Zr-fcu-bpdc/pdac-X%_OZ samples were further characterized by PXRD (Figures S10b, S17b) and ¹H NMR (Figures S20, S25, Tables S4, S8).

Acetic Acid Wash. About 50 mg of Zr-fcu-azo/sti-X%_OZ was vortexed for a few seconds in 20 mL of a 0.5 M acetic acid solution in DMF and left at room temperature for 24 h. The supernatant was removed and analyzed by ¹H NMR after decantation (Figure S22, Table S6). The crystals were washed twice with 20 mL of acetone. The acetone was removed after decantation, and the crystals were dried at 65 °C. The sample purity was verified by PXRD (Figure S10c), and the experimental organic content was analyzed by ¹H NMR of the digested samples (Figures S21, Table S5). Crystals of washed ozonated Zr-fcu-azo/sti-X% were then transferred into a glass sorption cell and activated under dynamic vacuum at 85 °C prior to the sorption experiments. Note that the Zr-fcu-bpdc/pdac-X% samples did not require this additional treatment to reveal their tuned porosity potential (Figures 3, S40b).

HF-Digestion Methodology. In a typical procedure, 10 mg of MOF was placed in an Eppendorf tube, to which 120 μL of a 5% aq. HF solution was added. The mixture was sonicated for 15 min, and then the slurry was placed in a 110 °C sand bath inside a fume hood

to evaporate overnight. The crude solid samples were highly soluble in DMSO-*d*⁶ without any need for addition of acid. Note that attempts with standard digestion methodologies were not successful, even when using the same quantities of HF and solvent. Therefore, the evaporation step is crucial for proper sample digestion. Moreover, the digested solutions obtained with our methodology did not require any specific (e.g., HF-resistant) PTFE NMR tubes.

■ ASSOCIATED CONTENT

Supporting Information

The Supporting Information is available free of charge on the ACS Publications website at DOI: 10.1021/jacs.8b09682.

Detailed synthetic procedures, microscopy, PXRD, ¹H NMR, additional sorption data (PDF)

■ AUTHOR INFORMATION

Corresponding Authors

*inhar.imaz@icn2.cat

*daniel.maspoch@icn2.cat

ORCID

Vincent Guillerm: 0000-0003-3460-223X

Jorge Albalad: 0000-0001-5850-6723

Inhar Imaz: 0000-0002-0278-1141

Daniel Maspoch: 0000-0003-1325-9161

Notes

The authors declare no competing financial interest.

■ ACKNOWLEDGMENTS

This work was supported by the Spanish MINECO (projects PN MAT2015-65354-C2-1-R), the Catalan AGAUR (project 2014 SGR 80), and the ERC under the EU-FP7 (ERC-Co 615954). It was also funded by the CERCA Programme/Generalitat de Catalunya. ICN2 acknowledges the support of the Spanish MINECO through the Severo Ochoa Centres of Excellence Programme, under Grant SEV-2013-0295. V.G. thanks the Generalitat de Catalunya for a Beatriu de Pinós fellowship (2014 BP-B 00155) (Marie Curie Fellowship, EU funded project ITHACA). J.A. and H.X. acknowledge the Generalitat de Catalunya for FI fellowships.

■ REFERENCES

- (1) (a) Subramanian, S.; Zaworotko, M. J. Porous Solids by Design: [Zn(4,4'-bpy)₂(SiF₆)₂]_n·xDMF, a Single Framework Octahedral Coordination Polymer with Large Square Channels. *Angew. Chem., Int. Ed. Engl.* **1995**, *34* (19), 2127–2129. (b) Kondo, M.; Yoshitomi, T.; Matsuzaka, H.; Kitagawa, S.; Seki, K. Three-Dimensional Framework with Channeling Cavities for Small Molecules: {[M₂(4,4'-bpy)₂(NO₃)₄·xH₂O]}_n (M = Co, Ni, Zn). *Angew. Chem., Int. Ed. Engl.* **1997**, *36* (16), 1725–1727. (c) Li, H.; Eddaoudi, M.; O'Keeffe, M.; Yaghi, O. M. Design and synthesis of an exceptionally stable and highly porous metal-organic framework. *Nature* **1999**, *402* (6759), 276–279. (d) Eddaoudi, M.; Kim, J.; Rosi, N.; Vodak, D.; Wachter, J.; O'Keeffe, M.; Yaghi, O. M. Systematic Design of Pore Size and Functionality in Isoreticular MOFs and Their Application in Methane Storage. *Science* **2002**, *295* (5554), 469–472. (e) Chui, S. S. Y.; Lo, S. M. F.; Charmant, J. P. H.; Orpen, A. G.; Williams, I. D. A chemically functionalizable nanoporous material [Cu₃(TMA)₂(H₂O)₃]_n. *Science* **1999**, *283* (5405), 1148–1150.
- (2) Themed issue: Metal-Organic Frameworks: (a) *Chem. Soc. Rev.* Zhou, H. C., Kitagawa, S., Eds.; **2014**, *43* (5), 5415–6172. Themed issue: Metal-Organic Frameworks: (b) *Chem. Rev.* Zhou, H. C., Long, J. R., Yaghi, O. M., Eds.; **2012**, *112* (2), 673–1268. Themed issue: Metal-Organic Frameworks: (c) *Chem. Soc. Rev.* Long, J. R., Yaghi, O. M., Eds.; **2009**, *38* (5), 1201–1508.

- (3) (a) Suh, M. P.; Park, H. J.; Prasad, T. K.; Lim, D.-W. Hydrogen Storage in Metal–Organic Frameworks. *Chem. Rev.* **2012**, *112* (2), 782–835. (b) He, Y.; Zhou, W.; Qian, G.; Chen, B. Methane storage in metal-organic frameworks. *Chem. Soc. Rev.* **2014**, *43* (16), 5657–5678. (c) Sumida, K.; Rogow, D. L.; Mason, J. A.; McDonald, T. M.; Bloch, E. D.; Herm, Z. R.; Bae, T.-H.; Long, J. R. Carbon Dioxide Capture in Metal–Organic Frameworks. *Chem. Rev.* **2012**, *112* (2), 724–781.
- (4) Farrusseng, D.; Aguado, S.; Pinel, C. Metal–Organic Frameworks: Opportunities for Catalysis. *Angew. Chem., Int. Ed.* **2009**, *48* (41), 7502–7513.
- (5) Horcajada, P.; Gref, R.; Baati, T.; Allan, P. K.; Maurin, G.; Couvreur, P.; Férey, G.; Morris, R. E.; Serre, C. Metal–Organic Frameworks in Biomedicine. *Chem. Rev.* **2012**, *112* (2), 1232–1268.
- (6) de Lange, M. F.; Verouden, K. J. F. M.; Vlucht, T. J. H.; Gascon, J.; Kapteijn, F. Adsorption-Driven Heat Pumps: The Potential of Metal–Organic Frameworks. *Chem. Rev.* **2015**, *115* (22), 12205–12250.
- (7) Kreno, L. E.; Leong, K.; Farha, O. K.; Allendorf, M.; Van Duyne, R. P.; Hupp, J. T. Metal–Organic Framework Materials as Chemical Sensors. *Chem. Rev.* **2012**, *112* (2), 1105–1125.
- (8) Belmabkhout, Y.; Guillerm, V.; Eddaoudi, M. Low concentration CO₂ capture using physical adsorbents: Are metal–organic frameworks becoming the new benchmark materials? *Chem. Eng. J.* **2016**, *296*, 386–397.
- (9) (a) Cohen, S. M. Postsynthetic Methods for the Functionalization of Metal–Organic Frameworks. *Chem. Rev.* **2012**, *112* (2), 970–1000. (b) Kim, M.; Cohen, S. M. Discovery, development, and functionalization of Zr(IV)-based metal–organic frameworks. *CryStEngComm* **2012**, *14* (12), 4096–4104. (c) Bloch, W. M.; Burgun, A.; Coghlan, C. J.; Lee, R.; Coote, M. L.; Doonan, C. J.; Sumbly, C. J. Capturing snapshots of post-synthetic metallation chemistry in metal–organic frameworks. *Nat. Chem.* **2014**, *6*, 906. (d) Garibay, S. J.; Cohen, S. M. Isoreticular synthesis and modification of frameworks with the UiO-66 topology. *Chem. Commun.* **2010**, *46* (41), 7700–7702.
- (10) (a) Yaghi, O. M.; O’Keeffe, M.; Ockwig, N. W.; Chae, H. K.; Eddaoudi, M.; Kim, J. Reticular synthesis and the design of new materials. *Nature* **2003**, *423* (6941), 705–714. (b) Chae, H. K.; Eddaoudi, M.; Kim, J.; Hauck, S. I.; Hartwig, J. F.; O’Keeffe, M.; Yaghi, O. M. Tertiary Building Units: Synthesis, Structure, and Porosity of a Metal–Organic Dendrimer Framework (MODF-1). *J. Am. Chem. Soc.* **2001**, *123* (46), 11482–11483. (c) Eddaoudi, M.; Moler, D. B.; Li, H. L.; Chen, B. L.; Reineke, T. M.; O’Keeffe, M.; Yaghi, O. M. Modular chemistry: Secondary building units as a basis for the design of highly porous and robust metal-organic carboxylate frameworks. *Acc. Chem. Res.* **2001**, *34* (4), 319–330. (d) Eddaoudi, M.; Kim, J.; O’Keeffe, M.; Yaghi, O. M. Cu₂[o-Br-C₆H₃(CO₂)₂]₂(H₂O)₂(DMF)₈(H₂O)₂: A Framework Deliberately Designed To Have the NbO Structure Type. *J. Am. Chem. Soc.* **2002**, *124* (3), 376–377. (e) Deng, H.; Grunder, S.; Cordova, K. E.; Valente, C.; Furukawa, H.; Hmadeh, M.; Gándara, F.; Whalley, A. C.; Liu, Z.; Asahina, S.; Kazumori, H.; O’Keeffe, M.; Terasaki, O.; Stoddart, J. F.; Yaghi, O. M. Large-Pore Apertures in a Series of Metal–Organic Frameworks. *Science* **2012**, *336* (6084), 1018–1023. (f) Furukawa, H.; Cordova, K. E.; O’Keeffe, M.; Yaghi, O. M. The Chemistry and Applications of Metal–Organic Frameworks. *Science* **2013**, *341* (6149), 1230444. (g) Guillerm, V.; Grancha, T.; Imaz, L.; Juanhuix, J.; Maspoch, D. Zigzag Ligands for Transversal Design in Reticular Chemistry: Unveiling New Structural Opportunities for Metal–Organic Frameworks. *J. Am. Chem. Soc.* **2018**, *140* (32), 10153–10157.
- (11) (a) Li, P.; Vermeulen, N. A.; Malliakas, C. D.; Gómez-Gualdrón, D. A.; Howarth, A. J.; Mehdi, B. L.; Dohnalkova, A.; Browning, N. D.; O’Keeffe, M.; Farha, O. K. Bottom-up construction of a superstructure in a porous uranium-organic crystal. *Science* **2017**, *356* (6338), 624–627. (b) Farha, O. K.; Eryazici, I.; Jeong, N. C.; Hauser, B. G.; Wilmer, C. E.; Sarjeant, A. A.; Snurr, R. Q.; Nguyen, S. T.; Yazaydin, A. Ö.; Hupp, J. T. Metal–Organic Framework Materials with Ultrahigh Surface Areas: Is the Sky the Limit? *J. Am. Chem. Soc.* **2012**, *134* (36), 15016–15021. (c) Férey, G.; Mellot-Draznieks, C.; Serre, C.; Millange, F.; Dutour, J.; Surblé, S.; Margiolaki, I. A chromium terephthalate-based solid with unusually large pore volumes and surface area. *Science* **2005**, *309* (5743), 2040–2042. (d) Guillerm, V.; Weseliński, Ł. J.; Belmabkhout, Y.; Cairns, A. J.; D’Elia, V.; Wojtas, Ł.; Adil, K.; Eddaoudi, M. Discovery and introduction of a (3,18)-connected net as an ideal blueprint for the design of metal-organic frameworks. *Nat. Chem.* **2014**, *6* (8), 673–680.
- (12) (a) Seki, K.; Takamizawa, S.; Mori, W. Design and Gas Adsorption Property of a Three-Dimensional Coordination Polymer with a Stable and Highly Porous Framework. *Chem. Lett.* **2001**, *30* (4), 332–333. (b) Nugent, P.; Belmabkhout, Y.; Burd, S. D.; Cairns, A. J.; Luebke, R.; Forrest, K.; Pham, T.; Ma, S.; Space, B.; Wojtas, Ł.; Eddaoudi, M.; Zaworotko, M. J. Porous materials with optimal adsorption thermodynamics and kinetics for CO₂ separation. *Nature* **2013**, *495* (7439), 80–84.
- (13) Sun, D.; Ma, S.; Ke, Y.; Collins, D. J.; Zhou, H.-C. An Interweaving MOF with High Hydrogen Uptake. *J. Am. Chem. Soc.* **2006**, *128* (12), 3896–3897.
- (14) (a) Cavka, J. H.; Jakobsen, S.; Olsbye, U.; Guillou, N.; Lamberti, C.; Bordiga, S.; Lillerud, K. P. A new zirconium inorganic building brick forming metal organic frameworks with exceptional stability. *J. Am. Chem. Soc.* **2008**, *130* (42), 13850–13851. (b) Schaate, A.; Roy, P.; Godt, A.; Lippke, J.; Waltz, F.; Wiebcke, M.; Behrens, P. Modulated Synthesis of Zr-Based Metal–Organic Frameworks: From Nano to Single Crystals. *Chem. - Eur. J.* **2011**, *17* (24), 6643–6651.
- (15) (a) Serre, C.; Mellot-Draznieks, C.; Surblé, S.; Audebrand, N.; Filinchuk, Y.; Férey, G. Role of solvent-host interactions that lead to very large swelling of hybrid frameworks. *Science* **2007**, *315* (5820), 1828–1831. (b) Dan-Hardi, M.; Chevreau, H.; Devic, T.; Horcajada, P.; Maurin, G.; Férey, G.; Popov, D.; Riekel, C.; Wuttke, S.; Lavalley, J.-C.; Vimont, A.; Boudewijns, T.; de Vos, D.; Serre, C. How Interpenetration Ensures Rigidity and Permanent Porosity in a Highly Flexible Hybrid Solid. *Chem. Mater.* **2012**, *24* (13), 2486–2492.
- (16) Eubank, J. F.; Nour, F.; Luebke, R.; Cairns, A. J.; Wojtas, Ł.; Alkordi, M.; Bousquet, T.; Hight, M. R.; Eckert, J.; Embs, J. P.; Georgiev, P. A.; Eddaoudi, M. On Demand: The Singular rht Net, an Ideal Blueprint for the Construction of a Metal–Organic Framework (MOF) Platform. *Angew. Chem., Int. Ed.* **2012**, *51* (40), 10099–10103.
- (17) (a) Sonnauer, A.; Hoffmann, F.; Froeba, M.; Kienle, L.; Duppel, V.; Thommes, M.; Serre, C.; Férey, G.; Stock, N. Giant Pores in a Chromium 2,6-Naphthalenedicarboxylate Open-Framework Structure with MIL-101 Topology. *Angew. Chem., Int. Ed.* **2009**, *48* (21), 3791–3794. (b) Koh, K.; Wong-Foy, A. G.; Matzger, A. J. A Crystalline Mesoporous Coordination Copolymer with High Microporosity. *Angew. Chem., Int. Ed.* **2008**, *47* (4), 677–680. (c) Feng, D.; Wang, K.; Su, J.; Liu, T.-F.; Park, J.; Wei, Z.; Bosch, M.; Yakovenko, A.; Zou, X.; Zhou, H.-C. A Highly Stable Zeotype Mesoporous Zirconium Metal–Organic Framework with Ultralarge Pores. *Angew. Chem., Int. Ed.* **2015**, *54* (1), 149–154. (d) Serra-Crespo, P.; Ramos-Fernández, E. V.; Gascon, J.; Kapteijn, F. Synthesis and Characterization of an Amino Functionalized MIL-101(Al): Separation and Catalytic Properties. *Chem. Mater.* **2011**, *23* (10), 2565–2572. (e) Feng, L.; Yuan, S.; Zhang, L.-L.; Tan, K.; Li, J.-L.; Kirchon, A.; Liu, L.-M.; Zhang, P.; Han, Y.; Chabal, Y. J.; Zhou, H.-C. Creating Hierarchical Pores by Controlled Linker Thermolysis in Multivariate Metal–Organic Frameworks. *J. Am. Chem. Soc.* **2018**, *140* (6), 2363–2372.
- (18) (a) Cliffe, M. J.; Wan, W.; Zou, X.; Chater, P. A.; Kleppe, A. K.; Tucker, M. G.; Wilhelm, H.; Funnell, N. P.; Coudert, F.-X.; Goodwin, A. L. Correlated defect nanoregions in a metal–organic framework. *Nat. Commun.* **2014**, *5*, 4176. (b) Bunck, D. N.; Dichtel, W. R. Mixed Linker Strategies for Organic Framework Functionalization. *Chem. - Eur. J.* **2013**, *19* (3), 818–827. (c) Park, J.; Wang, Z. U.; Sun, L.-B.; Chen, Y.-P.; Zhou, H.-C. Introduction of Functionalized Mesopores to Metal–Organic Frameworks via Metal–Ligand–Fragment Coas-

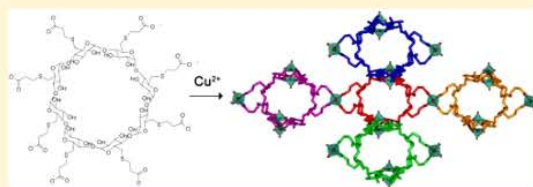
- sembly. *J. Am. Chem. Soc.* **2012**, *134* (49), 20110–20116. (d) Choi, K. M.; Jeon, H. J.; Kang, J. K.; Yaghi, O. M. Heterogeneity within Order in Crystals of a Porous Metal–Organic Framework. *J. Am. Chem. Soc.* **2011**, *133* (31), 11920–11923. (e) Yuan, S.; Zou, L.; Qin, J.-S.; Li, J.; Huang, L.; Feng, L.; Wang, X.; Bosch, M.; Alsalmeh, A.; Cagin, T.; Zhou, H.-C. Construction of hierarchically porous metal–organic frameworks through linker labilization. *Nat. Commun.* **2017**, *8*, 15356. (f) Fang, Z.; Bueken, B.; De Vos, D. E.; Fischer, R. A. Defect-Engineered Metal–Organic Frameworks. *Angew. Chem., Int. Ed.* **2015**, *54* (25), 7234–7254. (g) Bradshaw, D.; El-Hankari, S.; Lupica-Spagnolo, L. Supramolecular templating of hierarchically porous metal–organic frameworks. *Chem. Soc. Rev.* **2014**, *43* (16), 5431–5443. (h) Liang, W.; Coghlan, C. J.; Ragon, F.; Rubio-Martinez, M.; D’Alessandro, D. M.; Babarao, R. Defect engineering of UiO-66 for CO₂ and H₂O uptake – a combined experimental and simulation study. *Dalton Trans.* **2016**, *45* (11), 4496–4500.
- (19) (a) Wißmann, G.; Schaate, A.; Lilienthal, S.; Bremer, I.; Schneider, A. M.; Behrens, P. Modulated synthesis of Zr-fumarate MOF. *Microporous Mesoporous Mater.* **2012**, *152*, 64–70. (b) Gutov, O. V.; Molina, S.; Escudero-Adán, E. C.; Shafir, A. Modulation by Amino Acids: Toward Superior Control in the Synthesis of Zirconium Metal–Organic Frameworks. *Chem. - Eur. J.* **2016**, *22* (38), 13582–13587. (c) Marshall, R. J.; Hobday, C. L.; Murphie, C. F.; Griffin, S. L.; Morrison, C. A.; Moggach, S. A.; Forgan, R. S. Amino acids as highly efficient modulators for single crystals of zirconium and hafnium metal–organic frameworks. *J. Mater. Chem. A* **2016**, *4* (18), 6955–6963. (d) Qien, S.; Wragg, D.; Reinsch, H.; Svelle, S.; Bordiga, S.; Lamberti, C.; Lillerud, K. P. Detailed Structure Analysis of Atomic Positions and Defects in Zirconium Metal–Organic Frameworks. *Cryst. Growth Des.* **2014**, *14* (11), 5370–5372. (e) Trickett, C. A.; Gagnon, K. J.; Lee, S.; Gándara, F.; Bürgi, H.-B.; Yaghi, O. M. Definitive Molecular Level Characterization of Defects in UiO-66 Crystals. *Angew. Chem., Int. Ed.* **2015**, *54* (38), 11162–11167.
- (20) (a) Yue, Y.; Qiao, Z.-A.; Fulvio, P. F.; Binder, A. J.; Tian, C.; Chen, J.; Nelson, K. M.; Zhu, X.; Dai, S. Template-Free Synthesis of Hierarchical Porous Metal–Organic Frameworks. *J. Am. Chem. Soc.* **2013**, *135* (26), 9572–9575. (b) Yue, Y.; Fulvio, P. F.; Dai, S. Hierarchical Metal–Organic Framework Hybrids: Perturbation-Assisted Nanofusion Synthesis. *Acc. Chem. Res.* **2015**, *48* (12), 3044–3052. (c) Sun, L.-B.; Li, J.-R.; Park, J.; Zhou, H.-C. Cooperative Template-Directed Assembly of Mesoporous Metal–Organic Frameworks. *J. Am. Chem. Soc.* **2012**, *134* (1), 126–129. (d) Huang, H.; Li, J.-R.; Wang, K.; Han, T.; Tong, M.; Li, L.; Xie, Y.; Yang, Q.; Liu, D.; Zhong, C. An in situ self-assembly template strategy for the preparation of hierarchical-pore metal–organic frameworks. *Nat. Commun.* **2015**, *6*, 8847. (e) Qiu, L.-G.; Xu, T.; Li, Z.-Q.; Wang, W.; Wu, Y.; Jiang, X.; Tian, X.-Y.; Zhang, L.-D. Hierarchically Micro- and Mesoporous Metal–Organic Frameworks with Tunable Porosity. *Angew. Chem., Int. Ed.* **2008**, *47* (49), 9487–9491. (f) Zhao, Y.; Zhang, J.; Han, B.; Song, J.; Li, J.; Wang, Q. Metal–Organic Framework Nanospheres with Well-Ordered Mesopores Synthesized in an Ionic Liquid/CO₂/Surfactant System. *Angew. Chem., Int. Ed.* **2011**, *50* (3), 636–639. (g) Cao, S.; Gody, G.; Zhao, W.; Perrier, S.; Peng, X.; Ducati, C.; Zhao, D.; Cheetham, A. K. Hierarchical bicontinuous porosity in metal–organic frameworks templated from functional block co-oligomer micelles. *Chem. Sci.* **2013**, *4* (9), 3573–3577. (h) Wee, L. H.; Wiktor, C.; Turner, S.; Vanderlinden, W.; Janssens, N.; Bajpe, S. R.; Houthoofd, K.; Van Tendeloo, G.; De Feyter, S.; Kirschhock, C. E. A.; Martens, J. A. Copper Benzene Tricarboxylate Metal–Organic Framework with Wide Permanent Mesopores Stabilized by Keggin Polyoxometallate Ions. *J. Am. Chem. Soc.* **2012**, *134* (26), 10911–10919. (i) Shen, K.; Zhang, L.; Chen, X.; Liu, L.; Zhang, D.; Han, Y.; Chen, J.; Long, J.; Luque, R.; Li, Y.; Chen, B. Ordered macro-microporous metal–organic framework single crystals. *Science* **2018**, *359* (6372), 206–210.
- (21) Albalad, J.; Xu, H.; Gándara, F.; Haouas, M.; Martineau-Corcós, C.; Mas-Ballesté, R.; Barnett, S. A.; Juanhuix, J.; Imaz, I.; Maspoch, D. Single-Crystal-to-Single-Crystal Postsynthetic Modification of a Metal–Organic Framework via Ozonolysis. *J. Am. Chem. Soc.* **2018**, *140* (6), 2028–2031.
- (22) (a) Geletneky, C.; Berger, S. The Mechanism of Ozonolysis Revisited by ¹⁷O-NMR Spectroscopy. *Eur. J. Org. Chem.* **1998**, *1998* (8), 1625–1627. (b) Criegee, R. Mechanism of Ozonolysis. *Angew. Chem., Int. Ed. Engl.* **1975**, *14* (11), 745–752.
- (23) Deng, H.; Doonan, C. J.; Furukawa, H.; Ferreira, R. B.; Towne, J.; Knobler, C. B.; Wang, B.; Yaghi, O. M. Multiple Functional Groups of Varying Ratios in Metal–Organic Frameworks. *Science* **2010**, *327* (5967), 846–850.
- (24) (a) Marshall, R. J.; Forgan, R. S. Postsynthetic Modification of Zirconium Metal–Organic Frameworks. *Eur. J. Inorg. Chem.* **2016**, *2016* (27), 4310–4331. (b) Ragon, F.; Campo, B.; Yang, Q.; Martineau, C.; Wiersum, A. D.; Lago, A.; Guillerme, V.; Hemsley, C.; Eubank, J. F.; Vishnuvarthan, M.; Taulelle, F.; Horcajada, P.; Vimont, A.; Llewellyn, P. L.; Daturi, M.; Devautour-Vinot, S.; Maurin, G.; Serre, C.; Devic, T.; Clet, G. Acid-functionalized UiO-66(Zr) MOFs and their evolution after intra-framework cross-linking: structural features and sorption properties. *J. Mater. Chem. A* **2015**, *3* (7), 3294–3309.
- (25) (a) Yang, Q.; Guillerme, V.; Ragon, F.; Wiersum, A. D.; Llewellyn, P. L.; Zhong, C.; Devic, T.; Serre, C.; Maurin, G. CH₄ storage and CO₂ capture in highly porous zirconium oxide based metal–organic frameworks. *Chem. Commun.* **2012**, *48* (79), 9831–9833. (b) Hobday, C. L.; Marshall, R. J.; Murphie, C. F.; Sotelo, J.; Richards, T.; Allan, D. R.; Düren, T.; Coudert, F.-X.; Forgan, R. S.; Morrison, C. A.; Moggach, S. A.; Bennett, T. D. A Computational and Experimental Approach Linking Disorder, High-Pressure Behavior, and Mechanical Properties in UiO Frameworks. *Angew. Chem., Int. Ed.* **2016**, *55* (7), 2401–2405.
- (26) Marshall, R. J.; Richards, T.; Hobday, C. L.; Murphie, C. F.; Wilson, C.; Moggach, S. A.; Bennett, T. D.; Forgan, R. S. Postsynthetic bromination of UiO-66 analogues: altering linker flexibility and mechanical compliance. *Dalton Trans.* **2016**, *45* (10), 4132–4135.
- (27) Dubinin, M. M.; Zaverina, E. D.; Radushkevich, L. V.; Sorbtsiya, I. Struktura Aktivnykh Ugley 0.1. Issledovanie Adsorbtsii Organicheskikh Parov. *Zh. Fiz. Khim.* **1947**, *21* (11), 1351–1362.
- (28) Avci, C.; Ariñez-Soriano, J.; Carné-Sánchez, A.; Guillerme, V.; Carbonell, C.; Imaz, I.; Maspoch, D. Post-Synthetic Anisotropic Wet-Chemical Etching of Colloidal Sodalite ZIF Crystals. *Angew. Chem., Int. Ed.* **2015**, *54* (48), 14417–14421.
- (29) Guillerme, V.; Ragon, F.; Dan-Hardi, M.; Devic, T.; Vishnuvarthan, M.; Campo, B.; Vimont, A.; Clet, G.; Yang, Q.; Maurin, G.; Férey, G.; Vittadini, A.; Gross, S.; Serre, C. A series of isorecticular, highly stable, porous zirconium oxide based metal–organic frameworks. *Angew. Chem., Int. Ed.* **2012**, *51* (37), 9267–71.
- (30) Gomez-Gualdrón, D. A.; Gutov, O. V.; Krungleviciute, V.; Borah, B.; Mondloch, J. E.; Hupp, J. T.; Yildirim, T.; Farha, O. K.; Snurr, R. Q. Computational Design of Metal–Organic Frameworks Based on Stable Zirconium Building Units for Storage and Delivery of Methane. *Chem. Mater.* **2014**, *26* (19), 5632–5639.

A First Cyclodextrin-Transition Metal Coordination Polymer

Heng Xu,[†] Sabina Rodríguez-Hermida,[†] Javier Pérez-Carvajal,[†] Jordi Juanhuix,[‡] Inhar Imaz,^{*,†} and Daniel Maspoch^{*,§,†}[†]Catalan Institute of Nanoscience and Nanotechnology (ICN2), CSIC and The Barcelona Institute of Science and Technology, Campus UAB, 08193 Bellaterra Barcelona, Spain[‡]ALBA Synchrotron, 08290 Cerdanyola del Vallès, Barcelona, Spain[§]ICREA, Pg Lluís Companys 23, 08010 Barcelona, Spain

Supporting Information

ABSTRACT: The synthesis, X-ray crystallographic structure, and water uptake measurements of the first coordination polymer made of a cyclodextrin and a transition metal ion (in this case, Cu²⁺) are shown. This coordination polymer is made by connecting paddle-wheel Cu²⁺ units through a γ -cyclodextrin functionalized with eight carboxylate groups, is stable in water, and shows selective water-induced reversible structural transformations.



Coordination polymers (CPs)¹ can be defined as hybrid inorganic–organic networks extended in one, two, or three dimensions through coordination bonds. Since the introduction of the *design* concept by Robson in 1990s, the number of synthesized CPs has experienced an exponential growth.² Especially with the advent of the rich variety of permanent porosity properties found in CPs (known as porous CPs (PCPs) or metal–organic frameworks (MOFs)), CPs show today promise for myriad applications including gas adsorption, catalysis, separation, protective coatings for biomacromolecules, adsorption chillers or heat pumps, sensing and drug delivery, among many others.^{3–8} In this area, the continuous incorporation of new organic ligands has allowed developing novel CPs and fine-tuning their properties. Beyond the classical rigid multitopic carboxylate and N-donor based molecules that constitute the vast majority of ligands studied so far, recently an increasing interest exists in introducing more complex functional ligands to form CPs because they can directly incorporate their own functionalities in the coordination structures. For example, nanometer-sized molecules such as electro-active fullerenes,⁹ catalytic clusters such as polyoxometalates,¹⁰ and classical inclusion molecules such as calixarenes¹¹ or cyclodextrins^{12,13} (CDs) have started to be used as functional ligands for the formation of new CPs.

CDs are formed by six (α -CD), seven (β -CD), or eight (γ -CD) glucopyranose units bound via 1,4-glycosidic linkages. They show a toroid structure that is internally hydrophobic and externally hydrophilic. These characteristics make them very useful for encapsulating functional molecules in their cavities. For example, CDs able to encapsulate drugs can today be found in almost 40 different pharmaceutical products.¹⁴ However, even though CDs have been studied for more than hundred years, their coordination chemistry with metal ions has not been widely explored due to the difficulty to crystallize well-

defined systems and get correct structural data. In this area, some examples in which transition metal ions (e.g., Cu(II), Zn(II), Co(II), Mn(II), etc.) connect CDs forming sandwich or bucket-wheel type structures have been reported.¹⁵ More recently, Stoddart and co-workers have shown the possibility to assemble CDs with alkali metal ions to form PCP/MOFs. In 2010, they reported a first three-dimensional (3D) porous MOF (called CD-MOF-1) built up from combining γ -CD and K⁺ ions.¹² The X-ray crystal structure of CD-MOF-1 revealed the assembly of (γ -CD)₆ through K–OH linkages forming a body-centered cubic structure, wherein each K⁺ ion connects two CDs that occupy the faces of the cube. Later, similar CD-MOFs were obtained using salts of Rb⁺ (CD-MOF-2) and Cs⁺ (CD-MOF-3). Interestingly, both CD-MOF-1 and CD-MOF-2 showed BET surface areas of 1220 m²·g⁻¹ and 1110 m²·g⁻¹, respectively.

The inclusion properties of CDs offer interesting properties to CD-based MOFs. For instance, Stoddart et al. reported the highly selective adsorption of CO₂ by CD-MOF-2, by what is believed to be reversible carbon fixation inside the γ -CD involving carbonate formation and decomposition at room temperature. In addition, CD-MOF-1 and -2 demonstrated their ability to separate a wide variety of mixtures, including ethylbenzene from styrene, haloaromatics, terpenes, pinenes, and other chiral compounds.^{16–18}

Despite these many interesting properties, one of the limitations of these CD-based MOFs is still the weakness of the bond that supports these frameworks, that is, the bond between the hydroxyl groups of the γ -CD and the alkali metal ions. This means that these MOFs can be instantly dissolved in

Received: July 27, 2016

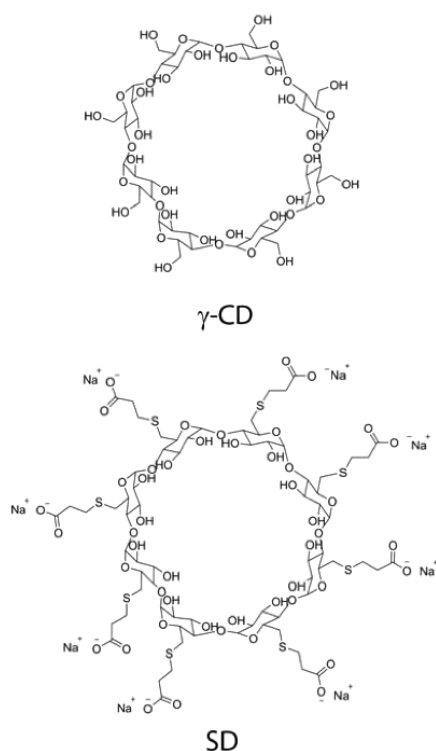
Revised: August 31, 2016

Published: September 13, 2016

an aqueous environment or degraded when exposed to humidity, greatly hampering some of their practical applications. To stabilize these CD-based MOFs, Furukawa et al. have explored the use of ethylene glycol diglycidyl ether to cross-link the CD-MOF-1 producing hydrogels.¹⁹ More recently, Falcaro et al. proposed a facile method to improve the hydrolytic stability of CD-MOF-1 by incorporating the hydrophobic C60 in their matrices, proving their potential use to encapsulate and release doxorubicin in aqueous media.²⁰

Another strategy that should provide robust coordination networks containing CDs is to strengthen the coordination bond between the CDs and the metal ions. Here, we report an initial step to achieve this goal by reporting the first example of a CP (hereafter called **Cu-SD**) made of a γ -CD and a transition metal ion. For this purpose, we used octakis-[6-deoxy-6-(3-mercaptopropanoic sodium)]- γ -cyclodextrin (SD; also known as org25969 or Sugammadex) as the organic ligand, and Cu^{2+} as the transition metal ion. SD is an octacarboxylate γ -CD in which each one of the eight C6 hydroxy groups of the γ -CD has been substituted with sulfurylpropionic acid arms (Scheme 1).

Scheme 1. Illustration of γ -CD and SD



SD is today a rapid and efficient selective relaxant binding agent approved by the FDA,²¹ acting as a trapping agent of the rocuronium bromide, a widely used neuromuscular blocker during anesthesia.^{22,23}

Cu-SD was prepared using a slow diffusion method. An aqueous solution (1.5 mL) containing SD (20 mg; 0.009 mmol) was initially placed into the bottom of a tube. Then, a mixture of $\text{H}_2\text{O}/\text{EtOH}$ (1:1, 4 mL) was carefully added on top of this solution as a buffer zone. Finally, an ethanolic solution

(1.5 mL) containing $\text{CuCl}_2 \cdot 2\text{H}_2\text{O}$ (20 mg; 0.117 mmol) was carefully added on top of the $\text{H}_2\text{O}/\text{EtOH}$ mixture. The diffusion proceeded at room temperature for a week in static conditions, resulting in blue cubic crystals suitable for single-crystal X-ray diffraction (SCXRD). The resulting crystals were collected by centrifugation and washed two times with a $\text{H}_2\text{O}/\text{EtOH}$ (1:1) mixture (2 mL each step) followed by another three times with pure EtOH (2 mL each step). The final yield was 40% (based on SD).

Crystallographic data were obtained from **Cu-SD** crystals at the XALOC beamline of the ALBA Synchrotron under synchrotron radiation ($\lambda = 0.79474 \text{ \AA}$) using a MD2M single axis diffractometer (Maatel, France) and a Pilatus 6M detector (Dectris, Switzerland).²⁴ Because of its sensitivity to solvent loss, a crystal of **Cu-SD** was measured mounted in a thin glass capillary suspended in the reaction mother liquor (mixture of $\text{H}_2\text{O}/\text{EtOH}$) and at a temperature of 293 K (to avoid water congelation). The crystal showed poor diffraction data with reflections of moderate intensity, which were further degraded rapidly after 120 deg oscillation. This poor density and fast degradation (seen in all measured crystals) could be attributed to the solvent loss. These 120 data frames were indexed, integrated, and scaled using the XDS²⁵ and IMOSFLM²⁶ programs. Absorption correction was not applied. The structure was solved by direct methods and subsequently refined by correction of F^2 against all reflections, using SHELXS2013 and SHELXL2013 within the WinGX package.^{27–29} All non-hydrogen atoms were refined with anisotropic thermal parameters by full-matrix least-squares calculations on F^2 using the program SHELXL2013. Hydrogen atoms were inserted at calculated positions and constrained with isotropic thermal parameters. The disorder associated with the oxygen atoms of the coordinated water molecules hindered the localization of their hydrogen atoms. One sulfur atom is distorted in two positions with 35% and 65% of occupancy. The structure contains some disorder molecules. Attempts to adequately model the disordered water molecules (10 electrons) were unsatisfactory; therefore, the PLATON/SQUEEZE routine was applied to mask out the disordered electron density.³⁰ The residual electron density was assigned to 46 water molecules per $[\text{Cu}_4(\text{SD})(\text{H}_2\text{O})_4]$ (1854 electrons per unit cell). Crystallographic and refinement data, bond distances, and angles and H-bond interactions are listed in Tables S1–S3.

The crystal data reveal the formation of a CP with formula $[\text{Cu}_4(\text{SD})(\text{H}_2\text{O})_4] \cdot 46\text{H}_2\text{O}$ (**Cu-SD**) that crystallizes in the tetragonal $P4m2n$ space group. **Cu-SD** shows a two-dimensional (2D) structure built up from linking the SD units through dinuclear $\text{Cu}_2(\text{OOC})_4(\text{H}_2\text{O})_2$ paddle-wheel clusters. Note here that other coordination systems found in the literature with transition metal ions are discrete structures, which are further extended via alkali metals or supramolecular bonds.¹⁵ In **Cu-SD**, all Cu^{2+} ions adopt a square base pyramid geometry (Addison parameter τ values within the 0.045–0.056 range) coordinated to four oxygen atoms belonging to four carboxylic groups and to one water molecule occupying the apical position (Figure 1a). The equatorial Cu–O distances vary between 1.92(1) Å and 1.98(1) Å . These distances are much shorter than the K–OH distances (between 2.79 and 2.84) found in CD-MOF-1¹² but are comparable to the Cu–O distances observed in the above-mentioned sandwich type Cu-CD systems (e.g., $\text{Li}_3[\text{Li}_3\text{Cu}_3(\alpha\text{-CDH}_6)_2]$ and $\text{Na}_3[\text{Na}_3\text{Cu}_3(\alpha\text{-$

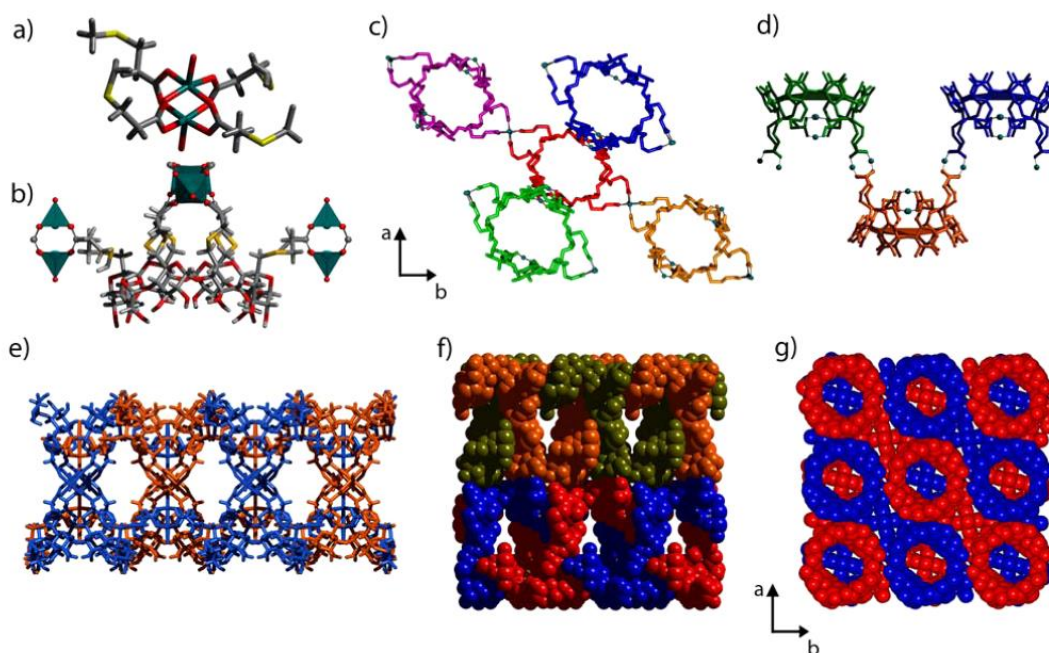


Figure 1. (a) Illustration of the paddle-wheel Cu^{2+} unit. (b) Illustration showing that each SD links to four paddle-wheel Cu^{2+} units. The dark cyan tetrahedral represents the coordination environment of Cu^{2+} ions. (c) View showing that each SD (red) is connected to four other SD linkers (pink, blue, orange, and green) through four paddle-wheel Cu^{2+} units. (d) Representation showing the coordination of each SD along the $\langle 110 \rangle$ direction. (e) Representation of the 2-fold interpenetrated layer along the $\langle 110 \rangle$ direction. (f, g) Space-filling view of the packing of the 2-fold interpenetrated layer, showing an offset ABA'B' packing. Each individual layer is highlighted with a different color. In (a) and (b), color code: O: red; S: yellow; C: gray; and Cu: dark cyan.

$\text{CDH}_{-6}]_2$ sandwiches, showing Cu–O distances between 1.90 and 1.98 Å.³¹

In the extended structure, each SD ligand is coordinated to eight Cu^{2+} ions. The eight flexible 3-mecaptopropionate arms are involved in the formation of four paddle wheel units involving four other SD ligands (Figure 1b,c). Each SD ligand shows four carboxylate arms pointing along the equatorial plane of the SD core, whereas the four remaining ones are pointing up or down of this equatorial plane with an angle of 70.5° (Figure 1d). This connectivity results in the formation of 2-fold interpenetrated layers running along the ab plane (Figure 1e). The interpenetrated layers establish H-bond interactions between them, involving the coordinated water molecule (O3w) and an O atom belonging to a carboxylate group (Figure S1 and Table S3). The association between these interpenetrated layers yields to an offset ABA'B' packing (Figure 1f,g). The multiple hydroxyl groups of the SD ligand are pointed out from the layers, allowing intermolecular H-bond interactions to be established between the sheets along the c axis (Table S3). Cu-SD displays a solvent accessible volume of 41.1% (corresponding to 5837.3 \AA^3) calculated using PLATON. This free volume is mainly located inside the two interpenetrated sheets (Figure S2), and it is filled of highly disordered water molecules (SQUEEZE results show a total of 46 guest water molecules).

As expected from what we observed during the crystal structure determination by SCXRD, crystals of Cu-SD rapidly lost guest molecules and underwent structural transformations when they were dried at room temperature. Powder X-ray

diffraction (PXRD) performed on the resulting crystals revealed a shift and a widening of most of the peaks, which was indicative of a loss of crystallinity as well as of structural rearrangements (Figure 2a). Unfortunately, cracking of the crystals during the drying process prevented us to solve the crystal structure corresponding to the dried phase by SCXRD (Figure 2b). Guest water molecules were fully removed from air-dried Cu-SD by heating the dried crystals under a vacuum (0.05 Torr) at 80°C for 1 h, as confirmed by elemental analysis and TGA measurements (Figure S3). Here, the PXRD pattern showed no significant differences in comparison to the dried sample at room temperature (Figure 2a), confirming that no further changes occur during this treatment. Attempts to study the adsorption of N_2 at 77 K and CO_2 at 195 K showed no evidence for gas uptake (Figure S4). However, these crystals (either dried at room temperature or heated under a vacuum at 80°C) showed evidence for the reversible uptake of water molecules. Indeed, when we reimmersed these crystals in water for 1 h, PXRD analysis of the resulting crystals revealed that the initial Cu-SD phase is recovered, demonstrating that the structural transition is reversible (Figure 2a,b). Remarkably, this reversible structural transition is selective to water since the PXRD of an air-dried Cu-SD sample soaked in liquid ethanol, dimethylformamide, and acetonitrile showed that the initial crystal structure cannot be recovered (Figure S5).

As this reversible transition must involve the loss and gain of many water molecules, we then investigated the water sorption properties of Cu-SD (Figure 2c,d). The collected water vapor sorption isotherm of a Cu-SD sample heated under a vacuum at

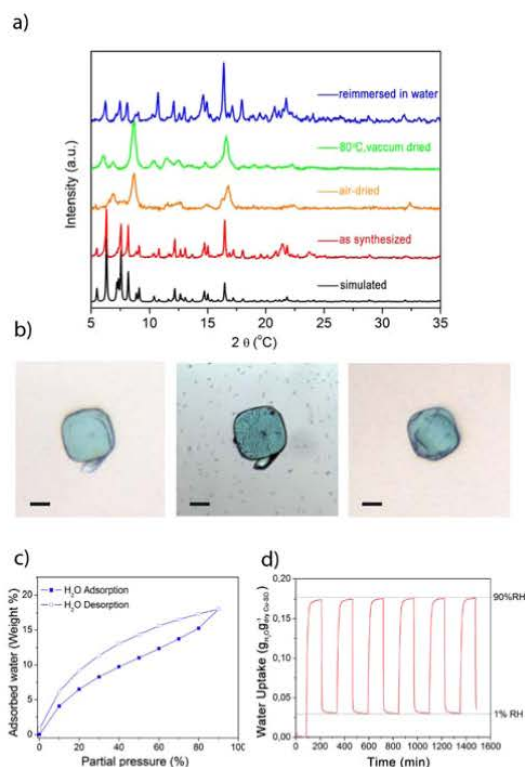


Figure 2. (a) PXRD patterns of as-synthesized Cu-SD (red), dried Cu-SD (orange), Cu-SD heated under a vacuum at 80 °C (green), and Cu-SD reimmersed in water (blue), compared to a simulated PXRD powder pattern (black). (b) Photographs of a single crystal of as-synthesized Cu-SD (left), dried Cu-SD showing cracking (center), and dried Cu-SD reimmersed in water (right). The scale bars correspond to 50 μm . (c) Water adsorption and desorption isotherm of Cu-SD. (d) Six consecutive cycles of water adsorption/desorption showing the perfect reversibility of the sorption process.

80 °C showed an adsorption branch representative of a type II trend.²⁷ The maximum water uptake was 0.175 g of water/g of Cu-SD at a RH of 90%, which corresponds to 28 water molecules per $[\text{Cu}_4(\text{SD})(\text{H}_2\text{O})_4]$. We then performed six water sorption/desorption cycles by alternately exposing the dry material to humid (90% RH) and dry (1% RH) environments (Figure 2d). Remarkably, the maximum uptake at 90% RH (ca. 17.5%) was not significantly modified with the number of cycles, confirming the stability of this framework.

In conclusion, we have reported the use of a γ -CD functionalized with eight carboxylate groups to synthesize the first cyclodextrin CP made with a transition metal ion. This CP shows a 2D coordination structure, is stable in water, and exhibits reversible structural transformations upon water sorption/desorption.

■ ASSOCIATED CONTENT

Supporting Information

The Supporting Information is available free of charge on the ACS Publications website at DOI: 10.1021/acs.cgd.6b01115.

Experimental section; crystallographic data; crystal structure images; TGA; and XRPD (PDF)

Accession Codes

CCDC 1495256 contains the supplementary crystallographic data for this paper. These data can be obtained free of charge via www.ccdc.cam.ac.uk/data_request/cif, or by emailing data_request@ccdc.cam.ac.uk, or by contacting The Cambridge Crystallographic Data Centre, 12 Union Road, Cambridge CB2 1EZ, UK; fax: +44 1223 336033.

■ AUTHOR INFORMATION

Corresponding Authors

*(I.I.) E-mail: inhar.imaz@icn2.cat.

*(D.M.) E-mail: daniel.masPOCH@icn2.cat.

Notes

The authors declare no competing financial interest.

■ ACKNOWLEDGMENTS

This work was supported by the Spanish MINECO (project PN MAT2012-30994) and the Catalan AGAUR (project 2014 SGR 80). I.I. thanks the MINECO for a RyC grant (RYC-2010-06530). H.X. thanks the Generalitat de Catalunya for an FI grant. ICN2 acknowledges the support of the Spanish MINECO through the Severo Ochoa Centers of Excellence Program, under Grant SEV-2013-0295.

■ REFERENCES

- (1) Batten, S. R.; Neville, S. M.; Turner, D. R. *Coordination Polymers: Design, Analysis and Application*; Royal Society of Chemistry: Cambridge, 2009.
- (2) Hoskins, B. F.; Robson, R. *J. Am. Chem. Soc.* **1989**, *111*, 5962–5964.
- (3) Kitagawa, S.; Kitaura, R.; Noro, S. *Angew. Chem., Int. Ed.* **2004**, *43*, 2334–2375.
- (4) Long, J. R.; Yaghi, O. M. *Chem. Soc. Rev.* **2009**, *38*, 1213–1214.
- (5) DeCoste, J. B.; Peterson, G. W. *Chem. Rev.* **2014**, *114*, 5695–5727.
- (6) Dou, Z.; Yu, J.; Cui, Y.; Yang, Y.; Wang, Z.; Yang, D.; Qian, G. *J. Am. Chem. Soc.* **2014**, *136*, 5527–5530.
- (7) Liang, K.; Ricco, R.; Doherty, C. M.; Styles, M. J.; Bell, S.; Kirby, N.; Mudie, S.; Haylock, D.; Hill, A. J.; Doonan, C. J.; Falcaro, P. *Nat. Commun.* **2015**, *6*, 7240–7247.
- (8) Jeremias, F.; Fröhlich, D.; Janiak, C.; Henninger, S. K. *New J. Chem.* **2014**, *38*, 1846–1852.
- (9) Peng, P.; Li, F.-F.; Neti, V. S. P. K.; Metta-Magana, A. J.; Echegoyen, L. *Angew. Chem., Int. Ed.* **2014**, *53*, 160–163.
- (10) Miras, H. N.; Vilá-Nadal, L.; Cronin, L. *Chem. Soc. Rev.* **2014**, *43*, 5679–5699.
- (11) Cholewa, P. P.; Dalgarno, S. J. *CrystEngComm* **2014**, *16*, 3655–3666.
- (12) Smaldone, R. A.; Forgan, R. S.; Furukawa, H.; Gassensmith, J. J.; Slawin, A. M. Z.; Yaghi, O. M.; Stoddart, J. F. *Angew. Chem., Int. Ed.* **2010**, *49*, 8630–8634.
- (13) Dodziuk, H. *Cyclodextrins and Their Complexes*; Wiley-VCH: Weinheim, Germany, 2006.
- (14) Loftsson, T.; Duchêne, D. *Int. J. Pharm.* **2007**, *329*, 1–11.
- (15) Prochowicz, D.; Kornowicz, A.; Justyniak, I.; Lewiński, J. *Coord. Chem. Rev.* **2016**, *306*, 331–345.
- (16) Gassensmith, J. J.; Furukawa, H.; Smaldone, R. A.; Forgan, R. S.; Botros, Y. Y.; Yaghi, O. M.; Stoddart, J. F. *J. Am. Chem. Soc.* **2011**, *133*, 15312–15315.
- (17) Gassensmith, J. J.; Kim, J. Y.; Holcroft, J. M.; Farha, O. K.; Stoddart, J. F.; Hupp, J. T.; Jeong, N. C. *J. Am. Chem. Soc.* **2014**, *136*, 8277–8282.
- (18) Hartlieb, K. J.; Holcroft, J. M.; Moghadam, P. Z.; Vermeulen, N. A.; Algaradah, M. M.; Nassar, M. S.; Botros, Y. Y.; Snurr, R. Q.; Stoddart, J. F. *J. Am. Chem. Soc.* **2016**, *138*, 2292–2301.

- (19) Furukawa, Y.; Ishiwata, T.; Sugikawa, K.; Kokado, K.; Sada, K. *Angew. Chem., Int. Ed.* **2012**, *51*, 10566–10569.
- (20) Li, H.; Hill, M. R.; Huang, R.; Doblin, C.; Lim, S.; Hill, A. J.; Baba-rao, R.; Falcaro, P. *Chem. Commun.* **2016**, *52*, 5973–5976.
- (21) Zhang, M.-Q.; Palin, R.; Bennett, D. J. PCT Int. Appl. WO 0140316 A1, 2001; *Chem. Abstr.* **2001**, *135*, 29151.
- (22) Adam, J. M.; Bennett, D. J.; Bom, A.; Clark, J. K.; Feilden, H.; Hutchinson, E.; Palin, R.; Prosser, A.; Rees, D. C.; Rosair, G. M.; Stevenson, D.; Tarver, G. J.; Zhang, M. Q. *J. Med. Chem.* **2002**, *45*, 1806–1816.
- (23) Bom, A.; Bradley, M.; Cameron, K.; Clark, J. K.; van Egmond, J.; Feilden, H.; MacLean, E. J.; Muir, A. W.; Palin, R.; Rees, D. C.; Zhang, M. Q. *Angew. Chem., Int. Ed.* **2002**, *41*, 265–270.
- (24) Juanhuix, J.; Gil-Ortiz, F.; Cuní, G.; Colldelram, C.; Nicolás, J.; Lidón, J.; Boter, E.; Ruget, C.; Ferrer, S.; Benach, J. *J. Synchrotron Radiat.* **2014**, *21*, 679–689.
- (25) Kabsch, W. *Acta Crystallogr., Sect. D: Biol. Crystallogr.* **2010**, *66*, 125–132.
- (26) Leslie, A. G. *Acta Crystallogr., Sect. D: Biol. Crystallogr.* **2006**, *62*, 48–57.
- (27) Sheldrick, G. M.; Dauter, Z.; Wilson, K. S.; Hope, H.; Sieker, L. C. *Acta Crystallogr., Sect. D: Biol. Crystallogr.* **1993**, *49*, 18–23.
- (28) Sheldrick, G. *Acta Crystallogr., Sect. C: Struct. Chem.* **2015**, *71*, 3–8.
- (29) Farrugia, L. J. *J. Appl. Crystallogr.* **2012**, *45*, 849–854.
- (30) Spek, A. L. *A Multipurpose Crystallographic Tool*; Utrecht University: Utrecht, The Netherlands, 2001.
- (31) Klüfers, P.; Piotrowski, H.; Uhlendorf, J. *Chem. - Eur. J.* **1997**, *3*, 601–608.